Advances in
Magnetic Force Microscopy

by

Óscar Iglesias-Freire

Doctoral thesis

submitted to Universidad Autónoma de Madrid in partial fulfilment of the requirements of the degree of

Doctor in Philosophy

Supervised by:

Dr. Agustina Asenjo Barahona

Material Science Institute of Madrid (ICMM-CSIC), April 2014

Descripción de la tesis

La piedra angular sobre la que se basa esta tesis es la microscopía de fuerza magnética y su uso para extraer información añadida del estudio de muestras ferromagnéticas. A lo largo del manuscrito, se ha estudiado una extensa variedad de materiales. Éste está dividido en cinco capítulos, cada uno de los cuales se centra en una temática diferente. Si bien aconsejamos seguir el orden establecido, el manuscrito está escrito de tal forma que el lector pueda **leer cada capítulo de manera independiente**. En algunas partes específicas se hace referencia a otros capítulos, en los que se comenta en más detalle algún asunto en particular.

El **primer capítulo**, a modo de **introducción**, repasa conceptos básicos que serán utilizados con frecuencia durante la descripción de los resultados experimentales. En primer lugar, se da una visión general sobre la situación actual en la que se encuentra el campo del nanomagnetismo, así como las principales razones que han motivado la realización de esta tesis. En segundo lugar, se recuerdan fundamentos básicos de magnetismo clásico y se introducen algunas de sus ecuaciones básicas. Después, se presentan las bases de la microscopía de fuerza atómica en modo dinámico, poniendo particular énfasis en la microscopía de fuerza magnética (*MFM*). Por último, se da una breve guía sobre la interpretación de las imágenes de *MFM*. Asimismo, al principio de cada capítulo se realiza una breve introducción específica a cada temática en él tratada.

El **segundo capítulo**, y el más extenso de esta tesis, versa sobre **procesos de inversión de la imanación** observados en diferentes muestras, bajo la influencia de un campo magnético externo. Está separado en dos partes, en función de si el comportamiento magnético está gobernado puramente por la forma de las nanoestructuras o si, en cambio, la estructura cristalina juega un papel importante. En el capítulo 2.2 se introduce un modo de medida particular basado en el *MFM* que permite la cuantificación de campos críticos en elementos nanoscópicos individuales. Este modo será usado con frecuencia en los capítulos restantes.

El **capítulo tercero** se centra en el solapamiento de información derivada de interacciones **electrostática y magnetostática**, que tiene lugar entre la punta sensora y muestras con marcados efectos de acumulación de carga. Se describe un método para separar, exitosamente, ambas contribuciones mediante el uso del llamado *Kelvin Probe Force Microscopy* durante los experimentos de *MFM*. Finalmente, se presentan dos aplicaciones de este método combinado en nanohilos planos de cobalto y en experimentos de *Scanning gate microscopy*.

El **cuarto capítulo** describe la fabricación y caracterización de **sensores de *MFM*** en nuestro laboratorio, obtenidos de una manera rápida, sencilla y económica. Estas puntas sensoras muestran

un rendimiento destacable en términos de resolución espacial, reducida influencia sobre el estado magnético de muestras blandas y sensibilidad química. Se muestra una comparación con diversas puntas comerciales, así como algunas aplicaciones prácticas. En particular, se presentan imágenes de *MFM* de alta resolución de diversas paredes de dominio. Estas puntas han sido utilizadas en los capítulos 2 y 3.

Por último, el **quinto capítulo** representa la parte más innovadora y original de esta tesis. Hace uso de la **disipación de energía** provocada por el campo magnético alterno al que está sujeta la punta de *MFM*, para extraer información de las propiedades magnéticas de la muestra. Bajo ciertas circunstancias, se observa una disminución de la disipación conforme la punta se aproxima a la muestra, y se da una explicación para este efecto. Asimismo, en el último apartado de esta tesis se describe una potencial aplicación de este fenómeno para la obtención de mapas tridimensionales del campo magnético que emerge de una muestra.

Al final del manuscrito, se resumen las principales conclusiones y se listan todos los artículos publicados en los que he participado.

En todos los trabajos descritos, se han realizado **simulaciones micromagnéticas** para apoyar y ayudar con la interpretación de los resultados experimentales; en cualquier caso, se consideran una herramienta complementaria para la explicación de los datos de *MFM*. La mayoría de las simulaciones han sido desarrolladas por nosotros, con las únicas excepciones de los capítulos 2.4 y 5.2. Para ello, se ha hecho uso del código *OOMMF*, de libre acceso, para simular cada muestra específica. Cabe mencionar que no se ha procedido a modificar ni desarrollar el código original.

Las referencias a otros trabajos publicados en libros o revistas de investigación se cuentan de manera independiente en cada capítulo y se encuentran listadas en la parte inferior de aquellas páginas en las que son mencionadas. De igual manera, el conteo de las figuras se reinicia al comenzar cada capítulo. Esta tesis ha sido escrita en lengua inglesa.

Outline of the thesis

The cornerstone of this thesis is the use of magnetic force microscopy to extract added information from ferromagnetic samples. An extensive variety of materials has been studied and is reported throughout the manuscript. It is divided in five chapters, each of which is devoted to a different subject. Although we recommend following the established order, the manuscript is written in such a way that the reader can **read any chapter independently**. At some specific points, reference to other chapters is pointed out, where more detail about a particular issue is given.

The **first introductory chapter** recalls basic concepts that will be often used when describing the experimental results. First, a short overview about state-of-the-art research in nanomagnetism is given, together with the main reasons that motivated the realization of this thesis. Then, fundaments on classical magnetism are presented and some of the basic equations are introduced. Third, basics of dynamic atomic force microscopy are reminded, with particular emphasis on magnetic force microscopy (*MFM*). Last, a brief guide on the interpretation of *MFM* images is given. In addition, a brief and more specific introduction is also given in the beginning of each chapter, focusing on the particular topic discussed.

The **second chapter** – and the longest one of this thesis – deals with **magnetization reversal processes** observed in different samples under the influence of an external magnetic field. It is separated in two parts, depending on whether the magnetic behavior is purely governed by the shape of the nanostructures or if the crystalline structure plays an important role. A particular *MFM*-based mode is presented in chapter 2.2, which allows for the quantification of critical fields in individual nanoscopic elements. This mode will be often used in the remaining chapters.

The **third chapter** focuses on the overlap of information of **electrostatic and magnetostatic** interactions taking place between the sensing tip and samples with strong charging effects. A successful separation of both contributions is then demonstrated by making use of the so-called *Kelvin* Probe Force Microscopy. Finally, applications of this combined method to cobalt stripes and scanning gate microscopy experiments are shown.

The **fourth chapter** describes the fabrication and characterization of **homemade *MFM* sensors** obtained in a fast, simple and low cost way. These *MFM* tips show a remarkable performance, in terms of spatial resolution, reduced influence in the magnetic state of soft samples and chemical sensitivity. A comparison with commercial probes is given and practical applications are shown. In

particular, high resolution *MFM* images of different kinds of domain walls are presented. These homemade probes have been used in chapters 2 and 3.

Last, the **fifth chapter** represents the most innovative and original part of this thesis. It makes use of the **energy dissipation** caused by the oscillating stray field sensed by the tip to extract information from the magnetic properties of the sample. Under certain circumstances, a counterintuitive decrease of dissipation is observed as the probe approaches the sample and an explanation for this effect is given. In addition, a potential application of this phenomenon for obtaining *3D* maps of the sample stray field is given in the very last section of this thesis.

At the end of this thesis, the main conclusions are summarized and all my published articles are listed.

In all the works reported, **micromagnetic simulations** have been used to support and help to interpret the experimental results. Nevertheless, they are considered to be a complementary tool in this thesis to explain *MFM* data. I carried out most of the presented simulations, with the only exceptions of chapters 2.4 and 5.2. For doing so, I made use of the free source *OOMMF* code for simulating each specific sample; however, I did not modified nor extended the original code.

References to other works published in books or research journals are counted in each chapter independently and are listed at the bottom of those pages where they are mentioned. In the same way, figure's count is reset in the beginning of every chapter. The language in which this thesis was written is the English language.

Chapter 1: Introduction

In this first chapter we introduce general concepts that will be repeatedly used throughout the manuscript, including fundamental ideas of magnetism and atomic force microscopy (*AFM*). Such basic concepts will be necessary to understand the results shown hereafter. More specific details will be given in the introductory part of each chapter, regarding further knowledge required to understand the studied phenomena, such as the use of advanced measuring modes (chapters 2 and 3) or basic theory for extracting dissipated energy from *AFM* measurements (chapter 5). We will start by briefly reviewing the main interests, achievements and ambitions of such an exciting topic as nanomagnetism and the motivation that gave rise to the realization of this thesis. Secondly, we will write the main equations of classical magnetism and shortly describe the energetic terms that are present in magnetic samples and are responsible for the different domain structures observed at the nanoscale. We will also introduce the use of micromagnetic simulations to predict spin configurations under specified conditions, which will be often used in the work shown in the following chapters. Then, we will give a general idea of the working procedure in atomic force microscopes and deduce basic equations that help to understand the underlying mechanisms, through which information about the sample properties is extracted. In particular, the case of magnetostatic interactions in magnetic force microscopy (*MFM*) will be commented to help with the interpretation of *MFM* images.

1. Nanomagnetism

Nanoscience and nanotechnology have already become one of the main pillars in nowadays research and these words are not odd anymore to the general audience. News about cutting-edge advances are often found on the front pages of the main newspapers and the society is aware of their potential for improving the quality of life and solving major problems it currently faces, as it is destined to become the new industrial revolution. Commercial developments are already available in sectors such as medicine, electronics, automotive industry, cosmetics, etc., which highlights one of the main added values of nanotechnology: its multidisciplinarity. Advances on nanotechnology have been possible mainly due to improvements in experimental techniques that allow fabricating and characterizing materials at the atomic and molecular scales. Such control promotes a much deeper understanding of the new phenomena that arise at this small scale, when the geometrical dimensions are in the order of some characteristic length. Figure 1. shows a diagram with the size scales of known elements:

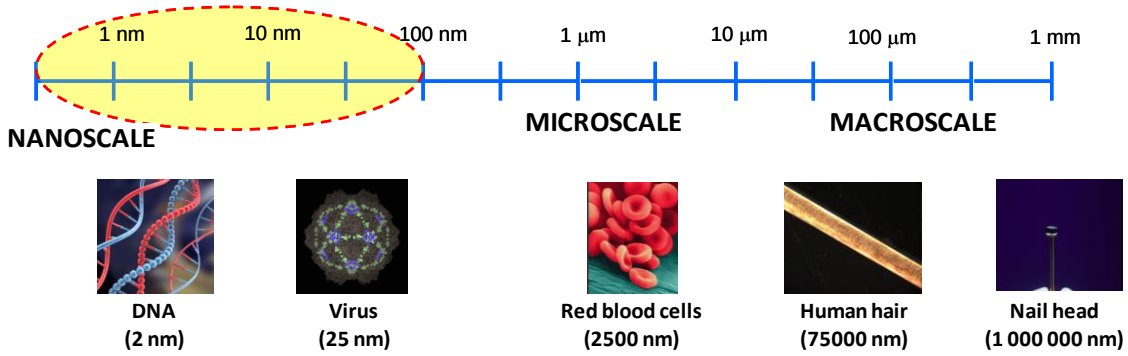

Figure 1.1: Length scale of well known objects.

Among all fields embraced by nanoscience, nanomagnetism is one of the most relevant elements. Nanomagnetism can be regarded as the area of research that deals with the magnetic properties of objects with at least one dimension in the nanoscopic range. Although the existence of permanent magnets has been known since ancient times, the origin of ferromagnetism is complex and requires the use of advanced physics involving quantum mechanics to explain such phenomenon. This quantum origin yields an opportunity to explore new physical phenomena and develop novel applications and devices. During the 20th century, magnetism became a central topic in condensed matter physics and, at the same time, remarkable progress was achieved in industrial applications. The exploration of fundamental phenomena in magnetic nanostructures enabled a tremendous development of computer industry, especially in the last three decades, that has had an imponderable impact in our ways of life. The benchmark corresponds to the discovery of giant magnetoresistance (*GMR*) in 1988 [1,2], considered the most outstanding breakthrough in nanomagnetism during the last quarter of the 20th century and for whose merits *Albert Fert* and *Peter Grünberg* were awarded the *Nobel Prize* in physics in 2007. These were the first experiments to reveal the spin dependence of the electric conductance, which gave birth to the field nowadays known as *spintronics*. In 1997, only 8 years later, modern hard disk drive systems based on *GMR* spin valves [3] were successfully implemented by Stuart S. P. Parkin at the *IBM* and allowed further miniaturizing and significant increase in storage density. Today, they are built in every computer and we make constant use of this technology. However, a physical limitation has already been reached in which thermal effects impede further miniaturization of conventional hard disks. This has driven the research on the field towards new sorts of logic devices in which information would be stored in domain walls of ferromagnetic elements such as domain wall logic [4], racetrack

[1] M. N. Baibich, J. M. Broto, A. Fert, F. N. van Dau, F. Petroff, P. Eitenne, G. Creuzet, A. Friedrich and J. Chazelas, Physical Review Letters 61 (1988) 2472-2475
[2] G. Binasch, P. Grünberg, F. Saurenbach and W. Zinn, Physical Review B 39 (1989) 4828-4830
[3] B. Dieny, V. S. Speriosu, S. S. P. Parkin, B. A. Gurney, D. R. Wilhoit and D. Mauri, Physical Review B 43 (1991) 1297
[4] D. A. Allwood, G. Xiong, C. C. Faulkner, D. Atkinson, D. Petit and R. P. Cowburn, Science 309 (2005) 1688-1692

memories [5] or magnetic vortices [6,7]. In addition to magnetic data storage, there have been seminal advances in earth sciences [8] and other promising applications that are being developed in areas such as ferrofluids [9] or magnetic sensors [10]. Remarkable is the potential that magnetic nanoparticles have shown in biology and medicine [11], either for biomolecule sorting and separation , drug delivery [12] or magnetic hyperthermia [13].

Bulk magnetometry techniques, such as vibrating sample magnetometry (*VSM*) and superconducting quantum interference devices (*SQUID*), allow extracting averaged information about the magnetization reversal processes and turn out to be very useful when dealing with macroscopic samples or very large numbers of similar nanostructures. This gives complementary information but, in the case of nanomagnetism, a precise understanding of the properties of magnetic nanostructures becomes a necessary step on the way to future technologies. On this step, experimental techniques with high enough resolution and sensitivity are essential for the detailed study of magnetic processes at the nanoscale.

There are many available techniques for analyzing magnetic nanostructures, each of them having its strength and drawback. Some, such as circular and linear dichroism, are based on the use of synchrotron radiation for elemental resolution and can yield quantitative information. The application of short laser pulses is converted into images through the magneto optical *Kerr* effect with high temporal resolution, allowing magnetization reversal processes to be studied in detail. Electron microscopes can also be used to extract useful information from magnetic samples in techniques such as *Lorentz* microscopy, electron holography, spin polarized low energy electron microscopy (*SPLEEM*) and scanning electron microscope with polarization analysis (*SEMPA*).

Especially relevant is the family of scanning probe microscopies, where spin polarized scanning tunnelling microscopy (*SP-STM*) is the only technique capable of truly atomic resolution [14,15]. In particular, magnetic force microscopy is probably the most extended magnetic imaging technique, also in the industrial sector, due to its versatility to achieve very high lateral resolution under most

[5] S. S. P. Parkin, M. Hayashi and L. Thomas, Science 320 (2008) 190-194
[6] Y. Gaidei, D. D. Sheka, F. G. Mertens, Applied Physics Letters 92 (2008) 012503
[7] R. Moriya, L. Thomas, M. Hayashi, Y. B. Bazaliy, C. Rettner and S. S. P. Parkin, Nature Physics 4 (2008) 368-372
[8] J. M. D. Coey, "Magnetism and Magnetic Materials" (Cambridge University Press, Cambridge 2009)
[9] S. Odenbach, "Ferrofluids" (Handbook of Magnetic Materials, vol. 16, Elsevier, Amsterdam 2006)
[10] M. Vázquez, A. Asenjo, M. P. Morales, K. R. Pirota, G. Badini-Confalonieri and M. Hernández-Vélez, "Sensors based on nanostructured materials" (Springer Science Business Medida, Berlin 2009)
[11] Q. A. Pankhurst, J. Conolly, S. K. Jones and J. Dobson, Journal of Physics D: Applied Physics 36 (2003) R167-R181
[12] C. Alexious and R. Jurgons, "Magnetic Drug Targeting" (Magnetism in Medicine: A Handbook, Wiley, Weinheim 2007)
[13] R. Hergt and W. Andrä, "Magnetic Hyperthermia and Thermoablation" (Magnetism in Medicine: A Handbook, Wiley, Weinheim 2007)
[14] R. Wiesendanger, Reviews of Modern Physics 81 (2009) 1495
[15] H. Hopster and H. P. Oepen, "Magnetic Microscopy of Nanostructures" (Springer, Berlin 2005)

possible conditions without sophisticated sample preparation. The first reports on *MFM* [16,17] date to 1987 and emerged as a variant of the atomic force microscope invented one year earlier [18]. Its lateral resolution reaches 10-15 nm with scan sizes up to around 100 μm, thus covering samples in the nanoscopic and mesoscopic regimes. It has already been widely used for imaging magnetic domain structures on a variety of magnetic materials, such as high density recording media [19], ultrathin films [20], patterned elements [21], nanoparticles [22], multilayers [23], nanowires [24], etc. Thus, *MFM* systems give the opportunity to work with a large variety of materials and study multiple domain structures.

2. Fundamentals of magnetism

Since the discovery in 1820 by Hans Christian Oersted of the true connection between electricity and magnetism and the invention by William Sturgeon of the electromagnet in 1824, a technological revolution was launched. However, despite the technical and theoretical triumphs of the electromagnetic revolution during the 19th century, the problem of explaining how a solid could possibly be ferromagnetic remained unsolved until the development of quantum mechanics. From the classical point of view, the magnetization of iron, M=1.76·10^6 A/m, implies a perpetually circulating surface current density of the same magnitude, which appears to be a wildly implausible proposition. According to modern physics, the magnetic properties of solids arise essentially from the magnetic moments of their atomic electrons. The interactions responsible for ferromagnetism were shown by *Werner Heisenberg* [25] in 1928 to be electrostatic in nature, originating from the quantum mechanical *Coulomb* repulsion of two nearby electrons, acting in conjunction with the *Pauli* principle.

In ferromagnetic materials, the direction along which electron spins point is a result of the competition between different energy terms that have diverse physical origins. The exchange energy is responsible for the existence in ferri- and ferromagnetic materials of a macroscopic net

[16] Y. Martin and H. K. Wickramasinghe, Applied Physics Letters 50 (1987) 1455
[17] J. J. Saenz, N. Garcia, P. Gruetter, E. Meyer, H. Heinzelmann, R. Wiesendanger, L. Rosenthaler, H. R. Hidberg and H. J. Guentherodt, Journal of Applied Physics 62 (1987) 4293
[18] G. Binnig, C. F. Quate and C. Gerber, Physical Review Letters 56 (1986) 930
[19] H. Mamin, D. Rugar, J. Stern, B. Teris and S. Lambert, Applied Physics Letters 53 (1988) 1563
[20] H. Mamin, D. Rugar, J. Stern, R. Fontana and P. Kasiraj, Applied Physics Letters 55 (1989) 318
[21] A. Wadas, P. Grütter and H. Guntherodt, Journal of Vaccuum Science Technology A8 (1990) 416
[22] M. Lederman, S. Schultz and M. Ozaki, Physical Review Letters 73 (1994) 1986
[23] H. Hug, B. Stiefel, A. Moser, I. Parashikov, A. Klieznik, D. Lipp, H. Guntherodt, G. Bochi, D. Paul and R. O'Handley, Journal of Applied Physics 79 (1996) 5609
[24] L. Billiard, J. Miltat, A. Thiaville, S. Dubois, J. Duvail and L. Piraux, Journal of Magnetism and Magnetic Materials 190 (1998) 1
[25] W. Heisenberg, Zeitschrift für Physik 49 (1928) 619-636

magnetization in the absence of external fields. *Heisenberg* described the quantum mechanical energy splitting between pairs of interacting neighboring electrons by the famous Hamiltonian:

$$H = -2 \cdot \hbar^2 \cdot \sum_{i>j} J_{ij} \cdot \widehat{\boldsymbol{S_1}} \cdot \widehat{\boldsymbol{S_2}} \qquad \textbf{(1.1)}$$

Positive values of the exchange constant ($J > 0$) indicate a ferromagnetic interaction, which tends to align the two spins parallel to each other. Normally, exchange interactions are very short-ranged, confined to electrons in orbitals on the same atom (intra-atomic exchange) or nearest neighbor atoms (direct exchange) but longer-ranged interactions can occur via intermediary atoms and this is termed superexchange. When calculating numerically the exchange energy term, the following expression is commonly used (see appendix A.1):

$$\frac{E_{exchange}}{V} = \frac{A}{{M_S}^2} \cdot \left[|\nabla \cdot M_x|^2 + \left|\nabla \cdot M_y\right|^2 + |\nabla \cdot M_z|^2 \right] \qquad \textbf{(1.2)}$$

where A is the exchange stiffness and M_S the saturation magnetization.

A second energy term in solids is related to the anisotropic character of crystalline lattices. A ferromagnetic material is said to have magneto-crystalline anisotropy if it takes more energy to magnetize it in certain crystalline directions than in others. The orbital motion described by the electrons around the nuclei couples with the electric crystalline field and gives rise to the first order contribution to magneto-crystalline anisotropy due to the spin-orbit coupling. A second order arises due to the mutual interaction of the magnetic dipoles but is often neglected. This effect is weak compared to the exchange interaction but of great relevance since materials with high magnetic anisotropy are usually hard to demagnetize; these are called *hard* ferromagnetic materials [26]. For example, the high anisotropy of rare earth metals (elements that present a strong spin-orbit coupling) is mainly responsible for the hardness of rare earth based magnets. On the other hand, materials with low magnetic anisotropy are usually called *soft* ferromagnets and their magnetization is easy to change. Analytical expressions for estimating the anisotropy energies, as well as the easy axis orientations in different crystal systems can be found in the literature [27], the most common formulae being:

[26] From J. M. D. Coey, "Magnetism and Magnetic Materials" (Cambridge University Press, Cambridge 2009): "*The terms hard and soft for magnets originated from the mechanical properties of the corresponding magnetic steels*"
[27] G. H. O. Daalderop, P. J. Kelly and M. F. H. Schuumans, Physical Review B 41 (1990) 11919-11937

$$\frac{E_{anisotropy}}{V} = \begin{cases} (K_1 \cdot \sin^2\theta + K_2 \cdot \sin^4\theta) & , \quad Uniaxial\ systems \\ \frac{K_1}{{M_S}^4} \cdot \left({M_x}^2 \cdot {M_y}^2 + {M_y}^2 \cdot {M_z}^2 + {M_z}^2 \cdot {M_x}^2\right) & , \quad Cubic\ systems \end{cases} \quad \textbf{(1.3)}$$

The first and second order magneto-crystalline anisotropy constants K_1 and K_2 have units of energy density, vary with temperature and are determined experimentally.

Third, whenever an external magnetic field is applied, a magnetic torque is exerted in misaligned magnetic moments that try to minimize their energy by orienting with the field. This term is called the Zeeman energy and has an analytical expression of the form [28]:

$$\frac{E_{Zeeman}}{V} = -\mu_0 \cdot \vec{\boldsymbol{M}} \cdot \vec{\boldsymbol{H}}_{\boldsymbol{ext}} \quad \textbf{(1.4)}$$

Last, there is an interaction between the spins themselves. The magnetostatic or dipolar energy can be considered as the interaction of the magnetic moments present in the sample with the field generated by the sample itself. It gives rise to coupling between neighboring nanostructures (if the field considered is generated by a neighboring object) or to the so-called demagnetizing energy (if the field arises from the same magnetized object). This energy term is commonly written in the following way:

$$E_{demag} = -\frac{\mu_0}{2} \cdot \int \vec{\boldsymbol{M}} \cdot \vec{\boldsymbol{H}}_{\boldsymbol{demag}} \cdot dV \quad \textbf{(1.5)}$$

where the integration is carried out over the whole volume of the ferromagnetic object, taken as a continuum. Note that the factor ½, as compared to the expression for the Zeeman energy, appears from the reciprocity principle, since the magnetic field emerges from spins within the sample. Due to its long range character, the magnetostatic energy depends on the shape of the system and leads to the commonly called *shape anisotropy*. The proper calculation of the magnetostatic energy belongs to the area of micromagnetism and is computationally costly. Deriving an expression for $\vec{\boldsymbol{H}}_{\boldsymbol{demag}}$ one gets (see appendix A.2):

$$\frac{E_{demag}}{V} = \frac{\mu_0}{8\pi} \cdot \vec{\boldsymbol{M}} \cdot \left[\iiint \vec{\nabla} \cdot \vec{\boldsymbol{M}}\left(\vec{\boldsymbol{r}'}\right) \cdot \frac{\vec{\boldsymbol{r}} - \vec{\boldsymbol{r}'}}{\left|\vec{\boldsymbol{r}} - \vec{\boldsymbol{r}'}\right|^3} \cdot d^3r' - \iint \hat{\mathbf{n}} \cdot \vec{\boldsymbol{M}}\left(\vec{\boldsymbol{r}'}\right) \cdot \frac{\vec{\boldsymbol{r}} - \vec{\boldsymbol{r}'}}{\left|\vec{\boldsymbol{r}} - \vec{\boldsymbol{r}'}\right|^3} \cdot d^2r' \right] \quad \textbf{(1.6)}$$

[28] L. D. Landau and E. M. Lifshitz, "Dynamics of continuous media" (Pergamon Press, 1981)

Nevertheless, a simple approximation can be made if the sample is considered to be a homogeneously magnetized ellipsoid, defining the demagnetizing factor *N* as:

$$\overrightarrow{\boldsymbol{H}}_{\boldsymbol{demag}} = -N \cdot \overrightarrow{\boldsymbol{M}} = -N \cdot M_S \cdot \hat{\boldsymbol{u}} \Rightarrow E_{demag} = -\frac{\mu_0}{2} \cdot N \cdot M_S \cdot V$$

with $\hat{u}$ being a unit vector along the direction of the uniform magnetization.

For a specific sample, the competition between all these energy terms results in a stable configuration that minimizes the overall energy. Very small samples will be governed by the exchange energy, which is intrinsically short range and strong, resulting in a single domain configuration along the magneto-crystalline easy axis. However, as the size is increased the long range influence between all the magnetic moments present in the sample becomes relevant and spins diverge at the borders of the nanostructure. For large enough size, the magnetization will break into domains. The domain structure consists of quasi-uniformly magnetized regions pointing to different directions and separated by narrow boundaries. The first experimental observations of domains were reported in 1931 [29,30], soon after that *Bloch* [31] described the concept of domain walls and later *Landau* and *Lifshitz* introduced the modern domain theory in 1935 [32]. The narrow boundaries between neighboring domains (or domain walls) are usually regions with large stray fields as opposed to domains, in which the spins are rather parallel. The width of a domain wall depends on the exchange stiffness *A* and the magnetocrystalline anisotropy energy K_1 of the material in such a way that large anisotropy favors the formation of narrow domain walls (in the order of 5 nm for hard magnetic materials), whereas in samples with a stronger relevance of the exchange interactions thicker domain walls are observed (around 100 nm for soft materials).

- Micromagnetism

Micromagnetism, formulated by William Fuller Brown Jr. in 1963 [33], is a modeling technique suitable for the study of magnetic phenomena at the micrometer and nanometer scales. In micromagnetism, the sample is divided or discretized into elements that are sufficiently small for the magnetization to be considered constant inside but large enough for the continuum approximation to be used; the specific atomic structure is thus ignored. An effective spin of modulus M_S is assigned to each cell and its orientation will depend on an effective field that takes

[29] L. Hámos and P. Thiessen, Zeitschrift der Physik 71 (1931) 442-444
[30] F. Bitter, Physical Review 38 (1931) 1903-1905
[31] F. Bloch, Zeitschrift der Physik 74 (1932) 295
[32] L. Landau and E. Lifshitz, Physikaliche Zeitschrift der Sowjetunion 8 (1935) 153
[33] W. F. Brown Jr., "Micromagnetics" (Wiley, New York 1963)

into account the four energy terms described above, making use of equations **(1.2)**, **(1.3)**, **(1.4)** and **(1.6)**:

$$dE_{density} = -\mu_0 \cdot d\vec{\boldsymbol{M}} \cdot \vec{\boldsymbol{H}}_{\boldsymbol{eff}} \Rightarrow \boxed{\vec{\boldsymbol{H}}_{\boldsymbol{eff}} = \frac{-1}{\mu_0} \cdot \frac{\partial E_{density}}{\partial M}}$$

$$E_{density} = \frac{E_{exchange} + E_{anisotropy} + E_{Zeeman} + E_{demag}}{V}$$

The time evolution of the magnetization is calculated using the *Landau-Lifshitz-Gilbert* equation:

$$\frac{d\vec{\boldsymbol{M}}}{dt} = -\gamma \cdot \vec{\boldsymbol{M}} \times \left(\vec{\boldsymbol{H}}_{\boldsymbol{eff}} - \eta \cdot \frac{d\vec{\boldsymbol{M}}}{dt} \right) \qquad \textbf{(1.7)}$$

where η is the damping parameter, which is characteristic of the material. The first term on the right side of equation **(1.7)** describes the precession of the magnetization around the effective field at each point. The second one accounts for a phenomenological damping that has not yet been derived theoretically.

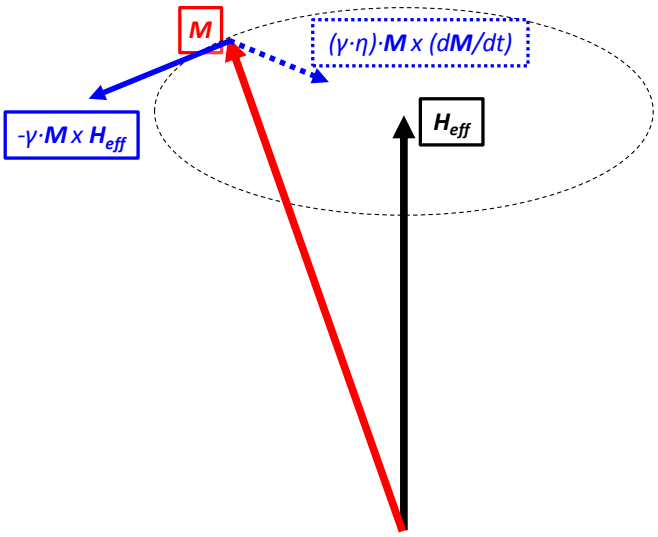

***Figure 1.2: LLG equation**. Dynamic evolution of the magnetization under the influence of an effective field (**Heff**), according to the Landau-Lifshitz-Gilbert equation.*

There are two physically relevant parameters that need to be taken into account when choosing the size of the discretized cells (or cell size): the exchange correlation length (l_{ex}) and the domain wall width parameter (δ_w).

$$l_{ex} = \sqrt{\frac{2 \cdot A}{\mu_0 \cdot {M_S}^2}} \quad ; \quad \delta_w = \pi \cdot \sqrt{\frac{A}{K_1}}$$

Essentially, the cell size must be smaller than these characteristic lengths but include enough atoms to ensure the validity of the continuum approximation.

Throughout this thesis, micromagnetic simulations have been frequently performed using an extended free source code labelled *Object Oriented MicroMagnetic Framework* (*OOMMF*) [34]. In chapter 2.4, our collaborating group made use of a finite element code labelled *MAGPAR* [35].

3. Fundamentals of dynamic atomic force microscopy

The atomic force microcope (*AFM*) makes use of a cantilever with a sharp tip (probe) at its end that is used to scan the sample surface. The cantilever is typically silicon or silicon nitride, with a tip radius of curvature in the order of few to tens of nanometers. When the tip is brought into proximity of a surface, forces between the tip and the sample lead to a measurable deflection of the cantilever according to Hooke's law.

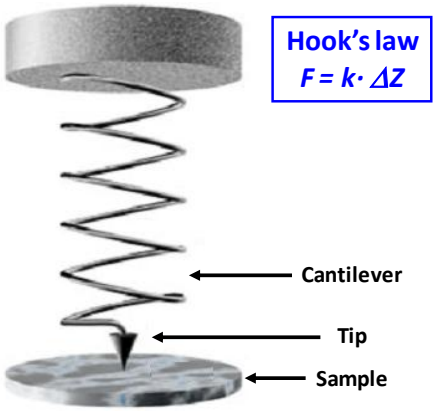

Figure 1.3: Model of the cantilever as a spring obeying Hook's law.

A variety of forces may be measured in *AFM*, including mechanical contact force, *van der Waals* forces, capillary forces, chemical bonding, electrostatic forces, magnetic forces, *Casimir* forces, solvation forces, etc. Along with force, additional quantities may simultaneously be measured through the use of specialized types of probes. The *AFM* can be operated in a number of modes and under different environments, depending on the application. Our case of interest involves dynamic

[34] http://math.nist.gov/oommf
[35] http://magnet.atp.tuwien.ac.at

modes, where the cantilever is vibrated at least at one of its resonance modes. In general, theory of dynamic atomic force microscopy is rather complex and tricky. Nevertheless, some assumptions are often made that ease its physical understanding. The most common one is the use of a point mass model to explain the dynamics of the oscillating probe and we will focus on it.

3.1. Point mass model

This model assumes the oscillating probe to be a point mass that oscillates harmonically subject to an elastic force characterized by an effective spring constant (k), which is different from the real spring constant of the lever. The effective mass of the model (m) is chosen so that equations of motion describe the real oscillation in the experiment and differs from the real tip mass. In addition, dissipative restoring forces damp the harmonic oscillation, with a damping coefficient μ.

- *Dynamic AFM*

In dynamic *AFM*, cantilevers are subject to a periodic driving force $F_{exc}(t) = F_0 \cdot \sin(\omega \cdot t)$ that keep them oscillating at a specific frequency ω. In the point mass model and in the absence of an interacting sample, the effective work done by $F_{exc}(t)$ during the motion of the point mass $z(t)$ must equal the work done by external forces on the entire real cantilever when the tip undergoes the identical motion. The equation of motion can thus be described as:

$$m \cdot \ddot{z}(t) + \mu \cdot \dot{z}(t) + k \cdot z(t) = F_0 \cdot \sin(\omega \cdot t)$$

The homogeneous solution for this second order differential equation corresponds to the transient motion of a static cantilever that is pinged out of its equilibrium position. The equation of such a system, dividing by the spring constant, is described by:

$$\frac{\ddot{z}(t)}{\frac{k}{m}} + \frac{\dot{z}(t)}{\frac{k}{\mu}} + z(t) = 0 \;\Rightarrow\; \frac{\ddot{z}(t)}{{\omega_0}^2} + \frac{\dot{z}(t)}{\omega_0 \cdot Q} + z(t) = 0$$

where the natural resonance frequency and quality factor of the system have been defined:

$$\boxed{\omega_0 = 2\pi \cdot f_0 = \sqrt{\frac{k}{m}} \quad ; \quad Q = \frac{m \cdot \omega_0}{\mu}} \qquad \textbf{(1.8)}$$

Full derivation of the solution to the former equation is presented in appendix B.1 and yields:

$$z(t) = e^{-\frac{\omega_0 \cdot t}{2Q}} \cdot \left[\frac{\dot{z}(0)}{\widehat{\omega}}\right] \cdot \sin(\widehat{\omega} \cdot t)$$

$$\widehat{\omega} = \omega_0 \cdot \sqrt{1 - \frac{1}{4Q^2}} \qquad \textbf{(1.9)}$$

This damped sinusoidal function describes the oscillating motion of cantilevers that are perturbed from their equilibrium position. Notice the important role that the quality factor Q plays, not just altering the oscillation frequency as seen in equation **(1.9)**, but also in the damping as it determines the settling time in transient oscillations. The oscillation amplitude decays by a factor of e when:

$$A(\tau) = \frac{A(0)}{e} \Rightarrow e^{-\frac{\omega_0 \cdot \tau}{2Q}} \cdot \left[\frac{\dot{z}(0)}{\frac{\omega_0}{2Q} \cdot \sqrt{4Q^2 - 1}}\right] = e^{-1} \cdot \left[\frac{\dot{z}(0)}{\frac{\omega_0}{2Q} \cdot \sqrt{4Q^2 - 1}}\right] \Rightarrow \boxed{\tau = \frac{2Q}{\omega_0}}$$

Thus, high quality factors are not suitable when one seeks fast scanning speeds. In a sense, the quality factor is a measure of the number of periods or oscillation cycles necessary for the perturbed oscillation to die off.

After having calculated the homogeneous solution, we now assume a particular solution of the form $z_p(t) = A \cdot \sin(\omega \cdot t - \phi)$. The following expressions are derived for the amplitude transfer function and phase shift:

$$\boxed{\left[\frac{A}{\left(\frac{F_0}{k}\right)}\right] = \frac{1}{\sqrt{\left[1 - \left(\frac{\omega}{\omega_0}\right)^2\right]^2 + \left(\frac{\omega}{\omega_0 \cdot Q}\right)^2}}} \qquad \textbf{(1.10)}$$

$$\boxed{\phi = \tan^{-1}\left\{\frac{\frac{\omega}{\omega_0}}{Q \cdot \left[1 - \left(\frac{\omega}{\omega_0}\right)^2\right]}\right\}} \qquad \textbf{(1.11)}$$

Derivation is detailed in appendix B.2. The general solution for dynamic *AFM* is the sum of the homogeneous and particular ones. This implies the combination of a sinusoidal motion with a damped oscillation; nevertheless, after a time of $2Q/\omega_0$ the transient oscillation resulting from the homogeneous solution becomes irrelevant, whereas the steady state solution describes a cantilever

oscillating at the same frequency of the driving force with an amplitude and a phase lag as specified by equations **(1.10)** and **(1.11)**, respectively. Both parameters are plotted in figure 1.4 [36].

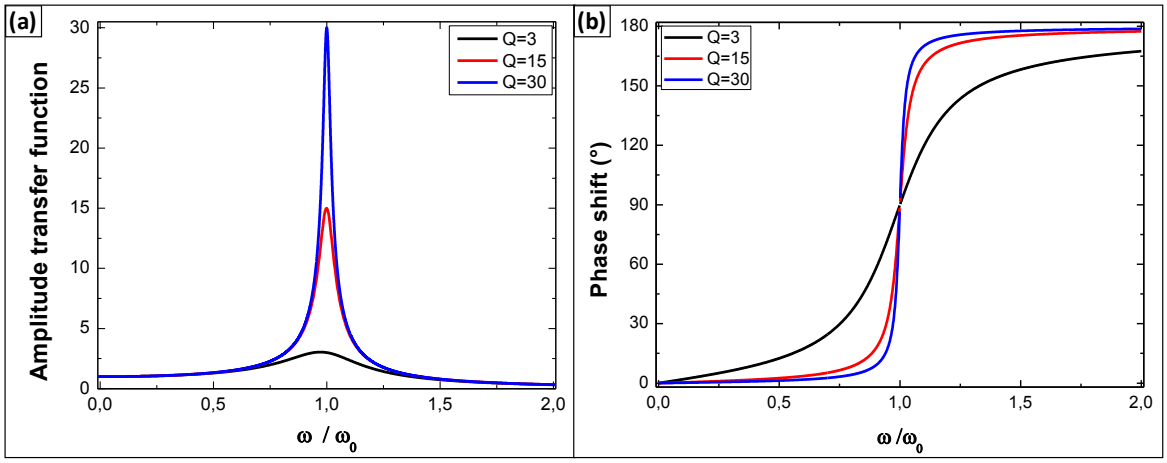

Figure 1.4: Point mass model. (a) *Oscillation amplitude and* ***(b)*** *phase shift of a directly excited cantilever, according to equations* ***(1.10)*** *and* ***(1.11)****.*

When excited at the natural frequency $\omega=\omega_0$, the cantilever oscillates with an amplitude Q times larger than the driving displacement $[A=Q\cdot(F_0/k)]$ and a phase shift of $\phi=90°$, regardless of the Q. Note that a direct excitation system has been considered, in which the driving force is not exerted mechanically. However, the most widespread method of cantilever driving – and the one used in all experiments presented in this thesis – is the piezoacoustic excitation, in which a piezoelectric element is used to vibrate the base of the cantilever. In this case, the equation of motion is slightly different since the cantilever base does not remain fixed. Nevertheless, for experiments in air or high vacuum in which the cantilever is driven at its natural resonance frequency, the base motion is so small (relative to tip displacement) that it can be neglected [37].

- *Tip-sample interactions*

If an interacting force comes into play, the equation of motion becomes difficult to solve and several approximations are usually made. The tip-sample interaction will depend on the absolute tip-sample distance $d(t)=Z_0+z(t)$, where Z_0 denotes the cantilever equilibrium position, and its velocity $\dot{d}(t)$:

$$m\cdot\ddot{z}(t)+\mu\cdot\dot{z}(t)+k\cdot z(t)=F_0\cdot\sin(\omega\cdot t)+F_{t-s}\left[\mathrm{d}(t),\dot{\mathrm{d}}(t)\right]$$

[36] The identity $tan^{-1}(x) = tan^{-1}(x+\pi)$ has been used for the phase shift plot.
[37] D. Kiracofe and A. Raman, Nanotechnology 22 (2011) 485502

If the tip-sample interaction is small enough to be considered a perturbation of the cantilever motion and one assumes the probe to vibrate with very small oscillation amplitudes, a Taylor expansion of the interaction around the equilibrium position yields:

$$m \cdot \ddot{z}(t) + \mu \cdot \dot{z}(t) + k \cdot z(t) = F_0 \cdot \sin(\omega \cdot t) + \left[F_{t-s}(z=0) + \left(\frac{dF_{t-s}}{dz}\right)\Big|_{z=0} \cdot z\right] \Rightarrow$$

$$m \cdot \ddot{z}(t) + \mu \cdot \dot{z}(t) + \left[k - \left(\frac{dF_{t-s}}{dz}\right)\Big|_{z=0}\right] \cdot z(t) = F_0 \cdot \sin(\omega \cdot t) + F_{t-s}(z=0)$$

The steady state solution of former equation is the same as the one given by equations **(1.10)** and **(1.11)**, with the following effective parameters:

$$k_{eff} = \left[k - \left(\frac{dF_{t-s}}{dz}\right)\Big|_{z=0}\right] \Rightarrow \omega_{0,eff} \approx \sqrt{\frac{k_{eff}}{m}} = \sqrt{\frac{k - \left(\frac{dF_{t-s}}{dz}\right)\Big|_{z=0}}{m}} = \omega_0 \cdot \sqrt{1 - \frac{\left(\frac{dF_{t-s}}{dz}\right)\Big|_{z=0}}{k}}$$

Considering the force gradient to be a perturbation of the periodic motion of the lever, so that $\left(\frac{dF_{t-s}}{dz}\right)\Big|_{z=0} \ll k$, the root square can be again expanded as a first order Taylor polynomial:

$$\omega_{0,eff} \approx \omega_0 \cdot \left(1 - \frac{\left(\frac{dF_{t-s}}{dz}\right)\Big|_{z=0}}{2 \cdot k}\right) \Rightarrow \boxed{\Delta\omega_0 \approx -\frac{\omega_0}{2 \cdot k} \cdot \left(\frac{dF_{t-s}}{dz}\right)\Big|_{z=0}} \qquad \textbf{(1.12)}$$

The force gradient $\left(\frac{dF_{t-s}}{dz}\right)\Big|_{z=0}$ has been implicitly assumed to remain constant during each oscillation cycle, which is equivalent to assume linear tip-sample forces. This approximation only remains valid for very small oscillations. In addition, it ignores higher oscillation modes and often does not directly compare to experimental observations [38]. However, a good insight into how the dynamics of the cantilever is affected by interactions with the sample can be extracted by this linear harmonic approximation. Thorough and more accurate analysis of the cantilever dynamics can be found in the literature [39] and will not be commented here.

[38] R. García and R. Pérez, Surface Science Reports 47 (2002) 197-301
[39] Y. Song and B. Bhushan, Journal of Physics: Condensed Matter 20 (2008) 225012

3.2. Experimental set up

All the *MFM* experiments shown throughout this manuscript were performed using *Nanotec Electrónica* systems and data acquisition was carried out using the *WSxM* software [40], with the only exception presented in section 5.3, in which experiments were made using a home built system [41] in Prof. *Peter Grütter*'s group at the *McGill University* of Montreal during one research stay I performed in 2011.

Figure 1.5 shows the experimental set-up used for the *MFM* measurements. It is based on a piezoacoustic excitation system, in which a small dither piezo integrated in the cantilever holder is driven by a sinusoidal voltage to mechanically excite the base of the cantilever at the desired frequency. A piezoelectric tube scanner is used for raster scanning the sample surface. The first model of tube scanner was developed in 1986 for use in *STM* [42] and is broadly extended in *AFM* nowadays. It can move the sample in the three spatial directions using a tubular piezo with a single interior contact and four external contacts. An advantage of the tube scanner is a better vibrational isolation, resulting from the higher resonant frequency of the single-crystal construction. Its main drawback is that the in-plane motion causes unwanted *z* motion, the so-called bow distortion.

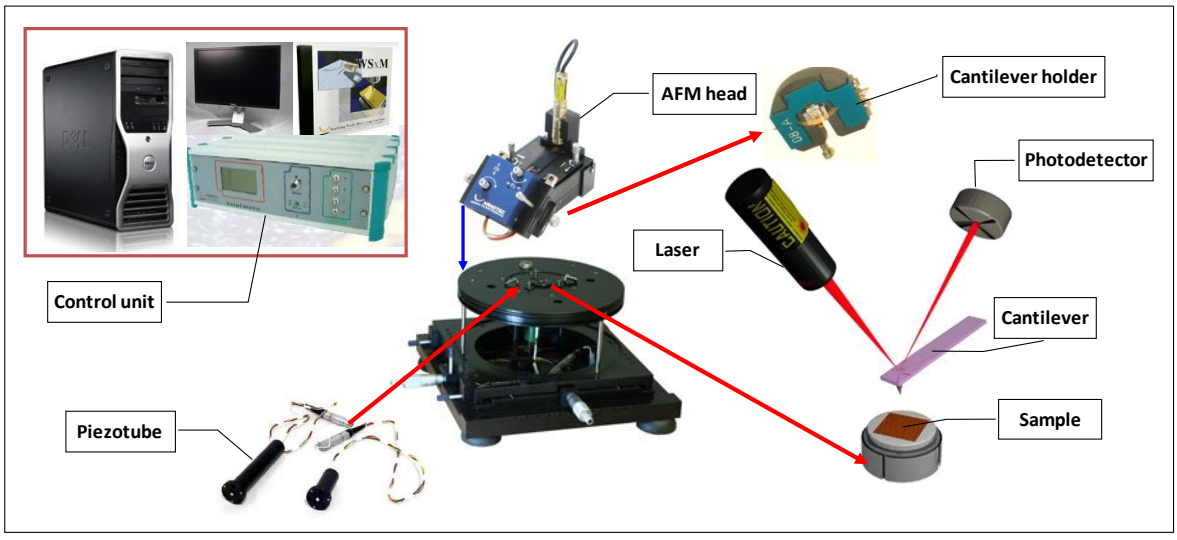

***Figure 1.5: The AFM setup**. Schematics of the microscope used throughout this thesis.*

For the detection system, a laser spot is focalized into the oscillating cantilever and the reflection of the beam is detected by a four quadrant photodiode. Each quadrant generates a voltage proportional

[40] I. Horcas, R. Fernandez, J. M. Gomez-Rodriguez, J. Colchero, J. Gomez-Herrero and A. M. Baro, Review of Scientific Instruments 78 (2007) 013705
[41] Y. Liu, Ph. D. dissertation, McGill University (Montreal, 1997)
[42] G. Binnig and D. P. E. Smith, Review of Scientific Instruments 57 (1986) 1688

to the intensity of the incident beam, in such a way that normal and lateral deflections of the cantilever from the equilibrium position can be precisely determined by subtracting the signals between different quadrants. At room temperature, the thermal energy excites the resonant modes of the cantilever; the oscillation amplitude at the first eigenmode due to thermal noise is in the order of tens of pm for the spring constant values dealt with in our experiments and becomes the limitant factor in the detection of the oscillation.

In the experimental set-up, magnetization reversal processes can be studied in detail by applying variable fields *in-situ*. For doing so, a controlled current is made to flow through two electromagnets that allow for the application of fields up to ±100 mT along the out-of-plane direction (*OOP*) and ±125 mT in the sample plane (*IP*). A remarkable mechanical stabilitiy has been achieved by substitution of magnetostrictive components by materials with a negligible magnetoelastic response [43].

All the results shown here were acquired using dynamic *AFM* and making the cantilever oscillate at the first resonance eigenmode. In dynamic *AFM*, the normal force (which is the photodiode output signal accounting for the vertical deflection of the lever) is fed into the key electronic component of an atomic force microscope: the lock-in amplifier.

- Lock-in amplifiers

Lock-in amplifiers are used to detect and measure very small *AC* signals, all the way down to a few nanovolts, and provide accurate measurements even when the small signal is obscured by noise sources many thousands of times larger. In essence, it multiplies the input signal (in our case, the **oscillating motion** of the cantilever detected by the photodiode) by a reference signal (the **excitation signal** used to mechanically excite the base of the lever). Noise signals at frequencies other than the reference frequency are rejected and do not affect the measurement. The mechanical response of the cantilever will be at the same frequency than the driving voltage, delayed by $\Delta\phi$, so that:

$$\begin{aligned} Oscillation\ of\ the\ cantilever: &\quad V_{input} = A_{osc} \cdot \sin(\omega t + \Delta\phi) \\ Excitation\ signal: &\quad V_{ref} = A_{exc} \cdot \sin(\omega t) \end{aligned}$$

and one can derive the so-called *in-phase* component of the input signal by multiplying them:

$$X = V_{input} \cdot V_{ref} = [A_{osc} \cdot \sin(\omega t + \Delta\phi)] \cdot [A_{exc} \cdot \sin(\omega t)] = \cdots$$

[43] M. Jaafar, J. Gómez-Herrero, A. Gil, P. Ares, M. Vázquez and A. Asenjo, Ultramicroscopy 109 (2009) 693

$$\cdots = \frac{A_{osc} \cdot A_{exc}}{2} \cdot \cos(\Delta\phi) - \frac{A_{osc} \cdot A_{exc}}{2} \cdot \cos(2\omega t + \Delta\phi)$$

In the derivation of former expression, only trigonometrical identities have been used (see appendix C). Two terms are obtained, the first one being a *DC* term and the second one being modulated at a high frequency in the order of $2\omega \approx 150$ kHz. Both of them contain the amplitude (A_{osc}) and phase lag ($\Delta\phi$) of the input signal, which are the quantities one is willing to extract. A low pass filter is then used to filter out the time varying voltages so the second term is attenuated. Thus, the lock-in amplifier outputs a *DC* signal that contains information about the amplitude and phase lag of the cantilever oscillation:

$$X = \frac{A_{osc} \cdot A_{exc}}{2} \cdot \cos(\Delta\phi)$$

If the same operation is repeated with the reference signal shifted by $\pi/2$ radians:

$$Y = V_{input} \cdot V_{ref}{}^{90^\circ} = [A_{osc} \cdot \sin(\omega t + \Delta\phi)] \cdot [A_{exc} \cdot \cos(\omega t)] = \cdots = \frac{A_{osc} \cdot A_{exc}}{2} \cdot \sin(\Delta\phi)$$

where a low pass filter is again considered to attenuate *AC* outputs. The *Y* output is called the *quadrature* component. Therefore, the oscillation amplitude and phase shift can be straightforwardly obtained by a simple operation:

$$\boxed{\begin{aligned} A_{osc} &= \sqrt{X^2 + Y^2} \\ \Delta\phi &= \tan^{-1}\left(\frac{Y}{X}\right) \end{aligned}}$$

This is how the intrinsic parameters of the oscillation are extracted experimentally. Note that signals whose frequencies are very close to the *lock-in* reference frequency may also be detected. The low pass filter bandwidth determines the bandwidth of detection. A narrower bandwidth will remove noise sources very close to the reference frequency, a wider bandwidth allows these signals to pass. Thus, cleaner values of A_{osc} and $\Delta\phi$ can be obtained by using narrower bandwidths at the expense of integrating over longer times. However, longer integration times imply slower scan speeds and delayed response of the feedback controllers, so a balance has to be found. In our experimental setups, two *lock-in* amplifiers are integrated in the control unit shown in figure 1.5. Typical low pass filter bandwidths used in the experiments are in the range of 700-8000 Hz. In particular, very long measurements shown in chapter 2.3 were carried out using bandwidths of 60 Hz to obtain very low noisy *MFM* images.

- Phase-locked loop (PLL)

In all the measurements shown throughout this manuscript, a *phase-locked loop* (*PLL*) was used. A *PLL* tracks the resonance frequency of the cantilever, even in the presence of hydrodynamic damping effects or tip-sample interactions that shift ω_0 as described by equations **(1.8)** and **(1.12)**.

Taking a look back at figure 1.4, it can be seen that a phase shift of 90º takes place between the driving force and the real cantilever oscillation, when the frequency is at the center of the resonance peak. This corresponds to the maximum power transfer. A *phase-locked loop* is a control system with a variable frequency oscillator that generates an output, which is related to the phase of an input signal. In our case, the *PLL* compares the phase of the cantilever oscillation (provided by the *lock-in* amplifier) with the phase of the periodic signal – generated by the internal frequency oscillator – and adjusts the oscillator to keep both phases with a 90º delay; the output signal generated by the oscillator is then used to excite the cantilever again. This is called a feedback loop.

3.3. Fundamentals of magnetic force microscopy

Dynamic magnetic force microscopy relies on relation **(1.12)** to measure magnetic force gradients from the experimental frequency shifts in the oscillating cantilever. If a magnetic coating is present in the sensing probe, the interaction between the stray field emerging from the sample and the magnetization distribution within the tip will give rise to a force gradient that can be mapped. Neglecting mutual influence between tip and sample, the magnetostatic [44] force arising from such interaction has the form:

$$\vec{F}_{t-s} = \mu_0 \cdot \int \vec{\nabla} \cdot \left(\vec{M}_{tip} \cdot \vec{H}_{sample}\right) \cdot dV_{tip} = \hat{k} \cdot \mu_0 \cdot \int \sum_{i=x,y,z} \frac{\partial}{\partial z}\left(M_{tip,i} \cdot H_{sample,i}\right) \cdot dV_{tip} \qquad \textbf{(1.13)}$$

where $\hat{k}$ is the unit vector along *Z* and it has been assumed that the cantilever lies on the *XY* plane, so that the normal force is exerted in the *Z* direction. In general, obtaining an expression for the stray field emerging from the magnetization distribution within the sample involves using equation **(A.2.1)** (see appendix A.2). This is a complex problem and different approaches have been addressed in the literature [45]. If the tip is small enough, one can approximate it to an effective point

[44] The magnetostatic and *Zeeman* terms are the same in essence; here both analytical expressions become equal since only the tip volumen is integrated, so that the ½ term in equation **(1.5)** is not necessary.
[45] P. Grütter, H. J. Marmin and D. Rugar, "Scanning Tunneling Microscopy II" (Springer, Berlin 1992)

dipole that accounts for the total magnetization $\vec{m}_{tip} = \int \vec{M}_{tip} \cdot dV_{tip}$ and get rid of the integral in former equation:

$$\vec{F}_{t-s} = \mu_0 \cdot \left[m_x \cdot \frac{\partial H_{sample,x}}{\partial z} + m_y \cdot \frac{\partial H_{sample,y}}{\partial z} + m_z \cdot \frac{\partial H_{sample,z}}{\partial z} \right]$$

so that the frequency shift is:

$$\Delta\omega \approx -\frac{\omega_0 \cdot \mu_0}{2 \cdot k} \cdot \left[m_x \cdot \frac{\partial^2 H_{sample,x}}{\partial z^2} + m_y \cdot \frac{\partial^2 H_{sample,y}}{\partial z^2} + m_z \cdot \frac{\partial^2 H_{sample,z}}{\partial z^2} \right]$$

If the point dipole is oriented along the vertical (out of plane) direction:

$$\boxed{\Delta\omega \approx -\frac{\omega_0 \cdot \mu_0 \cdot m_{tip}}{2 \cdot k} \cdot \frac{\partial^2 H_{sample,z}}{\partial z^2}} \qquad \textbf{(1.14)}$$

In the dipole approximation, the measured frequency shift depends on the second derivative of the stray field. Already in 1988, *Marmin* and co-workers [46] modeled the tip as a point dipole and could use the so gained information to qualitatively understand the measured data. In order to achieve good agreement with experimental data, the dipole should be located at a specific position within the effective magnetic tip volume [47]; knowing about the dipole moment and its position can be achieved by calibration with well-known stray fields [48]. The dipolar approximation can be applicable for hard tips whose interacting region is small compared to the length over which the field varies significantly.

Another point probe approach models the *MFM* tip as a monopole moment and is suitable for long and elongated sensors. In this case, the magnetization is considered homogeneous along the *Z* direction, so from equation **(1.13)**:

$$\vec{F}_{t-s} = \hat{k} \cdot \mu_0 \cdot \int \frac{\partial}{\partial z} \left(M_{tip,z} \cdot H_{sample,z} \right) \cdot dV_{tip} = \hat{k} \cdot \mu_0 \cdot \int M_{tip} \cdot \frac{\partial}{\partial z} H_{sample} \cdot dz_{tip} = \hat{k} \cdot \mu_0 \cdot M_{tip} \cdot H_{sample}$$

The frequency shift is then:

$$\boxed{\Delta\omega \approx -\frac{\omega_0 \cdot \mu_0 \cdot M_{tip}}{2 \cdot k} \cdot \frac{\partial H_{sample}}{\partial z}} \qquad \textbf{(1.15)}$$

[46] H. J. Marmin, D. Rugar, J. E. Stern, B. D. Terris and S. E. Lambert, Applied Physics Letters 53 (1988) 1563
[47] U. Hartmann, Physical Review A 137 (1989) 475
[48] L. Kong and S. Y. Chou, Applied Physics Letters 70 (1997) 2043

In the monopole approximation, the frequency shift depends on the first derivative of the sample stray field. This approximation is valid for long and narrow tips, in which only the magnetic charges at the bottom side of the probe contribute to the signal.

- Interpretation of *MFM* images

MFM images correspond to frequency shift maps (as long as a *PLL* is enabled, as is the case here) obtained at relatively large tip-sample distances, where the magnetostatic coupling is dominant. As sketched in figure 1.6, depending on the relative tip-sample separation distance interactions of diverse origins are dominant. Short range interactions, such as Pauli repulsion and chemical bonding, are responsible for the atomic contrast observed in *AFM* experiments in ultra high vacuum conditions. Under ambient conditions, adhesion and capillarity effects are important when the tip comes close to the surface, whereas *van der Waals* forces are typically responsible for changes in the cantilever dynamics used to track the topography, at separations of few nanometers. In order to extract information from magnetostatic and electrostatic interactions, it usually becomes necessary to withdraw the tip by few tens of nanometers until these interactions dominate. As a consequence, lower resolution can be achieved in magnetic force microscopy experiments.

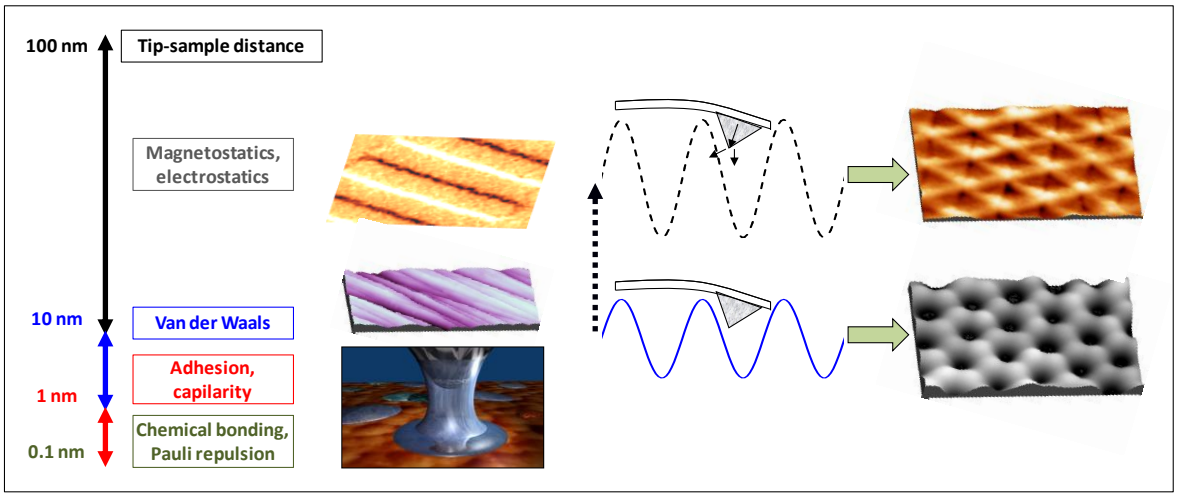

***Figure 1.6: Dominant forces as a function of distance**. Schematics of the interactions that govern the cantilever dynamics, depending on the separation distance. Typically, van der Waals forces are used to track the topography at distances of few nanometers, from which the cantilever is then lifted by 20-50 nm to obtain the MFM image.*

In the most widespread operating procedure, called the lift-mode or retrace-mode, the tip scans twice over the sample surface at two different separations. A first scan is performed at distances of few nm to extract the topographic profile. Then, the tip is retracted by some tens of nanometers and, instead of scanning parallel to the sample plane, the system repeats the same profile obtained

during the first pass. This allows for higher resolution because eventual crosstalk with topographic features (caused by protuberances in the sample surface) is minimized. Frequency shifts in the cantilever oscillation during this retrace scan form the *MFM* image.

The interpretation of *MFM* images can be complex and even different domain structures present in the sample may yield similar contrast. Assuming the sensing magnetization at the tip apex to be oriented perpendicular to the sample plane (*Z* direction), it is deduced from equations **(1.12)** and **(1.13)** that contrast in *MFM* images arises from the variation along *Z* of the vertical component of the interaction, i.e. $\partial F_Z/\partial z$; therefore, the relevant parameter is the decay of H_Z with distance.

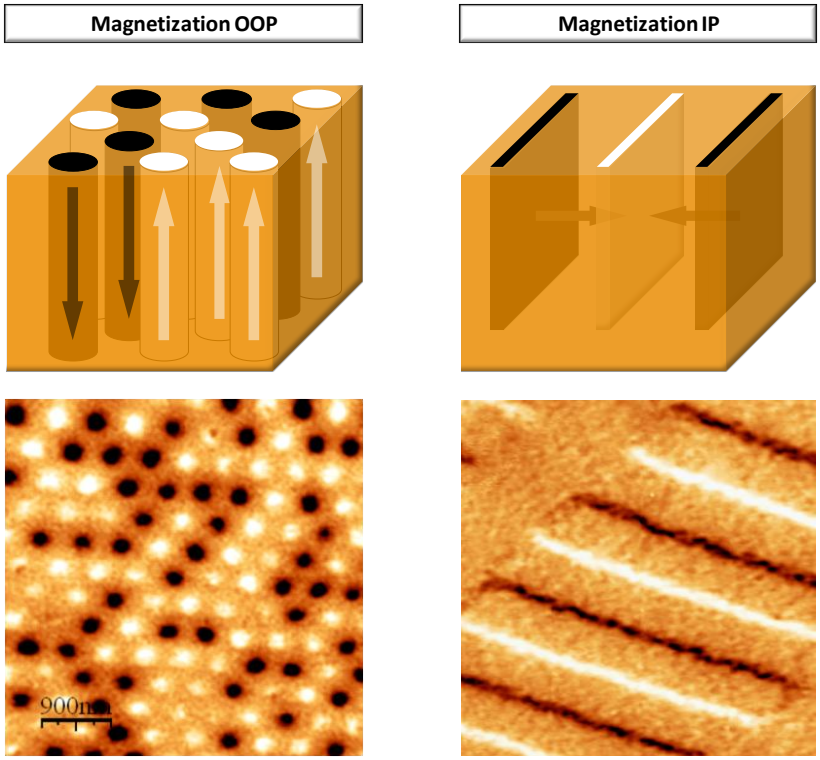

***Figure 1.7: Interpretation of MFM images**. **(left)** Contrast observed when imaging samples with an OOP magnetization accounts for magnetic domains. **(right)** In the case of IP magnetization, it highlights the presence of domain walls.*

But how does that relate to the domain structure in the sample? As depicted in figure 1.7, when imaging samples with the magnetization pointing perpendicular to the sample plane (*OOP*) contrast corresponds to the domains themselves (left column). On the contrary, if the magnetic moments lay in-plane (*IP*) contrast accounts for domain walls (right column); in general, wherever the magnetization diverges. Therefore, a practical way of interpreting *MFM* images is considering them as maps of magnetic charges, whose sources are local divergences of the magnetization.

Appendix A: Exchange and magnetostatic energies in micromagnetic simulations

- A.1: Exchange energy

From the Heisenberg Hamiltonian introduced in equation **(1.1)**, considering a constant exchange constant and including the numerical values within *J*:

$$E_{exchange} = -J \cdot \sum_{i,j} \widehat{\boldsymbol{S}}_{\boldsymbol{i}} \cdot \widehat{\boldsymbol{S}}_{\boldsymbol{j}} = -J \cdot S^2 \sum_{i,j} \cos \phi_{ij}$$

where ϕ_{ij} is the angle between neighboring spins $\boldsymbol{S_i}$ and $\boldsymbol{S_j}$, which in ferromagnetic materials is very small ($|\phi_{ij}|<<1$) so we can expand the cosine to a first order as:

$$E_{exchange} = -J \cdot S^2 \cdot \sum_{i,j} \left(1 - \frac{1}{2} \cdot {\phi_{ij}}^2\right) = {E_{exchange}}^0 + \frac{J \cdot S^2}{2} \cdot \sum_{i,j} \left({\phi_{ij}}^2\right)$$

The first term corresponds to a ferromagnet with all spins aligned parallel to each other and can be disregarded by redefining the zero energy level. For the second term, since $\boldsymbol{S_i}$ and $\boldsymbol{S_j}$ are unit vectors:

$$\left|\widehat{\boldsymbol{S}}_{\boldsymbol{i}} - \widehat{\boldsymbol{S}}_{\boldsymbol{j}}\right|^2 = \left|\widehat{\boldsymbol{S}}_{\boldsymbol{i}}\right|^2 + \left|\widehat{\boldsymbol{S}}_{\boldsymbol{j}}\right|^2 - 2 \cdot \left|\widehat{\boldsymbol{S}}_{\boldsymbol{i}}\right| \cdot \left|\widehat{\boldsymbol{S}}_{\boldsymbol{j}}\right| \cdot \cos \phi_{ij} = 2 \cdot \left(1 - \cos \phi_{ij}\right) \approx {\phi_{ij}}^2$$

Expanding the variable in a Fourier series:

$$\left|\phi_{ij}\right| \approx \left|\widehat{\boldsymbol{S}}_{\boldsymbol{i}} - \widehat{\boldsymbol{S}}_{\boldsymbol{j}}\right| \approx \left|\left(r_{ix} \cdot \frac{\partial}{\partial x} + r_{iy} \cdot \frac{\partial}{\partial y} + r_{iz} \cdot \frac{\partial}{\partial z}\right) \cdot \widehat{\boldsymbol{S}}\right| \approx \left|\left(\vec{r} \cdot \vec{\nabla}\right) \cdot \widehat{\boldsymbol{S}}\right|$$

Substitution in the equation yields:

$$E_{exchange} = \frac{J \cdot S^2}{2} \cdot \sum_{i=1}^{N} \sum_{\boldsymbol{S_i}} \left|\left(\vec{r} \cdot \vec{\nabla}\right) \cdot \widehat{\boldsymbol{S}}\right|$$

In this expression, the first summation runs over every spin, whereas the second one only over first neighbors. Changing the summatory to an integral over the whole ferromagnetic body, in cubic crystals we have [49]:

$$E_{exchange} = A \cdot \int \left[(\nabla S_x)^2 + \left(\nabla S_y\right)^2 + (\nabla S_z)^2\right] \cdot dV$$

where *A* is the exchange stiffness constant defined by:

$$A = \frac{J \cdot S^2}{a} \cdot c$$

[49] A. Aharoni, "Introduction to the theory of ferromagnetism" (Oxford University Press, 1996)

with *a* being the lattice constant and *c*=1, 2 or 4 corresponds to the base atoms in a simple cubic, body centered cubic and face centered cubic lattice, respectively.

- A.2: Magnetostatic energy

The demagnetizing or dipolar field can be derived from the magnetostatic Maxwell's equations for a body with no electric currents. These are Ampère's and Gauss's laws:

$$\vec{\nabla} \times \vec{H}_{demag} = 0 \quad ; \quad \vec{\nabla} \cdot \vec{B} = 0 \Rightarrow \vec{\nabla} \cdot \vec{H}_{demag} = -\vec{\nabla} \cdot \vec{M}$$

The general solution of Ampère's law can be expressed as the gradient of a scalar potential:

$$\vec{H}_{demag} = -\vec{\nabla} \cdot U$$

This yields:

$$\vec{\nabla}^2 \cdot U = \begin{cases} \vec{\nabla} \cdot \vec{M}, & inside\ the\ object \\ 0\ , & outside\ the\ object \end{cases}$$

The boundary conditions require that:

$$U_{inside} = U_{outside}$$
$$\frac{\partial U_{inside}}{\partial n} - \frac{\partial U_{outside}}{\partial n} = \vec{M} \cdot \vec{n}$$

Here ***n*** is the surface normal and (*∂/∂n*) is the derivative with respect to distance from the surface. The general solution for the magnetic scalar potential is:

$$U(\vec{r}) = -\frac{1}{4\pi} \cdot \iiint \frac{\vec{\nabla}' \cdot \vec{M}\left(\vec{r'}\right)}{\left|\vec{r} - \vec{r'}\right|} \cdot d^3r' + \frac{1}{4\pi} \cdot \iint \frac{\hat{\mathbf{n}} \cdot \vec{M}\left(\vec{r'}\right)}{\left|\vec{r} - \vec{r'}\right|} \cdot d^2r'$$

So that making use of equation **(1.5)**, the magnetostatic energy turns out to be:

$$E_{demag} = -\frac{\mu_0}{2} \cdot \int \vec{M} \cdot \vec{H}_{demag} \cdot dV = \frac{\mu_0}{2} \cdot \int \vec{M} \cdot \vec{\nabla} \cdot U \cdot dV \Rightarrow$$

$$\Rightarrow \frac{E_{demag}}{V} = \frac{\mu_0}{8\pi} \cdot \vec{M} \cdot \left[\iiint \vec{\nabla} \cdot \vec{M}\left(\vec{r'}\right) \cdot \frac{\vec{r} - \vec{r'}}{\left|\vec{r} - \vec{r'}\right|^3} \cdot d^3r' - \iint \hat{\mathbf{n}} \cdot \vec{M}\left(\vec{r'}\right) \cdot \frac{\vec{r} - \vec{r'}}{\left|\vec{r} - \vec{r'}\right|^3} \cdot d^2r' \right] \qquad \textbf{(A.2.1)}$$

Appendix B: Solutions for the equation of motion of oscillating cantilevers

- B.1: Perturbed static cantilevers

The equation of motion to solve is:

$$\frac{\ddot{z}(t)}{{\omega_0}^2} + \frac{\dot{z}(t)}{\omega_0 \cdot Q} + z(t) = 0$$

We propose a solution of the form: $z(t) = A^* \cdot e^{r \cdot t}$. Substituting:

$$A^* \cdot \left[\frac{r^2}{{\omega_0}^2} + \frac{r}{\omega_0 \cdot Q} + 1\right] \cdot e^{r \cdot t} = 0 \Rightarrow \frac{r^2}{{\omega_0}^2} + \frac{r}{\omega_0 \cdot Q} + 1 = 0 \Rightarrow r = -\frac{\omega_0}{2Q} \cdot \left[1 \pm \sqrt{1 - 4Q^2}\right]$$

Thus:

$$z(t) = A \cdot e^{-\frac{\omega_0 \cdot t}{2Q}\left[1+\sqrt{1-4Q^2}\right]} + B \cdot e^{-\frac{\omega_0 \cdot t}{2Q}\left[1-\sqrt{1-4Q^2}\right]}$$

Two different cases must be considered, depending on the radicand's sign:

(i) $\quad 1 - 4Q^2 > 0 \Leftrightarrow Q < {}^1/_2$

This is called overdamped oscillation and will not be considered here. Essentially, an overdamped cantilever reaches the equilibrium position without completing a full oscillation cycle.

(ii) $\quad 1 - 4Q^2 < 0 \Leftrightarrow Q > {}^1/_2$

The underdamped oscillation is the case of interest for atomic force microscopy. It yields following solution:

$$z(t) = e^{-\frac{\omega_0 \cdot t}{2Q}} \cdot \left[A \cdot e^{-i \cdot \frac{\omega_0 \cdot t}{2Q} \cdot \sqrt{4Q^2-1}} + B \cdot e^{i \cdot \frac{\omega_0 \cdot t}{2Q} \cdot \sqrt{4Q^2-1}}\right] \Rightarrow$$

$$\Rightarrow z(t) = e^{-\frac{\omega_0 \cdot t}{2Q}} \cdot \left[(A + B) \cdot \cos\left(\frac{\omega_0 \cdot t}{2Q} \cdot \sqrt{4Q^2 - 1}\right) + (B - A) \cdot i \cdot \sin\left(\frac{\omega_0 \cdot t}{2Q} \cdot \sqrt{4Q^2 - 1}\right)\right]$$

Let us define the new constants $C = (A + B)$ and $D = (B - A) \cdot i$,

$$\Rightarrow\ z(t) = e^{-\frac{\omega_0 \cdot t}{2Q}} \cdot \left[C \cdot \cos\left(\frac{\omega_0 \cdot t}{2Q} \cdot \sqrt{4Q^2 - 1}\right) + D \cdot \sin\left(\frac{\omega_0 \cdot t}{2Q} \cdot \sqrt{4Q^2 - 1}\right)\right]$$

that are determined by the initial conditions:

$$C = z(0)\ \ ;\ \ D = \frac{\dot{z}(0) + \frac{\omega_0}{2Q} \cdot z(0)}{\frac{\omega_0}{2Q} \cdot \sqrt{4Q^2 - 1}}$$

If we assume that the probe was in its equilibrium position when it was perturbed, the final solution is obtained:

$$\Rightarrow\ z(t) = e^{-\frac{\omega_0 \cdot t}{2Q}} \cdot \left[\frac{\dot{q}(0)}{\frac{\omega_0}{2Q} \cdot \sqrt{4Q^2 - 1}}\right] \cdot \sin\left(\frac{\omega_0 \cdot t}{2Q} \cdot \sqrt{4Q^2 - 1}\right)$$

where the frequency of the oscillating term can be defined as:

$$\widehat{\omega} = \frac{\omega_0}{2Q} \cdot \sqrt{4Q^2 - 1} = \omega_0 \cdot \sqrt{1 - \frac{1}{4Q^2}}$$

Finally:

$$\boxed{z(t) = e^{-\frac{\omega_0 \cdot t}{2Q}} \cdot \left[\frac{\dot{q}(0)}{\widehat{\omega}}\right] \cdot \sin(\widehat{\omega} \cdot t)}$$

- B.2: Directly excited cantilevers

The equation of motion to solve now is:

$$\frac{\ddot{z}(t)}{{\omega_0}^2} + \frac{\dot{z}(t)}{\omega_0 \cdot Q} + z(t) = \frac{F_0}{k} \cdot \sin(\omega \cdot t)$$

The particular solution is assumed to be of the form: $z_p(t) = A \cdot \sin(\omega \cdot t - \phi)$, yielding:

$$-\left(\frac{\omega}{\omega_0}\right)^2 \cdot A \cdot \sin(\omega \cdot t - \phi) + \frac{\omega}{\omega_0 \cdot Q} \cdot A \cdot \cos(\omega \cdot t - \phi) + A \cdot \sin(\omega \cdot t - \phi) = \frac{F_0}{k} \cdot \sin(\omega \cdot t)$$

rearranging terms:

$$\left[1-\left(\frac{\omega}{\omega_0}\right)^2\right]\cdot\sin(\omega\cdot t-\phi)+\frac{\omega}{\omega_0\cdot Q}\cdot\cos(\omega\cdot t-\phi)=\frac{\left(\frac{F_0}{A}\right)}{k}\cdot\sin(\omega\cdot t)$$

Both parameters A and ϕ are defined as constants, as long as the driving signal remains unchanged and no additional perturbation takes place. Thus, we can obtain their expressions by choosing proper times:

- $t_1=0$

$$\left[1-\left(\frac{\omega}{\omega_0}\right)^2\right]\cdot\sin(-\phi)+\frac{\omega}{\omega_0\cdot Q}\cdot\cos(-\phi)=0\ \Rightarrow$$

$$\Rightarrow\left[1-\left(\frac{\omega}{\omega_0}\right)^2\right]\cdot\sin(\phi)=\frac{\omega}{\omega_0\cdot Q}\cdot\cos(\phi)\Rightarrow\boxed{\phi=\tan^{-1}\left\{\frac{\frac{\omega}{\omega_0}}{Q\cdot\left[1-\left(\frac{\omega}{\omega_0}\right)^2\right]}\right\}}$$

- $t_2=\frac{\phi}{\omega}$

$$\left[1-\left(\frac{\omega}{\omega_0}\right)^2\right]\cdot\sin\left(\omega\cdot\frac{\phi}{\omega}-\phi\right)+\frac{\omega}{\omega_0\cdot Q}\cdot\cos\left(\omega\cdot\frac{\phi}{\omega}-\phi\right)=\frac{\left(\frac{F_0}{A}\right)}{k}\cdot\sin\left(\omega\cdot\frac{\phi}{\omega}\right)\Rightarrow$$

$$\Rightarrow\frac{A}{\left(\frac{F_0}{k}\right)}=\frac{\omega_0\cdot Q}{\omega}\cdot\sin(\phi)$$

Using the following identity among inverse trigonometric functions:

$$\tan^{-1}(x)=\sin^{-1}\left(\frac{x}{\sqrt{1+x^2}}\right)\ \Rightarrow\ \sin[\tan^{-1}(x)]=\frac{x}{\sqrt{1+x^2}}$$

we can operate further, so:

$$\frac{A}{\left(\frac{F_0}{k}\right)}=\frac{\omega_0\cdot Q}{\omega}\cdot\sin\left\{\tan^{-1}\left[\frac{\frac{\omega}{\omega_0}}{Q\cdot\left[1-\left(\frac{\omega}{\omega_0}\right)^2\right]}\right]\right\}=\frac{\omega_0\cdot Q}{\omega}\cdot\frac{\frac{\frac{\omega}{\omega_0}}{Q\cdot\left[1-\left(\frac{\omega}{\omega_0}\right)^2\right]}}{\sqrt{1+\left[\frac{\frac{\omega}{\omega_0}}{Q\cdot\left[1-\left(\frac{\omega}{\omega_0}\right)^2\right]}\right]^2}}$$

Simplifying terms:

$$\boxed{\left[\frac{A}{\left(\frac{F_0}{k}\right)}\right]=\sqrt{\frac{1}{\left[1-\left(\frac{\omega}{\omega_0}\right)^2\right]^2+\left(\frac{\omega}{\omega_0\cdot Q}\right)^2}}}$$

Appendix C: Signal multiplication in lock-in amplifiers

Having the following signals:

$$\begin{aligned} &Oscillation\ of\ the\ cantilever: && V_{input} = A_{osc} \cdot \sin(\omega t + \Delta\phi) \\ &Excitation\ signal: && V_{ref} = A_{exc} \cdot \sin(\omega t) \end{aligned}$$

the *lock-in* amplifier multiplies one by the other to extract A_{osc} and $\Delta\phi$.

$$X = [A_{osc} \cdot \sin(\omega t + \Delta\phi)] \cdot [A_{exc} \cdot \sin(\omega t)] = (A_{osc} \cdot A_{exc}) \cdot \sin(\omega t + \Delta\phi) \cdot \sin(\omega t)$$

Using the trigonometrical identity $sin(\alpha + \beta) = sin\,\alpha \cdot cos\,\beta + cos\,\alpha \cdot sin\,\beta$, one gets:

$$\begin{aligned} X &= (A_{osc} \cdot A_{exc}) \cdot [\sin^2 \omega t \cdot cos\,\Delta\phi + \sin \omega t \cdot cos\,\omega t \cdot \sin \Delta\phi] = \\ &= \frac{(A_{osc} \cdot A_{exc})}{2} \cdot [2 \cdot \sin^2 \omega t \cdot cos\,\Delta\phi + 2 \cdot \sin \omega t \cdot cos\,\omega t \cdot \sin \Delta\phi] = \\ &= \frac{(A_{osc} \cdot A_{exc})}{2} \cdot [\sin^2 \omega t \cdot cos\,\Delta\phi + \sin^2 \omega t \cdot cos\,\Delta\phi + 2 \cdot \sin \omega t \cdot cos\,\omega t \cdot \sin \Delta\phi] \end{aligned}$$

Adding the term $[(\cos^2 \omega t - \cos^2 \omega t) \cdot \cos \Delta\phi]$ does not modify the result; doing that and rearranging terms:

$$X = \frac{(A_{osc} \cdot A_{exc})}{2} \cdot [(\sin^2 \omega t + \cos^2 \omega t) \cdot cos\,\Delta\phi - (\cos^2 \omega t - \sin^2 \omega t) \cdot cos\,\Delta\phi + 2 \cdot \sin \omega t \cdot cos\,\omega t \cdot \sin \Delta\phi]$$

Making use of the identities $\sin(2\alpha) = 2 \cdot \sin(\alpha) \cdot \cos(\alpha)$ and $\cos(2\alpha) = \cos^2(\alpha) - \sin^2(\alpha)$, we get:

$$X = \frac{(A_{osc} \cdot A_{exc})}{2} \cdot [cos\,\Delta\phi - \cos 2\omega t \cdot cos\,\Delta\phi + \sin 2\omega t \cdot \sin \Delta\phi]$$

Equivalently:

$$\boxed{X = \frac{(A_{osc} \cdot A_{exc})}{2} \cdot [cos(\Delta\phi) - \cos(2\omega t + \Delta\phi)]}$$

Chapter 2: Magnetization reversal processes by Variable Field-Magnetic Force Microscopy

In this chapter, we present the most relevant works carried out throughout my thesis in collaboration with different research groups, in which magnetic domains and magnetization reversal processes were studied by making use of our variable field magnetic force microscope (*VF-MFM*). It is divided in two parts, each of which is dedicated to materials whose magnetic behavior is governed by their **shape** (first part) or is strongly influenced by the **magneto-crystalline anisotropy** (second part). The samples described cover a set of different materials (permalloy, polycrystalline and epitaxial cobalt, an alloy of iron cobalt copper and lanthanum strontium manganite) processed through a variety of fabrication methods (electron beam lithography and lift-off techniques, focused electron beam induced deposition, electrochemical deposition into alumina templates, molecular beam epitaxy, focused ion beam and chemical vapour deposition). Four of the studies described in this chapter have already given rise to articles published in international journals. In addition, the remaining one is currently being reported and will be sent for peer reviewing within the next weeks.

The first part of current chapter focuses on polycrystalline samples whose magnetic configuration is determined by their **shape anisotropy** and includes three sections, each one is dedicated to a different sample. The first section presents the study of magnetostatic coupling between neighboring permalloy nanostripes and has been recently published [1]. The sample was fabricated by Dr. *L. Pérez* and Dr. *Ó. de Abril* from the *Universidad Complutense de Madrid* (*UCM*) and the magnetic characterization was carried out by means of our *VF-MFM* system. Plenty of literature can be found regarding domain wall pinning and propagation [2,3,4] and magnetization switching processes [5,6,7] of permalloy nanowires and nanostripes. Up to now, almost all the studies have focused on the behavior of a single nanostripe or in a small collection of them whereas, in real devices, high density of nanowires should be used in order to reach high storage density. When stripes are placed close to each other, magnetostatic coupling between them can affect their magnetic behavior. Some studies can be found on interactions between neighboring stripes in

[1] **Ó. Iglesias-Freire**, M. Jaafar, L. Pérez, Ó. de Abril, M. Vázquez and A. Asenjo, Journal of Magnetism and Magnetic Materials 355 (2014) 152-157
[2] D. Atkinson, D. A. Allwood, G. Xiong, M. D. Cooke, C. C. Faulkner and R. P. Cowburn, Nature Materials 2 (2003) 85
[3] Y. Nakatani, A. Thiaville and J. Miltat, Nature Materials 2 (2003) 521
[4] D. Petit, A-V. Jausovec, H. T. Zeng, E. Lewis, L. O'Brien, D. Read and R. P. Cowburn, Physical Review B 79 (2009) 214405
[5] D. Atkinson, D. S. Eastwood and L. K.Bogart, Applied Physics Letters 92 (2008) 022510
[6] M. Hayashi, L. Thomas, C. Rettner, R. Moriya, X. Jiang and S. S. P. Parkin, Physical Review Letters 97 (2006) 207205
[7] L. K. Bogart, D. Atkinson, K. O'Shea, D. McGrouther and S. McVitie, Physical Review B 79 (2009) 054414

different materials, such as cobalt [8,9,10], nickel [11,12], iron [13] or Fe_3Pt [14], but cylindrical wires embedded in alumina membranes are mostly studied and conclusions are extracted from bulk magnetometry measurements (*VSM* or *SQUID*). These yield averaged information over macroscopic regions, making measurements encompass multitude of elements and making it harder to reach a full understanding of the magnetization reversal process of each element individually. Magneto-optical Kerr effect (*MOKE*) magnetometry can alternatively be used as a local technique but its resolution is limited to the micrometric range. In our study, we present *MFM* data and micromagnetic simulations of the magnetic behavior of high aspect ratio nanostripes and, in particular, magnetostatic coupling between them.

In the second section, a particular methodology for obtaining *MFM* images is introduced. This was developed in our group during the first year of my *PhD* and published in 2011 [15]. In that article, this procedure is used to obtain hysteresis loops of individual polycrystalline cobalt planar wires or stripes, fabricated in Prof. *J. M. de Teresa*'s group at the *University of Zaragoza*. Critical fields in magnetic nanostripes are important parameters when dealing with single domain structures, as they are valuable candidates for the development of different applications such as high density and high speed magnetic information storage, magnetic random access memories, magnetic sensors and logic devices. Such nanostructures present different magnetic behavior depending on their shape, size, aspect ratio and distance between adjacent elements. This particular operating mode has been used in different parts of this thesis and its results will not only be shown in current chapter.

The last section of this first part introduces an ongoing work in collaboration with the group of Prof. *Manuel Vázquez* at the *Material Science Institute of Madrid*. It focuses on the study of the domain structures happening in modulated cylindrical $Fe_{28}Co_{67}Cu_5$ nanowires grown by electrodeposition into aluminium oxide membranes that serve as templates. In the last years, ferromagnetic-nonmagnetic multilayer nanowire arrays and binary systems, including Co and Fe alloys, have been reported to show appealing magnetic and magnetotransport properties [16,17,18,19]. In

[8] J. M. García, A. Asenjo, J. Velázquez, D. García and M. Vázquez, Journal of Applied Physics 85 (1999) 5480
[9] H. Cao, Z. Xu, H. Sang, D. Sheng and C. Tie, Advanced Materials 13 (2001) 121
[10] J. Bao, C. Tie, Z. Xu, Q. Ma, J. Hong, H. Sang and D. Sheng, Advanced Materials 14 (2002) 44
[11] J. Bao, D. Xu, Q. Zhou, Z. Xu, Y. Feng and Y. Zhou, Chemistry of Materials 14 (2002) 4709
[12] I. Z. Rahman, A. Boboc, K. M. Razeeb and M. A. Rahman, Journal of Magnetism and Magnetic Materials 290 (2005) 246
[13] Q-F. Zhan, J-H. Gao, Y-Q. Liang, N-L. Di and Z-H. Cheng, Physical Review B 72 (2005) 024428
[14] D-L. Sun, J-H. Gao, X-Q. Zhang, Q-F. Zhan, W. He, Y. Sun and Z-H. Cheng, Journal of Magnetism and Magnetic Materials 321 (2009) 2737
[15] M. Jaafar, L. Serrano-Ramón, **O. Iglesias-Freire**, A. Fernández-Pacheco, M. R. Ibarra, J. M. de Teresa and A. Asenjo, Nanoscale Research Letters 6 (2011) 407
[16] H. J. Blythe, V. M. Fedosyuk, O. I. Kasyutich and W. Schwarzacher, Journal of Magnetism and Magnetic Materials 208 (2000) 201
[17] Y. W. Wang, L. D. Zhang, G. W. Meng, X. S. Peng, Y. X. Jin and J. Zhang, Journal of Physical Chemistry B 106 (2002) 2502

particular, the family of FeCo nanowires exhibit the necessary capability to be employed in novel generation of rare-earth-free permanent magnets due to their high *Curie* temperature, large saturation magnetization and high shape anisotropy. Their magnetic properties can be tuned by adjusting the alloy composition, adding other elements [20,21,22] or by suitable thermal treatments [23]. In particular, the presence of copper atoms has been attributed to enhance the magnetic hardness [24]. In this work, we study the domain distribution in single $Fe_{28}Co_{67}Cu_5$ cylindrical nanowires with a modulated diameter, both experimentally by using our magnetic force microscope and numerically with the support of micromagnetic simulations. A report embracing these results is currently in preparation.

In addition to the influence that the shape of the sample has in its magnetic behavior, the **magneto-crystalline anisotropy** can also play a key role in the magnetic configuration. Finding ways to tune the magneto-crystalline anisotropy is of great interest as, in order to increase the efficiency of the spin torque transfer effect in magnetic nanowires, it is necessary to use materials with strong crystalline anisotropy [25]. The second part of current chapter comprises two additional sections in which the crystalline anisotropy becomes relevant. The first of them – fourth in the overall account – deals with epitaxial cobalt stripes with competing anisotropies, a work resulting from a collaboration with Dr. *O. Chubykalo-Fesenko* that yielded a paper published in 2013 [26]. Different configurations have been found in samples with competing anisotropies, including longitudinal or transversal single domains and more complex domain structures with closure domains [27,28,29]. However, the exact structure of domain walls (*DWs*) and their evolution during reversal processes have not been discussed and remain open. A detailed description of the distribution of spins in *DWs* unveils the mechanisms involved in the magnetization reversal. Furthermore, it affects the nature and strength of pinning effects [30], which are particularly relevant for devices based on controlled domain wall motion or relying on domain wall stray fields [31,32,33]. In our work, we characterize the

[18] Y. Dahmane, L. Cagnon, J. Voiron, S. Pairis, M. Bacia, L. Ortega, N. Benbrahim and A. Kadri, Journal of Physics D: Applied Physics 39 (2006) 4523
[19] V. Vega, J. García, W. O. Rosa, L. G. Vivas, V. M. Prida, B. Hernando and M. Vázquez, Journal of Nanoscience and Nanotechnology 12 (2012) 7501
[20] P. S. Fodor, G. M. Tsoi and L. E. Wenger, Journal of Applied Physics 91 (2002) 8186
[21] R. L. Wang, S. L. Tang, Y. G. Shi, X. L. Fei, B. Nie and Y. W. Du, Journal of Applied Physics 103 (2008) 07D507
[22] L. Q. Liu, B. Xiang, X. Z. Zhang, Y. Zhang and D. P. Yua, Applied Physics Letters 88 (2006) 063104
[23] D. H. Qin, L. Cao, Q. Y. Sun, Y. Huang and H.-L. Li, Chemical Physics Letters
[24] C. Bran, Yu. P. Ivanov, J. García, R. P. del Real, V. M. Prida, O. Chubykalo-Fesenko and M. Vázquez, Journal of Applied Physics 114 (2013) 043908
[25] A. D. Kent, J. Yu, U. Rudiger and S. S. P. Parkin, Journal of Physics: Condensed Matter 13 (2001) R461
[26] Yu. P. Ivanov, **O. Iglesias-Freire**, E. V. Pustovalov, O. Chubykalo-Fesenko and A. Asenjo, Physical Review B 87 (2013) 184410
[27] C. L. Dennis, R. P. Borges, L. D. Buda, U. Ebels, J. F. Gregg, M. Hehn, E. Jouguelet, K. Ounadjela, I. Petej, I. L. Prejbeanu and M. J. Thornton, Journal of Physics: Condensed Matter 14 (2002) R1175
[28] C. Hassel, F. M. Römer, R. Meckenstock, G. Dumpich and J. Lindner, Physical Review B 77 (2008) 224439
[29] A. Biehler, M. Kläui, M. Fonin, C. König, G. Güntherodt and U. Rüdiger, Physical Review B 75 (2007) 184427
[30] E. R. Lewis, D. Petit, A-V. Jausovec, L. O'Brien, D. E. Read, H. T. Zeng and R. P. Cowburn, Physical Review Letters 102 (2009) 057209
[31] D. A. Allwood, T. Schrefl, G. Hrkac, I. G. Hughes and C. S. Adams, Applied Physics Letters 89 (2006) 014102

domain structures and *DWs* experimentally within these stripes with competing anisotropies and give theoretical support to our statements.

In the fifth overall section, we present a study on domain structures in manganite nanoislands, a work done in collaboration with Prof. *X. Obradors*' group from the *Material Science Institute of Barcelona* (*ICMAB*) that gave rise to a publication in the beginning of 2012 [34]. Magnetic oxides have become an intense area of research in recent years and, among them, the mixed valence perovskite manganite $La_{1-x}Sr_xMnO_3$ (*LSMO*) has triggered plenty of interest due to the physical phenomena that it exhibits, such as colossal magnetoresistance [35,36]. In particular, *LSMO* with strontium doping of x=0.3 displays ferromagnetic and metallic behavior at room temperature and hence results especially appealing from its potential applicability. In most cases, these *LSMO* nanostructures are obtained by patterning continuous films into islands using optical and electron beam lithography or by combining *EBL* with ion milling [37,38,39]. However, it is in general difficult to process oxides in such manner and to accomplish lateral sizes below 0.5 μm without radiation damage or ion implantation [37]. In this context, the bottom-up self-assembly approach based on chemical solution deposition (*CSD*) used in this work offers an effective route to overcome the shortcomings of lithography based techniques, while uniformly covering large areas (in the order of cm^2) without requirements of vacuum environment [40,41,42].

[32] P. Vavassori, V. Metlushko, B. Ilic, M. Gobbi, M. Donolato, M. Cantoni and R. Bertacco, Applied Physics Letters 93 (2008) 203502
[33] A. Torti, V. Mondiali, A. Cattoni, M. Donolato, E. Albisetti, A. M. Haghiri-Gosnet, P. Vavassori and R. Bertacco, Applied Physics Letters 101 (2012) 142405
[34] J. Zabaleta, M. Jaafar, P. Abellán, C. Montón, **O. Iglesias-Freire**, F. Sandiumenge, C. A. Ramos, R. D. Zysler, T. Puig, A. Asenjo, N. Mestres and X. Obradors, Journal of Applied Physics 111 (2012) 024307
[35] J. M. D. Coey, M. Viret and S. von Molnar, Advanced Physics 48 (1999) 167
[36] A. Urushibara, Y. Moritomo, T. Arima, A. Asamitsu, G. Kido and Y. Tokura, Physical Review B 51 (1995) 14103
[37] Y. Takamura, R. V. Chopdekar, A. Scholl, A. Doran, J. A. Liddle, B. Harteneck and Y. Suzuki, Nano Letters 6 (2006) 1287
[38] M. Mathews, R. Jansen, G. Rijnders, J. C. Lodder and D. H. A. Blank, Physical Review B 80 (2009) 064408
[39] E. J. Kim, J. L. R. Watts, B. Harteneck, A. Scholl, A. Young, A. Doran and S. Yuri, Journal of Applied Physics 109 (2011) 07D712
[40] M. Gibert, T. Puig, X. Obradors, A. Benedetti, F. Sandiumenge and R. Huhne, Advanced Materials 19 (2007) 3937
[41] C. Moreno, P. Abellán, A. Hassini, A. Ruyter, A. Pérez del Pino, F. Sandiumenge, M. J. Casanove, J. Santiso, T. Puig and X. Obradors, Advanced Functional Materials 19 (2009) 2139
[42] J. Zabaleta, N. Mestres, P. Abellan, M. Gibert, F. Sandiumenge, T. Puig and X. Obradors, Nanotechnology 21 (2010) 025302

I. Samples with magnetic configurations governed by shape anisotropy

1. Magnetization reversal in permalloy stripes

An array of permalloy nanostripes was grown by a combination of electron beam lithography (*EBL*), sputtering and lift-off processes, using silicon wafers as substrates. The nanostripes are 25 nm thick, 100 nm wide and 5 µm long. Both lateral and longitudinal separation distances between neighboring stripes are 500 nm. The *MFM* characterization was performed under in plane magnetic fields applied either parallel or perpendicular to the main axis of the nanostructures, as indicated in each case. The same commercial *Nanosensors PPP-LM-MFMR* probe (k≈2.8 N/m, f≈75 kHz) was used throughout the experiments shown here. Micromagnetic simulations were carried out using the *OOMMF* code, using standard Permalloy parameters (M_S=8.6·10^5 A/m, A=13·10^{-12} J/m, $k1$=0). The black/white background contrast in the simulations stands for a negative/positive divergence of the magnetization. This should yield analogous information compared to an *MFM* image, where the contrast actually arises from the axial field lines emerging wherever the sample magnetization diverges locally. Colored arrows are also plotted, representing the mean local orientation of the magnetization. In this case, red/blue colored arrows stand for a negative/positive z-component of the local magnetization.

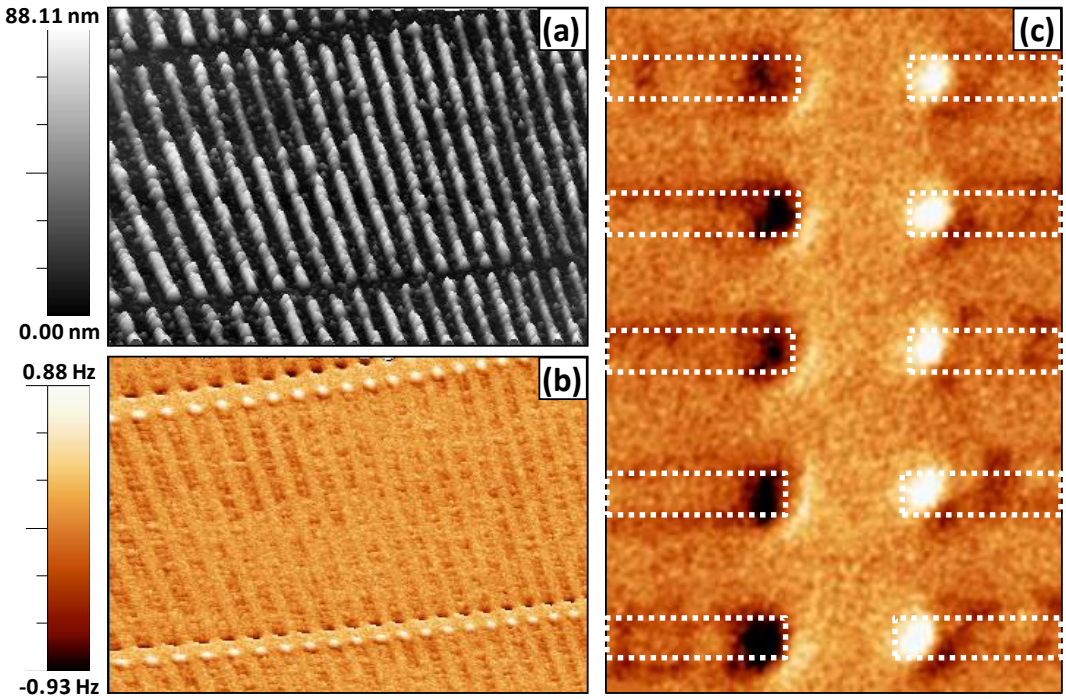

Figure 2.1: The Py nanostripes. ***(a)*** *Topography and* ***(b)*** *MFM image in the remanent state after saturation along the main axis of the stripes. Images size 10 µm × 7 µm.* ***(c)*** *Zoom in on (b), image size 1.6 µm × 2.4 µm.*

The high aspect ratio of the nanostripes is observed in the topographic image shown in figure 2.1.a. The *MFM* picture in figure 2.1.b was obtained in the remanent state, after saturating the sample parallel to the easy axis. A weak contrast is recorded along the stripes due to the single domain configuration, whereas the large divergence of the magnetization at the stripe ends causes a stronger interaction with the *MFM* tip (figure 2.1.c). *MFM* images in this figure show all the stripes with their magnetization pointing along the shape-induced easy axis, parallel to each other, suggesting that a low magnetostatic coupling between neighboring stripes is present, since no influence in the magnetic state of the surrounding nanostructures is seen. In order to gain insight into such coupling, series of *MFM* experiments were carried out under external fields applied whether along the easy (longitudinal) or the hard (transversal to the longitudinal one) axis.

The magnetization reversal process along the in-plane hard axis is presented next. Figure 2.2.a shows the remanent state after ex-situ saturation with 1 Tesla along the vertical direction in the images (see black arrow). The strong shape anisotropy causes the magnetization at remanence to point along the easy axis direction, forming a single domain configuration. In the case of perfectly symmetric stripes, there would be no preferential polarity for the single domains at remanence. However, every single misalignment of the external field will break the symmetry of the energy landscape and cause most of the domains to point along the same direction. We believe this is the reason why most of the stripes in figure 2.2.a have a parallel magnetization. In addition, a small misalignment of the in-situ magnetic field applied during the experiment is expected.

The contrast at the ends of the nanostructures becomes asymmetric under applied fields due to the development of closure domains (see fig. 2.2.c). Furthermore, as the field is increased this contrast decreases significantly (see fig. 2.2.d). Gradually, the magnetization rotates away from the longitudinal axis and a dipolar contrast can be observed across the stripes for large magnetic fields (fig. 2.2.e-f). For a proper interpretation of the magnetization reversal process, we should be aware that the contrast in the images can also be influenced by eventual changes in the magnetization of the *MFM* sensing tip at high fields. In particular, when imaging at relatively high fields it is crucial to rule out eventual contrast contributions caused by changes in the magnetization orientation of the tip. The hysteresis loop of the *MFM* probe used throughout these experiments was performed by imaging a hard disk sample while sweeping the external field. No significant change was found in the magnetic configuration at the tip apex, apart from a slight tilt of its magnetization, under the maximum field used in the experiments.

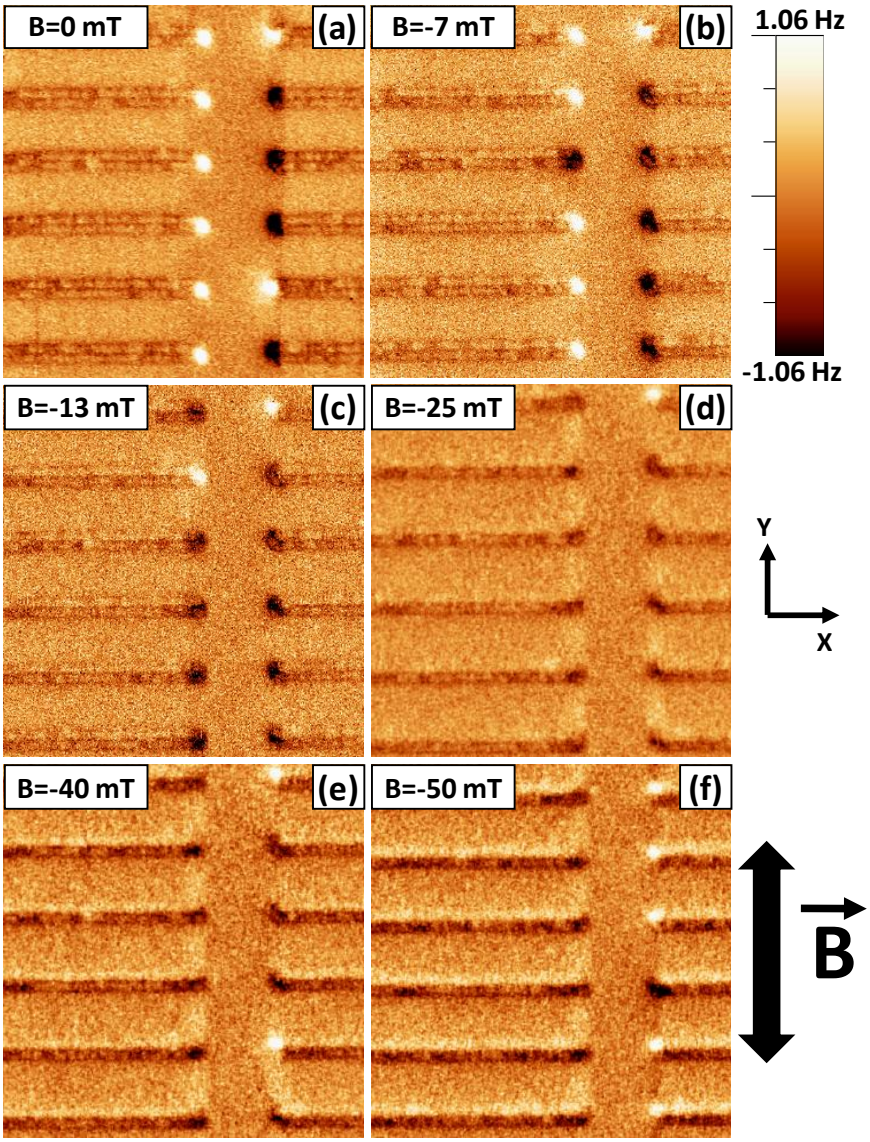

Figure 2.2: The hard axis. *Sequence of (3 µm × 3 µm) MFM images obtained under different magnetic fields applied along the hard-axis.*

In order to clarify the evolution of the contrast observed in the *MFM* pictures, we simulated the magnetic behavior of a single nanostripe with similar dimensions to the experimental case. Figure 2.3 shows the equilibrium magnetization distribution under different fields applied whether along its hard or easy axis. In the first case (hard axis, fig. 2.3.a), the initial saturating field was slightly misaligned from the hard axis, in order to break the symmetry of the system. A field component of 0.1 mT was applied along the easy axis when saturating the stripe and removed thereafter. As a result, switching off the field lets the spins turn back to their easy axis (with a polarity determined by this previous 0.1 mT component), giving rise to an intense contrast at the ends of the stripes caused by closure domains. This behaviour yields a close to zero magnetization along the hard axis in the remanent state, as observed in the hysteresis loop shown in figure 2.3.c. As the external field

increases, the closure domains evolve to a dipolar contrast observable along the transversal direction. Due to the considerable energy expense that is required to get magnetized along the hard axis direction, just a weak contrast is observed experimentally for the maximum applied fields (fig. 2.2.e-f), since they are not large enough to completely reorientate the spins.

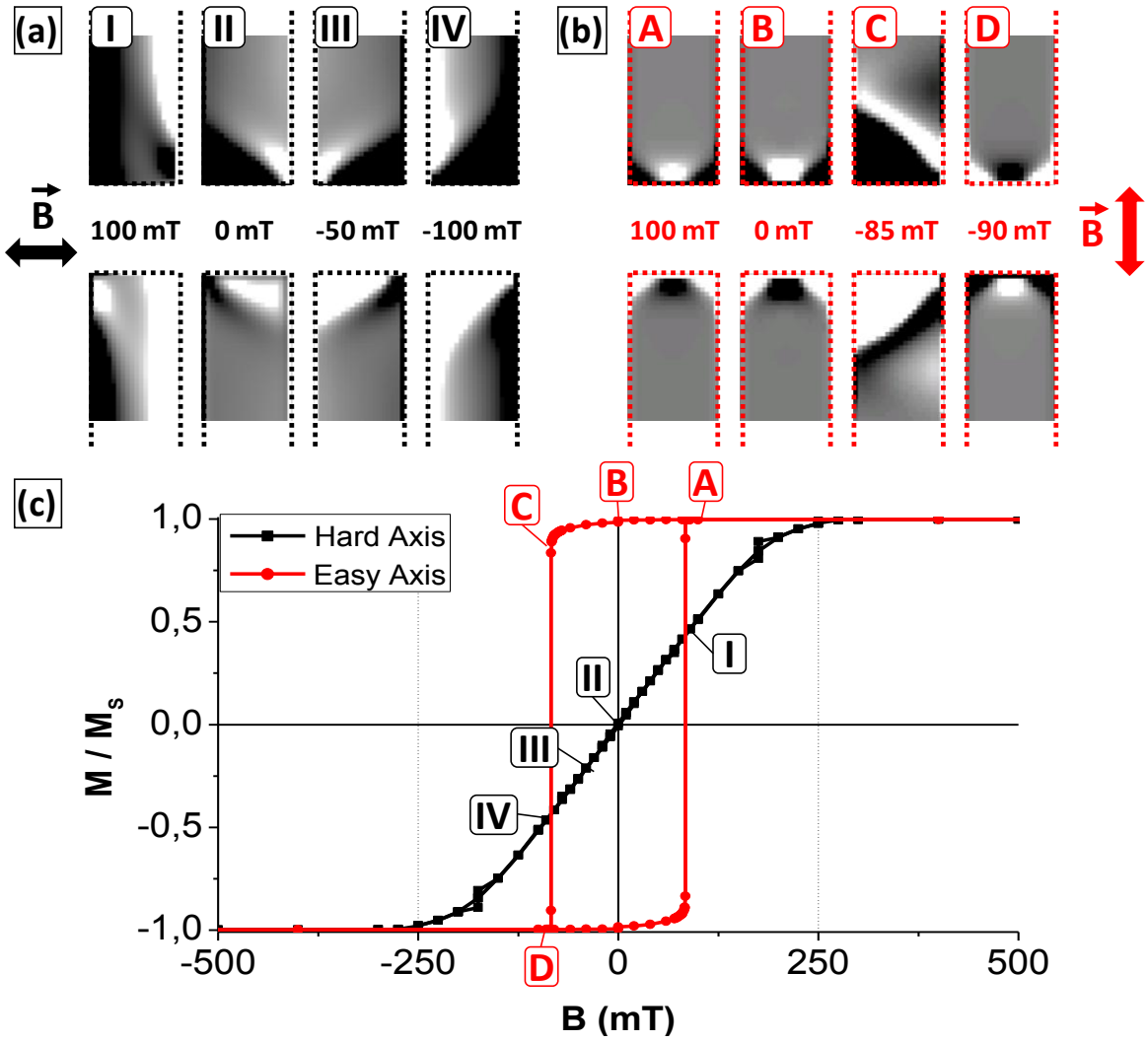

Figure 2.3: Micromagnetic simulations. *A single Py nanostripe (5 µm x 100 nm x 25 nm) was simulated; for clarity reasons, both ends of the same stripe are shown for each case.* ***(a)*** *When large external fields are applied along its hard axis, a transversal dipolar contrast is observed across the stripe (I). For small fields, closure domains are seen at both ends (II)-(III).* ***(b)*** *Closure domains are also formed at the ends, when an external field close to the switching field is applied along the easy axis (C).* ***(c)*** *Simulated hysteresis loops along the easy and hard axis, for the single stripe.*

In the case of magnetic fields applied along the easy axis (fig. 2.3.b), the nanostructure presents a single domain configuration for a large range of fields, including remanence, with the characteristic dark-bright contrast at the ends of the stripe. However, closure domains are formed close to the switching field, before two 180º domain walls nucleate at both ends and propagate along the stripe.

Thus, these nanostripes reverse their magnetization abruptly by means of domain wall nucleation-propagation-annihilation processes, which are much faster than the scan speed of force microscopes and, therefore, out of our present scope. In figure 2.4, a series of *MFM* images obtained under magnetic fields applied along the easy axis is presented. A particular nanostructure has been highlighted as a guide for the eye in order to follow the collective evolution of the magnetic configuration of the whole array. Remarkably, no correlation was found between the magnetic state of one nanostructure and the one of its neighbors. On the one hand, the adjacent elements of a nanostripe can have their magnetization pointing parallel or antiparallel to itself, with no apparent preference. On the other hand, the elements placed in front of a stripe can also be magnetized parallel or antiparallel, as seen in figure 2.4.

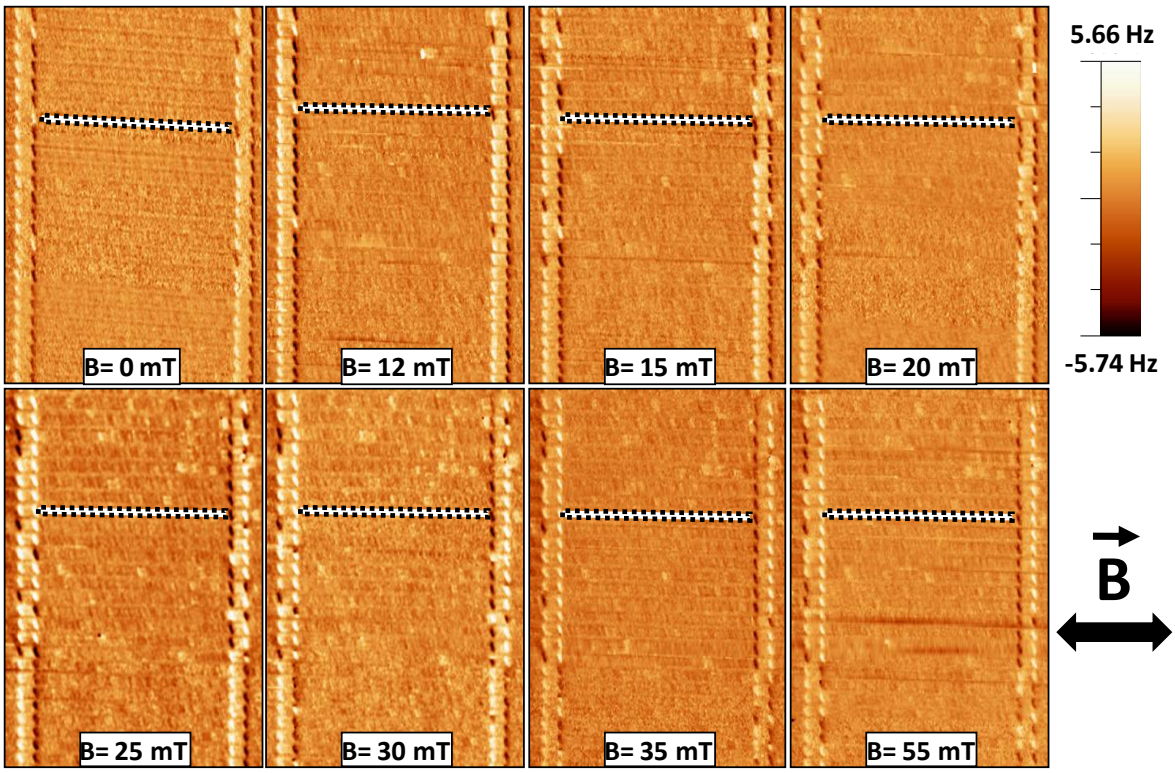

Figure 2.4: The easy axis. *Sequence of (7 µm × 13 µm) MFM images obtained at different magnetic fields applied along the easy-axis of the nanostripes. A particular stripe has been highlighted, as a guide for the eye.*

As seen above, experimental results are in good agreement with the simulated images in both situations, when fields are applied along the hard and easy axis. Next, we will focus on the magnetostatic coupling between neighboring nanostructures. In order to estimate what the critical distance might be, for which the interaction between neighbors becomes relevant and influence the magnetic behavior of the single elements, arrays of permalloy planar wires with variable separation distances were simulated. To achieve reasonable computing times, the length of these nanostripes has been reduced down to 1 µm, whereas both width and thickness were kept constant at 100 nm

and 25 nm, respectively. Nevertheless, no significant difference on the magnetic behavior of individual nanostripes is expected, provided that we still keep a large aspect ratio. Both longitudinal and transversal separation distances among neighboring wires were varied, in order to estimate the critical length for which the dipole-dipole interaction becomes negligible.

For large enough distances, magnetization reversal processes taking place in each wire should be analogous to those of an isolated single stripe. This is the case for stripes whose separation distance is larger than around 500 nm, where two 180º walls are nucleated at both stripe ends and propagate until they annihilate in the central region of every magnetic nanostructure (fig. 2.5).

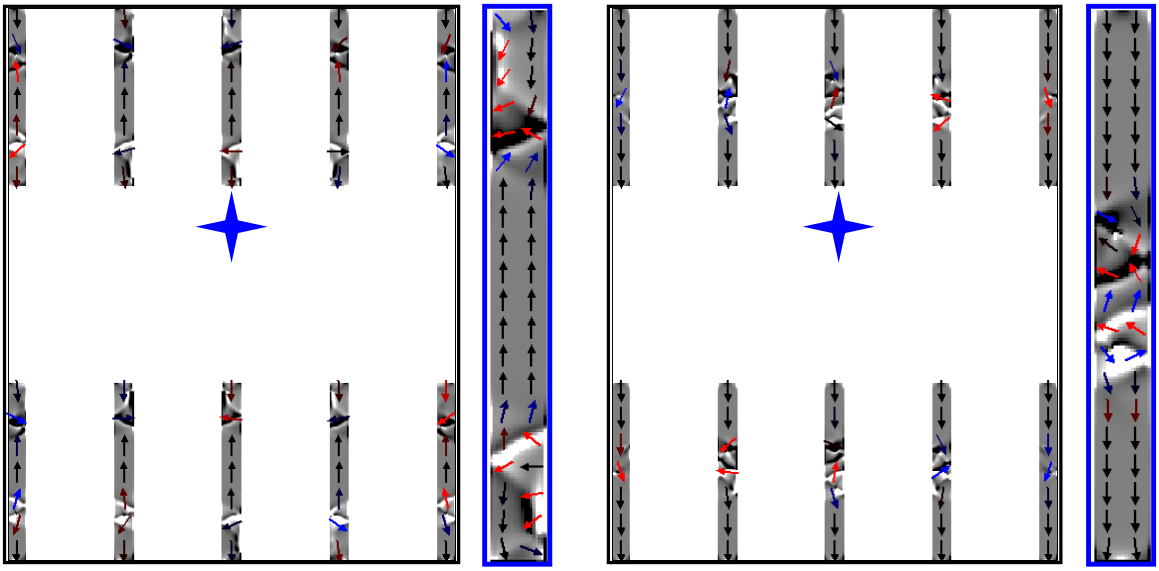

Figure 2.5: Arrays of nanostripes (I). *Simulated evolution of the magnetization for an array of permalloy nanostripes, placed longitudinally 1100 nm and transversally 500 nm apart from each other. This set of images corresponds to the reversal process taking place at the switching field, applied along the easy axis. Two 180º domain walls are nucleated in both sides of the stripes and propagate fast. Nanostripes highlighted with a blue cross are magnified and shown next to the simulation image.*

By decreasing the transversal separation (perpendicular to the stripe long axis) below this critical value, stripes are not independent anymore and prefer reversing their magnetization in groups. The first elements to switch their polarity are those placed at the ends of the array and once this process has started, it gradually spreads out to the neighboring nanostructures, as can be observed in the sequence in figure 2.6. Stripes within each row reverse its magnetization one at a time, being those placed at the center of the image the last ones to do it.

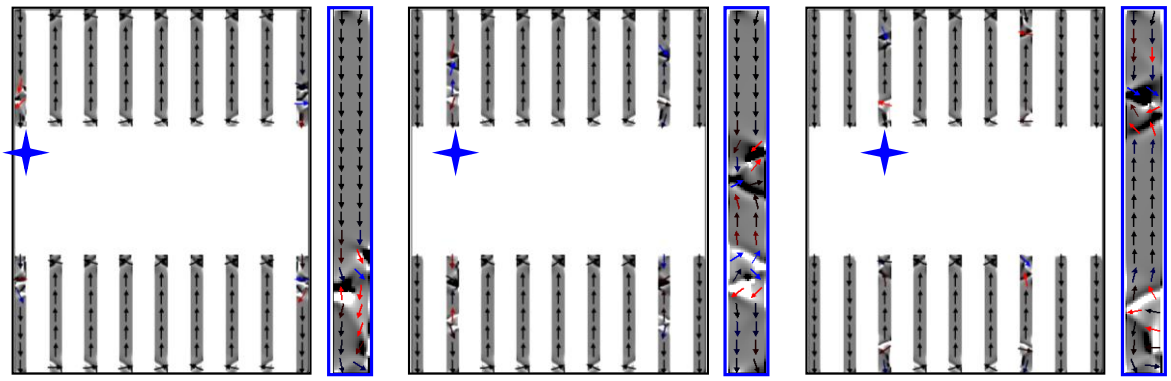

Figure 2.6: Transversal proximity. *Magnetization switching process for an array of stripes with longitudinal and transversal separation distances of 1100 nm and 250 nm, respectively. A magnetic field of 89 mT was applied along the easy axis in every image. Stripes within a row reverse their magnetization gradually.*

In addition, the magnetostatic coupling along the longitudinal axis was checked. Stripes placed far enough from each other act as independent structures until the longitudinal separation decreases below 500 nm, where they start behaving as single elements with domain walls "jumping" between neighboring wires (fig. 2.7.a). In this case, domain walls nucleate at the free ends of the outermost stripes and propagate inwards all along the wires until they annihilate at the opposite stripe side, inducing the formation of a domain wall in the contiguous end of the neighboring nanostructure. Thus, domain walls "jump" from stripe to stripe, yielding every column of wires a single-element-like behavior.

Interestingly, the experimental case shown in the previous section lies in the boundary of an eventual magnetostatic coupling, as predicted by the simulations. The weakness of this coupling is reflected in figure 2.7.b, where a mixture of the explained scenarios can be observed. On the one hand, domain walls originate at the outermost edges, propagating and inducing the switching in the neighboring structures. On the other hand, these walls do not "jump" between stripes since, close before they reach the opposite end of the stripe, a second series of domain walls originates right there and start propagating to the opposite direction. This second set of walls is responsible for inducing the switching process in the neighboring wires. As a result, simulations suggest that 500 nm is the critical separation distance for the permalloy stripes to be magnetostatically coupled, both in the longitudinal and transverse directions.

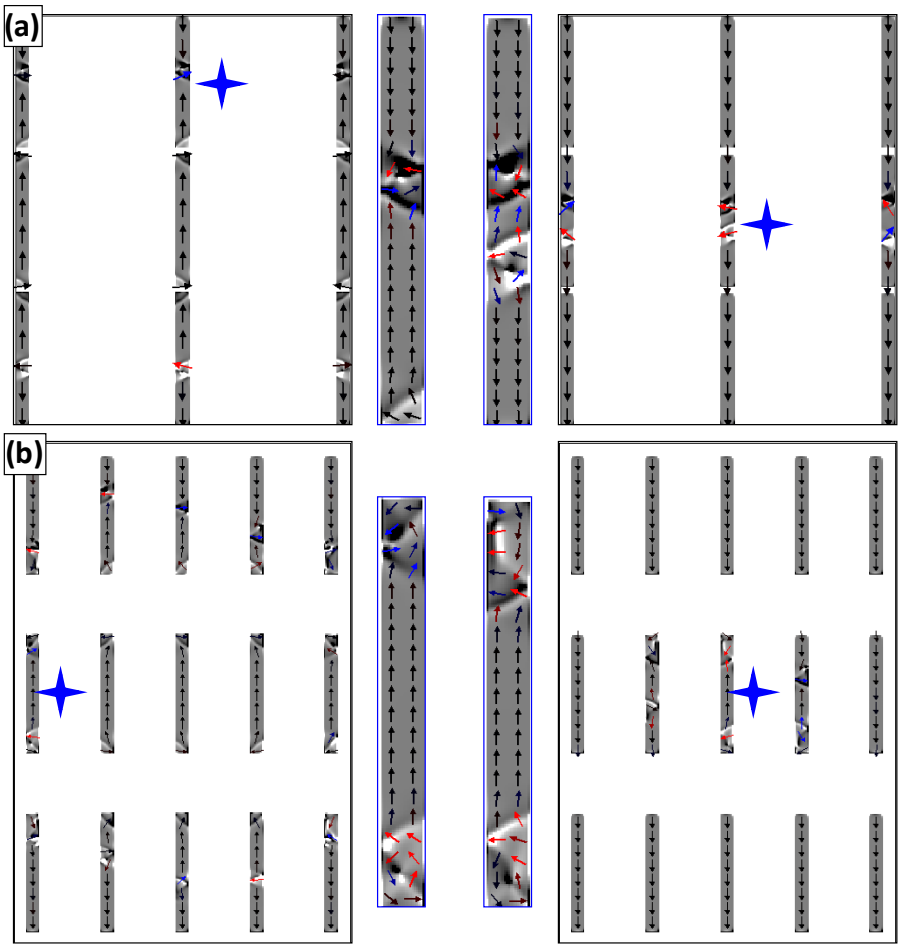

Figure 2.7: Arrays of nanostripes (II). *Simulated evolution over time of the reversal process for an applied field of* ***(a)*** *-92 mT and* ***(b)*** *-82 mT, along the easy axis. (a) Longitudinal (transversal) separation distances between stripes are 50 nm (1100 nm). Columns of stripes behave as single structures, with domain walls nucleating at the free ends of the outermost stripes, propagating along them and "jumping" into neighboring nanostructures. (b) Both longitudinal and transversal separations are 500 nm, equivalent to the experimental case. A mixed behavior (see text) suggests that 500 nm is the critical length for the magnetostatic coupling between stripes.*

As conclusions, the magnetization reversal process in arrays of high aspect ratio Py nanostripes was investigated in parallel by magnetic force microscopy imaging and micromagnetic simulations. As expected from the dominant shape anisotropy, the stable remanent magnetic state of the stripes consists of a single domain structure. Applying external fields allows observing the formation of closure domains and micromagnetic simulations helped us to unveil its structure in detail. The separation distances between neighboring stripes (500 nm) is enough to overcome the magnetostatic coupling and avoid a multistripe character of the whole array. In fact, micromagnetic simulations predict the critical distance for the onset of magnetostatic coupling between neighboring elements to be around this distance, i.e. 500 nm. Remarkably, simulations predict stripes with a small longitudinal separation to behave as quasi-single elements, with domain walls nucleating at the outermost ends of the array, propagating and "jumping" between stripes.

2. MFM as a function of magnetic field: 3D Modes

A number of different modes has been developed to measure topographies with scanning force microscopes, such as amplitude modulation, frequency modulation, jumping mode [43] and pulsed force microscopy [44]. In addition, advanced operating modes – such as force volume [45] and the so-called *3D modes* [46] – are intended for different purposes and allow varying different parameters during the measurement. In this section, we use a particular variant of the *3D modes* for studying magnetization reversal processes. When measuring with a scanning probe microscope, one usually records all parameters of the cantilever oscillation (deflection, oscillation amplitude and phase or frequency shifts) while the tip scans two-dimensional areas of the sample. Such parameters are then related to the interactions present between the tip and the sample, so that physical properties can be unveiled from them. Consequently, three-dimensional images are obtained in which two of the variables correspond to spatial directions. The same oscillation parameters are recorded in *3D modes* imaging; however, the other two variables are defined by the user and do not necessarily involve spatial directions. For instance, one can study variations of the tip-sample interaction while changing the electric biasing, the driving force, the tip-sample distance or any external parameter one might think of, such as the ambient pressure or temperature. In our case, we will choose a particular spatial direction along which the tip will be continuously moving (*X* axis) while the magnetic field (*Y* axis) is gradually changed. As a result, we obtain *MFM* images – corresponding to the frequency shift maps – along a specific profile as a function of the applied magnetic field.

We have applied these *3D modes* to quantify critical magnetic fields in different sorts of magnetic nanostructures. This procedure allows observing the evolution of magnetic states of individual nanostructures with the external field. In previous works [47,48], the evolution of the frequency shift – or phase shift – against the magnetic field was measured at a single position of the nanostructures. However, changes in the relative tip-sample position during the measurement – caused, for example, by thermal drift – can have drastic effects on the measurement. Moreover, when applying magnetic fields magnetostrictive responses of some microscope components can provoke relatively large displacements. Recording the frequency shift of the oscillating cantilever along a specific profile has the advantage of yielding magnetization changes in different regions of the nanostructure and, in addition, minimizes the effect of eventual spurious variations in the tip-sample position during the experiment. As in standard *AFM*, the cantilever deflection and the

[43] P. J. de Pablo, J. Colchero, J. Gómez-Herrero and A. M. Baró, Applied Physics Letters 73 (1998) 3300
[44] A. Rosa, E. Weilandt, S. Hild and O. Marti, Meas. Sci. Technol. 1 (1997)
[45] O. van der Werf, C. A. J. Putman, B. G. Groth and J. Greve, Applied Physics Letters 65 (1994) 1195
[46] C. Gómez-Navarro, A. Gil, M. Álvarez, P. J. de Pablo, F. Moreno-Herrero, I. Horcas, R. Fernández-Sánchez, J. Colchero, J. Gómez-Herrero and A. M. Baró, Nanotechnology 13 (2002) 314-317
[47] X. Zhu, P. Grütter, V. Metlushko and B. Ilic, Applied Physics Letters 80 (2002) 2676
[48] Y. Endo, H. Fujimoto, S. Kumano, Y. Matsumura, I. Sasaki, Y. Kawamura, M. Yamamoto and R. Nakatani, Journal of Applied Physics 103 (2008) O7D918

oscillation amplitude are simultaneously recorded, in order to assure optimum feedback conditions. Thus, we believe this *MFM* based operating mode to be a versatile method for characterizing magnetic nanostructures, the typical measuring time being around 1 minute. It can also be used to quantify switching fields of *MFM* probes by using hard magnetic samples and recording contrast inversions in the images. This was done prior to the experiments shown here and, in order to avoid unexpected changes of contrast, the applied fields were below the switching field of the probe.

Hysteresis loops of individual cobalt stripes

Here, we will introduce the usefulness of this method by characterizing polycrystalline cobalt stripes that were grown by focused electron beam induced deposition in the group of Prof. *J. M. de Teresa* and *R. Ibarra*, at the *University of Zaragoza*. The sample fabrication was carried out in a commercial *FEI dual-beam* equipment using a field emission scanning electron microscope with $Co_2(CO)_8$ as gas precursor, Si substrates and electron-beam conditions of 2.1 nA beam current, 10 keV beam energy, and 1 μs dwell time. A suitable set of growth parameters produce Co nanodeposits with high Co content (95%), magnetotransport properties similar to those of pure Co [49] and good domain wall conduit behavior [50]. Notice that, due to the polycrystalline character of the Co deposits, its magnetic behaviour is controlled by the shape anisotropy instead of by magneto-crystalline anisotropy. All probes used in this set of experiments were commercial Si cantilevers (*Nanosensors PPP-FMR*, k=1.5 N/m and f_0= 75 kHz) home coated in our lab with a 25 nm thick Co film and a 2 nm Cr capping layer. As will be explained in chapter 4, these specifications were selected in order to prevent the influence of the tip stray field in the magnetic state of the sample.

As can be seen in the topographic image in figure 2.8.a, the length of the grown planar wires is found to be roughly constant (5.3 ± 0.1 μm), whereas their width and thickness range from 0.1 to 2.25 μm and from 20 to 140 nm, respectively. Large separations between elements were thought to avoid significant influence between neighboring structures through dipolar interactions. Figure 2.8.b shows the variability in the as-grown magnetic state of ten stripes with different aspect ratios. The observed spin distributions range from complex multi domain to single domain configurations, also being present intermediate structures with closure domains at both ends. As has been previously discussed by *Fernández-Pacheco* and co-workers [51], magnetization reversal in this type of wires is not expected to be significantly influenced by structural defects; essentially, shape

[49] A. Fernández-Pacheco, J. M. de Teresa, R. Córdoba and M. R. Ibarra, Journal of Physics D: Applied Physics 42 (2009) 055005
[50] A. Fernández-Pacheco, J. M. de Teresa, R. Córdoba, M. R. Ibarra, D. Petit, D. E. Read, L. O'Brien, E. R. Lewis, H. T. Zeng and R. P. Cowburn, Applied Physics Letters 94 (2009) 192509
[51] A. Fernández-Pacheco, J. M. de Teresa, A. Szkudlarek, R. Córdoba, M. R. Ibarra, D. Petit, L. O'Brien, H. T. Zeng, E. R. Lewis, D. E. Read and R. P. Cowburn, Nanotechnology 20 (2009) 475704

anisotropy suffices to explain the reversal process. Thus, domain wall pinning effects caused by defects are not expected for the nanostructures studied here.

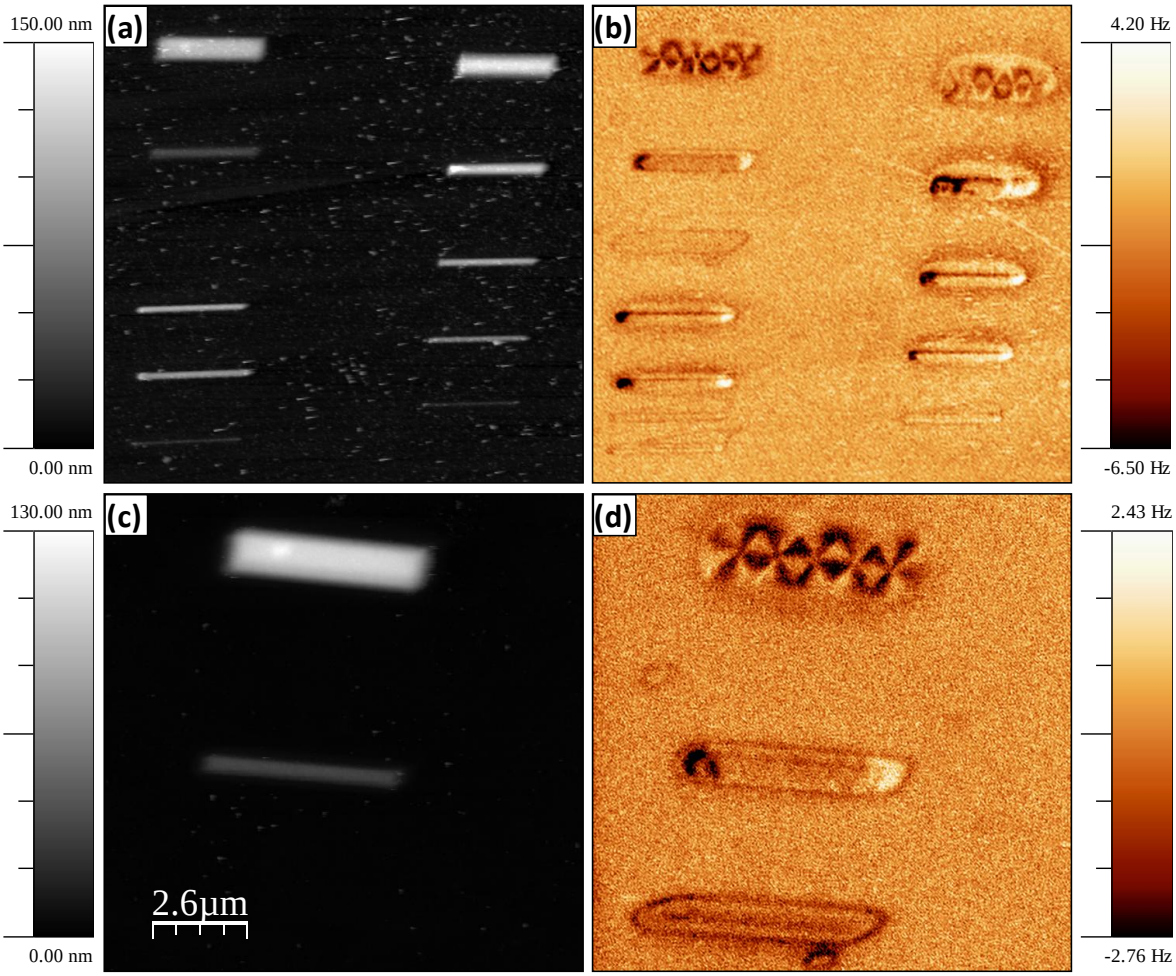

Figure 2.8: The cobalt stripes. (a) *Topography and* ***(b)*** *MFM image showing polycrystalline Co stripes of variable aspect ratio; image size: (22×24) µm*^{2}*.* ***(c)*** *&* ***(d)*** *Magnified images providing a better resolution.*

Interestingly, two "phantom" stripes are faintly visible in the left column of stripes in figure 2.8.b whereas no prominent features are seen in the corresponding topographic map. This effect is caused by charge accumulation on the substrate due to the fabrication technique, an effect that will be discussed in detail in chapter 3. More detailed images of two of the widest stripes are seen in figure 2.8.c-d, where the intricate magnetic contrast yielded by the widest element seems to be difficult to interpret at first sight. The other nanostructure has a single domain character in the central region with closure domains at the longitudinal ends.

The magnetization reversal processes for stripes within each regime will be discussed in the following. Figure 2.9 displays *MFM* images of one of the widest elements, recorded for different

applied fields. Complementarily, simulated images show equilibrium steps during the reversal process for a cobalt stripe of the same dimensions. These numerical calculations are in qualitative good agreement but lack in quantitative precision; for that reason, only the experimental field values are displayed. In the remanent state and after *ex-situ* saturation along the stripe long axis, a complex magnetic structure is experimentally observed (uppermost image in fig. 2.9.a). The corresponding simulated image turns very helpful since it describes the contrast as caused by the presence of several vortices along the stripe. The combination of vortices with the square shape of the magnetic element yields such fan-like color distribution in the *MFM* maps.

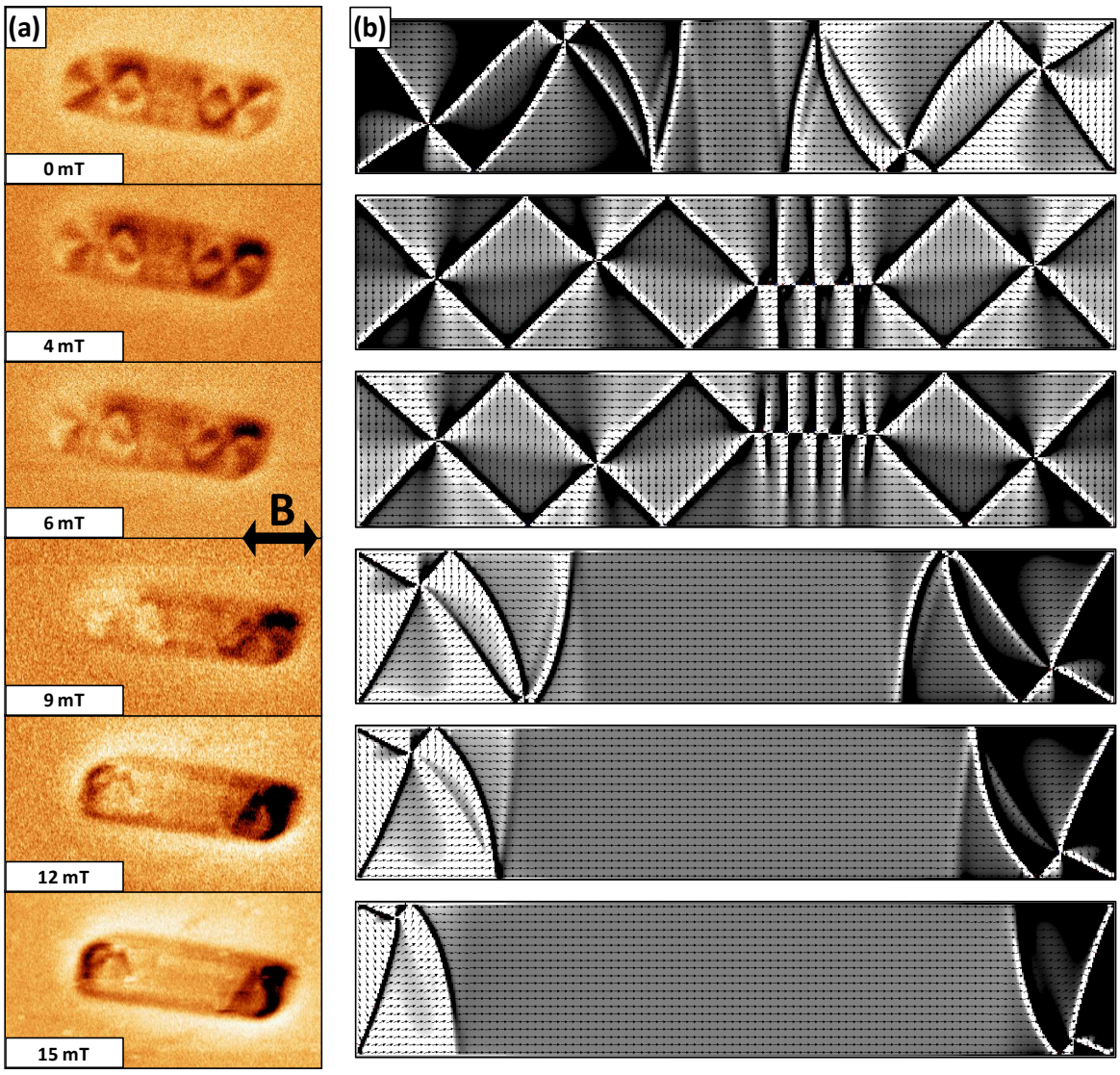

Figure 2.9: The widest stripes. (a) *Sequence of MFM images of a (5.2 x 1.1 x 0.1) μm³ Co stripe measured at variable in-plane fields after ex-situ saturation with -500 mT.* ***(b)*** *Sequence of micromagnetic simulation images describing the experimental spin configurations. Simulated images do not correspond to the same field values as in the experiment.*

By gradually applying a horizontal field, vortices change their position moving perpendicular to that direction. For sufficiently large values, the ones present in the central region of the stripe annihilate at the long edges. At this point, a central single domain region is observed, in which spins point parallel to each other. At both ends, single vortices form closure domains (lowermost images in figures 2.9.a-b). These vortices approach the edges of the nanostructure and annihilate once a strong enough field is reached, leaving the sample in a reversed single domain state.

Multiple-vortex mediated reversals are also observed when decreasing the stripe width, as observed in the two elements shown in figure 2.10. A similar behavior is observed in the uppermost one, as compared to the one described in figure 2.9, with vortices forming along the whole nanostructure (see fig. 2.10.b). However, for width values of around 400 nm, a single domain is observed, in which vortex closure domains are distinguishable at both ends (see bottom stripe in fig. 2.10.c). When the field reaches a critical value, a sudden reversal takes place in these elements. Finally, the shape anisotropy in the narrowest stripes provides them with a single domain behavior, where no closure domains are observed in the experiments. In this case, the magnetization is reversed by means of a fast domain wall nucleation-propagation-annihilation process.

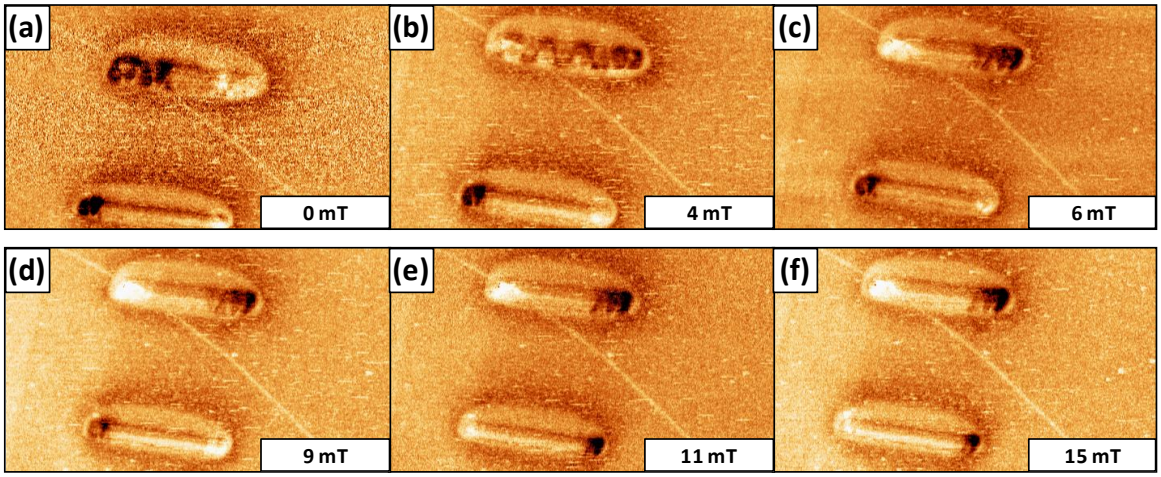

Figure 2.10: Stripes of intermediate widths. *Evolution with an external horizontal field of the magnetic state of two stripes with dimensions (5.2 μm x 510 nm x 120 nm) and (5.3 μm x 400 nm x 95 nm).*

All the information extracted so far was obtained from standard *MFM* measurements and their comparison to simulations. We will now extend our knowledge by using the aforementioned *3D modes*. First, a topographic image and its corresponding standard *MFM* map of a 1 μm wide stripe were obtained (fig. 2.11.a-b). The same intricate contrast is observed with the presence of four magnetic vortices. *3D modes* experiments were performed by continuously scanning the tip along the white profile in figure 2.11.a at a tip-sample distance of around 30 nm, while sweeping the

external field. Results are shown in the frequency shift images shown in figures 2.11.c-d. In the same way as in standard *MFM* images, $\Delta\omega$ yields information about the magnetic properties of the sample and, assuming the magnetization in the tip remains unchanged during the measurements, is directly related to the sample magnetization. Hence, every horizontal line reveals the magnetic state of the sample along the dashed line in figure 2.11.a for a specific field value, indicated on the vertical axis.

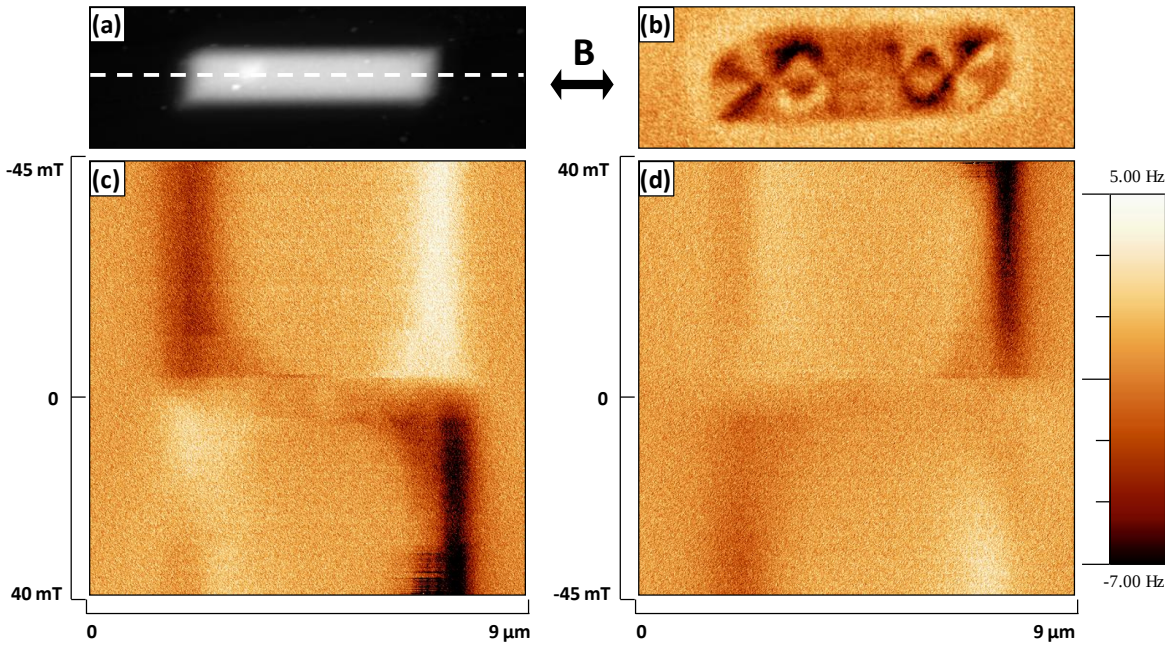

Figure 2.11: 3D modes (I). (a) *Topography and* ***(b)*** *corresponding MFM image of a stripe 1 µm in width and 105 nm thick. 3D modes images recorded with the tip scanning along the dashed profile line in (a), while sweeping the external field from* ***(c)*** *negative to positive fields and* ***(d)*** *vice versa.*

For large fields – corresponding to the upper- and lowermost regions in figure 2.11.c and d – the stripe lies in the saturation state and presents a single domain structure. This configuration yields a characteristic dark-bright contrast at the ends of the structure. As the field is decreased down to around 15 mT, some contrast appears in the central region of the planar wire, which is caused by the nucleation of vortices along the magnetic element, as is shown in the sequence displayed in figure 2.9.e. In particular, a complex combination of dark and bright contrast is observed in the remanent state, when no external field is applied, due to the high divergence of the magnetization resulting from such spin distribution. By reversing the field direction it is possible to record vortices displacements that move away from the profile along which the probe is scanning and, thus, no signal is recorded in the central part of the stripe anymore. Eventually, over a certain value vortices annihilation takes place and a subsequent loss of contrast along the magnetic structure is

seen. Finally, a reversed bright-dark contrast at the stripe ends is obtained, corresponding to the reversed saturation state.

A different behavior is observed in narrower elements. Figure 2.12 shows the topography and its corresponding *MFM* image of a 260 nm wide stripe, with a comparable thickness to the one shown in figure 2.11. *3D modes* measurements performed with the probe moving along the stripe main axis – for magnetic fields ranging between (-35 mT, 30 mT) – indicate the presence of a single domain configuration with a bi-stable character. On the way back from saturation (uppermost horizontal lines in figures 2.12.c-d), the characteristic dipolar contrast is seen for the whole range of fields, until a sudden change happens. Magnetization reversal processes take place via a fast domain wall nucleation-propagation-annihilation mechanism, much faster than the scan speed of our set up. Thus, a reversed single domain contrast is recorded from one line to the following one, once the switching field has been reached.

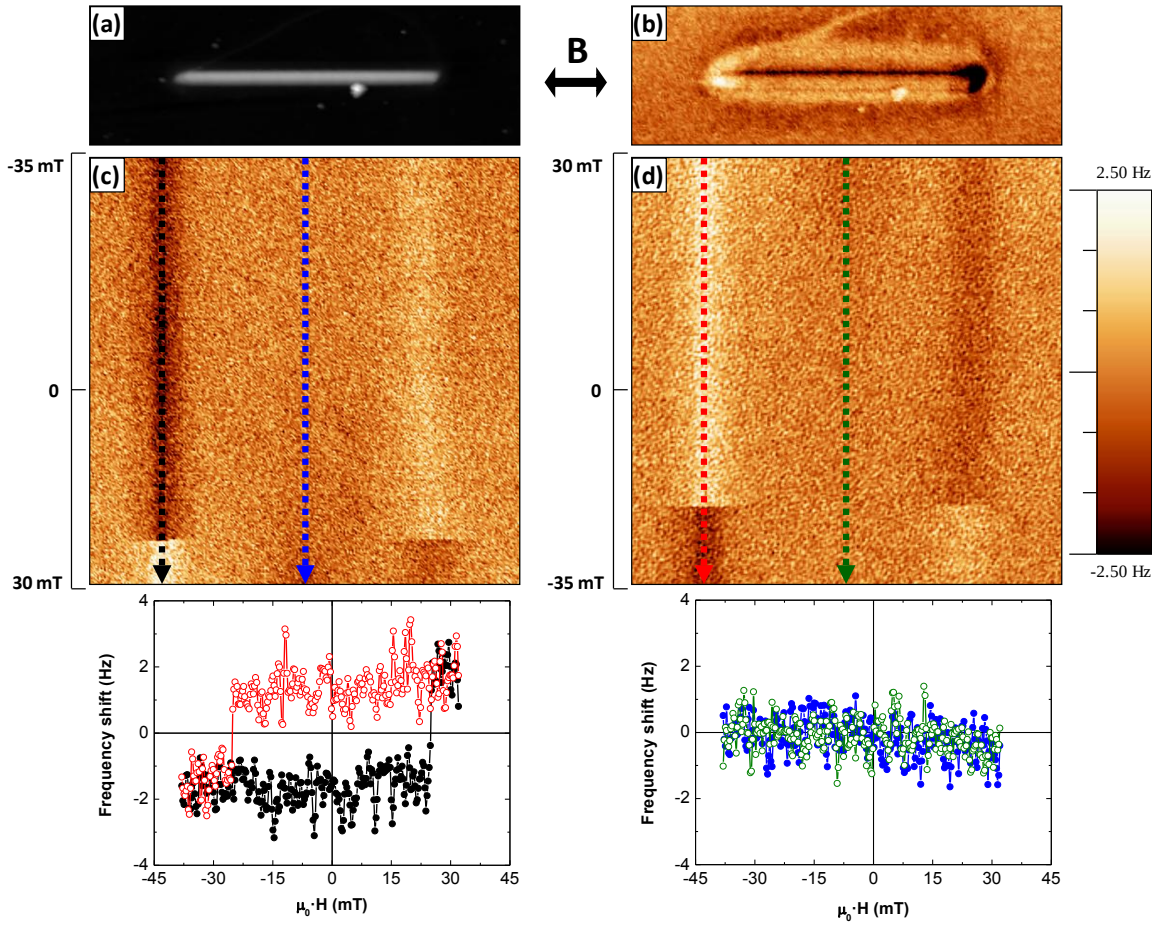

Figure 2.12: 3D modes (II) (a) *Topography and* ***(b)*** *MFM image at remanence of a (5.4 μm x 260 nm x 95 nm) stripe. 3D modes images measured from* ***(c)*** *negative to positive fields and* ***(d)*** *vice versa. Graphs show the profiles along the corresponding dashed lines in the 3D modes images. Error in the field calibration is in the order of the dot size.*

Plotting the contrast along vertical profiles in the *3D modes* maps gives us information about the variation of the magnetostatic interaction between tip and sample, as the applied field is changed. By doing this at one end of the stripe (black and red profiles in figs 2.12.c-d), the hysteresis loop of this single stripe is obtained. Using this method, a switching field of 24 ± 2 mT is obtained for this nanostructure. Its single domain character is evident when plotting a vertical profile in the central region of the stripe, since no change in the tip-sample interaction is observed (blue and green profiles in fig. 2.12). Data shown in the hysteresis loops have been smoothed to slightly decrease the noise. Notice that a subtle asymmetry is observed in the hysteresis loops between positive and negative frequencies. This is expected and usually observed in magnetic force microscopy and is due to the enhanced sensitivity of the system to attractive interactions (negative $\Delta\omega$) as compared to repulsive force gradients (positive $\Delta\omega$).

Thus, this particular operating mode yields a method for quantifying critical fields in magnetic samples, such as switching fields in samples with single domain character or vortices nucleation and annihilation fields. The high spatial resolution characteristic of scanning force microscopy represents an advantage compared to other characterization techniques, since it allows for characterization of single nanostructures well below the micrometer scale. High magnetic field resolutions can be achieved by choosing small steps (in the examples shown in figures 2.11 and 2.12, field steps of 0.17 mT and 0.13 mT were used, respectively), while performing low time consuming measurements, typically in the order of 1-2 minutes. However, it is important to point out that a systematic error associated to the stray field of the probe is introduced in the quantification of critical fields. As it is well known, the magnetic coating at the tip apex creates non-negligible magnetic fields that add up to the applied one. Additionally, in our case a non negligible error is present when calibrating the field applied at the sample position. Nevertheless, this *3D modes* procedure represents an improvement compared to standard *MFM*, since no topographic feedback is used during the experiment; on the contrary, the probe remains at a tip-sample distance of several tens of nanometers without approaching the sample. Therefore, the influence of the stray field is minimized.

Switching field of cobalt stripes as a function of thickness

Due to the relatively large variability in dimensions resulting from this fabrication technique, it becomes not straightforward to grow stripes with homogeneous profiles and the desired values of width and thickness. The efforts of our collaborating group turned out to be successful and a sample was fabricated, in which most of the stripes present a comparable length in the range of (7.0 ± 0.1) μm (see figure 2.13). Their dimensions and large enough aspect ratios provide them with a

single domain character and square hysteresis loops caused by fast *DW* propagation magnetization reversals. Thus, *3D modes* seems to be a fast and suitable way to study the dependence of the switching field on the stripe thickness. Homemade *MFM* probes were used due to the excessive influence that the commercial ones had in the magnetic state of the sample, at the expense of getting lower sensitivities. Refer to chapter 4 for further information on these probes.

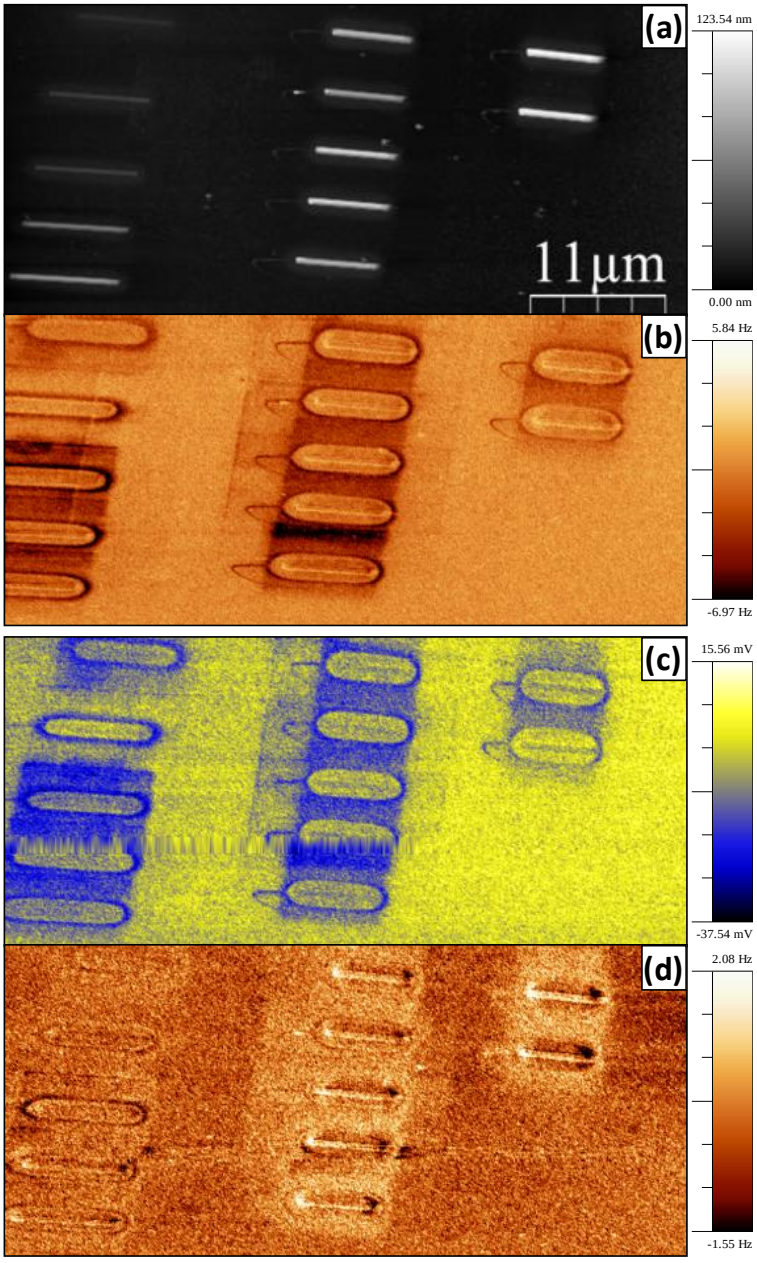

Figure 2.13: Co stripes of similar length. ***(a)*** *Topography of polycrystalline cobalt nanostripes, nine of them having comparable lengths in the range (7.0 ± 0.1) µm.* ***(b)*** *Excitation frequency image obtained during the retrace scan, where strong dark halos are observed around the stripes. The expected single domain contrast is not observed in the stripes.* ***(c)*** *Surface potential and* ***(d)*** *pure MFM images obtained in the same area with the Kelvin feedback enabled. The image in (c) accounts for electrostatic interactions and the one in (d) only for magnetostatics. Notice the drop in the frequency range as compared to (b), revealing that the magnetic information was masked beneath charging effects.*

Unexpected dark halos are observed around the nanostripes in the frequency shift image (fig. 2.13.b), where the magnetic information of the sample is usually obtained. As will be demonstrated in chapter 3, such contrast arises from charging effects that are present in the regions surrounding the stripes, giving rise to subsequent frequency shifts that mask the magnetic information. Small prominences around 5 nm high are seen in the topography as well, revealing that some material with small cobalt content has grown around the stripes. It will be explained that, by enabling an additional feedback loop to cancel out electrostatics known as *Kelvin Probe Force Microscopy* (*KPFM*), it becomes possible to separate both contributions and obtain pure *MFM* contrast (fig. 2.13.c-d). In fact, halos are perfectly seen in the surface potential image presented in figure 2.13.c, which accounts for electrostatic interactions between tip and sample. It is even possible to distinguish the paths followed by the electron beam during the deposition process; however, no particular feature is noticeable along the stripes themselves. On the contrary, the typical single domain character is clearly observable in the pure *MFM* image (fig. 2.13.d, compare to fig. 2.13.b).

Using the *3D modes*, hysteresis loops were obtained for all the stripes presenting a comparable width, in the range of (350 ± 10) nm. They are six elements, five of whose results are shown in the graph of figure 2.14. These experimental data (black profile) show a gradual decrease of the switching field as the stripes become thicker. The experimental error was limited by the low signal-to-noise ratio provided by the sensing tips.

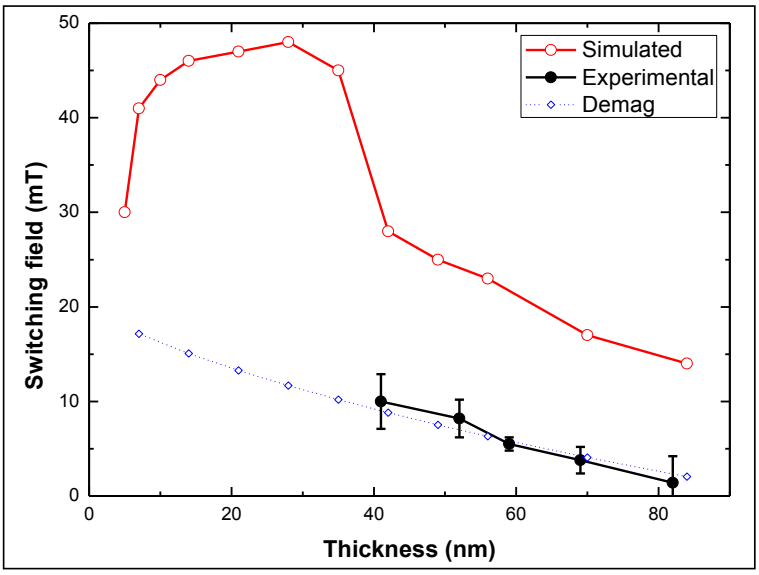

Figure 2.14: Switching field vs thickness. *Dependence of the switching field versus the stripe thickness, obtained* ***(black)*** *experimentally using the 3D modes, with the Kelvin feedback enabled (see figure 3.7);* ***(red)*** *from micromagnetic simulations, where larger values are expected due to the usual overestimation associated to them and* ***(blue)*** *from the theoretical demagnetizing factors.*

An approach using the demagnetizing field approximation is plotted as a blue dashed line. Demagnetizing fields were estimated through the theoretical demagnetizing factors, which for the case of a rectangular stripe can be obtained from their lateral dimensions using the formula given by *Aharoni* [52]. An arbitrary offset was added to the calculated demagnetizing fields, which can be regarded as the external field necessary to reverse the magnetization in a very thin stripe with the same length and width considered in the calculations (7000 x 350) nm^2. It has a value of 20 mT for the blue curve shown in figure 2.14. However, the simple demagnetizing factor approach is only valid for samples where the internal field can be considered uniform throughout the stripe and that reverse the magnetization by coherent rotation. In order to make a reliable statement, micromagnetic simulations must be used.

Simulations were performed for stripes of the nominal experimental dimensions (350 nm x 7 μm x thickness) using again the *OOMMF* code. The resulting fields at which the magnetization switches are plotted as a red profile in figure 2.14, with the external field being applied along the *Y* axis. A similar slope is seen as in the former cases for thicknesses over 40 nm; however, numerical values are offset to larger values. As usual, only a qualitative agreement is reached and, since no thermal effects or structural defects are considered in the simulations, the switching fields are overestimated. By contrast, a different trend is predicted for small thicknesses, up to around 30 nm, where the switching field increases rapidly with the stripe height; thus, a transition between reversal modes seems to take place. Such a transition between reversal mechanisms has already been reported for experimental $Ni_{80}Fe_{20}$ systems by *Vavassori* and co-workers [53].

Figure 2.15 presents the simulated spin configurations during the reversal for three different thicknesses. Images shown do not correspond to equilibrium states but to snapshots extracted during the dynamic reversal. For very low thicknesses, simulations predict the formation of multiple *Neél* domain walls all along the elongated element, as can be clearly seen in the upper image of figure 2.15.a. To further help with the interpretation of the simulations, cross sections of the stripes – taken at the positions highlighted with arrows – are presented as well.

As the thickness increases, less energy is gradually required for spins to point out of the sample plane. For thicknesses close to the pronounced drop in H_{sw} (fig. 2.15.b), reversal takes place through propagating vortex walls that nucleate and annihilate at the longitudinal edges, with the magnetization essentially lying *IP*.

[52] A. Aharoni, Journal of Applied Physics 83 (1998) 3432-3434
[53] P. Vavassori, V. Bonanni, G. Gubbiotti, A. O. Adeyeye, S. Goolaup and N. Singh, Journal of Magnetism and Magnetic Materials 316 (2007) e31-e34

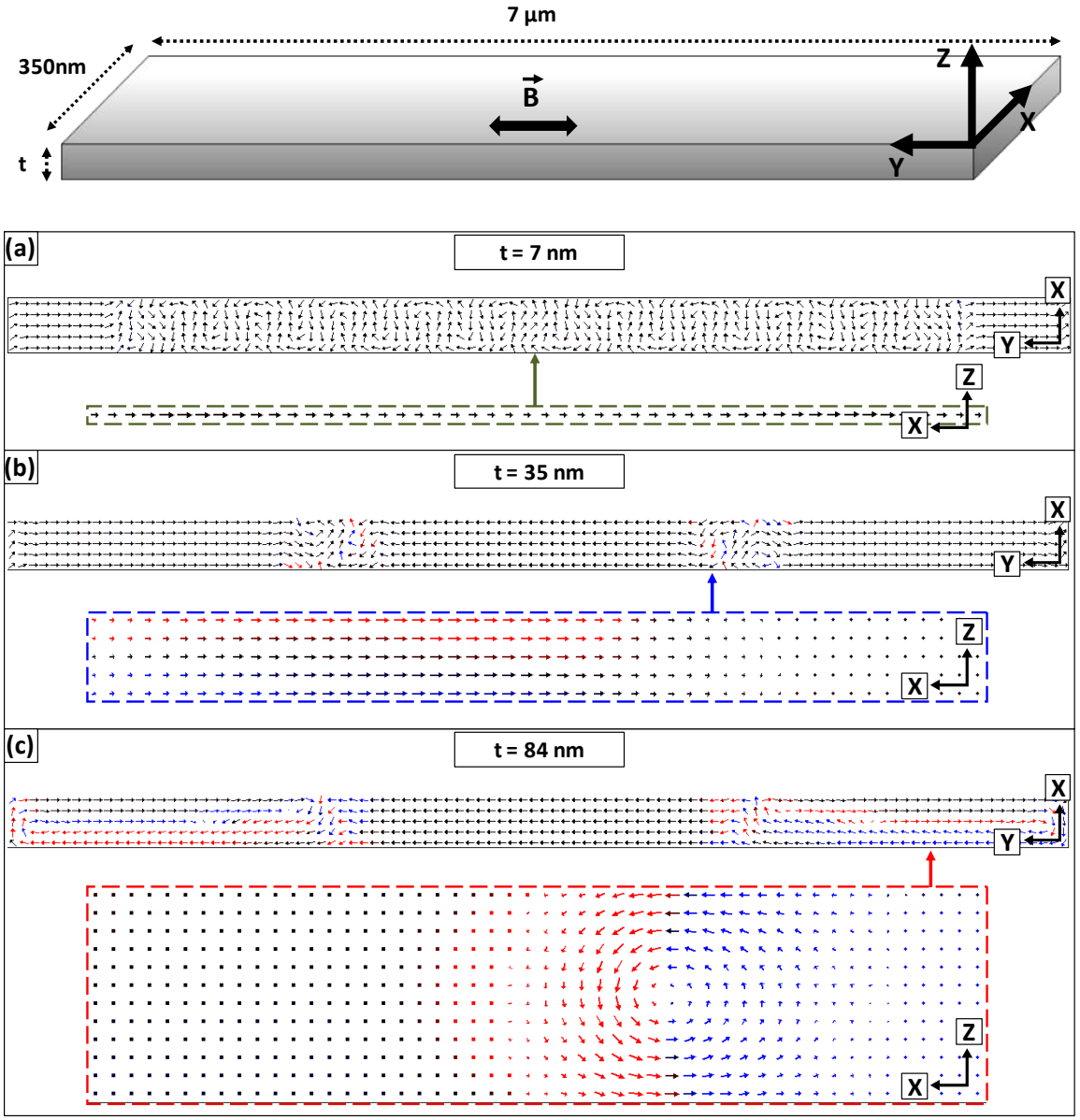

Figure 2.15: The three regimes. *Magnetization reversal predicted by micromagnetic simulations for Co stripes 350 wide (X axis) and 7 µm long (Y axis) and variable thickness of* ***(a)*** *7 nm,* ***(b)*** *35 nm and* ***(c)*** *84 nm, with negligible magneto-crystalline anisotropy. Top views (top) and cross sections at the possitions highlihgted with arrows (bottom) of non-equilibrium steps during the reversal process.*

In the elements of largest thicknesses, two asymmetric *Bloch* walls [54] are predicted to carry out the reversal, as can be seen in figure 2.15.c. Taking a look at the cross section, a similarity becomes clear between this configuration and the longitudinal vortex walls, which mediate the magnetization reversal in cylindrical nanowires [55] of similar dimensions. Indeed, the aspect ratio between the two transversal dimensions has decreased down to four in figure 2.15.c.

[54] A. Hubert and R. Schäfer, "Magnetic Domains" (Springer, Berlin 1998)
[55] L. G. Vivas, R. Yanes, O. Chubykalo-Fesenko and M. Vázquez, Applied Physics Letters 98 (2011) 232507

Consequently, at least three regimes are found, with this numerical approach, in the inversion type. In addition, it is possible to observe the presence of closure domains in the equilibrium states of the thickest stripes, close to the switching field. This can be inferred from the simulated hysteresis loops, as shown in figure 2.16:

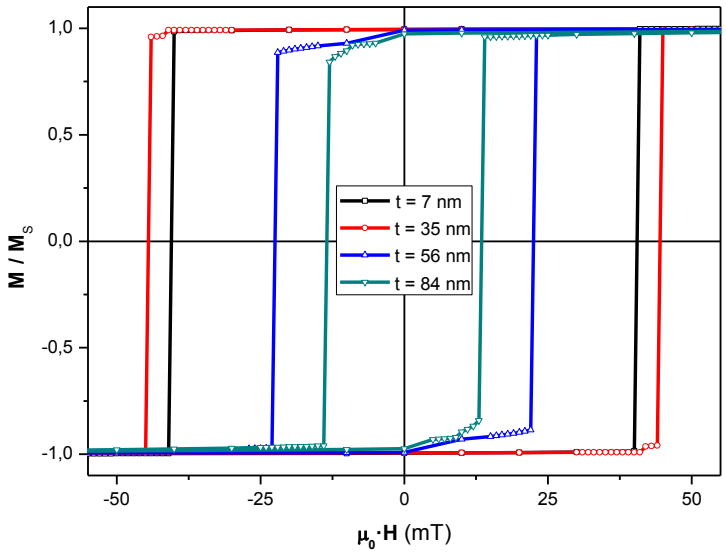

Figure 2.16: Simulated loops. *Hysteresis loops for stripes of four different thicknesses, obtained from simulations. The presence of closure domains in the equilibrium states of thick stripes can be extracted from the graphs.*

These closure domains give rise to a decreased magnetization observable in the loops before the sudden jump takes place. They consist of domain walls of the same types described above, as they are indeed responsible for initializing the reversal process from the ends of the elongated nanostructures. Thus, vortex *DWs* are observed at the ends of stripes with intermediate thicknesses and asymmetric *Bloch* walls in the case of the thickest elements. On the contrary, no closure domains are observed when the height of the nanostructures lies below 25-30 nm.

Unfortunately, the sixth experimental stripe not shown in figure 2.14, even although being an ideal candidate to experimentally check this change of reversal mode due to its 17 nm thickness, could not be characterized because of the too low magnetostatic coupling to the *MFM* probe that yielded no signal over the experimental noise. Thus, this transition remains as a predicted result.

3. Domain structures in modulated $Fe_{28}Co_{67}Cu_5$ nanowires

Cylindrical $Fe_{28}Co_{67}Cu_5$ nanowires with a very high aspect ratio were fabricated by Dr. *C. Bran* in the group of Prof. *M. Vázquez* at the *Material Science Institute of Madrid* (Spain) within the pores of alumina layers that serve as templates [56,57]. Such aluminium oxide layers – containing cylindrical pores of tunable diameter arranged in hexagonal order – were obtained after carrying out a two-step anodization process on 99.999 % pure aluminium foils in an H_2SO_4 aqueous solution (3 wt. %) at a constant temperature of 0 ºC. During the first anodization step, a constant voltage of 25 V was applied for 16 hours. After dissolving the pores formed in the 1st anodization using a mixed solution of chromium oxide and phosphoric acid, the surface of the Al substrate keeps the hexagonal structure created in the 1st step, acting as a mask for the 2nd anodization.

The modulated nanopores were synthesized in the 2nd anodization step by periodically applying pulses of 25V, called mild anodization (*MA*) pulses, and 35V, hard anodization (*HA*) pulses. The geometry of the nanochannels (i.e length, diameters, shape) is controlled not only by time, voltage or temperature but also by the shape of the hard anodization pulses [58]. During the 2nd anodization, and in order to avoid the breakdown of the anodized film during the first *HA* pulse, the duration of the first *MA* pulse was extended to 15 minutes, followed by alternating mild and square hard pulses applied for 150 s and 200 ms, respectively, and repeated 10 times to assure a pore length of about 40 μm. The resulting cylindrical modulated pores are formed by segments with diameters of around 22 and 35 nm, respectively, while the center-to-center inter-wire distance is kept constant at 65 nm. After the anodization process, the aluminium substrate was removed with an aqueous solution composed of copper chloride and hydrochloric acid and the alumina barrier layer is etched with an aqueous solution of H_3PO_4 (5 wt. %). A gold layer was sputtered on one side of the alumina templates to ensure a good conductivity needed for the electrochemical deposition.

$Fe_{28}Co_{67}Cu_5$ nanowires around 7 μm in length were subsequently grown into the cylindrical modulated pores by electrodeposition from a sulfate-based electrolyte containing $CoSO_4{\cdot}7H_2O$ (35 g/l), $CuSO_4{\cdot}5H_2O$ (2 g/l), $FeSO_4{\cdot}7H_2O$ (15 g/l), H_3BO_3 (10 g/l) and ascorbic acid (10 g/l). The electrochemical deposition was carried out under potentiostatic conditions by applying −1.8 V versus the Ag/AgCl reference electrode, keeping the temperature of the electrolyte at 25ºC and the *pH* value at about 3.0. As a result, a macroscopic membrane enclosing a very large number of ferromagnetic nanowires is obtained. The membrane was then divided into different pieces so that bulk magnetometry measurements were performed, on the one hand, whereas dissolution of the

[56] C. R. Martin, Science 266 (1994) 1961-1966
[57] H. Masuda and K. Fukuda, Science 268 (1995) 1466-1468
[58] I. Minguez-Bacho, S. Rodriguez-López, M. Vázquez, M. Hernández-Vélez and K. Nielsch, Nanotechnology 25 (2014) 145301

alumina and subsequent deposition onto a Si substrate was followed up by *TEM* and *MFM* analysis of single $Fe_{28}Co_{67}Cu_5$ elements, on the other hand. In a previous report [24], *XRD* spectra showed these type of nanowires to crystallize in an FeCo *BCC* phase textured along the [110] direction. In order to help with the analysis of their magnetic properties presented later, we will now give some detail about the resulting crystalline structure on the inside of the nanostructures.

For doing the characterization, different pieces of the same alumina membrane were dissolved using a mixed solution of CrO_3 and H_3PO_4. Nanowires were then repeatedly water washed while separating them with the help of a small magnet. Last, the water was replaced by ethanol and a drop of dissolved nanowires spread on top of a Si substrate by spin coating. Wires usually tend to gather together, especially during the washing step, so that spin coating dispersion becomes necessary. A negative side effect turns out to be an enhanced probability of the wires to fracture; broken fragments can thus be found in some examples shown in this report. For long enough elements, slight bending may also take place.

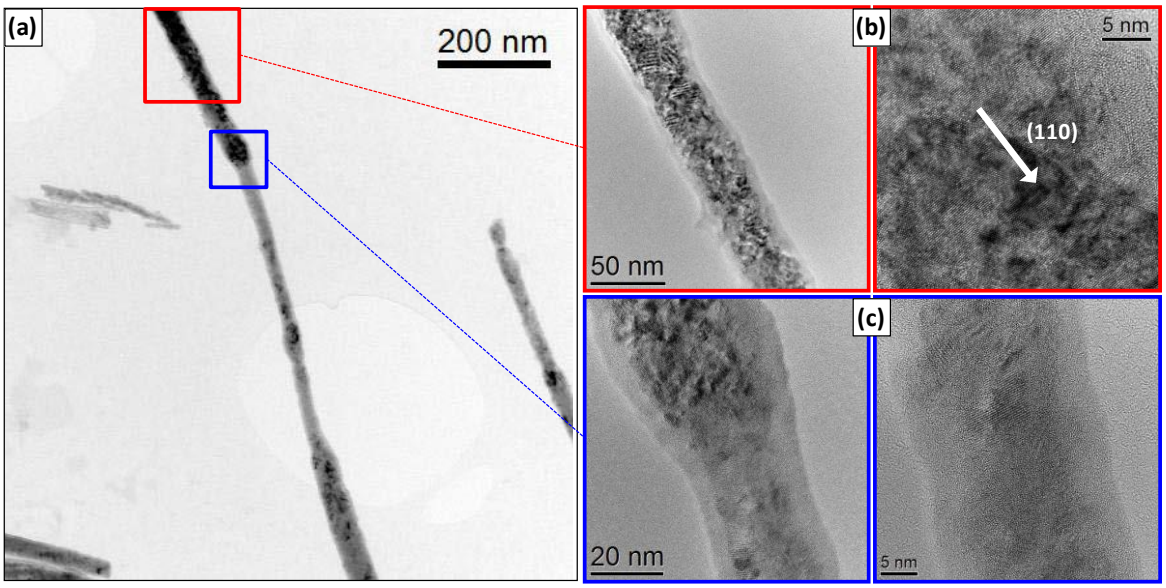

Figure 2.17: TEM characterization of dissolved modulated $Fe_{28}Co_{67}Cu_5$ nanowires. ***(a)*** *A modulation step in the diameter is clearly observed in the single nanowire.* ***(b)*** *Zoom in images on the area highlighted with a red square in (a), showing a BCC unit cell highly textured along the [110] direction.* ***(c)*** *Magnified images of the area framed in blue in (a), revealing a less strong texture.*

High resolution transmission electron microscopy (*HR-TEM*) characterization was performed by Dr. *C. Magén* at the *Nanoscience Institute of Aragón* (*INA*) to evaluate the resulting crystallinity and structural properties of the nanostructures. The composition of the nanowires alloy was also checked by *Energy Dispersive X-ray* spectroscopy (*EDX*) to be the aforementioned one. A step-like variation in the diameter of a single nanowire can be easily identified in figure 2.17.a, where the

very high aspect ratio of these nanostructures becomes evident. Magnified images of the square areas framed in red and blue are presented in figures 2.17.b and c, respectively. There, an amorphous layer with a roughly constant thickness of 5 nm is observed throughout the whole nanowire, regardless of the local diameter, whose origin might be the mismatch between the crystalline structure of the wire and the alumina on the pore walls during the growth process. Regions where the diameter remains constant are estimated to be around 500-700 nm long, with diameters varying from around 35 nm in the thicker parts (fig. 2.17.b) to 22 nm in the thinner ones (fig. 2.17.c). Inner regions of the nanostructure present a *BCC* crystalline order with the thicker parts being highly textured along the [110] direction, whereas thinner fragments show considerably weaker texture. Notice that a morphological roughness of several nanometers is observed on the surface of the nanowire, as well as at the interface between the external amorphous and the crystalline inner parts. Its effect will be commented later during the *MFM* analysis.

Hysteresis loops were obtained from a different piece of the same alumina membrane (encompassing a large number of $Fe_{28}Co_{67}Cu_5$ nanostructures) at room temperature by vibrating sample magnetometry (*VSM*). Magnetic fields up to ±1.7 T were applied, able to nearly saturate magnetically the sample along both the longitudinal and transversal directions. According to the shape and enclosed areas of both loops (fig. 2.18.a), an effective longitudinal magnetization easy axis is deduced. The resulting loop for the case of a longitudinal field suggests the existence of relatively large magnetostatic interactions between neighboring elements, as expected from the small inter-pore distance. As a result, a remanent magnetization of 41 % the saturation value is obtained. Saturation fields of 0.8 and 1 T along the easy and hard axis are extracted from the graph.

As will be described later in detail, the magnetic behavior of individual cylindrical nanowires has been simulated under different conditions. Figure 2.18.b shows the hysteresis loop along the easy axis of a modulated element with two thick and two thin segments (red curve), compared to the evolution of two wires with homogeneous diameters of 22 and 36 nm (green and blue curves, respectively). The three of them show a bi-stable character (see inset in figure 2.18.b) with high remanent magnetizations (over 98 % the saturation value), as expected from single-domain individual wires. In the case of homogeneous wires, the reversal process is mediated by two vortex walls nucleating at both longitudinal ends and propagating inwards. Larger fields are required for the 22 nm element to flip the orientation as compared to the 36 nm one. As will be shown later, one of the ends of the simulated nanowire is 36 nm in diameter (corresponding to a thick segment). The reversal process of such element begins with a vortex wall nucleating at this end and this explains the similarities of the hysteresis loops between the modulated and 36 nm straight wires (fig. 2.18.b). The slightly lower value of the magnetization seen in the modulated structure close before the *Barkhausen* jump is associated to magnetization curling taking place at the discontinuities.

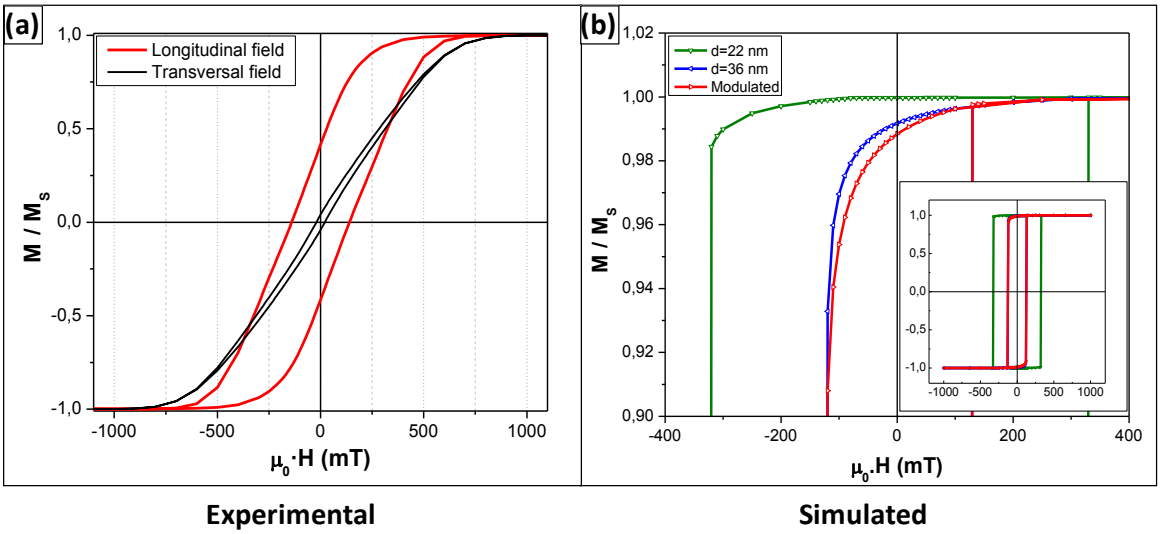

Figure 2.18: Hysteresis loops. (a) *VSM hysteresis loops of modulated $Fe_{28}Co_{67}Cu_5$ nanowires embedded within the Al_2O_3 membrane, with the field applied along the wires' longitudinal axis (red curve) and a transversal direction (black profile).* ***(b)*** *Simulated hysteresis loops of cylindrical homogeneous (d=22 nm and d=36 nm) and modulated nanowires.*

Knowing about the nanowires structural characteristics paves the way to extract more accurate information from magnetic force microscopy images and interpret the influence of the periodic diameter modulation. Intuitively, since small defects cause the magnetization to diverge – and, consequently, magnetic charges to appear –, a periodic *MFM* contrast is expected to be measured along the nanostructures, corresponding to the transitions between segments of different diameter.

The topography of some modulated nanowires can be seen in figure 2.19.a. The high aspect ratio nanostructures present a clear periodic modulation noticeable in the topographic map, where it is possible to discern the wider and thinner segments. It is worth recalling that, when using scanning force microscopies such as *MFM*, objects are presented with broadened lateral dimensions due to the convolution of tip-sample interactions over the tip volume. Nevertheless, very high accuracy is obtained in the height profiles. In the experiments presented in this report, even although nanowires of much larger diameters seem to be present, the height values measured are in outstanding agreement with the 22 and 35 nm values deduced from *TEM* imaging.

A very good dispersion of nanowires was achieved after dissolution of the alumina membrane, with a large density of individual elements observed in the experimental images. However, series of nanostructures aligned up in a row were also found in different parts of the sample, a likely consequence of the dipolar-like magnetostatic interactions between dissolved wires during the drying step on the silicon substrate. As already pointed out in the *TEM* analysis, some nanowires

display a slight bending which we attribute to an enhanced weakness of the thinner parts, consequence of their reduced diameter and lower crystalline texture (see fig. 2.17.c).

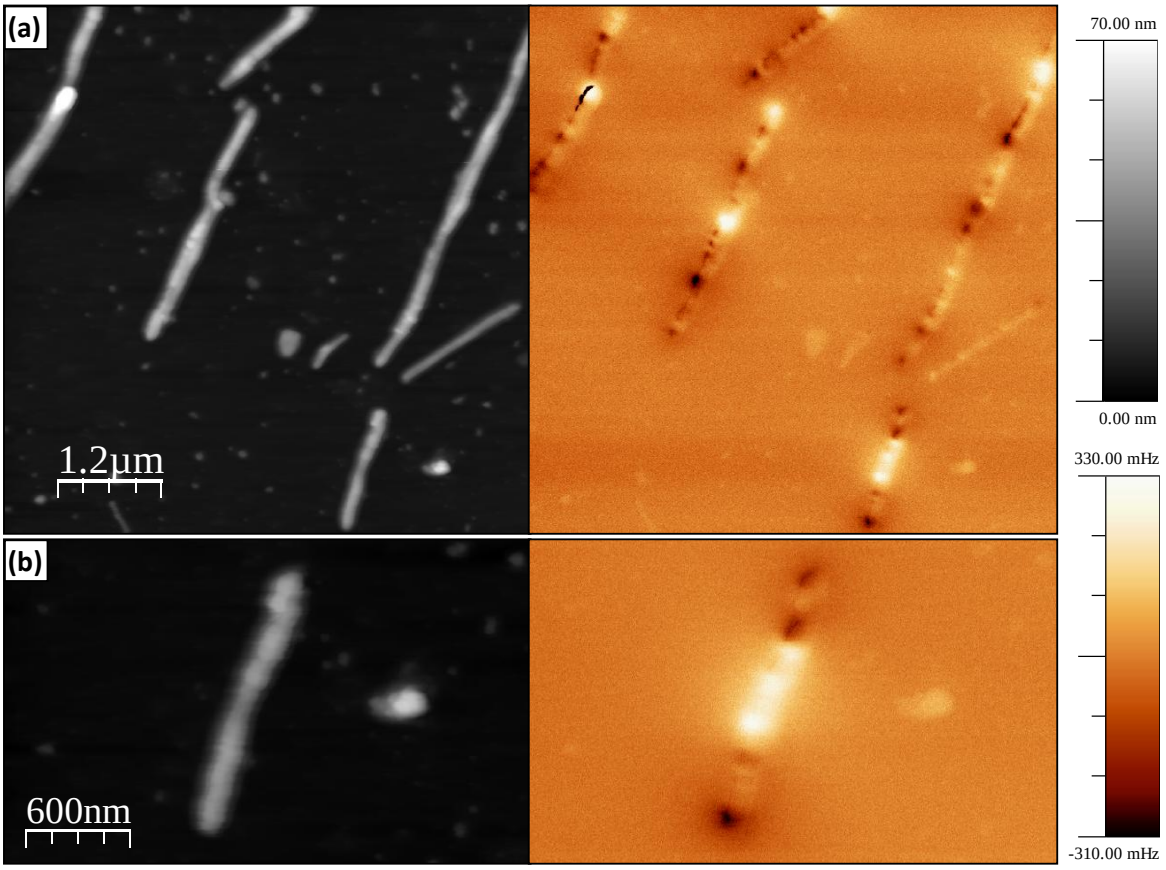

***Figure 2.19: The as-grown magnetic state**. Modulated nanowires deposited onto a Si substrate, showing the domain structure before any field was applied (see text). **(a)** (20 x 7.5) μm^2 images displaying the topography and the magnetic configuration of nanowires. **(b)** Magnified nanowire present in the lower part of (a).*

Figure 2.19.a shows the corresponding *MFM* image in a quasi-as-grown state. As mentioned before, a small magnet was used to separate the *NWs* from the solvent during the washing step, so that eventual changes in the magnetization might have been induced. A direct interpretation of the *MFM* images seems to be rather difficult. To a first sight, they seem to indicate the existence of complex configurations involving many *DWs*, as every nanowire displays multitude of attractively and repulsively interacting regions (dark and bright contrast in the *MFM* images, respectively). The same behavior is also observed in short nanostructures, as the one presented in figure 2.19.b.

As a general overview, we mention that two main types of magnetic contrast are observed: relatively intense spots, which are not only present at the ends of the wires but also at specific positions along the nanostructures, and series of weaker and alternating bright/dark contrasts observed along the elements. Each of them will be later attributed to a different source. We should

note that no significant charge accumulation was found to be present in the wires, so crosstalk of electrostatic interactions into the *MFM* maps can be disregarded.

In order to check the magnetic hardness of these nanostructures, measurements were carried out while applying an external in-plane field along the horizontal direction of figure 2.20. The sequence of images shown there was recorded applying fields along opposite directions in order to identify and interpret eventual changes in the domain structure of nanowires. As was expected from the bulk hysteresis loops shown in figure 2.17, it was not possible to saturate the sample with the magnetic fields achievable *in-situ*. Nevertheless, changes in the magnetic state are observed and highlighted by arrows in figure 2.20.

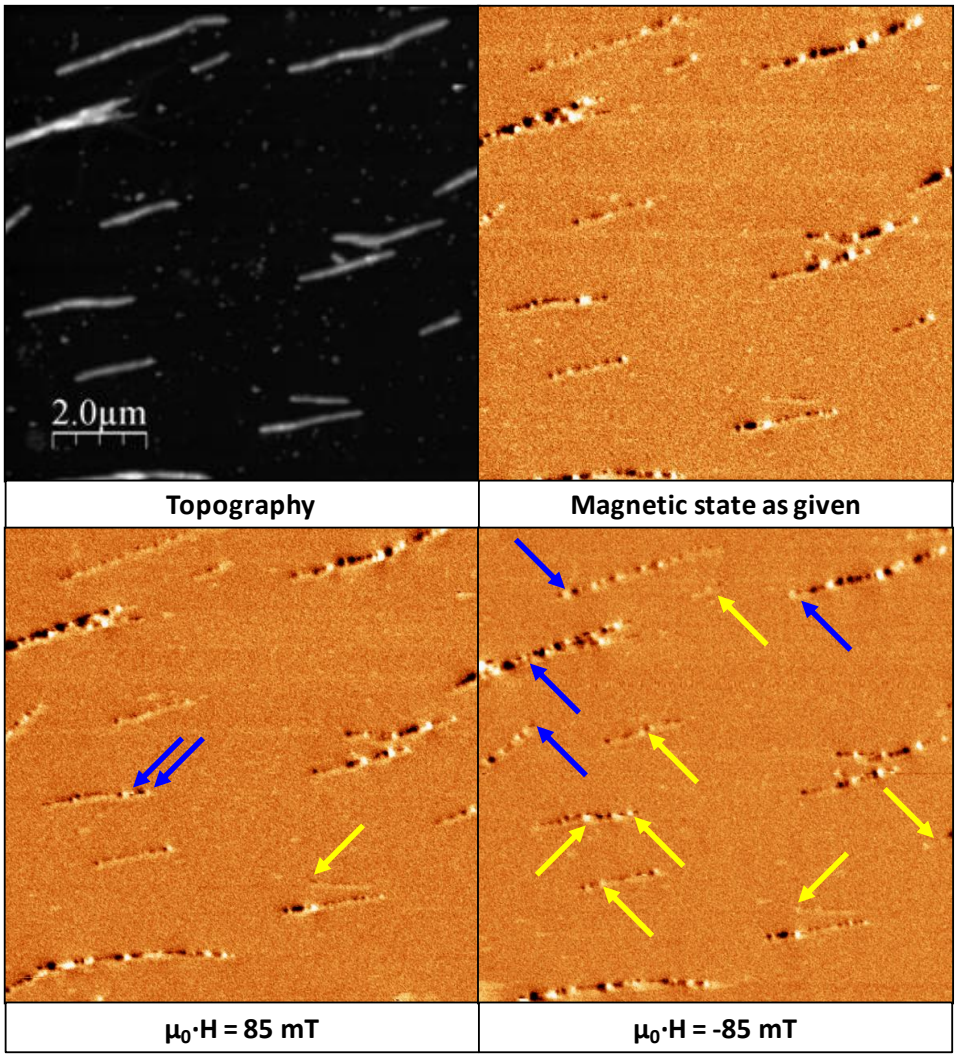

Figure 2.20: Magnetic hardness of the modulated nanowires. *Topography and sequence of MFM images recorded under an external magnetic field applied along the horizontal direction. Blue arrows indicate changes in long structures, attributed to DWs nucleation/annihilation processes. Yellow arrows highlight changes in the shortest wires.*

Essentially, just minor changes are observable during the field sweep both in long nanowires (blue arrows) as well as in short wires (yellow arrows). Since the magnetization seems to change only locally, we attribute these variations to domain wall nucleation/annihilation processes. Thus, the modulated geometry proves to enhance the domain wall pinning.

- *The remanent state*

In order to unveil this challenging domain structure, the sample was saturated with an external field (1.7 Tesla) applied along a well defined direction (horizontally in figure 2.21) and *MFM* experiments were again performed. According to the macroscopic hysteresis loops shown in figure 2.17.a, one might expect the wires to effectively saturate under such large fields and to possess a single domain character going back to zero fields. This remanent state is shown in figure 2.21.a, where several isolated nanowires can be identified. Relatively strong magnetic contrast is not only visible at the longitudinal ends (typically observed in single domain samples with the magnetization lying in the sample plane) but also at different position along the wires. This becomes even more evident watching the high resolution *MFM* image shown in figure 2.21.b.

In addition to these intense spots, a quite periodic but considerably weaker contrast is also noticeable in the zoomed picture shown in figure 2.21.c. One may notice the good signal-to-noise ratio achieved in the experiment by looking at the frequency shift scale bar, which reveals the net divergence of the magnetization in the sample to be rather small, despite the clear and well defined contrasts observed in the images. We will now focus on the first type of contrast and will deal with these fainter features at the end of the section.

In order to do so, micromagnetic simulations were carried out using the *OOMMF* code to simulate the resulting spin distribution in a 2 μm long cylindrical nanowire with a step edge modulated diameter varying between 22 and 36 nm and a period length of 500 nm. A cubic cell size of (2x2x2) nm^3 was used, with the experimental values for the saturation magnetization M_S=1.59·10^6 A/m and exchange stiffness A=10.7·10^{-12} J/m. The magnetocrystalline anisotropy has been assumed not to play a significant role in the magnetization reversal process taking place in these nanostructures, according to the conclusions reported by *Bran* and co-workers [24]. Simulated *MFM* images are shown in a black-white color scale that stands for a negative-positive divergence of the magnetization. In addition, arrows are also plotted that account for the averaged orientation of local spins; in this case, a blue-red color scale represents a negative-positive component of the local magnetization along the nanowire axis.

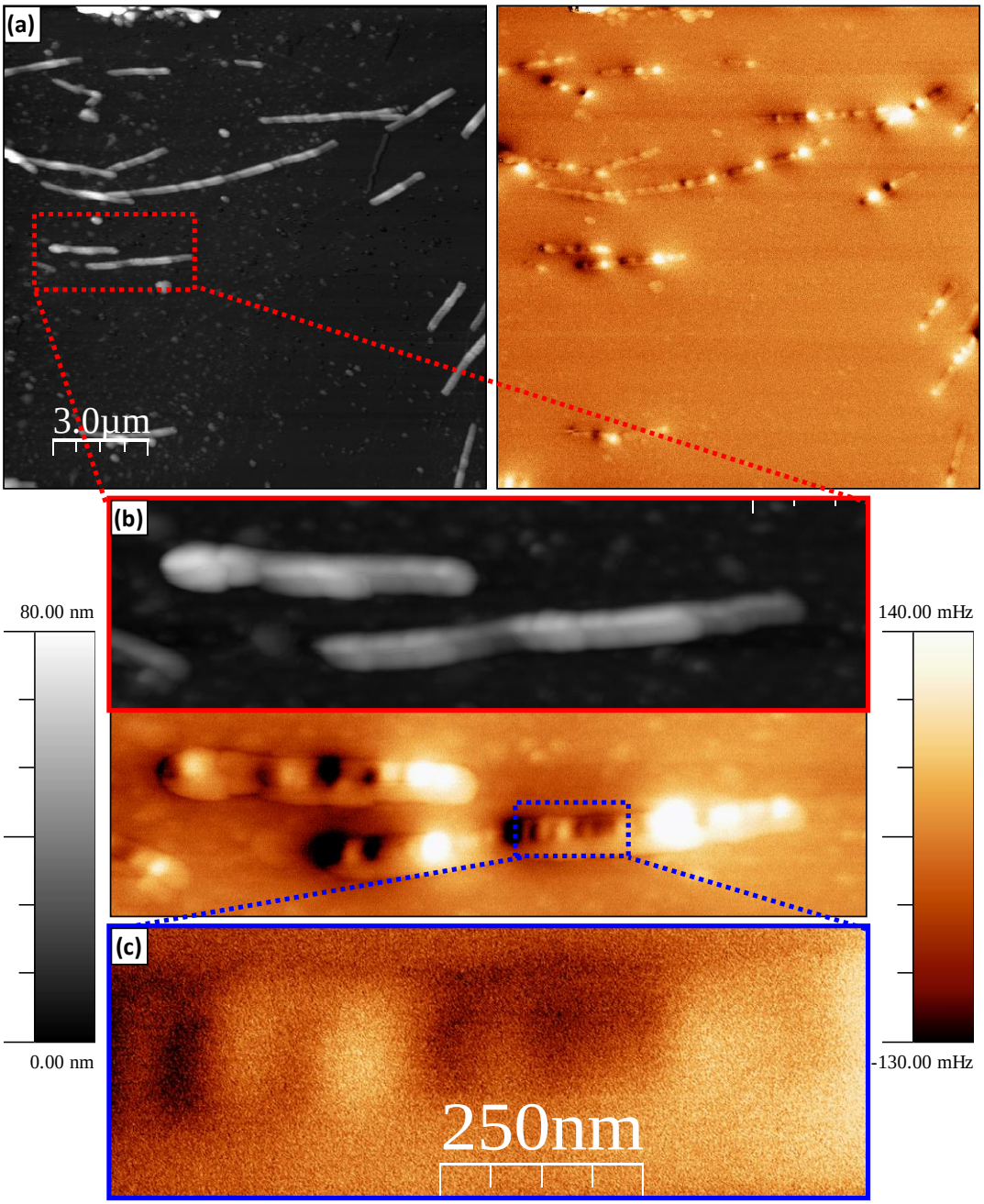

Figure 2.21: The remanent state. *Nanowires after ex-situ saturation with a field of 1.7 T along the horizontal direction. The red and blue square areas in* ***(a)*** *and* ***(b)*** *are shown magnified in the high resolution images* ***(b)*** *and* ***(c)****, respectively.*

A comparison between the experimental nanostructure seen at the bottom of figure 2.21.b and a simulated wire is presented in figure 2.22, with both elements being in their remanent state. A dashed white line has been plotted in the experimental images to help correlate the magnetic contrast with the modulated shape. In both cases, an individual wire comprising a series of two thick and two thin parts is seen. Very good agreement is observed between theory and experiment, in particular if one focuses on the strong spots observed in the *MFM* images. As revealed by the

simulated hysteresis loop of this element, already shown in figure 2.18.b, a single domain state is predicted to be the equilibrium configuration at remanence. The local orientation of the magnetization is depicted in figure 2.22.c, where no domain wall is observed. Therefore, the origin of the strong divergence is purely shape-induced. The sharp modulation in the diameter of the wire introduces discontinuities at which magnetic moments strongly diverge to minimize the magnetostatic energy. As a result, magnetization curling takes place (fig. 2.22.d) in narrow regions that extend over 10-20 nm into the thicker segments of the nanowire.

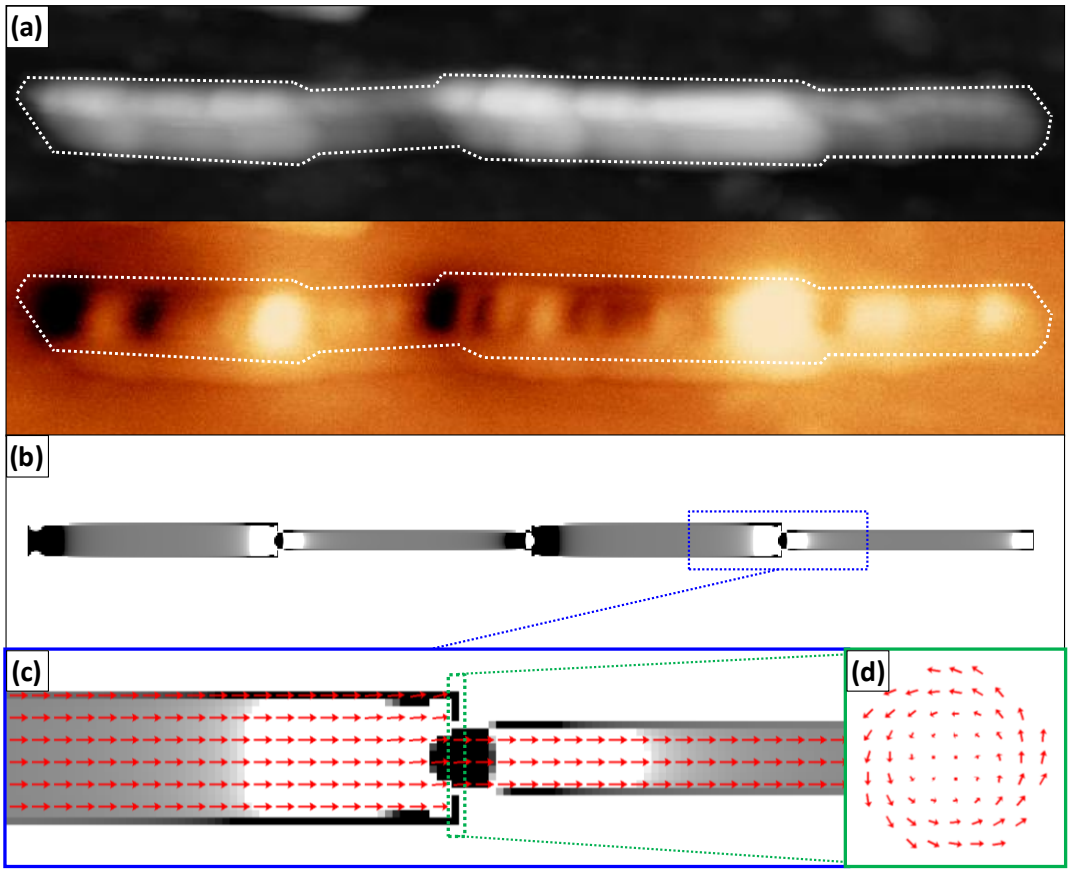

***Figure 2.22: The contrast at remanence**. **(a)** High resolution images showing an individual $Fe_{27}Co_{68}Cu_5$ nanostructure. Strong dark/bright spots are observable in the MFM map. **(b)** Simulated configuration at remanence for a modulated wire with two thick and two thin parts, equivalent to the experimental case. A single domain state is obtained with large divergence of the magnetic moments at the discontinuities. **(c)** Zoom in on the blue framed region in (b). Arrows indicate average directions of the simulated spins. **(d)** Cross section view of the area enclosed by the dashed square line in (c).*

A direct consequence arising from this is the fact that one has to be careful with the interpretation of magnetic force microscopy data to characterize modulated nanostructures. Single domain states do not longer show a simple dipolar-like contrast at the longitudinal ends but a series of alternating dark/bright spots, with even consecutive regions yielding equivalent contrasts (see right side of the nanowire in figure 2.22).

- *The demagnetized state*

Having clarified that, it now becomes tricky to discern between the single domain regions (with a modulated contrast caused by the divergent magnetization) and pinned *DWs* (separating two antiparallel domains). Figure 2.23 shows a large number of modulated $Fe_{28}Co_{67}Cu_5$ nanowires after demagnetizing the sample under an alternating applied field of decreasing amplitude along the horizontal direction. In order to achieve both a good interpretation of the domain structures and statistical significance, these images were recorded for about 20 hours each, allowing the *lock-in* amplifier to filter out most part of noise sources. As a result, high resolution and enhanced signal-to-noise ratio were obtained, with a frequency shift noise as low as 20-25 mHz.

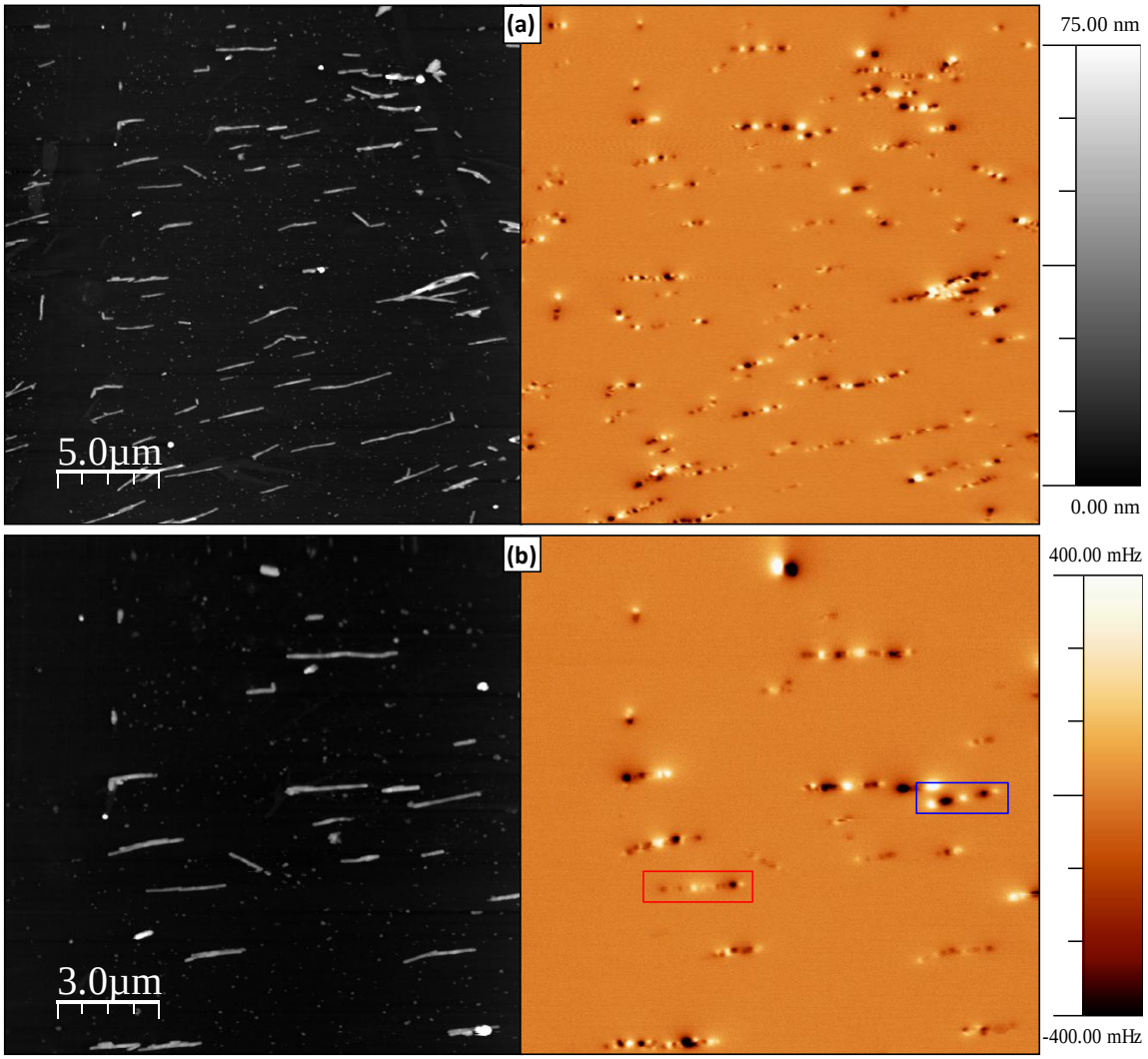

***Figure 2.23: The demagnetized state**. High resolution images of another area of the sample showing nanowires in their demagnetized state. A frequency shift noise of 20-25 mHz is present in the MFM pictures on the right, yielding a very good signal-to-noise ratio.*

A complex contrast is again observed in the wires. Now, being aware of the strong influence that the modulated shape has in the magnetic properties, we will analyze in detail the two nanowires highlighted with a color frame in former figure, which account for the general behavior observed experimentally. The one enclosed in a blue square is zoomed in and shown next:

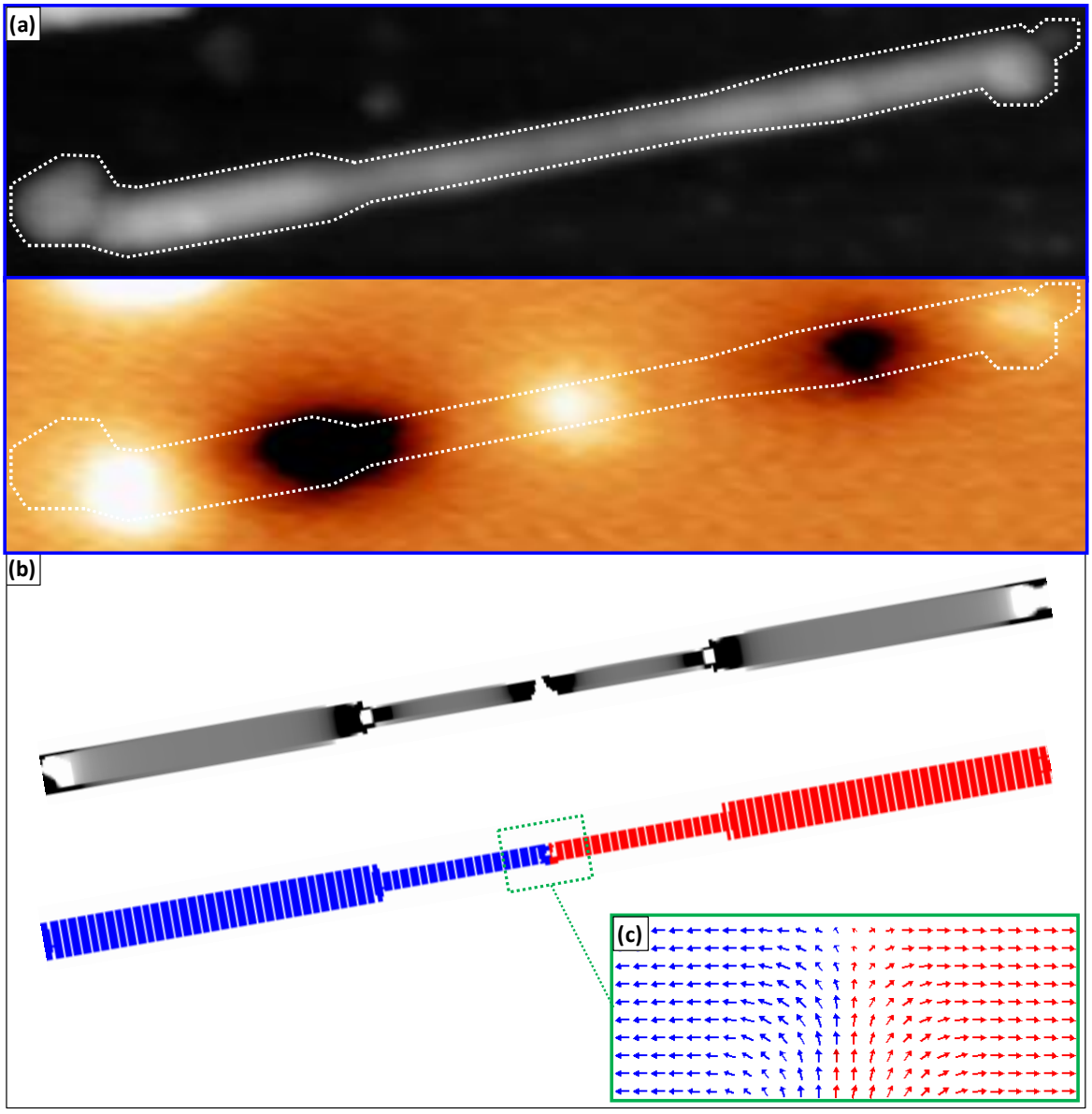

Figure 2.24: The demagnetized domain structure (I). (a) *Nanowire highlighted in blue in figure 2.23. The lateral size of the image is 2.7 μm.* ***(b)*** *Simulated (non-equilibrium) state describing the experimental contrast to a good extent, starting with a randomly distributed spin orientation and observing its evolution without any applied field. The same structure is shown twice: displaying the divergence of the magnetization (up, in a black-gray-white color-scale) and the domain orientation (down, where red and blue stand for spins pointing to the left and to the right, respectively).* ***(c)*** *Zoom in on the wall observable in (b), describing it as a transversal DW.*

From the topographic map it is possible to deduce a central thin part surrounded by two thicker regions. Apart from two defects at the ends of this wire, a rather good and straight shape is observed. A quick look at the corresponding *MFM* image reveals both ends of the nanostructure to be repeled (bright contrast stands for positive frequency shifts) by the sensing tip, already indicative of the existence of a domain wall. Figure 2.24.b shows a simulated nanostructure similar to the former case yielding an equivalent contrast as in the experimental image, with repulsive charges at both ends and a transversal *DW* in the center (see fig. 2.24.c) separating two antiparallel domains (colored red and blue in fig. 2.24.b).

For simulating the demagnetized state, the magnetic moments were initially set to be randomly oriented and their evolution was studied under no applied field. Note that the simulated state shown in figure 2.24.b was not in its equilibrium configuration but corresponds to a step during the dynamic evolution. In the experimental case, *DWs* seem to be located at any position, including the thin segments. A possible reason for that might be enhanced pinning effects associated to the difficulty of crystallites to fill the pores into which nanowires are grown, for such small dimensions ($d \approx 22$ nm).

Another significant example of a demagnetized wire is presented next, showing the red framed area in figure 2.23. The topography indicates the presence in reality of two fragments of wires that have aligned up. The one on the left displays a defined shape with two segments (a thin part and a thicker one) that, according to the simulation shown in figure 2.25.b, may well be in a single domain state. On the contrary, it becomes difficult to discern a pattern in the geometry of the second fragment lying on the right side. We believe this illustrates an intermediate situation between well defined variations of the diameter resulting from the external modulation and small local changes, a variability that is expected to happen when patterning large amounts of nanostructures. A very smooth modulation seems to take place in the central region of the wire, giving rise to a very subtle contrast in the *MFM* image. Two bright spots are again observed at the respective ends, revealing the existence of another pinned *DW*, which we attribute to be responsible of the intense dark stain on the right side of the nanostructure.

Simulations introduced in figure 2.25.b explain and give a plausible interpretation for the experimental results. However, it is important to note that both wires were not simulated simultaneously; instead, separate calculations were used and the resulting configurations were put together into the same figure. Therefore, no magnetostatic coupling between the nanostructures was taken into account. Again, the wire presenting a transverse domain wall was not in its equilibrium state but in an intermediate configuration between the initial random state and the most stable one.

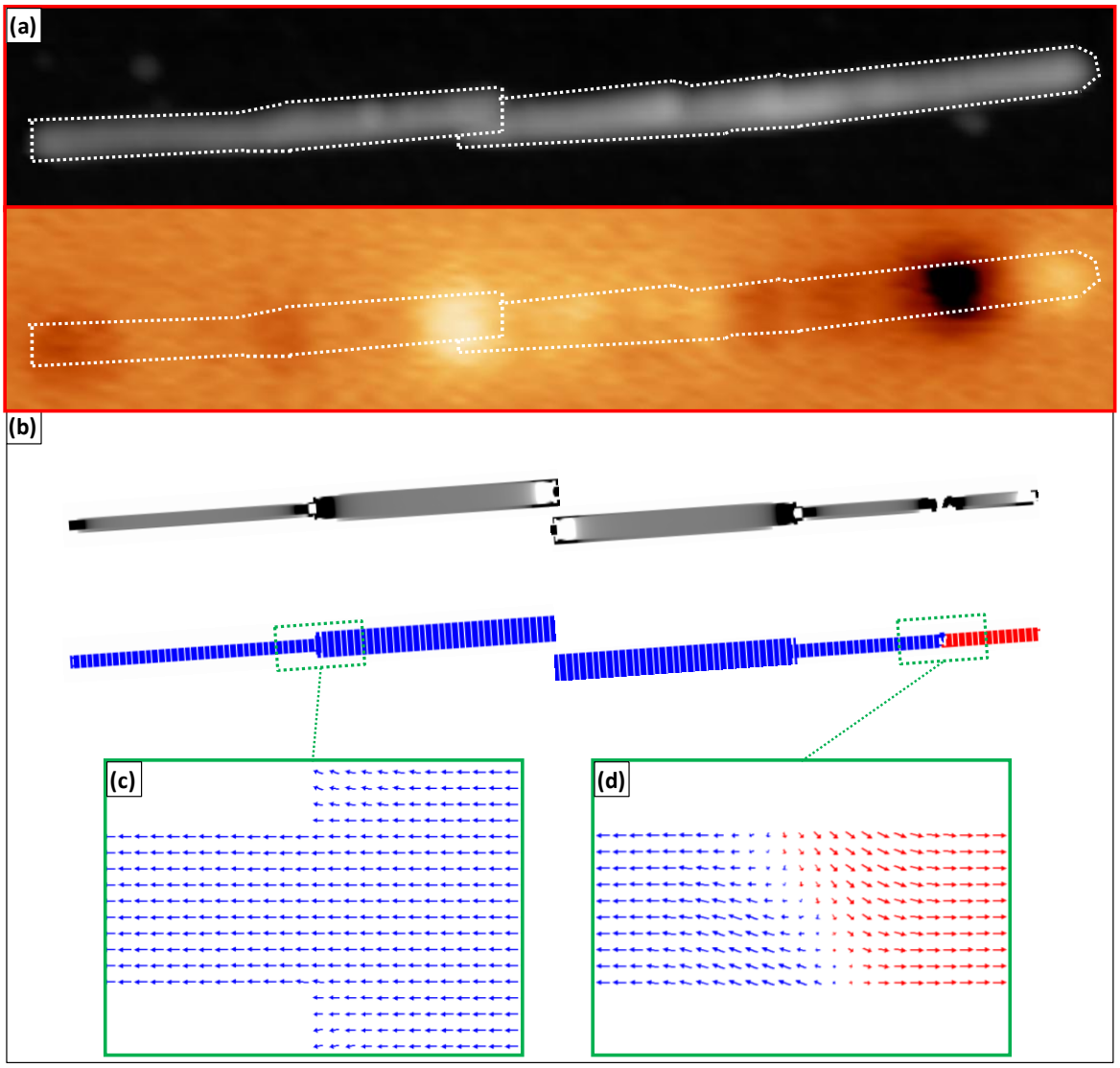

Figure 2.25: The demagnetized domain structure (II). (a) *Nanowire highlighted in red in figure 2.23. The lateral size is 3 μm.* ***(b)*** *Two separately simulated nanowires reproducing the experimental data. The one on the left is in its equilibrium single domain state (see the monotonous blue contrast in the lower row), whereas the one on the left shows a dynamic snapshot with a domain wall.* ***(c)*** *&* ***(d)*** *Magnified images of the regions highlighted in (b).*

We just showed two examples that give a general view of the behavior observed in the demagnetized state, where pinned domain walls are observed experimentally. In general, longer nanostructures show more complex contrasts, which in essence represent a superposition of the results shown in figures 2.24 and 2.25, as a larger number of *DWs* may be pinned at different positions along it.

- *The origin of the weak contrast*

Last, we give some detail about the quite periodic and relatively weak contrast observed in some nanostructures, particularly described in figure 2.21.c. We have shown that abrupt changes in the diameter of the nanostructures cause relatively large divergence in the magnetization. In addition, smoother changes (such as the ones present in fig. 2.25.a) also cause local spins to reorientate, in order to account for the shape variation. In general, there is a correlation between topographic protuberances and the existence of contrast in the corresponding *MFM* image. The fact that some roughness was observed and pointed out in the *TEM* analysis of figure 2.17 brings us to attribute the weak contrast observed along every nanowire to structural deviations from flat cylindrical surfaces. Thus, we suggest the nanowires to possess two sorts of geometrical discontinuities: small morphological roughness associated to the growth process (that yield faint contrast in the images) and abrupt steps induced on purpose by the modulated voltage (responsible for intense contrast spots). One can easily control the second kind but more difficult seems to deal with the first one, in particular when growing nanowires with a diameter as small as 20 nm.

In order to support this assumption, straight nanowires of the same composition (i.e. $Fe_{28}Co_{67}Cu_5$) were fabricated with a constant diameter of 40 nm, similar to the thicker parts in the modulated wires described so far. In this case, no modulation was induced on purpose during the fabrication of the alumina nano-porous template. Two simultaneously recorded topographic and *MFM* images are introduced in figure 2.26. Despite the "double-tip" effect observable in the topography, an individual nanowire with a very flat and straight geometry is seen.

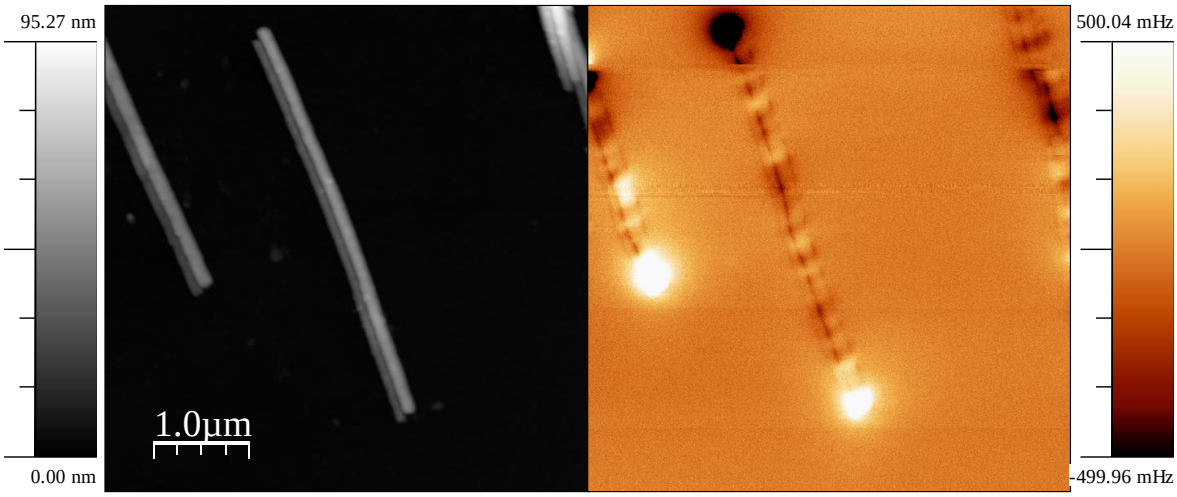

***Figure 2.26: Homogeneous $Fe_{28}Co_{67}Cu_5$ nanowires**. Individual nanowire with no modulation in the diameter. The corresponding MFM image shows the wire to be in a single domain state and reflects the same weak contrast along the nanostructure observed for the case of modulated wires.*

The corresponding magnetic image clearly shows a single domain state, according to the strong contrasts at both longitudinal ends, with the same succession of weak dark/bright stains along the nanostructure that was observed and commented for the case of modulated wires. It thus suggests that the morphological rippling generated during the growth process plays a role. Furthermore, the influence it has in the *MFM* images cautions against eventual misinterpretation of data. Similar effects might also be measured in very narrow nanowires of different ferromagnetic materials if the resulting nanostructures present substantial corrugation and enough sensitivity is reached during the measurement.

Summarizing, we discussed the magnetic properties of very narrow and magnetically hard cylindrical $Fe_{28}Co_{67}Cu_5$ nanowires with a modulated diameter ranging between 22 and 35 nm. Characterizing the magnetic properties of single nanostructures with such small dimensions is available to few techniques. If one opts for using magnetic force microscopy, it is important to be aware of the effects that properties such as shape and morphology can have in the magnetization, for a correct interpretation of data. Here, we unveiled the effect of step-edge modulated diameters in the local orientation of the magnetization and the subsequent *MFM* contrast observed experimentally. Resulting images with complex contrast are obtained that require a careful non-trivial interpretation of results. With the help of micromagnetic calculations, we showed the remanent configuration to be a single domain state and the existence of pinned domain walls when the sample is demagnetized. Even the simplest remanent state gives rise to series of attractive and repulsive regions along each modulated nanowire and reasons for that are given. This can be of great help for future works, whenever information wants to be extracted from nanostructures with abrupt shape variations. Furthermore, morphological roughness was found to induce local changes in the local orientation of spins and the effect of corrugations of only few nanometers was measured experimentally. We believe to have shown that a thorough analysis with *MFM* and, eventually, the help of simulations can be used to extract the actual domain configuration from very narrow samples with sophisticated geometries.

II. Samples with relevant magneto-crystalline anisotropy

In this second part of the chapter, we present experimental results in samples with well defined structures, in which the magneto-crystalline anisotropy plays a relevant role. As a result, more complex configurations occur when both magnetostatic and magneto-crystalline anisotropies are present and compete with each other.

4. Magnetization reversal in cobalt stripes with competing anisotropies

Ferromagnetic stripes with internal magneto-crystalline anisotropy were fabricated by epitaxial deposition of the magnetic layer onto single crystalline vicinal Si(111) by the group of Prof. *E. V. Pustovalov*, at the *Far Eastern Federal University of Vladivostok*. Vicinal surfaces can be described as stairs-like surfaces, where steps involving a low number of atoms separate flat terraces [59]. Since atoms belonging to the step edges have a different number of nearest neighbors than the atoms in the underlying bulk, steps give rise to a lattice distortion. In our sample, the vicinal substrate originates from a 4º miscut angle along the $[11\bar{2}]$ direction, where the miscut is defined as the misorientation between the atomic plane and the sample surface, as sketched in figure 2.27. Thus, miscutting results in atomic terraces that "step down" in the direction of the miscut.

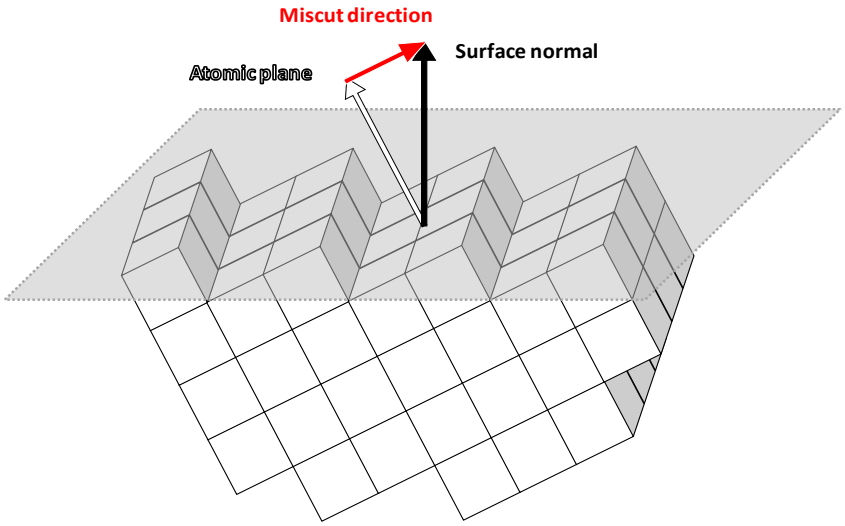

Figure 2.27: The vicinal substrate. *Schematics of a vicinal substrate resulting from a miscut angle of 27 º.*

A 10 nm thick Co(111) film was deposited onto the vicinal Si(111) substrate by molecular beam epitaxy in an ultra-high-vacuum (*UHV*) system with a base pressure of $4 \cdot 10^{-11}$ mbar. Prior to the cobalt deposition, a copper buffer layer was grown on top of the Si(111) surface to prevent

[59] F. Leroy, P. Müller, J. J. Métois and O. Pierre-Louis, Physical Review B 76 (2007) 045402

intermixing of Co and Si and smooth the mismatch of their lattice parameters. The best crystalline quality in the magnetic film is obtained with a 2 nm Cu(111) buffer layer, as has been reported [60]. Scanning tunnelling microscopy observations revealed the presence of terraces about 30 nm wide separated by 1.5 nm high steps (fig. 2.28.a). These terraces force the magnetic moments in the cobalt layer to point parallel to the edges, defining a uniaxial anisotropy.

Taking this into account, a set of 50 μm long stripes and variable width (see caption of fig. 2.28) was patterned with the long axis being perpendicular to the terraces, as can be seen in figure 2.28.b. By doing this, a competing effect between crystalline and shape anisotropies is created. Removal of the magnetic material in the surrounding (50 x 50) μm^2 was performed by focused ion beam (*FIB*) etching, using Ga^+ ions under an accelerating voltage of 30 kV at a rate of 0.1–1.0 nA. Despite the advantages of *FIB* to pattern nanostructures, a known associated drawback is the influence that implanted gallium ions have in the magnetic properties of the resulting samples [61]. However, in this case no relevant changes were observed in the regions close to the milled edges.

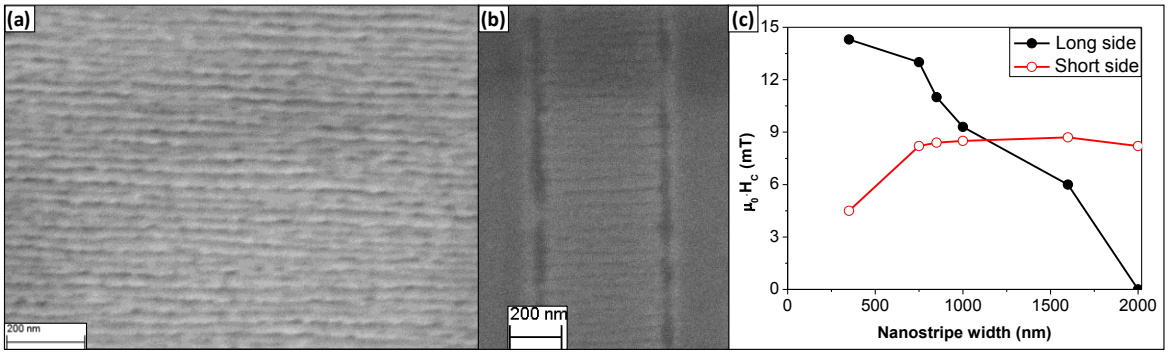

Figure 2.28: The epitaxial cobalt. *SEM images of* ***(a)*** *a 10 nm thick Co(111) film deposited onto vicinal Si(111) and* ***(b)*** *a patterned stripe with the main axis being perpendicular to the steps, after removal of the surrounding material.* ***(c)*** *Evolution of the coercive fields as a function of the stripe width, measured by MOKE, for stripes 350 nm, 750 nm, 850 nm, 1 μm, 1.6 μm and 2 μm wide. Error in the MOKE values are in the order of the dot size.*

In this work, we prove the induced magneto-crystalline anisotropy to be strong enough to compete with and even overcome the shape anisotropy. Characterization of the domain structure in every nanostructure is presented and the competition between both anisotropies is analyzed. We show that the effective magnetic anisotropy – resulting from both magneto-crystalline and shape contributions – can be controlled by tuning the geometrical dimensions. Then, a detailed study of the magnetization reversal process is shown. Last, the influence of structural or geometric defects on the nucleation of domain walls during the magnetization reversal process is discussed.

[60] A. V. Davydenko, Yu. P. Ivanov and L. A. Chebotkevich, Journal of Magnetism and Magnetic Materials 324 (2012) 1248-1252
[61] I. V. Roshchin, J. Yu, A. D. Kent, G. W. Stupian and M. S. Leung, IEEE Transactions on Magnetics 37 (2001) 2101

Throughout this work, experimental results are supported by micromagnetic simulations, performed with the finite element code *MAGPAR* [62] by the group of *Dr. O. Fesenko-Chubykal*o at the *Material Science Institute of Madrid.* Due to computing restrictions, a mesh size of 5 nm, a constant length to width aspect ratio of 10 and a constant thickness of 10 nm were used, with widths ranging from 100 nm to 700 nm. The magneto-crystalline anisotropy constant was chosen to be K_1=6.3·10^4 J/m^3 – obtained from the anisotropy field in the hysteresis loops of epitaxial Co films – and an exchange stiffness of A=13·10^{-12} J/m and a saturation magnetization of $\mu_0 \cdot M_S$=1.75 T were used. In general terms, calculations are in qualitative good agreement with the experimental data but quantitative values disagree. As usual, such discrepancy is attributed to thermal effects, the presence of defects in the experimental samples and local variations in the magneto-crystalline easy axis orientation due to inhomogeneities in the terraces.

Hysteresis loops of every nanostructure were measured by *MOKE*, applying magnetic fields both along the stripe main axis and perpendicularly to it. The obtained coercive fields can be observed in figure 2.28.c as a function of the stripe width. The magnetization reversal processes seem to depend on the width of the nanostripes. If the field is applied along the main axis (black profile in fig. 2.28.c), which in fact turns advantageous to the shape anisotropy, a monotonously decreasing H_C is observed with increasing width. It indicates the loss of relevance of the shape for the widest elements, where the anisotropy induced by the substrate seems to govern the magnetic properties. This becomes evident when taking a look at the hysteresis loops in figure 2.29, where hysteresis loops of the 750 nm wide stripe are displayed. The squareness observed in the upper row (field along the short side), together with the high remanent saturation of around 80 %, confirms the dominance of the crystalline energy. With increasing width, the long side becomes a harder axis that is reflected in low coercive field with an almost non-hysteretic behavior.

On the contrary, when the field is applied along the short side (i.e. crystalline easy axis), a very slow increase of H_C is seen for thicknesses over 600 nm (red profile in fig. 2.28.c), with a drop for the smallest widths. A different behavior seems to take place in the narrowest stripe (w =350 nm), where a coercive field around one half times the value for the widest elements suggests a hard competition between the two anisotropies. In order to get a deeper insight into the spin configurations and processes involved during the magnetization reversal, we carried out a thorough characterization of the stripes by magnetic force microscopy, which is described next.

[62] W. Scholz, J. Fidler, T. Schrefl, D. Suess, R. Dittrich, H. Forster and V. Tsiantos, Comp. Mat. Sci. 28 (2003) 366-383

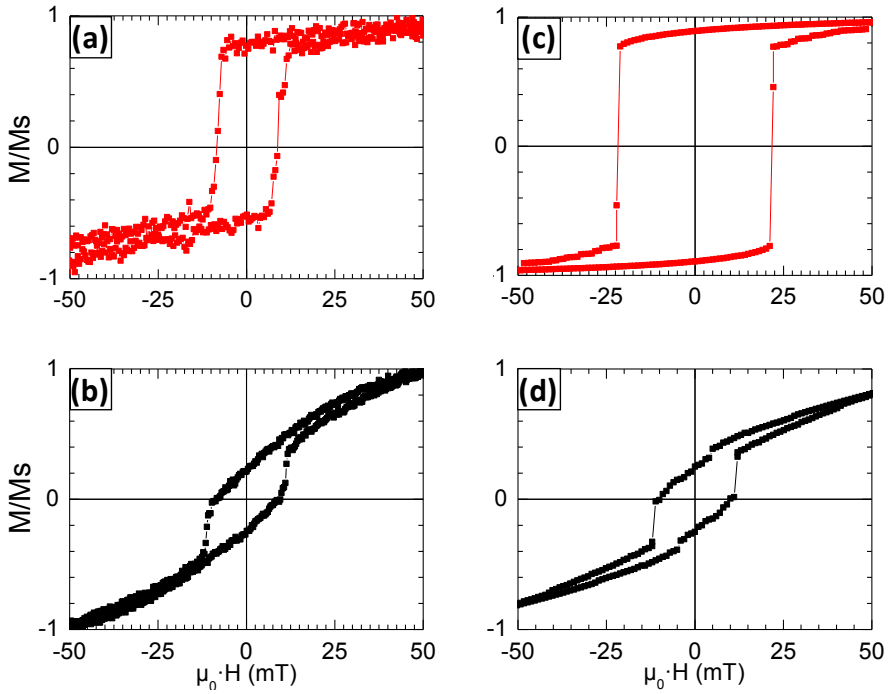

Figure 2.29: Hysteresis loops. *(Left column) Experimental and (right column) simulated hysteresis loops for the stripe 750 nm in width.* ***(a)*** *&* ***(c)*** *describe the reversal process with the field applied along the short axis, whereas* ***(b)*** *&* ***(d)*** *correspond to the long axis.*

Domain structure characterization by means of MFM

For the *MFM* characterization, homemade probes with a 20 nm thick sputtered cobalt layer were used. The reason for this is the excessive stray field created by commercial sensors, even specific low moment probes, as well as the search for better spatial resolutions. A more detailed description of our *MFM* tips is presented in chapter 4, refer to that part of the manuscript for further information. Topographies show the stripes to have a very flat granular surface with smooth roughness (fig. 2.30.a); however, some defects – originated during the *FIB* etching process – are present on the sides of the stripe. These features give rise to a faint bright contrast in the *MFM* images that should not be interpreted as resulting from magnetostatic interactions.

Examples of such *MFM* images are shown in figure 2.30 as well, where the resulting domain structure for three different stripes after long axis saturation can be observed. Nanostripes with largest widths (fig. 2.30.d) show a transversal single domain behavior. The crystalline anisotropy clearly overcomes the magnetostatic influence, resulting in single domain areas comprising the vast majority of the stripe. This is in agreement with the nearly zero coercive field measured by *MOKE* (black profile in figure 2.28.c). Closure domains are expected to be present at the longitudinal ends of the widest nanostructures and will be discussed later.

For the case of stripes of intermediate width a different configuration is observed, in which a transversal domain structure is observed at remanence (fig. 2.30.c). An enhanced magnetostatic coupling now favors the formation of such domains with alternating polarities. Nevertheless, the transversal anisotropy is still dominant. As it can be seen, these domains are separated by well defined domain walls that yield a clear *MFM* contrast. We attribute the difference in domain size for each polarity to a misalignment of the applied field with respect to the stripe axis, which is estimated to be of few degrees. In such case, the external field on the way down from saturation can be decomposed into two components: one parallel to the main axis and a second one perpendicular to it; the latter accounting for a preferential domain polarity as it breaks the symmetry of the system and favors a specific orientation of the transversal domains.

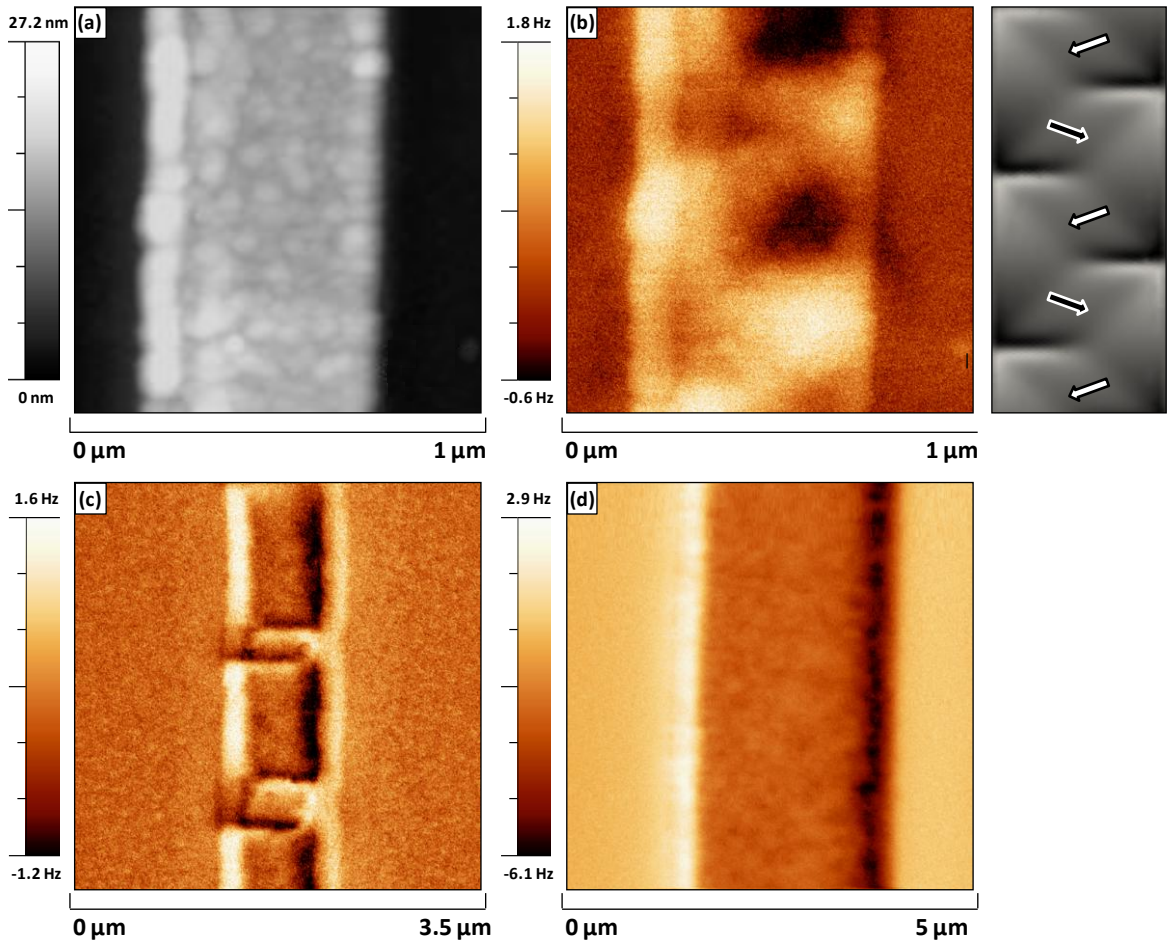

Figure 2.30: The domain structures. *MFM images obtained in the remanent state after saturating along the long axis the nanostripes of width* ***(a)-(b)*** *350 nm,* ***(c)*** *750 nm and* ***(d)*** *2000 nm. A simulated MFM image is shown in (b) with arrows describing the local orientation of the magnetization.*

Particularly interesting becomes the case of the narrowest nanostructure, which shows a different behavior as compared to the described ones. In it, a symmetric chess-like configuration is visible

(fig. 2.30.b). Such domain structure has already been reported [27,63,64] but, unfortunately, images most often lack in good spatial resolution and are then presented excessively equalized. From those experiments, authors deduce the presence of transversal domains pointing across the stripes and no information about the domain walls can be extracted. Figure 2.30.b presents a detailed *MFM* image of the 350 nm wide stripe, in which smooth variations of the magnetization can be observed. Very slight influence of the topography is present and gives rise to a faint granular contrast but we believe information on the domain structure of this nanostripe is optimized under these conditions. Domain walls between adjacent domains are mildly defined and are, thus, indicative of a non abrupt transition of the magnetization orientation. In contrast to the statement given in the literature [27,63], magnetization does not seem to lie completely along the short side but rather describes a wiggly path (see the simulated *MFM* image in fig. 2.30.b). This is in agreement with the *MOKE* characterization where ratios for the remanent to saturation magnetization are found to be 0.49 and 0.44, with the field applied parallel to the long and short axis, respectively.

Magnetization reversal processes

After analyzing the domain structure of the stripes in the remanent state, we studied in detail the magnetization reversal process of the intermediate elements, as they show a more complex behavior involving well defined domain walls. Figure 2.31 presents the evolution of the magnetization in the 750 nm wide structure, as the external field – applied along the long axis – is decreased from positive saturation and reversed. As the Zeeman energy decreases on the way from saturation, the magnetization gradually becomes wavy due to the influence of the stepped substrate over the crystalline anisotropy and a quasi-periodic contrast is observed (fig. 2.31.a). Further decrease of the field provokes an enhanced contrast on the lateral sides and the appearance of transition regions with a high magnetization divergence (fig. 2.31.b). At lower fields, this large divergence acts indeed as a seed for the formation of well defined domain walls (fig. 2.31.c and .d), a domain configuration that remains present for a wide range of fields. Again, a preferential domain polarity seems to be present possibly due to the non parallel external field direction.

A deeper insight into the spin configuration is provided by simulations. Figures 2.31.I-II show simulated *MFM* images describing the experimental contrast observed at remanence (fig. 2.31.d) and around the coercive field (fig. 2.31.e), respectively. The key step during the reversal process takes place between these successive situations. In between, the contrast of *DWs* reverses from a configuration in which the upper and lower parts are dark and bright, respectively (fig. 2.31.d-I), to

[63] I.L. Prejbeanu, L. D. Buda, U. Ebels, M. Viret, C. Fermon and K. Ounadjela, IEEE Transactions on Magnetics, 37 (2001) 2108
[64] K. Gross, P. Szary, O. Petracic, F. Brüssing, K. Westerholt and H. Zabel, Physical Review B 84 (2011) 054456

another one where they are bright and dark (fig. 2.31.e-II). Having a careful look at the simulated maps, one realizes that magnetic vortices that were present on one side of the walls (positions of these vortices have been highlighted with white circles in the simulations) have moved to the opposite one along the *DW* plane. Although domains actually maintain the same orientation, the longitudinal component of the magnetization at the vortices positions has reversed. Taking into account that many vortices are present in the wire, this explains the jump in the hysteresis loop displayed in figures 2.29.b and d. The new vortices positions serve as starting points for the magnetization to point along the reversed field direction (fig. 2.31.f, remember the field is applied along the stripe's main axis). As the strength of the reversed field increases sufficiently, domain walls become dimmer and vortices disappear as spins gradually orientate along the stripe main axis. This indicates the loss of a well defined domain structure, as observed in figure 2.31.g.

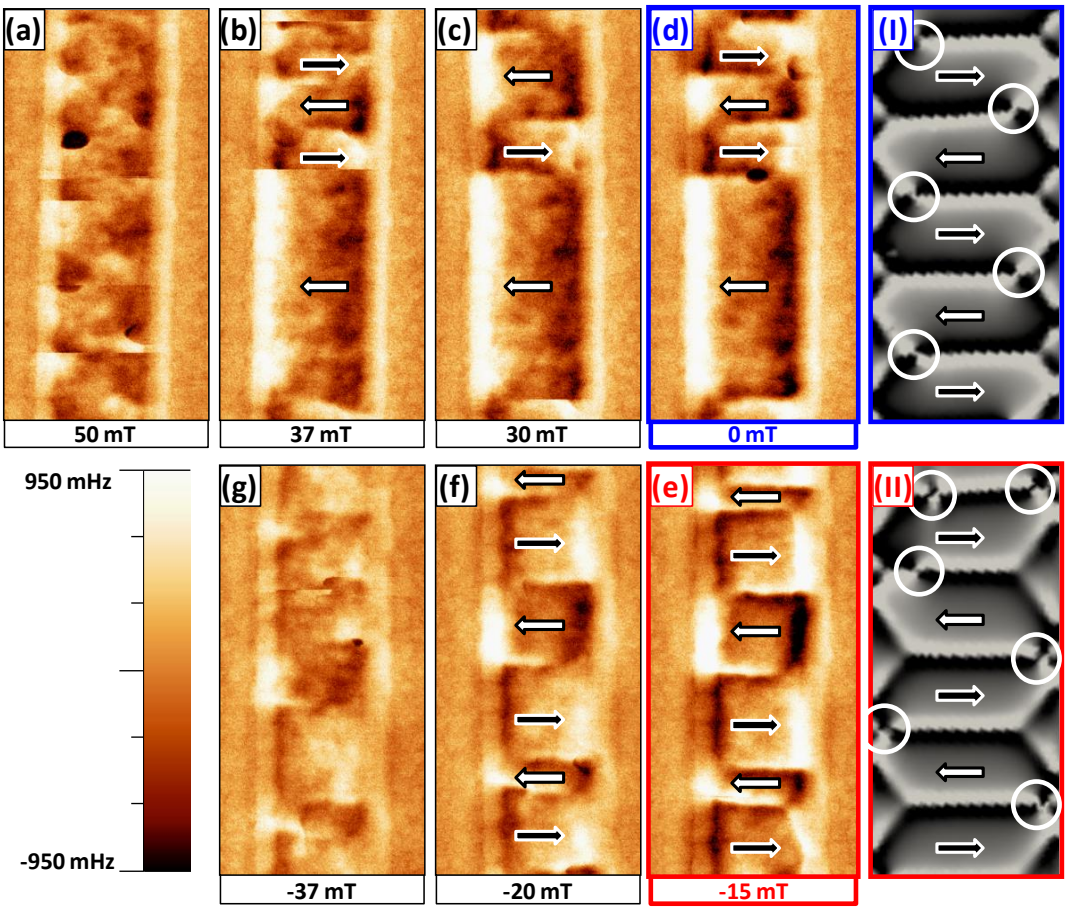

Figure 2.31: The reversal process (a) – (g) *Sequence of MFM images showing the domain structure of the 750 nm wide stripe at different magnetic fields applied along the main axis. Arrows indicate the orientation of the magnetic domains in each case. Well defined domain walls are observed during most part of the field range. Blue and red colored frames around (d) and (e) highlight the contrast reversal taking place in the DWs.* ***(I)*** *&* ***(II)*** *Simulated configurations describing the DW reversal, corresponding to the situations occurring in (d) and (e), respectively. Note that the same areas are shown in both images. Open circles point out positions of magnetic vortices.*

Local hysteresis loops by means of 3D modes

Another useful parameter measurable in this set of stripes is the switching field, in particular in the widest single domain elements. As explained in section 2 of this chapter, a versatile way for obtaining hysteresis loops is to take advantage of the *3D modes*. For carrying out this kind of experiments, the same profile is continuously scanned across the stripes while the external field is swept. At the retrace distance, *van der Waals* forces are negligible and magnetostatics becomes then dominant. When the switching field is reached, a sudden contrast reversal is recorded in the frequency shift image. A resulting hysteresis loop image is shown in figure 2.32 for the same 750 nm wide stripe analyzed before; in this case, with field applied along the short direction. The profile drawn by a blue arrow is plotted on the right side and describes the sudden jump observed by *MOKE* in figure 2.29.a:

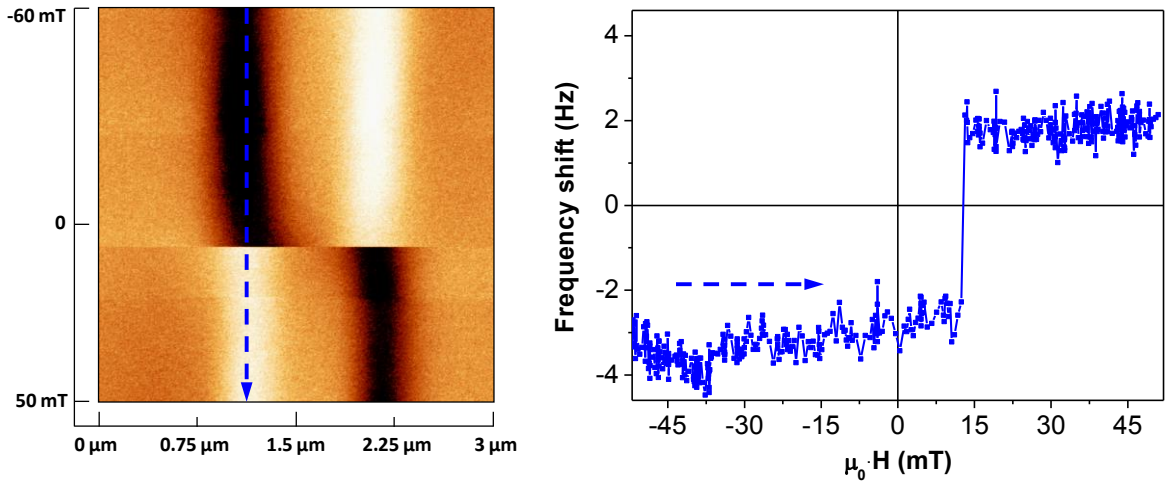

Figure 2.32: Hysteresis loop of a single stripe. *Frequency shift 3D mode image performed on the 750 nm wide stripe with the external field applied along its short axis. The field was swept from −60 mT to +50 mT and a switching field value of 12 mT is obtained from the profile plotted on the right.*

These experiments were only performed in the widest stripes since they are particularly useful for the quantification of switching fields in samples with abrupt changes in the domain configuration. Higher complexity arises if one tries to estimate coercive fields or smooth changes in other kind of samples. In order to obtain more reliable values and for statistical purposes, loops were repeated 10 times in each stripe and the resulting average fields are provided in table 2.i. The values obtained with the force microscope are in reasonable agreement with the *MOKE* values but provide bigger values, as well as a larger error.

Stripe width (nm)	*MFM average coercive field (mT)*	*MOKE average coercive field (mT)*
750	10.7 ± 2.0	8.2 ± 0.5
1000	9.8 ± 2.0	8.5 ± 0.2
1600	9.6 ± 2.0	8.7 ± 0.2
2000	9.9 ± 2.0	8.2 ± 0.3

***Table 2.i**: Comparison between coercive fields obtained by means of VF-MFM and MOKE, for the widest stripes with the external field applied along the short axis.*

Former experiments were done scanning over central areas of the wires. Another interesting region to perform *3D modes* measurements is at the longitudinal ends of the stripes, since a different behavior is expected with eventual nucleation of domain walls. As can be seen in figure 2.33.a for the 2 μm wide element, these regions present geometric defects that can act as preferential nucleation sites during the magnetization reversal process. The *MFM* image at remanence (figure 2.33.b) shows the characteristic single domain behavior throughout the extensive central part of the nanostructure, whereas a slightly different contrast can be seen at the end.

The *3D modes* experiment presented in figure 2.33.c was carried out scanning along the white profile drawn in figure 2.33.a. For large magnetic fields, a single domain is also observed in this part of the stripe but, as *H* drops below a certain value, some contrast appears in the central region. For low enough fields a domain wall is nucleated and suddenly disappears at fields around remanence, causing the magnetization reversal and so the reversed contrast observed in the remaining part of the image. Here, the switching field value is smaller than the one shown in table 2.i, when experiments were done in the central region of the stripe. One has to keep in mind that local stray fields associated to *MFM* probes have a non negligible in-plane component that can indeed influence the magnetic state of the sample.

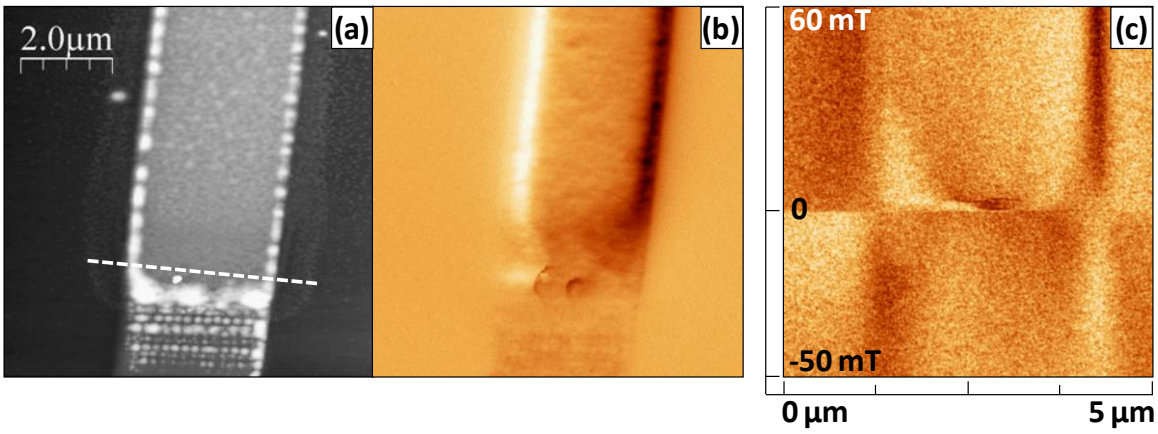

***Figure 2.33: The end of the stripe. (a)** Topography at one end of the 2000 nm wide stripe. **(b)** Corresponding MFM image. **(c)** 3D mode image obtained along the white profile in (a) with the magnetic field swept from +60 to −50 mT.*

Defects are also present in the lateral sides of the stripes, so it may also be interesting to study their influence in the *DW* nucleation. With that purpose, small defects were defined in a simulated stripe. The results arising from simulations show those defects to be preferential nucleation sites for *DWs*, leading to a non periodic domain structure with tilted domain walls (fig. 2.34.d). However, the interaction between *DWs* after the formation of vortices seems to determine their final positions (fig. 2.34.e), although influenced by the place where they were nucleated (at least, for this defect size). In order to study this effect in our lab, an original experiment was carried out, again involving the *3D modes*. The topographic map of the 750 nm wide stripe is presented in figure 2.34.a, where the white dashed line indicates the profile along which the tip was scanned. Therefore, the *3D modes* map (fig. 2.34.b) gives information about the nucleation and evolution of *DWs* along this profile, as the field – parallel to the long axis – was decreased down to remanence.

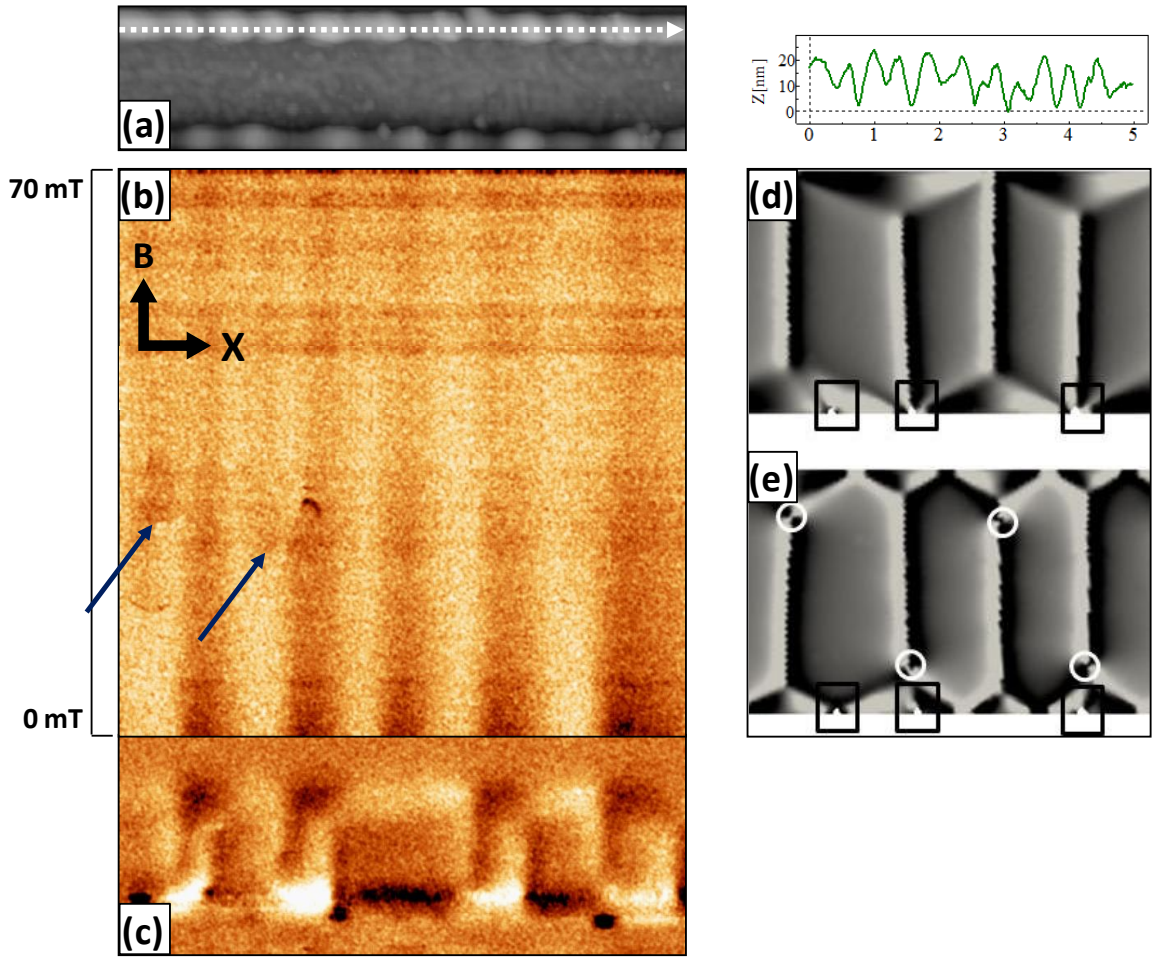

Figure 2.34: The influence of defects. ***(a)*** *Topography of the 750 nm wide stripe and* ***(b)*** *3D modes image obtained while scanning the tip along the profile shown in (a) for varying fields between 70 mT and remanece. DW movement and annihilation are observed and highlighted by dark blue arrows.* ***(c)*** *MFM image measured after the 3D modes experiment. Notice the coincidence between the lower part of (b) and the upper edge of the stripe in (c).* ***(d)*** *&* ***(e)*** *Micromagnetic simulations for a 750 nm wide stripe introducing very small edge defects (marked with squares): (a) before vortex nucleation; (b) after vortex nucleation. Open circles highlight the vortex core positions.*

It is possible to observe *DW* displacements and annihilations during the field sweep, when comparing the upper- and lowermost parts of figure 2.34.b (changes are highlighted by dark blue arrows). On the way down to remanence, magnetization starts describing a wiggly path that causes the contrast seen in the upper part of the *3D modes* image. We believe that the frontiers between regions with opposite contrast are influenced by defects on the sides of the nanostructure, analogously to the situation shown in figure 2.34.d. According to the *MFM* experiment described in figure 2.31, nucleation fields of the characteristic single vortex *DWs* present at remanence are around 30 mT. That corresponds to the central part of figure 2.34.b and coincides with the movement of *DWs*. The situation is analogous to the one in figure 2.34.e, described in former paragraph. As a result, the domain wall position, even though influenced by the region where it was formed, does not always correspond to its nucleation site. We suggest that domain wall nucleation is influenced by structural defects but subsequent displacement takes place due to wall interactions. Notice the similarity in the contrast between the lower part of figure 2.34.b and the upper part of figure 2.34.e, where the *MFM* image measured right after the *3D modes* experiment is shown. It is worth remarking that the positions of the *DWs* at remanence are reproducible, i.e. they were found located at the same sites after successive saturation processes.

Summarizing, the influence of a stepped Si(111) substrate in the magnetic properties of patterned epitaxial Co stripes was analyzed. This corrugation in the substrate induces a magneto-crystalline easy axis in the cobalt layer parallel to terraces. Different magnetic configurations are present, depending on the aspect ratio, and magnetization reversal takes place via different mechanisms. Compared to previous results published in the literature, *MFM* images with enhanced resolution allow us to unveil a chess-like domain structure for the narrowest structures. As a result, the magnetization does not seem to lie completely along the short side but rather describes a wiggly path with smooth domain walls, indicative of an effective compensation of anisotropies. Furthermore, we were able to characterize the domain walls present in stripes of intermediate width as single vortex *DWs* and detect their evolution during the reversal process. All these results have been supported by means of micromagnetic simulations. Last, the useful *3D modes* were used to quantify switching fields in the largest stripes – which show a transversal single domain behavior – and to study the influence of structural defects in the reversal process of nanostructures. Defects act as nucleation sites, as expected, but domain wall positions seem to be determined by wall to wall interactions.

5. Magnetic configuration in $La_{0.7}Sr_{0.3}MnO_3$ islands

This work focuses on the magnetic structure of self-assembled epitaxial $La_{0.7}Sr_{0.3}MnO_3$ (*LSMO*) nanoislands grown by chemical solution deposition (*CSD*) onto (001)-oriented yttria stabilized zirconia (*YSZ*) substrates. In particular, the influence that size, morphology, crystallographic structure and strain have on the magnetic properties of our *LSMO* nanoislands is adressed. Detailed description about the growth process, as well as about morphological and structural characterization can be found elsewhere [34]. Essentially, *LSMO* islands are found to have truncated square pyramid geometries with thicknesses between 10-40 nm and lateral sides between 50-150 nm (fig. 2.35). All experiments shown in this section were carried out in a low humidity environment at a retrace distance of 30 nm, which proved to be optimal for obtaining good magnetic sensitivity while avoiding cross-talk with the topographic signal. Commercial *Nanosensors PPP-MFMR* and *PPP-LM-MFMR* probes (k≈2.8 N/m, f≈75 kHz) were used.

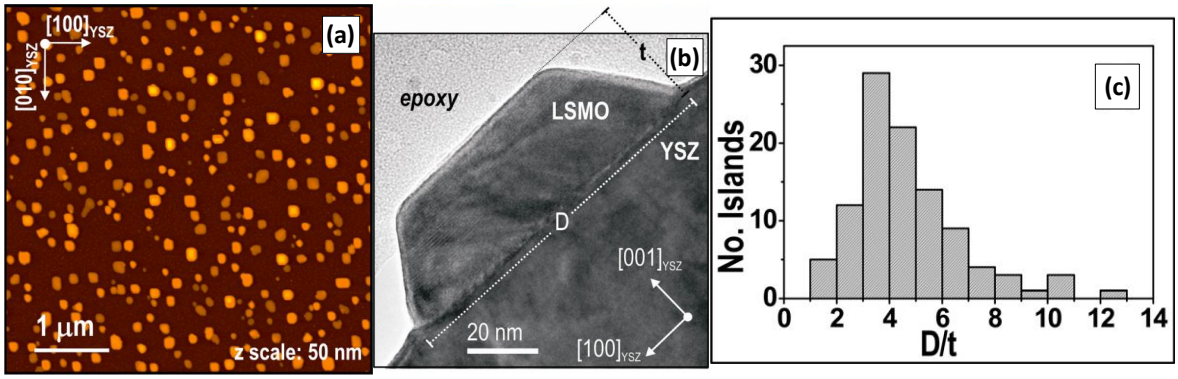

Figure 2.35: The LSMO nanoislands. ***(a)*** *5x5 μm² topographic image of LSMO nanoislands grown on (001)-YSZ.* ***(b)*** *Cross-sectional TEM image of an LSMO nanoisland with a lateral side to thickness aspect ratio of (D/t)~3.5; displaying the typical truncated pyramid geometry.* ***(c)*** *Experimental distribution of the (D/t) aspect ratio.*

Figure 2.36.a shows the magnetization curves measured at 110 K with an *IP* and *OOP* applied field and reveals an easy axis lying mainly within the sample plane. A coercive field of 15 mT and a saturation magnetization of M_S=(480±50) kA/m at 35 K, somewhat below the value for bulk *LSMO* (590 kA/m), were also obtained. A competition between shape and crystalline anisotropies seems to take place, when having a look at the hysteresis loops. Ferromagnetic resonance (*FMR*) experiments (fig. 2.36.b) indicate the existence of an easy magnetization axis along the [110] direction with a magnetocrystalline anisotropy constant K_1(150 K)=(5±1) kJ/m³. This is in the same order of reported values for (001) *LSMO* films which show the [110] easy axis [65,66].

[65] K. Steenbeck and R. Hiergeist, Applied Physics Letters 75 (1999) 1778
[66] K. Steenbeck, T. Habisreuther, C. Dubourdieu and J. P. Sénateur, Applied Physics Letters 80 (2002) 3361

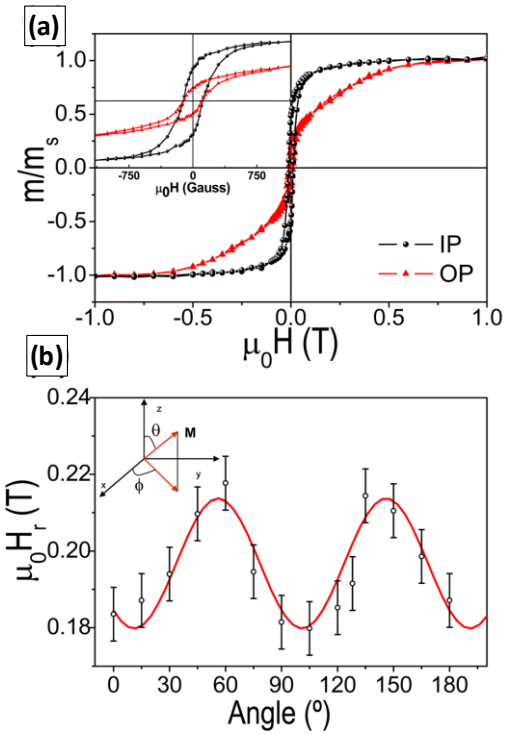

Figure 2.36: Averaged magnetic properties. (a) *Measured in-plane (IP) and out-of-plane (OP) magnetic hysteresis loops (110 K) evidence the in-plane anisotropy of the system.* ***(b)*** *Results from the FMR measurements, where open symbols represent the measured in-plane dependence of the resonant field H_r at 150 K.*

Previous experiments give an idea of macroscopic values for a large amount of nanoislands. Thus, our role was to carry out *MFM* experiments in order to unveil the magnetic properties of individual elements and correlate them to the geometric dimensions. It is worth reminding that the magnetic coating in *MFM* tips increases the final diameter of the probe, hence lowering the lateral resolution achieved in the experiment. Here, the convolution between tip and sample was taken into account in order to evaluate lateral dimensions and corrected using the *WSxM* software [67].

Figure 2.37 displays the topography and its corresponding *MFM* image of the surface, recorded after nearly saturating tip and sample along opposite *OOP* directions with a magnetic field of 500 mT. We may observe three different magnetic configurations depending on the islands' thickness and lateral size. Essentially, the largest islands show a multi-domain structure with an *IP* magnetization and strong contrast at the edges, whereas a vortex state seems to be present in the medium-size ones, with a characteristic contrast in the center of the object. However, the magnetic configuration of the smallest *LSMO* islands could not be resolved due to the too small interaction with the sensing tip, compatible with an *IP* magnetization as was suggested by the hysteresis loops. The presence of such different domain configurations is in agreement with the macroscopic

[67] I. Horcas, R. Fernández, J. M. Gómez-Rodríguez, J. Colchero, J. Gómez-Herrero and A. M. Baró, Review of Scientific Instruments 78 (2007) 013705

hysteresis loops measured along the *OOP* direction, where a remanent magnetization of around $M_S/4$ and a non negligible coercive field are seen, thus suggesting multi-domain configurations with some *OOP* component.

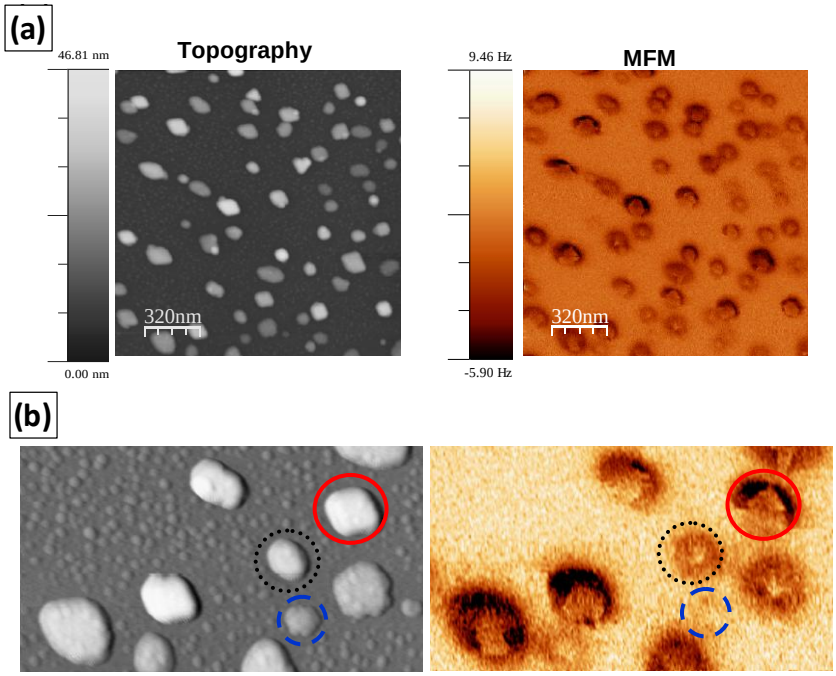

Figure 2.37: The magnetic structure. ***(a)*** *Topographic and MFM images of LSMO nanoislands at room temperature.* ***(b)*** *Detailed images of a smaller area, showing LSMO nanoislands of different aspect ratios. Dashed, dotted and solid line circles highlight nanoislands with single domain, vortex, and multidomain magnetic configurations, respectively.*

There is a clear correlation between the geometrical dimensions of the *LSMO* nanoislands and their magnetic state. Statistical processing of *MFM* images measured at different spots of the sample indicates the aforementioned configurations to fall into three different regions within the width vs. thickness graph shown in figure 2.38.a. Nanoislands with a multi-domain configuration correspond to those with largest *D* and *t* values; nanoislands with relatively large thickness and lateral size below 110 nm display a vortex state, in good agreement with previous observations in magnetic metal nanostructures [68,69,70], while the smallest nanoislands present a low contrast that seemingly corresponds to a homogeneous in-plane magnetization. In spite of this experimental faint contrast being at the limit of detection, the observed diversity of magnetic configurations cannot be inferred from *SQUID* hysteresis loops since, in such macroscopic measurements, all size dependent behaviors add up and reflect the average magnetic characteristics of the nanoisland ensemble.

[68] T. Shinjo, T. Okuno, R. Hassdorf, K. Shigeto and T. Ono, Science 289 (2000) 930
[69] R. P. Cowburn, D. K. Koltsov, A. O. Adeyeye, M. E. Welland and D. M. Tricker, Physical Review Letters 83 (1999) 1042
[70] A. Wachowiak, J. Wiebe, M. Bode, O. Pietzsch, M. Morgenstern and R. Wiesendanger, Science 298 (2002) 577

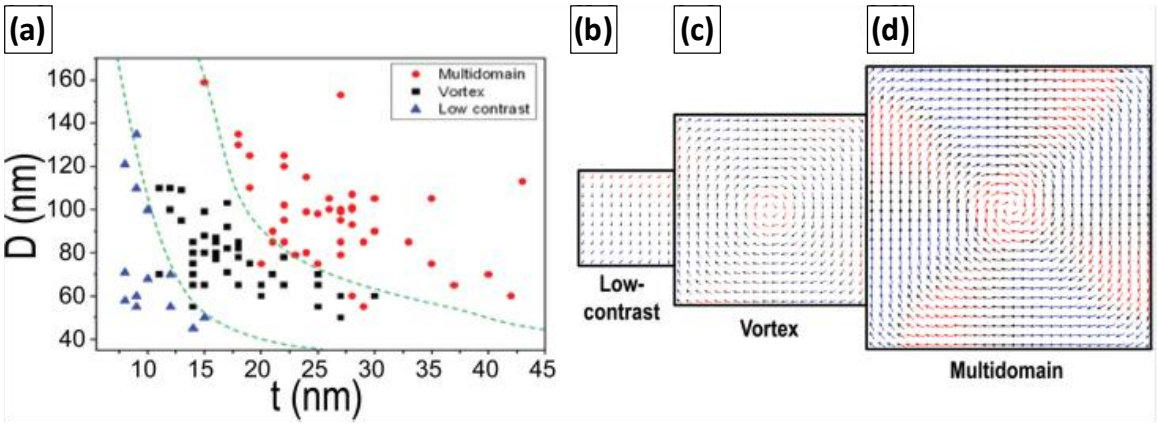

Figure 2.38: The three regimes. (a) *Phase diagram extracted from a set of MFM measurements, showing the magnetic configuration of the self-assembled LSMO nanoislands as a function of their width (D)-thickness (t) dimensions (dashed lines have been included as a guide to the eye). Micromagnetic simulations for the equilibrium state of* ***(b)*** *small,* ***(c)*** *medium size and* ***(d)*** *large nanoislands, after saturation along the OOP direction (data scale: 25 kA/m, blue-red colors stand for the outward-inward OOP component of the magnetization, respectively).*

In order to help with the interpretation of the experimental images, micromagnetic simulations were performed with *OOMMF* using the experimental parameters for the saturation magnetization (M_S=48·10^4 A/m) and anisotropy constant (k_1=5·10^3 J/m^3) and an exchange stiffness of A=1.73·10^{-12} J/m. The equilibrium magnetization distribution in the remanent state after *IP* saturation is shown in figure 2.38 for the three regimes considered. The smallest nanostructures, with a size of (50x50x10) nm^3 (fig. 2.38.b), show a single domain remanent state. This, together with the weaker interaction between tip and sample arising from the low amount of material present, causes the faint experimental contrast. Medium size islands, with dimensions of (90x90x15) nm^3 (fig. 2.38.c), show a magnetic vortex configuration, with the magnetization rotating in plane around the center of the structure, where the magnetic moments are pointing out of the sample plane. The largest simulated islands, with a size of (150x150x30) nm^3 (fig. 2.38.d), show a vortex state in remanence, as well, but a larger magnetization divergence is present close to the borders. We believe this is the origin of the contrast at the edges of the largest nanoislands in the experimental *MFM* images.

Chapter 3: Distinguishing electrostatic and magnetic interactions

As detailed in the introduction of this thesis, scanning probe microscopies can be used to detect different short, medium and long range interactions with high sensitivity and lateral resolution. The two long range interactions particularly relevant at the usual tip-sample separation distances used in *MFM* experiments are electrostatics and magnetostatics. Eventually, electrostatic force gradients can be large enough to mislead the user about the actual magnetic state of the sample. On the one hand, care should then be taken with samples presenting low magnetic moment such as organic nanomagnets [1], magnetic oxide films [2], superparamagnetic particles [3,4] and carbon based materials [5,6], since spurious *van der Waals* and electrostatic interactions might be present and yield a measurable frequency shift on the cantilever oscillation. On the other hand, samples might be composed of different materials (for instance, the substrate and patterned material, when using lithographies or templates), each one presenting a different surface potential. This heterogeneous electrostatic interaction might be misinterpreted as part of the domain configuration of the magnetic material.

Two different approaches can be used to confirm the magnetic origin of the observed contrast. The first one consists of studying the contrast response in frequency shift images as **in-situ magnetic fields** are varied [7,8,9]. This method does not yield the pure magnetic information but its overlap with electrostatics. Changes on the contrast must be assessed to the presence of a magnetic response within the sample but information about its actual spin configuration is still lacking. The second one, proposed here, relies on using **a combination of *MFM* with *Kelvin* Probe Force Microscopy** (*KPFM*) [10,11] to compensate the electrostatic force gradient. This method separates both contributions and allows obtaining true *MFM* pictures. Little attention has been paid to this issue despite its relevance in some cases and current chapter is focused on it.

[1] J. Gómez-Segura, O. Kazakova, J. Davies, P. Joseph-Franks, J. Veciana and D. Ruiz-Molina, Chemical Communications 45 (2005) 5615-5617
[2] Y. Wu, Y. Suzuki, U. Rüdiger, J. Yu, A. D. Kent, T. K. Nath and C. B. Eom, Applied Physics Letters 75 (1999) 2295
[3] C. S. Neves, P. Quaresma, P. V. Baptista, P. A. Carvalho, J. P. Araujo, E. Pereira and P. Eaton, Nanotechnology 21 (2010) 305706
[4] S. Schreiber, M. Savla, D. V. Pelekhov, D. F. Iscru, C. Selcu, P. C. Hammel and G. Agarwal, Small 4 (2008) 270
[5] J. Cervenka, M. I. Katsnelson and C. F. J. Flipse, Nature Physics 5 (2009) 840
[6] P. Esquinazi, D. Spemann, R. Höhne, A. Setzer, K.-H. Han and T. Butz, Physical Review Letters 91 (2003) 227201
[7] R. Engel-Herbert, T. Hesjedal, J. Mohanty, D. M. Schaadt and K. H. Ploog, Physical Review B 73 (2006) 104441
[8] S. Foss, C. Merton, R. Proskch, G. Skidmore, J. Schmidt, E. D. Dahlberg, T. Pokhil and Y.-T. Cheng, Journal of Magnetism and Magnetic Materials 190 (1998) 60
[9] A. Asenjo, D. García, J. M. García, C. Prados and M. Vázquez, Physical Review B 62 (2000) 6538
[10] M. Nonnenmacher, M. P. O'Boyle and H. K. Wickramasinghe, Applied Physics Letters 58 (1991) 2921
[11] T. Glatzel, S. Sadewasser and M. C. Lux-Steiner, Applied Surface Science 210 (2003) 84

1. Fundamentals of Kelvin Probe Force Microscopy (KPFM)

Magnetic force microscopy measurements are typically recorded at relatively large distances, at which atomic corrugations are negligible and the sample can be considered to be a flat surface. In the simplest model of a perfect plane capacitor, the electric field can be easily calculated by means of Gauss' theorem and turns out to be constant at every point between plates:

$$\oiint \vec{E} \cdot d\vec{S} = \frac{Q}{\varepsilon_0} \Rightarrow E \cdot 2S = \frac{\sigma \cdot 2S}{\varepsilon_0} \Rightarrow E = \frac{\sigma}{\varepsilon_0} \Rightarrow \phi = \frac{\sigma}{\varepsilon_0} \cdot d$$

The electrostatic energy stored in such a capacitor is given by:

$$W = \frac{1}{2} \cdot \iiint \vec{E} \cdot \vec{D} \cdot dV_{olumen} = \frac{\varepsilon_0}{2} \cdot \iiint |\vec{E}|^2 \cdot dV_{olumen} = \frac{\sigma^2}{2\varepsilon_0} \cdot V_{olumen}$$

The volume can be expressed in terms of the capacitance as:

$$C = \frac{Q}{\phi} = \frac{\sigma \cdot A}{\phi} = \frac{\sigma \cdot V_{olumen}}{\phi \cdot d} \Rightarrow V_{olumen} = \frac{C \cdot d}{\sigma} \cdot \phi$$

giving the expression:

$$W = \frac{\sigma^2}{2\varepsilon_0} \cdot \frac{C \cdot d}{\sigma} \cdot \phi = C \cdot \left(\frac{\sigma \cdot d}{2\varepsilon_0}\right) \cdot \phi = \frac{1}{2} \cdot C \cdot \phi^2$$

Assuming again, as it was done in the introduction of this thesis, that the cantilever is mainly sensitive to the vertical component of the tip-sample interacting force (i.e., the force constant $k_Z << k_X, k_Y$) and for large tip-surface distances compared to atomic dimensions, we calculate:

$$\boxed{|\vec{F_z}| = -\frac{\partial}{\partial z}\left(\frac{1}{2} \cdot C \cdot \phi^2\right) = -\frac{1}{2} \cdot \frac{\partial C}{\partial z} \cdot \phi^2} \qquad \textbf{(3.1)}$$

The electrostatic field between the tip and the sample is a result of the so-called contact potential difference (*CPD*). The electric potential on the surface of a metal depends on the surface reconstruction, contamination, etc., and so does the *CPD*. Thus, different *CPD* may be measured on the same sample when using two different probes, even if they were fabricated in the same way. In the case of heterogeneous samples, where more than one material is present, dissimilar metals can show an electric potential difference even at equilibrium. Thus, different *CPD* are expected for each material.

Kelvin Force Probe Microscopy (*KPFM*) uses a feedback loop to cancel out electrostatic interactions with the sample and provide *CPD* images. For doing so, the system excites the probe **electrostatically** with a sinusoidal voltage. Thus, the cantilever is excited at two frequencies simultaneously, when using the *KPFM* mode: piezoacustically at the first resonant mode – used for topography measurements – and electrostatically at a different one. This second excitation frequency (ω_2) may be the second flexural eigenmode – used in the amplitude modulation *KPFM* (*AM-KPFM*) – that takes advantage of its quality factor to amplify the mechanical response, or a relatively small frequency – used in the frequency modulation *KPFM* (*FM-KPFM*) – out of the first mode bandwidth to avoid crosstalk.

In both variants, the *KPFM* feedback uses a second *lock-in* to cancel out the cantilever response to the electrostatic interaction; however, different modulated signals are brought into it in each case. In *AM-KPFM*, the signal coming out from the photodiode is fed directly into this second *lock-in* (which is referenced to ω_2), in such a way that only the information around the second eigenmode is extracted. By contrast, in the *FM-KPFM* mode the output of the first *lock-in* is analyzed, as will be detailed later.

Similar to standard *AFM*, amplitude modulation *KPFM* directly detects forces, whereas frequency modulation *KPFM* detects force gradients. One should keep in mind that tip-sample interactions cause the intrinsic resonance frequencies of the lever to shift. Thus, *AM-KPFM* is optimized when using a second *PLL* feedback that tracks the second resonance mode whenever it is shifted by the sample influence. Otherwise, any interaction will cause the oscillation amplitude at ω_2 to decrease; however, this drop will not be associated to a *CPD* compensation. This additional *PLL* setup is not necessary when operating the *FM-MFM* mode.

In general, higher lateral resolution is achieved in *FM-KPFM* [11,12] because only the final part of the tip is sensitive to the force gradient, whereas most part of it – and even the cantilever – can contribute to the electrostatic force. For large enough distances, electrostatic forces decrease smoothly and their force gradient becomes very small. However, forces themselves can reach values high enough to contribute significantly to the measurement. As a result, the lateral resolution is reduced by an averaging effect between the tip and cantilever. According to *Enevoldsen* and co-workers [13], resolution in *FM-KPFM* is typically in the order of the tip apex dimension. Nevertheless, it has been demonstrated that both *FM-* and *AM-KPFM* can show atomic scale resolution [13], although the mechanisms responsible for the contrast are still controversial [14].

[12] U. Zerweck, C. Loppacher, T. Otto, S. Grafstrom and L.M. Eng, Physical Review B 71 (2005) 125424
[13] G. H. Enevoldsen, T. Glatzel, M. C. Christensen, J. V. Lauritsen and F. Besenbacher, Physical Review Letters 100 (2008) 236104

Regarding the energy resolution of the contact potential difference, higher precisions are obtained in *AM-KPFM* in general terms [11,15]. Amplitude modulation *KPFM* measures the *CPD* from the resonance peak of the oscillating cantilever, greatly enhancing the signal-to-noise ratio. Conversely, frequency modulation *KPFM* detects the *CPD* through a frequency demodulator and additional noise is then generated, limiting the energy resolution.

But how does the *KPFM* feedback work? As mentioned above, an intrinsic electric potential difference is present between probe and sample, the so-called contact potential difference (V_{CPD}). In addition to it, a *DC* bias may also be applied in a controlled way between them (ϕ_{DC}). Last, the *KPFM* system excites the cantilever with a sinusoidal bias voltage of amplitude A_{AC}. Therefore, the total potential difference (ϕ) between them is:

$$\phi = \phi_{DC} - V_{CPD} + A_{AC} \cdot \sin(\omega_2 \cdot t)$$

The electrostatic force sensed by the probe is:

$$\left|\overrightarrow{F_z}\right| = -\frac{1}{2} \cdot \frac{\partial C}{\partial z} \cdot \phi^2 = -\frac{1}{2} \cdot \frac{\partial C}{\partial z} \cdot [\phi_{DC} - V_{CPD} + A_{AC} \cdot \sin(\omega_2 \cdot t)]^2 \Rightarrow \quad \textbf{(3.2)}$$
$$\Rightarrow \cdots \Rightarrow \left|\overrightarrow{F_z}\right| = F_{DC} + F_{\omega} \cdot \sin(\omega_2 \cdot t) + F_{2\omega} \cdot \sin\left(2\omega_2 \cdot t - \frac{\pi}{2}\right)$$

It can be expressed as a function of three additive terms. The first term remains constant over time and is responsible for a cantilever bending, the second one varies with a frequency ω_2 and the third one, with twice ω_2. Remember that ω_2 is the excitation frequency chosen for the *KPFM* feedback, in our case in the order of few kHz. The constants introduced in last equation are defined as:

$$F_{DC} = -\frac{1}{2} \cdot \frac{\partial C}{\partial z} \cdot \left({\phi_{DC}}^2 + {V_{CPD}}^2 - 2 \cdot \phi_{DC} \cdot V_{CPD} + \frac{{A_{AC}}^2}{2}\right)$$
$$\boxed{F_{\omega} = -A_{AC} \cdot (\phi_{DC} - V_{CPD}) \cdot \frac{\partial C}{\partial z}} \quad \textbf{(3.3)}$$
$$F_{2\omega} = -\frac{{A_{AC}}^2}{4} \cdot \frac{\partial C}{\partial z}$$

The *KPFM* system uses a *lock-in* referenced to ω_2 to extract the value of F_{ω}, filtering out the other two terms. Then, it tries to nullify F_{ω} by tuning the tip *DC* bias (ϕ_{DC}) in a controlled way. This nullification takes place when ϕ_{DC}=V_{CPD} (see equation **(3.3)**), in such a way that the output of the

[14] L. Nony, F. Bocquet, C. Loppacher and T. Glatzel, Nanotechnology 20 (2009) 264014
[15] C. Sommerhalter, T. Glatzel, T. W. Matthes, A. Jager-Waldau and M. C. Lux-Steiner, Applied Surface Science 157 (2000) 263

KPFM feedback yields the contact potential difference between tip and sample. Since the *CPD* is compensated, no electrostatic interaction will be present and pure *MFM* images can be obtained.

Equation **(3.1)** was derived from the capacitive energy between two parallel metal plates and is valid for *CPD* measurements on metallic surfaces. However, a space charge layer (*SCL*) is well known to be present on the surface of semiconductors and its effects have to be considered when measuring on a semiconductor surface. This is out of the scope of present thesis but an analysis of the electrostatic force between a metallic *AFM* probe and a semiconducting sample is given by *Hudlet* and co-authors [16], who derived an expression for the term oscillating at ω_2 and concluded that the measured *CPD* for a semiconducting surface differs from the work function of the material due to the *SCL* near the semiconductor surface.

It is important to note that the aforementioned description of the *Kelvin* mode only takes into account the long range character of electrostatic interactions, which is the relevant case in *MFM* experiments. However, atomically resolved *KPFM* images [17,18] testify that electrostatic forces also have a short range character. Equation **(3.1)** is improper to describe this contrast, first because the expression does not have a short range character and second because this expression derives from a classical electrostatic approach between continuous-like metallic bodies and hence does not take into account atomic fluctuations of the surface potential. In some works [19,20] there is strong evidence that short range electrostatic forces scale not only quadratically but also linearly with the applied bias voltage, which causes the compensating bias to neither reflect the tip surface *CPD* nor the local surface potential, but rather an effective value which is convoluted by the geometry of the tip. Recent theoretical studies on *AM-* and *FM-KPFM* suggested that both modes have the same limitation in spatial resolution in the sub-nanometer regime [14].

- Experimental set-up

All measurements presented in this chapter were performed using the frequency modulation *KPFM* mode with a sinusoidal electrostatic excitation at a frequency ω_2=7 kHz and an excitation voltage A_{AC}=500 mV. A sketch of the three feedback loops used in the experiments is shown in figure 3.1. The output signal coming out from the photodiode (normal force) and carrying the information about the cantilever oscillation is fed into the first *lock-in* amplifier, which is referenced to the frequency of the first eigenmode used for the topographic feedback ($\omega_{exc} \approx 75\ kHz$). It extracts

[16] S. Hudlet, M. Saintjean, B. Roulet, J. Berger and C. Guthmann, Journal of Applied Physics 77 (1995) 3308
[17] S. Kitamura and M. Iwatsuki, Applied Physics Letters 72 (1998) 3154
[18] K. Okamoto, K. Yoshimoto, Y. Sugawara and S. Morita, Applied Surface Science 210 (2003) 128
[19] F. Krok, K. Sajewicz, J. Konior, M. Goryl, P. Piatkowski and M. Szymonski, Physical Review B 77 (2008) 235427
[20] F. Bocquet, L. Nony, C. Loppacher and T. Glatzel, Physical Review B 78 (2008) 035410

information about both the oscillation amplitude and phase shift at this faster frequency; the first one is fed into the main feedback to control the tip-sample distance, whereas the second one is used by the *PLL* feedback to keep the cantilever oscillating at resonance [21].

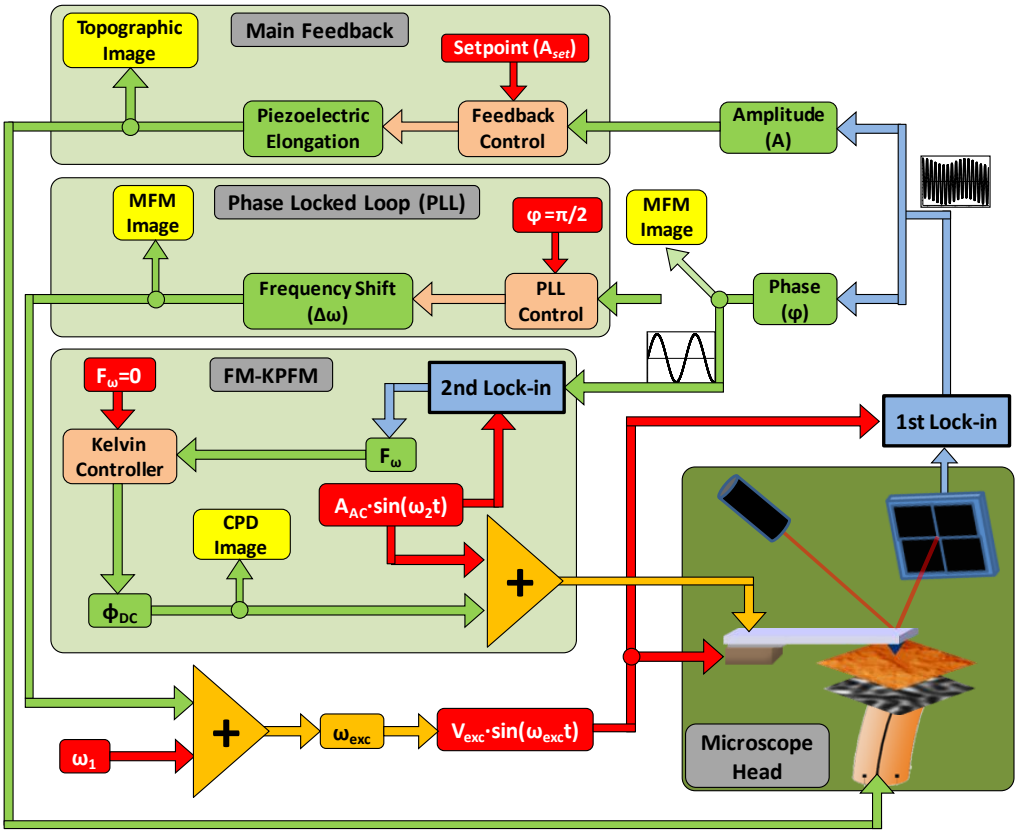

Figure 3.1: The three feedback loops. *Schematics of the three simultaneous feedback loops used in the experiments: amplitude modulation AFM (AM-AFM) with a phase locked loop (PLL) and frequency modulation KPFM (FM-KPFM).*

So far, the operating mode is analogous to the standard *PLL*-assisted amplitude modulation mode, described in chapter 1. The main difference introduced by the *FM-KPFM* is a modulation in the phase signal coming out of the first *lock-in*. Remember that interactions cause the resonance frequency of the cantilever to shift (see eq. **(1.12)**). Thus, a sinusoidal tip biasing results in a periodic phase shift oscillating at the same frequency ($\omega_2 \approx 7$ *Hz*). This phase shift signal is analyzed with the second *lock-in* to extract its oscillation amplitude at ω_2 (which is actually the term F_ω in equation **(3.2)**). The third feedback loop, i.e. the *KPFM* system tries to nullify the oscillation amplitude at ω_2 (or F_ω) by applying a *DC* tip biasing. When the *DC* bias equals the tip-sample contact potential difference, no modulation in the phase shift signal is measured at ω_2.

[21] As was mentioned in chapter 1, the actual magnitudes used in the experimental set-up for these feedbacks are the *in-phase* and *quadrature* components and not the amplitude and phase themselves. This allows for faster scanning speeds since no subsequent calculation is necessary. In any case, the use of a *PLL* ensures that no phase shifts are present so that the in-phase component equals the oscillation amplitude.

The reader might be confused about the fact that the modulation at ω_2 is carried by the phase even when the *PLL* is enabled. The reason for that is the relatively long operating time of the phase locked loop compared to ($1/\omega_2$), which is in the order of 0.1 ms for the typical values used in the experiments. If one seeks fast scan speeds, high values of ω_2 are desired. However, this modulation frequency should be far from the first eigenmode in order to avoid crosstalk and allow for the first (analog) *lock-in* to integrate over several cycles and filter out spurious resonances. In our experiments, a bandwidth of 8 kHz was used for the first *lock-in* (corresponding to 10 oscillation cycles of the first mode). This cutoff frequency represents the maximum appropriate value for ω_2, as signals at higher frequencies will start being filtered out by the *lock-in*.

Another possible way of implementing the *FM-KPFM* mode consists of using lower ω_2, at the expense of decreased scan speeds. For slow enough modulations ($\omega_2 < 1$ kHz), the *PLL* is able to track this modulation and flatten the phase channel. Then, the output of the *PLL* and not the phase should be fed into the second *lock-in* to extract information about electrostatics. Using such slow modulations lets the first *lock-in* integrate over a much larger number of cycles. However, a drawback of this option is that the signal modulated at ω_2 must go through additional electronics, i.e. the *PLL* itself, so additional noise may be introduced in the measurement.

2. Distinguishing interactions by a MFM-KPFM combination

To estimate the eventual overlap of the two conservative interactions that can take place in some cases, we studied a series of straight and *L* shaped cobalt nanostripes grown by focused electron beam induced deposition (*FEBID*) by the group of Prof. *J. M. de Teresa*'s at the *University of Zaragoza*. The straight elements, 5 μm long and 500 nm wide, have thicknesses ranging from 10 nm to 400 nm. In addition, the *L* shaped structures have a long arm of 10 μm and a short one of 5 μm, their width varying from 125 nm up to 2 μm with thickness between 50 nm and 200 nm. The sample preparation is analogous to the one described in chapter 2.2, refer to it for more detail. In the experiments, homemade *MFM* probes with a 25 nm cobalt layer were used (see chapter 4 for more information). Results shown here were published during the second year of my thesis [22].

During the *FEBID* fabrication process, charge accumulation takes place in the substrate. Secondary electrons generated when the electron beam hits the substrate may not have enough energy to overcome the work function of the surface and penetrate the bulk. As a consequence, they may become trapped in the surrounding area of the stripes. Some of these secondary electrons can reach

[22] M. Jaafar, **O. Iglesias-Freire**, L. Serrano-Ramón, M. R. Ibarra, J. M. de Teresa and A. Asenjo, Beilstein Journal of Nanotechnology 2 (2011) 552-560

the surface near the scanning area, even at distances of more than 1 μm, with enough energy to partially decompose gas molecules, producing a parasitic deposit or a so called "halo". However, the decomposition of the precursor gas in this halo is not complete. As a consequence, an insulating material is formed around the wires whose major components are C and O (with Co content below 20%). Secondary electrons may also get trapped in the halo, consequently increasing the surface potential. In addition, a thin native oxide layer (around 2 nm) covers the Co thin film as soon as samples are exposed to ambient atmosphere. These insulating side effects enhance charge accumulation in the deposit region, thus changing its surface potential.

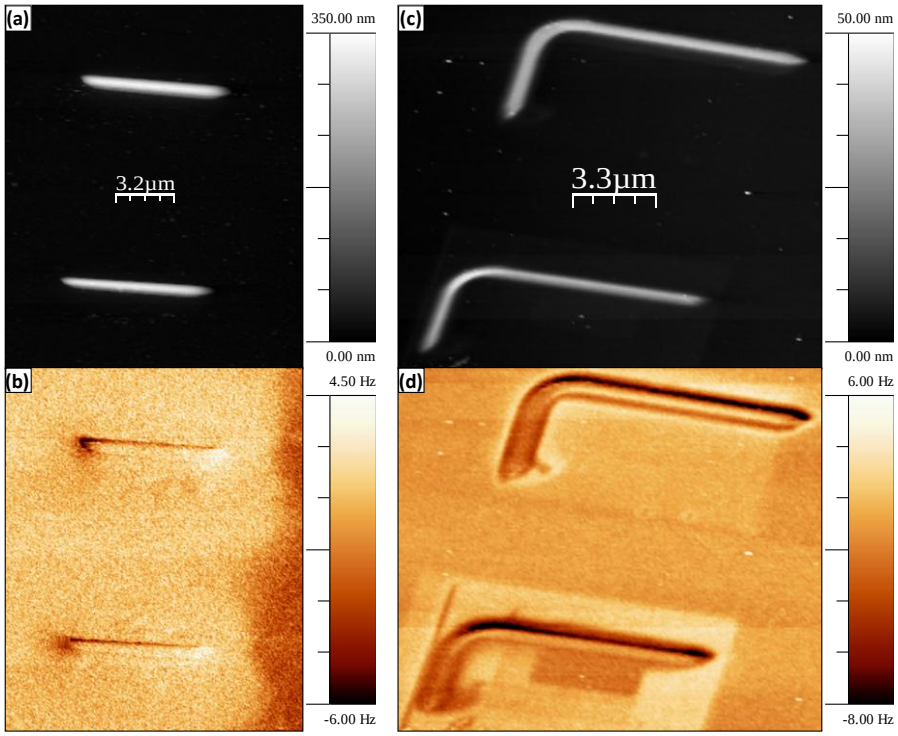

Figure 3.2: Straight and L shaped stripes. (a) & (c) *Topography and* ***(b) & (d)*** *frequency shift images corresponding to the cobalt planar wires and L shaped structures, respectively. No tip-sample bias was applied. The oscillation amplitude was 5 nm during the topographic scan and 8.5 nm during retrace scan.*

Figure 3.2 shows topography and frequency shift maps at a retrace distance of 30 nm for both patterned structures, after magnetic saturation along the horizontal direction in the images. Intuitively and due to their strong shape anisotropy, a characteristic single domain (dipole like) magnetic contrast is expected for the straight stripes, while a more complex configuration might be present in the *L* shaped structures. In the first case, this typical bright-dark contrast at the end of the wires can be observed, whereas a fancy structure seems to be deduced from the frequency shift image in the *L* shaped stripes. The latter might be interpreted as a longitudinal *DW* along the longest side of the nanostructure, thus revealing the existence of an unexpected strong transversal magneto-crystalline anisotropy. In addition, contrast is observed in the non-magnetic substrate.

In order to check their reliability as *MFM* images, the presence of electrostatic interactions due to eventual charging effects must be evaluated. A first simple test consists of recording the cantilever frequency shift as the tip-sample bias ϕ_{DC} is swept. As explained in former section, the electrostatic force gradient has a parabolic dependence on the voltage difference. From equation **(3.2)** and without exciting the cantilever at a second frequency ω_2:

$$\frac{\partial\left|\vec{F_z}\right|}{\partial z} = \frac{1}{2}\cdot\frac{\partial^2 C}{\partial z^2}\cdot(\phi_{DC} - V_{CPD})^2$$

By substituting this into equation **(1.12)** one gets:

$$\Delta\omega \approx -\frac{\omega_0}{2\cdot k}\cdot\frac{\partial\left|\vec{F_z}\right|}{\partial z} = -\frac{\omega_0}{4\cdot k}\cdot\frac{\partial^2 C}{\partial z^2}\cdot(\phi_{DC} - V_{CPD})^2$$

Such quadratic dependence of $\Delta\omega$ on the bias is expected and indeed observed in figure 3.3, where the bias was changed while keeping the tip at the same position. For ensuring this condition, the topographic feedback was enabled during the sweep. Two parabolas were obtained, placing the tip over the substrate and over the stripe shown in the upper part of figure 3.2.a. The maximum of a parabola is indicative of the bias voltage necessary for nullifying the contact potential difference (*CPD*) between the tip and sample, since:

$$\frac{d(\Delta\omega)}{d\phi_{DC}} = -\frac{\omega_0}{2\cdot k}\cdot\frac{\partial^2 C}{\partial z^2}\cdot(\phi_{DC} - V_{CPD}) \quad ; \quad \frac{d(\Delta\omega_{max})}{d\phi_{DC}} = 0 \Rightarrow \phi_{DC} = V_{CPD}$$

These values were found to be ϕ_{DC}=320 mV in the central part of the stripe and ϕ_{DC}'=-300 mV in the substrate (fig. 3.3). Any different tip bias results in a decrease of the resonance frequency, as a result of the attractive interaction. Note that a change of over 3 Hz is recorded in the oscillation frequency, as the bias is swept from -1.5 to 0 V. The fact that lower frequency shifts are commonly observed in standard *MFM* experiments highlights the risk of misinterpreting data.

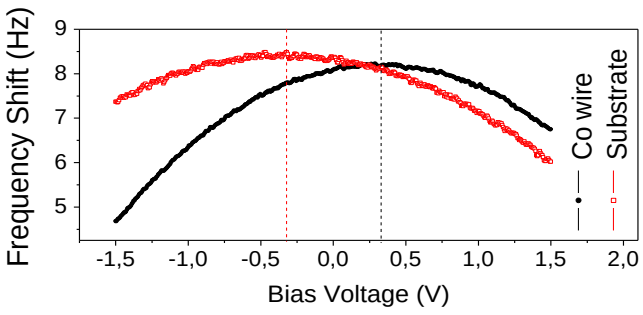

Figure 3.3: Δω vs bias. *Frequency shift dependence on the tip-sample bias, obtained* ***(black curve)*** *in the central part of the stripe shown in the upper part of figure 3.2.a and* ***(red curve)*** *with the tip placed over the substrate.*

The implementation of the *KPFM* feedback is shown in figure 3.4, where the uppermost row shows the topography of one element of each kind, with their corresponding frequency shift images (*KPFM* off) right below in the second row. Turning on the *KPFM* feedback allows for separating the information on magnetostatic and electrostatic interactions into frequency shift (fig. 3.4.c, g) and *CPD* images (fig. 3.4.d, h), respectively. In the case of straight wires, the unexpected contrast observed previously in the substrate turns out to have an electrostatic origin. A more dramatic effect is observed in the case of *L* shaped stripes, where the pure *MFM* image (fig. 3.4.g) shows a nice vortex wall structure, which was completely hidden beneath electrostatics when no *Kelvin* loop was used. Notice the scale bar range difference between both experiments. The *CPD* images clearly show the areas raster scanned by the electron beam during the sample fabrication and reveal the existence of charge accumulation processes.

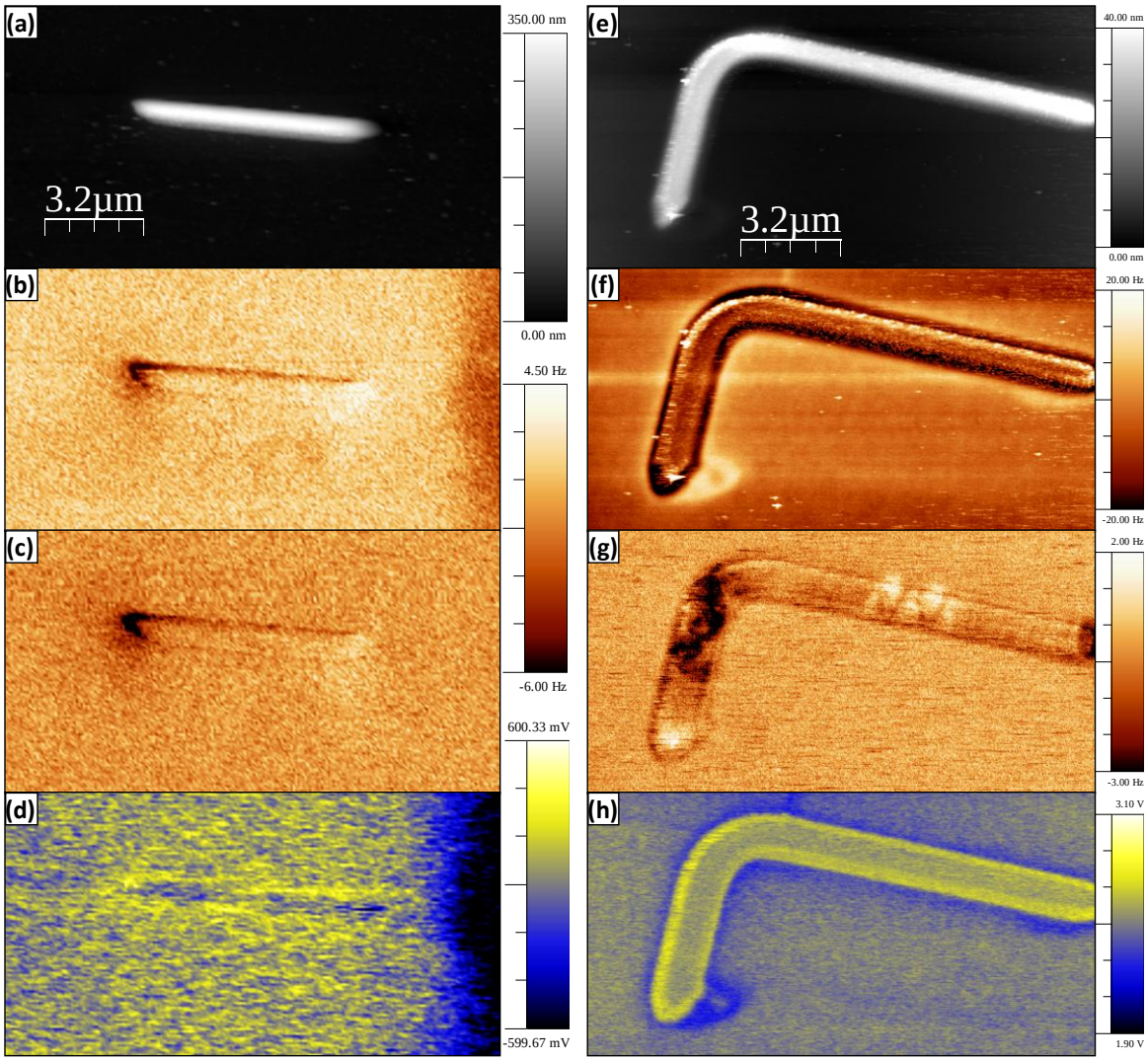

Figure 3.4: The Kelvin implementation. *Topography of a* ***(a)*** *straight and* ***(e)*** *L shaped stripe. Corresponding excitation frequency images taken with the KPFM feedback* ***(b)*** *&* ***(f)*** *disabled and* ***(c)*** *&* ***(g)*** *enabled. (d) & (h) Contact potential difference (CPD) images reflecting charge accumulated during the fabrication process.*

It thus becomes evident that one must be careful when interpreting *MFM* images under certain circumstances. First, whenever a fabrication technique is used that may cause charging effects in samples, in particular when dealing with insulating substrates. Second, when dealing with samples with a low net magnetic moment, since small electrostatic interactions might cover up magnetism. Last, when trying to determine whether a sample presents magnetic behavior [23]. In all these cases, the use of a *MFM-KPFM* combination is strongly recommended.

Applying external fields with the MFM-KPFM combination

Having shown the *MFM-KPFM* implementation to work reliably, we will proceed to apply external magnetic fields and record the evolution of the domain configuration. Figure 3.5 presents pure *MFM* maps of one of the *L* shaped planar wires, under the influence of a variable in-plane (*IP*) field applied along the horizontal direction of the images. For relatively large fields – in the order of 100 mT – the magnetic element is shown to be in a nearly saturated state (fig. 3.5.a and c) and the magnetic moments, pointing parallel to the field direction, give rise to a bright-dark contrast across the short arm of the *L*. The remanent configuration that is left after removing the field is a single domain state with the spins following the geometrical shape. The polarity is determined by the direction of the previous saturating field (fig. 3.5.b and d).

Compared to the topographic data (figure 3.5.f), there seems to be a sample widening in the *MFM* and *CPD* images. This might be due to the presence of the halo mentioned in the description of the sample fabrication. Notice that contrast is also observed in the halo surrounding the short arm when small fields are applied, as observed in figures 3.5.b and d, revealing that magnetic material has also been deposited there. Although no current was flowing through the electromagnet, a remanent field of 5 mT is present. Finally, in spite of the large field range used in the experiment, no remarkable change is observed in the *CPD* images shown in figures 3.5.e and h (which correspond to the situations in a and d), as is expected since the work function does not depend on external fields (at least, in mesoscopic physics as is the case).

[23] D. Martínez-Martín, M. Jaafar, R. Pérez, J. Gómez-Herrero and A. Asenjo, Physical Review Letters 105 (2010) 257203

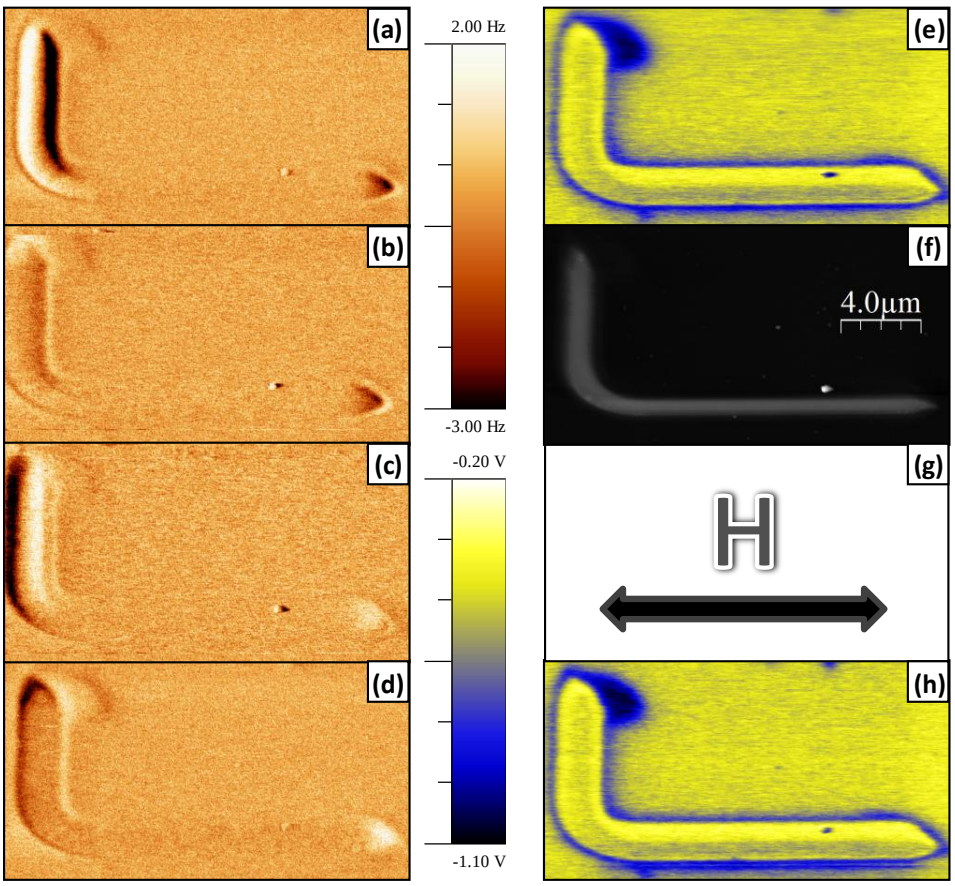

Figure 3.5: MFM-KPFM with applied fields (I). *Evolution of the magnetic structure in an L shaped stripe, as a function of an external field applied along the in-plane direction indicated in (g). The field sequence shows successive pure MFM images measured at* ***(a)*** *-100 mT,* ***(b)*** *-5 mT,* ***(c)*** *100 mT and* ***(d)*** *5 mT. The two CPD images displayed, for fields of* ***(e)*** *-100 mT and* ***(h)*** *0 mT, show no difference.*

In this kind of *L* shaped nanostructures, magnetic fields are commonly applied with a relative misalignment in order to nucleate *DWs* on purpose. This is the case introduced in figure 3.6, where a sequence of *MFM* and *CPD* images is shown for a different *L* shaped structure, as the horizontal field is swept. The first configuration observed (fig. 3.6.b) is the *as-grown* magnetic state and shows two *DWs* separating three domains. This domain structure rapidly disappears as the external field is increased up to saturation (fig. 3.6.c-d) and a single domain structure is present on the way down back to remanence (fig. 3.6.e). The as-grown magnetic state is not observed anymore in the absence of field. However, the effect of the field misalignment becomes relevant during the magnetization reversal process since a *DW* is not only nucleated – as in the aligned case, where it propagates and annihilates much faster than the microscope scan speed – but remains present for a large range of fields (fig. 3.6.f-g). Finally, this single *DW* disappears and the sample reaches saturation along the opposite direction (fig. 3.6.h). Again, no remarkable changes are observed in the corresponding contact potential difference images, as the magnetic field is varied. Notice that the contrast present in all the images shown has the same scale.

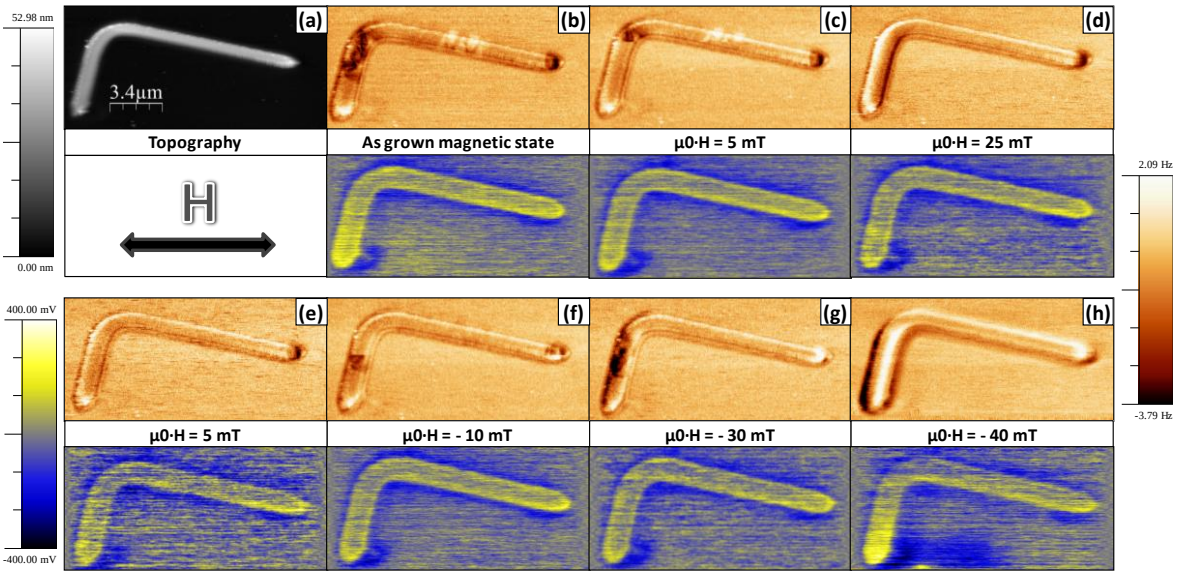

Figure 3.6: MFM-KPFM with applied fields (II). (a) *Topography of another L shaped stripe and* ***(b)-(h)*** *sequence of MFM and corresponding CPD images, showing the evolution under an IP field with a misalignment of around 10 º.*

Thus, a reliable implementation of the *MFM-KPFM* combination has been demonstrated and utilized to obtain the domain structure of *L* shaped stripes, as well as the reversal mechanisms involved for small misalignments of the external field. Notice that, due to the strong charging effects, it would not have been possible to obtain such information without the simultaneous use of the *KPFM* feedback.

3D modes with the MFM-KPFM combination

In chapter 2, a particular procedure was introduced (the so-called *3D modes*), in which *MFM* experiments were carried out with the tip continuously scanning along the same profile of the sample, while the applied field was changed in small steps. As a result, useful $\Delta f(X, H)$ images were obtained that allow quantifying critical fields, such as the switching field of stripes with a bi-stable behavior. This operating mode can also be implemented using the *KPFM* feedback, which turns out to be very useful in the case of single domain nanostructures with strong charging effects. Good examples of these are the straight cobalt stripes described in section 2.2. In particular, figure 3.7 shows three of the stripes whose switching fields were quantified in figure 2.14 using the *3D modes*, while simultaneously cancelling out electrostatics.

As can be seen in figure 3.7.b, charges trapped on the sample surface cause again standard *MFM* maps to give mixed information about the magnetic properties and the surface potential. The *Kelvin* loop separates both contributions (fig. 3.7.c-d) and a real *MFM* image is obtained. A halo of

magnetic material is again observed surrounding the planar nanowires and it even shows a magnetization orientation similar to the one in the stripes. Performing now a *3D modes* measurement along one of the nanostructures yields an image like the one shown in figure 3.7.e. There, a sudden jump is observed in the frequency shift channel for a certain value of the applied field, which corresponds to the magnetization reversal. On the contrary, no significant change is seen in the *CPD* image (fig. 3.7.f), as expected.

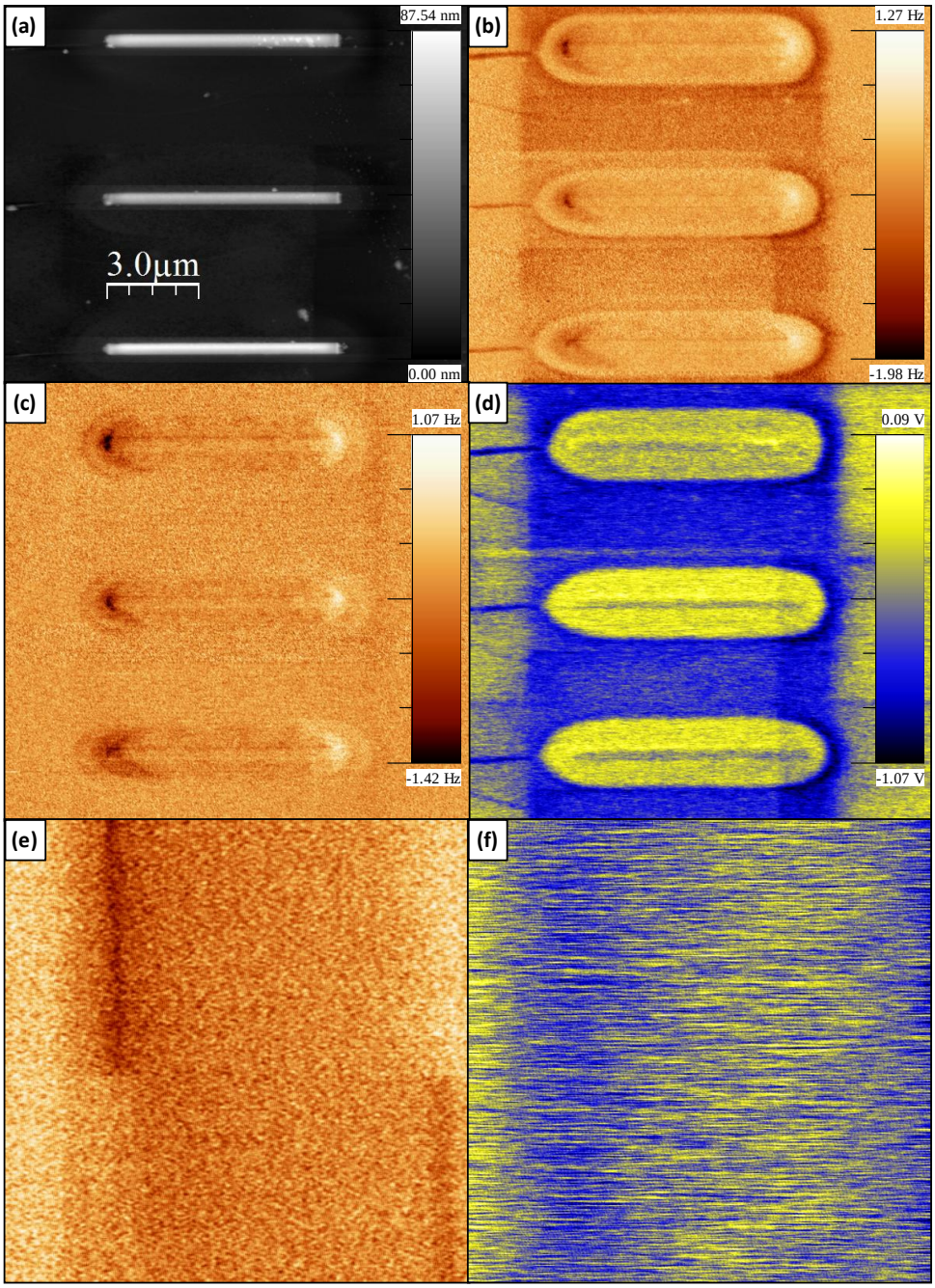

***Figure 3.7: 3D modes with the MFM-KPFM combination**. **(a)** Topography and **(b)** corresponding frequency shift image of three single domain Co nanostripes. **(c)** Pure MFM and **(d)** CPD images obtained after enabling the KPFM controller. 3D modes **(e)** frequency shift and **(f)** CPD maps measured in one nanostructure to extract its switching field.*

All the images shown in figure 3.7 were recorded using a homemade *MFM* probe, in order to minimize the stray field emerging from the tip and thereby the influence over the sample. By doing this, more realistic values of the switching field can be obtained. Therefore, that experiment is a good example of a simultaneous combination of different implementations presented in this thesis: the use of homemade probes with reduced influence in the sample (chapter 4), the switching field quantification in single nanostructures by means of the *3D modes* (chapter 2.2) and the implementation of the *MFM-KPFM* operating mode (chapter 3).

3. MFM-KPFM combination for calibration of MFM probes

An interesting application of this *MFM-KPFM* combination is presented in this section. It was developed in collaboration with the group of Dr. *O. Kazakova* from the *National Physical Laboratory* (*NPL*), with the aim of evaluating the magnetic field gradient emanating from an *MFM* tip using graphene *Hall* sensors. It has given rise to two research articles published during the final part of my doctoral thesis [24,25].

The collaborating group is interested in reaching quantitative magnetic force microscopy measurements by being able to perform meticulous calibration of *MFM* probes. Microscopic *Hall* sensors are suitable for such probe calibration and have already been used [26,27,28], but in particular graphene based *Hall* devices benefit from high sensitivity [29] and robustness to large biasing currents [30]. However, electrostatic forces exerted between the current-biased device and the metallically coated probe give rise to parasitic electric fields [31]. The resulting measurement of the transverse *Hall* voltage is thus the superposition of both electric and magnetic field contributions, making it difficult to accurately determine the tip's stray field. In our work, the implementation of the *MFM-KPFM* combination is applied to eliminate the parasitic electric field between both conductors seeking a precise calibration method of probes.

[24] V. Panchal, **Ó. Iglesias-Freire**, A. Lartsev, R. Yakimova, A. Asenjo and O. Kazakova, IEEE Transactions on Magnetics 49 (2013) 3520-3523
[25] R. K. Rajkumar, A. Asenjo, V. Panchal, A. Manzin, **Ó. Iglesias-Freire** and O. Kazakova, Journal of Applied Physics (58th Conference on MMM) 115 (2014) 172606
[26] A. Thiaville, L. Belliard, D. Majer, E. Zeldov and J. Miltat, Journal of Applied Physics 82 (1997) 3182
[27] H. Guillou, A. D. Kent, G. W. Stupian and M. S. Leung, Journal of Applied Physics 93 (2003) 2746
[28] V. N. Matveev, V. I. Levashov, V. T. Volkov, O. V. Kononenko, A. V. Chernyh, M. A. Knjazev and V. A. Tulin, Nanotechnology 19 (2008) 475502
[29] V. Panchal, K. Cedergren, R. Yakimova, A. Tzalenchuk, S. Kubatkin and O. Kazakova, Journal of Applied Physics 111 (2012) 07E509
[30] J. Moser, A. Barreiro and A. Bachtold, Applied Physics Letters 91 (2007) 3
[31] A. Baumgartner, T. Ihn, K. Ensslin, G. Papp, F. Peeters, K. Maranowski and A. Gossard, Physical Review B 74 (2006) 1-7

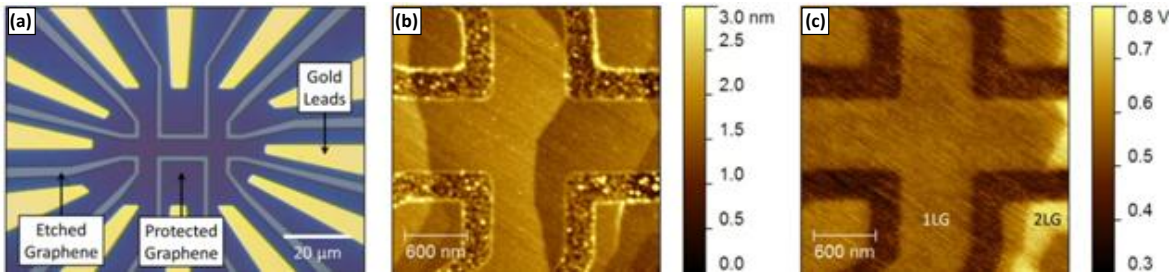

Figure 3.8: Epitaxial graphene devices. (a) *Optical image of a 5 μm device showing the gold leads and the patterned resist protecting the graphene.* ***(b)*** *Topography and* ***(c)*** *surface potential images of a 0.6-μm wide device.*

One-two layer epitaxial graphene was grown on the Si-terminated face of a nominally on-axis 4H-SiC(0001) substrate at 2000 °C and 1 bar argon gas pressure in a sublimation furnace. At high temperatures, the SiC crystal is decomposed layer by layer causing the silicon atoms to sublimate, leaving the carbon atoms behind to form the graphene honeycomb lattice. The resulting material is n-doped, owing to charge transfer from the interfacial layer. Further details on the fabrication and characterization have been reported [32]. Double-cross devices were defined in three steps, involving electron beam lithography, oxygen plasma etching and thermal deposition of Cr/Au electrical contacts (fig. 3.8.a). Prior to experiments, contact mode *AFM* was used to clean the devices of resist residues, as the resist is known to dope graphene and affect the transport properties [33,34].

Four different devices were used here, with the specifications shown in table 3.i. The sensitivity of the sensors, in the form of their *Hall* coefficient ($R_H = V_H/I_{bias}B$), was determined by sweeping a *DC* magnetic field and measuring the *Hall* voltage for variable bias currents. However, *MFM* probes generate inhomogeneous fields that are concentrated in relatively small areas, so that the largest devices may become inappropriate and yield noisier measurements.

Size (μm)	R_4 (kΩ)	R_H (Ω/T)	n_e (cm^{-2})	μ (cm^2/Vs)	B_{min} at I_{bias} = 60 μA (μT/√Hz)
0.6	29.5	296	2.1×10^{12}	803	4.9
1	33.6	838	7.5×10^{11}	998	3.7
10	22.7	715	8.7×10^{11}	170	3.7
15	26.2	1022	6.1×10^{11}	3124	1.3

Table 3.i: *Transport measurements for epitaxial graphene devices with a width of 0.6-15 μm. R_4 is the 4-point resistance, R_H is the Hall coefficient, n_e is the electron density, μ is electron mobility and B_{min} is the minimal detectable field.*

[32] C. Virojanadara, M. Syväjarvi, R. Yakimova, L. Johansson, A. Zakharov and T. Balasubramanian, Physical Review B 78 (2008) 1-6
[33] O. Kazakova, V. Panchal and T. Burnett, Crystals 3 (2013) 191–233
[34] S. Lara-Avila, K. Moth-Poulsen, R. Yakimova, T. Bjørnholm, V. Fal'ko, A. Tzalenchuk and S. Kubatkin, Advanced Materials 23 (2011) 878-882

In this work, the *MFM* probe acts as a scanning gate that modifies the transversal Hall voltage by means of its localized stray field. When scanning a *DC* current biased Hall sensor in the dynamic mode, an oscillating Lorentz force is exerted on the electrons that gives rise to an *AC* transverse voltage (fig. 3.9). This output signal (V_{XY}) is filtered with an external *lock-in* amplifier referenced to the actual oscillation frequency of the cantilever and recorded at each pixel. For doing so, the normal force signal detected by the photodiode of our microscope is fed into the external *lock-in* reference input. In addition to the magnetic interaction, there will most likely be a surface potential difference between the graphene layer and the tip apex. Therefore, as the probe scans, electrons are also subject to oscillating Coulomb forces. The response of the *Hall* sensor to the parasitic electric field indeed masks the magnetic field response, making accurate measurements of the magnetic signal difficult. However, these fields can be eliminated by enabling the *KPFM* feedback simultaneously, as will be shown later. Under these circumstances, the V_{XY} values measured with the external *lock-in* correspond to the transversal voltage amplitude induced by the tip during one oscillation cycle. In other words, it gives information about differences in the values of the stray field generated by the tip at two points: the closest and the furthest ones.

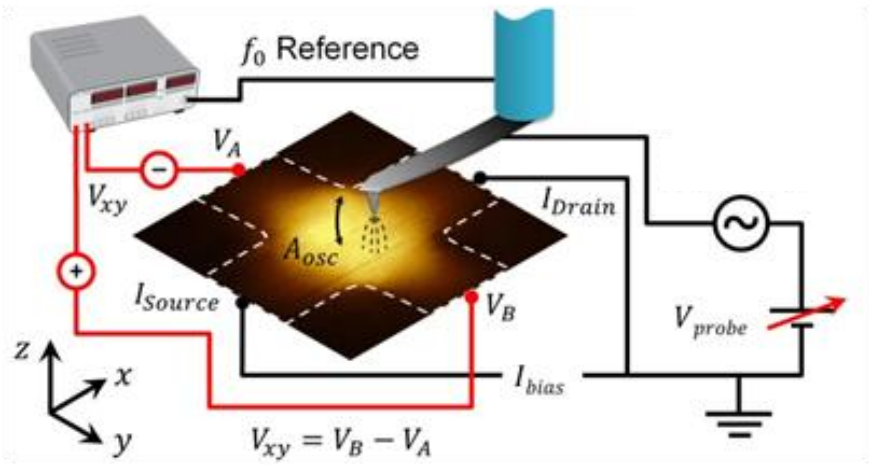

Figure 3.9: Schematics of the measurement set-up used in the experiments. *A transversal alternating voltage V_{XY} is induced by the tip in the graphene cross, consequence of Coulomb and Lorentz deviations of electrons, at the oscillation frequency. An external lock-in is used to extract the information.*

First, the case of a disabled *KPFM* feedback is considered. The response of graphene *Hall* device to the inhomogeneous fields generated by a homemade probe with a 20 nm thick Co coating, as a bias current of I_{bias}= +70 μA is driven across the 600 nm device, is displayed in figure 3.10.a. The dominating features in the V_{XY} map are peaks at the corners of the active sensing area. When the probe is gating above corners 1 & 3 (corners 2 & 4) of the sensor, the flow of electrons is diverted towards V_B (V_A), resulting in a rise (drop) in V_{XY}. The corner effect can thus be understood by considering electrostatic deflections of electrons, originating in the probe-sample capacitive

coupling. Analogous contrasts are also obtained when scanning these graphene devices with non-magnetic metallic probes, as was done with Pt/Ir coated probes. In essence, these features are identical to those observed in scanning gate microscopy experiments and are well documented [31,35].

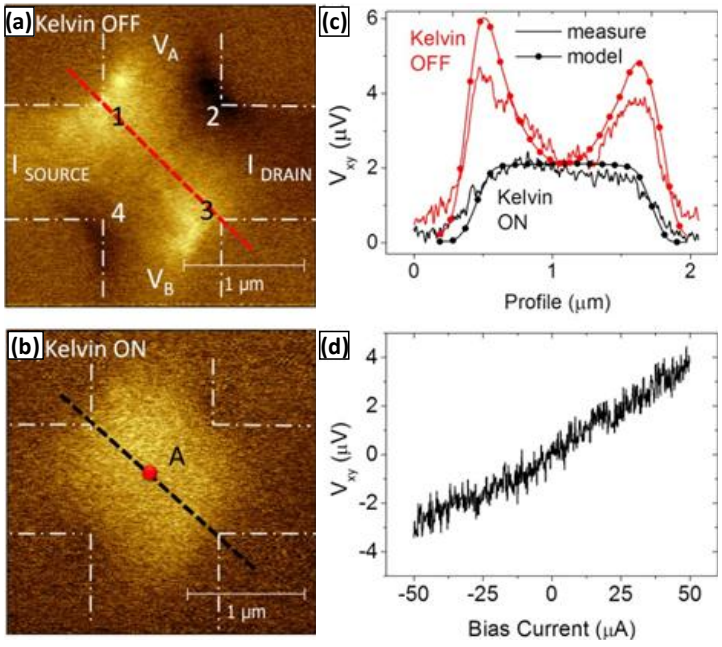

Figure 3.10: Hall voltage. *Experimental transverse Hall voltage images of the 600 nm wide device at I_{bias} = +70 µA, obtained with a 20 nm Co coated homemade probe with the KPFM feedback loop* ***(a)*** *disabled and* ***(b)*** *enabled. White lines outline the contour of the device.* ***(c)*** *Profiles obtained along the dashed lines as indicated in (a)-(b).* ***(d)*** *Dependence of V_{XY} on the biased current as measured at the device centre (point A in (b)). Measurements in (d) performed for a commercial MESP probe.*

When the current direction is reversed to +70 µA, the voltage polarity flips at the corners (fig. 3.11.a-d), as it also happens to the signal at the center of the cross (fig. 3.11.a and b). This effect is described in figures 3.11.e-h, where local deviations of electrons are sketched. In the case of a nullification of the probe-sample *CPD*, the V_{XY} response is a consequence of only the modulated magnetic stray field at the oscillation frequency. This is the case shown in figure 3.10.b, where the aforementioned features at the corners are suppressed and the remaining *Hall* voltage can be associated to *Lorentz* forces. The measured values of the *Hall* voltage are significantly smaller than in the previous case, as the magnetic contribution to the electron deflection is usually less intense.

The black profile in figure 3.10.c shows a maximum coupling to the probe stray field when the probe is located in the central region of the graphene cross, yielding a rather homogeneous value of V_{XY}. The *Hall* voltage measured under these circumstances is shown to increase linearly with the

[35] L. Folks, A. S. Troup, T. D. Boone, J. A. Katine, M. Nishioka, M. Grobis, G. J. Sullivan, A. Ikhlassi, M. Field and B. A. Gurney, Journal of Physics: Condensed Matter 21 (2009) 255802

biased current (fig. 3.10.d), the expected trend for *Lorentz* force driven voltages. The smooth change in the slope of V_{XY} observed as the tip approaches the device edges extends over distances larger than 500 nm, as seen in figure 3.10.c. As soon as the probe approaches the cross edge by around 250 nm, V_{XY} decays smoothly until it finally vanishes when the tip is located around 250 nm outside from the cross. This yields a way to estimate the effective radius of influence of different *MFM* probes, as it gives information about the effective area over which the stray field is able to deflect electrons to the lateral electrodes of the device.

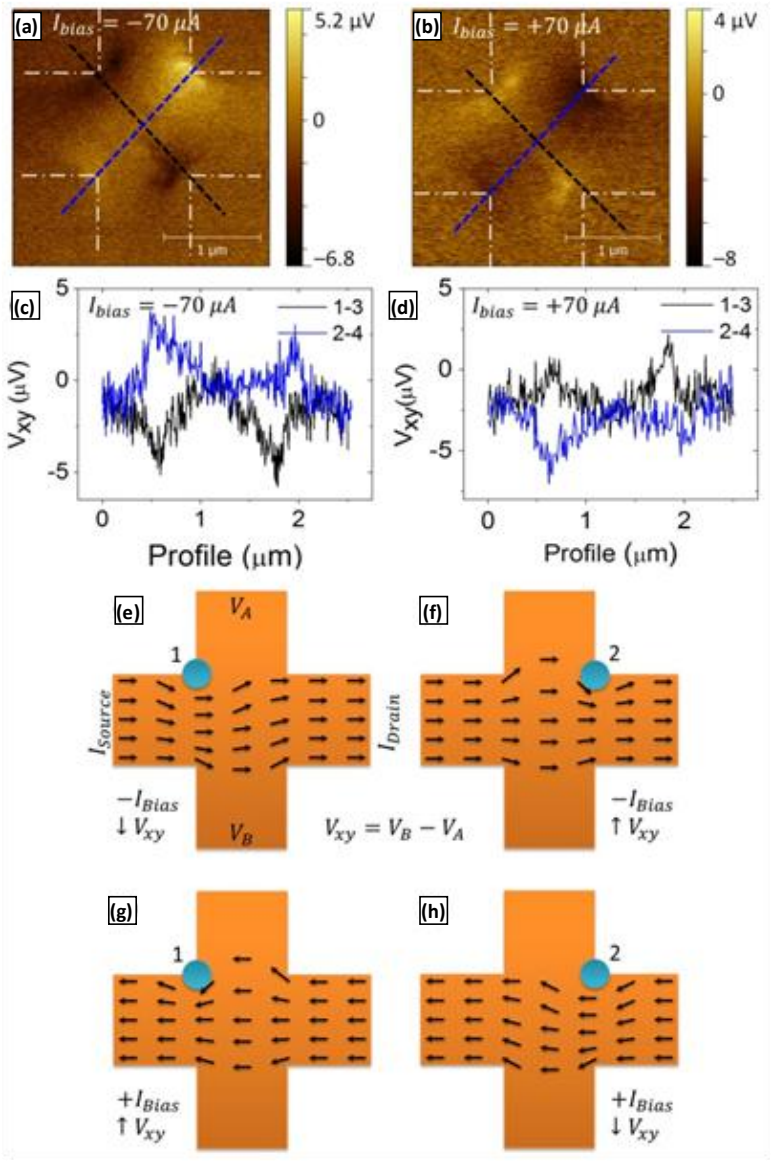

Figure 3.11: Effect of the bias current direction. *SGM mapping of the transverse voltage signal in the 600 nm wide graphene Hall cross with a bias current of* ***(a)*** I_{bias} *= –70 µA and* ***(b)*** *+70 µA. KPFM feedback loop was disabled. White lines outline the contour of the device.* ***(c)*** *and* ***(d)*** *Line profiles obtained along the dashed lines as indicated in (a) and (b), respectively. Schematic of the current distribution when the probe (*$V_{probe} < V_{sample}$*) locally gates at corners 1 and 2 at bias current of* ***(e)-(f)*** $I_{bias}<0$ *and* ***(g)-(h)*** $I_{bias} >0$*. The blue circle represents the location of the probe and arrows represent the flow of electrons.*

Investigations into the orientation of the probe magnetization can provide unambiguous proof of carriers being affected by the *Lorentz* force. The maps in figure 3.12.a-b, obtained with the *KPFM* feedback on, show the polarity of the signal on the device to reverse as the probe magnetization is switched by application of an external magnetic field. Small peaks at the corners of the *Hall* device – whose polarity remains unchanged when the magnetization of the tip is reversed – can be still observed, proving the separate nature of electrostatic and magnetic signals. We can thus conclude that the voltage measured using the *MFM-KPFM* combination is the response to the *Lorentz* force resulting from the probe stray magnetic field alone.

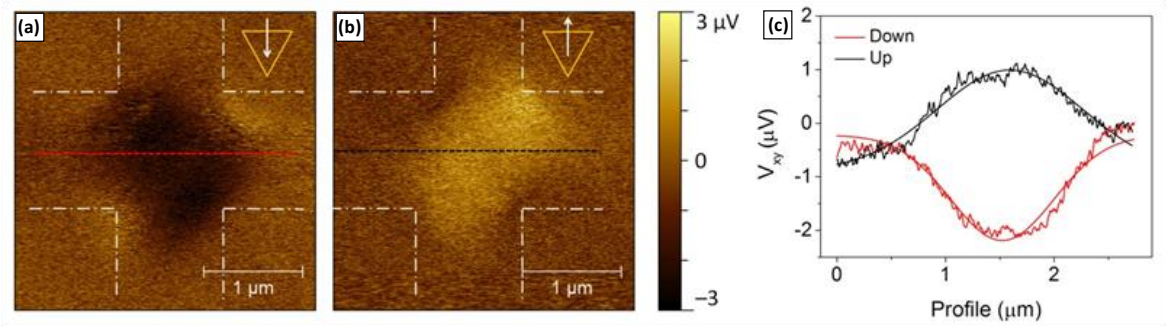

Figure 3.12: Effect of the probe magnetization. *SGM mapping of the transverse voltage signal in 0.6-µm wide Hall cross. Images were taken using a homemade probe magnetized* ***(a)*** *downwards and* ***(b)*** *upwards, with the KPFM feedback loop on. The bias current is* $I_{bias} = -70$ *µA.* ***(c)*** *Line profiles obtained along the dashed lines as shown in (a) and (b).*

Summarizing, in this chapter we demonstrated the successful and simultaneous implementation of *MFM-KPFM* measurements. We gave evidence of the relevance that charge accumulation effects may have when trying to identify the magnetic structure of certain samples and provided a ways to separate electrostatic from magnetostatic interactions, avoiding misinterpretation of data. By applying external fields, we obtained the real evolution of the magnetic states, whereas the *CPD* images remained unchanged. Last, a particular application for scanning gate microscopy is provided, in which graphene *Hall* sensors were used to estimate the stray field of *MFM* probes.

Chapter 4: Homemade *MFM* tips for specific purposes

As it has already been mentioned in different sections throughout this manuscript, homemade *MFM* sensors fabricated in our lab were used to characterize specific samples; this chapter describes the fabrication and characterization of such homemade probes. We will briefly compare their lateral resolution to that of commercial probes and, then, some additional examples of their usefulness for specific purposes will be presented. Last, micromagnetic simulations will show the field dependence on distance and the relevance of the apex geometry on the stray field. A report describing the performance of these probes is currently in preparation.

Conventional *MFM* probes consist of pyramid-like Si or SiN tips with a ferromagnetic thin film coating. Plenty of literature can be found where authors try to obtain enhanced resolutions by engineering probes. Several works focused on reducing the physical size of the magnetic material of the tip, either by using focused ion beam (*FIB*) milled tips [1,2], electron beam deposited tips [3,4] or stencil-deposited metal dots onto an *AFM* tip [5]. In another approach, probes with carbon nanotubes (*CNTs*) have been fabricated for *MFM* imaging either by mechanical attachment [6,7,8] or direct growth on commercial pyramid tips [9]. Although good control in terms of angle and position can be achieved when attaching *CNTs* to Si tips by using nanomanipulators [10], it requires sophisticated and time-consuming processes.

Other approaches used magnetic nanowires [11] or coated carbon nanocones [12] to improve the detection of small domains. In general, all these methods involve a considerable amount of time, effort and the use of advanced fabrication techniques for engineering the tips; in addition, the achievable resolution is not greatly enhanced compared to commercial tips so their applicability is limited to particular cases of interest.

[1] G. N. Phillips, M. Siekman, L. Abelmann and J. C. Lodder, Applied Physics Letters 81 (2002) 29
[2] L. Gao, L. P. Yue, T. Yokata, R. Skomski, S. H. Liou, H. Takahoshi, H. Saito and S. Ishio, IEEE Transactions on Magnetics 40 (2004) 2194
[3] G. D. Skidmore and E. D. Dahlberg, Applied Physics Letters 71 (1997) 3293
[4] Y. M. Lau, P. C. Chee, J. T. L. Thong and V. Ng, Journal of Vacuum Science and Technology A 20 (2002) 1295
[5] A. R. Champagne, A. J. Couture, F. Kuemmeth and D. C. Ralph, Applied Physics Letters 82 (2003) 1111
[6] N. Yoshida, M. Yasutake, T. Arie, S. Akita and Y. Nakayama, Japanese Journal of Applied Physics 1 41(2002) 5013
[7] H. Kuramochi, T. Uzumaki, M. Yasutake, A. Tanaka, H. Akinaga and H. Yokohama, Nanotechnology 16 (2005) 24
[8] A. Winkler, T. Mühl, S. Menzel, R. Kozhuharova-Koseva, S. Hampel, A. Leonhardt and B. Büchner, Journal of Applied Physics 99 (2006) 104905
[9] Z. Deng, E. Yenilmez, J. Leu, J. E. Hoffman, E. W. J. Straver, H. Dai and K. A. Moler, Applied Physics Letters 85 (2004) 6263
[10] W. Y. Song, K. Y. Jung, B.H. O and B. C. Park, Review of Scientific Instruments 76 (2005) 025107
[11] J. M. García-Martín, A. Thiaville, J. Miltat, T. Okuno, L. Vila and L. Piraux, Journal of Physics D: Applied Physics 37 (2004) 965-972
[12] I.-C. Chen, L.-H. Chen, A. Gapin, S. Jin, L. Yuan and S.-H. Liou, Nanotechnology 19 (2008) 075501

Intrinsically related to the lateral resolution is the magnetic sensitivity of the probe. In order to achieve better signal-to-noise ratios, one may want larger amounts of magnetic material to be deposited at the tip apex. Unfortunately, this results in larger tip radii and subsequent lower lateral resolution; furthermore, the influence in the sample magnetic state will be increased. Depending on the specific properties of each sample, a balance between resolution and sensitivity must be found. For this reason, different kinds of commercial *MFM* probes are available for sale. Specific low moment or side coated probes (having lower amounts of ferromagnetic material) can be found at the expense of an enhanced price over 50 €/probe. In addition, best lateral resolution is achieved with super-sharp tips at a cost over 100 €/probe.

The importance of choosing a proper tip is shown in figure 4.1, where two lithographed samples of $Ni_{80}Fe_{20}$ circular dots (25 nm thick and 1 μm in diameter) were imaged using commercial probes. A standard sensor (fig. 4.1.a) yielded *MFM* images with strong attractive contrast in the central regions of the dots, which was caused by reorientation of spins away from the sample plane due to the excessive stray field. On the other hand, a commercial low moment probe (fig. 4.1.b) displayed the real magnetic structure, with bright and dark points reflecting the core polarity of the single vortex states present in each dot. Notice the difference in the scale bars of both magnetic images.

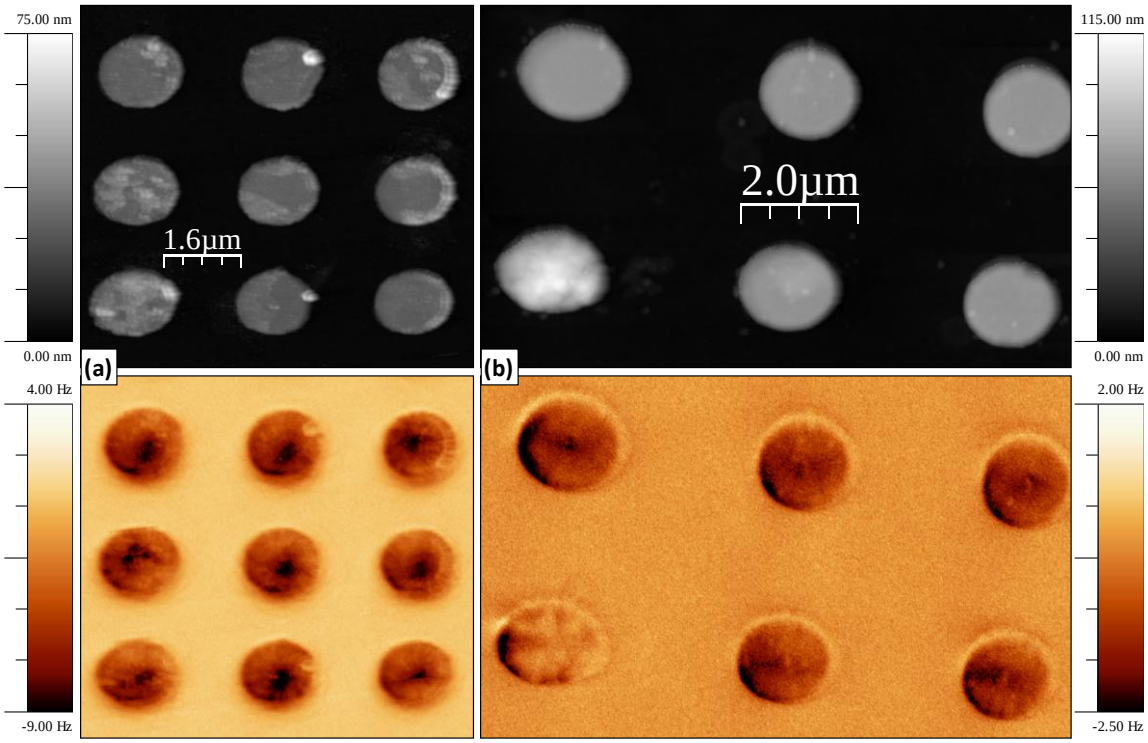

Figure 4.1: Influence of the stray field of MFM probes. *$Ni_{80}Fe_{20}$ circular dots 1 μm in diameter and 25 nm thick, measured using* ***(a)*** *a standard Nanosensors PPP-MFMR probe, where the magnetic state is modified due to the excessive stray field, and* ***(b)*** *a low moment Nanosensors PPP-LM-MFMR sensor, where single vortices with different polarities can be observed.*

Unfortunately, even the stray field emerging from these low moment commercial probes becomes too large for some samples and result in irreversible changes in their magnetic state. Our goal is to go a step further and be able to tune the tip used for each case, particularly regarding the irreversible influence of the stray field in soft magnetic samples. Therefore, this work is not focused on pushing the limits of *MFM* resolution; instead, we aim to fabricate customized tips with high lateral resolution and a reduced influence in the sample, in a fast and low cost way, in the order of 20-25 €/probe. As will be shown, both objectives have been achieved.

1. Fabrication and characterization

These homemade tips are fabricated by sputter-coating commercial *AFM* sensors (*Nanosensors PPP*) with a polycrystalline Co thin film, in a home-built high-vacuum chamber and with a specific incidence angle that allows covering up one side of the pyramid. The deposition parameters are carefully chosen to yield highly flat surfaces with small grain size, which ensures higher lateral resolutions for the *MFM* tips. A thorough study of the influence that these parameters have in the Co growth is described in *M. Jaafar*'s thesis [13], as well as a description of the experimental set-up. Starting from a base pressure of $5 \cdot 10^{-6}$ mbar, argon gas is introduced into the chamber until a pressure of $1.0 \cdot 10^{-2}$ mbar is reached. Inert gases are usually employed as the sputtering gas because they tend not to react with the target material and because of their high molecular weight that causes higher sputtering rates. Plasma is then generated using an *AC* magnetron sputtering with an input power of 100 W and is confined on the target surface by a permanent magnet located behind the target surface. Positively charged Ar^+ ions are accelerated toward the negatively biased 99.99 % pure Co target, resulting in material being sputtered and deposited onto the side walls of the tips.

Figure 4.2: Deposition of the magnetic coating. *Commercial AFM tips are sputter-coated with a polycrystalline Co film.*

[13] Doctoral thesis of Miriam Jaafar (Autonomous University of Madrid, 2009)

Sputtering is not a highly directional technique; nevertheless, there is a preferential direction of deposition. A residual magnetic film was observed to cover up most part of the tip and cantilever; however, calibration with *AFM* reveals this residual thickness to be less than 1 nm. Different thicknesses have been used, depending on the properties of the studied sample; however, we will focus here on the most commonly utilized ones: 20 nm and 25 nm.

No capping layer is subsequently deposited onto the Co film. Although the outtermost atomic layers of cobalt are well known to oxidize in ambient conditions, we believe this affects a very superficial region of the coating and the oxide does not avoid obtaining good imaging results. In fact, experiments performed on purpose four months after deposition revealed no measurable loose of sensitivity. Furthermore, as it was demonstrated in sections 3.2 and 3.3, these probes allow for *Kelvin Probe Force Microscopy* measurements even without deposition of a metallic capping film. It is worth pointing out that this methodology represents a fast, accessible and rather cheap process. A time lapse of around 1 hour is needed to reach the high vacuum conditions specified above. The plasma onset is instantaneous and the deposition step takes 1-2 minutes. Although we sputter coat few tips at the same time, tens of them might be placed in a region where the deposition rate can be considered to be homogeneous, within the small home built chamber at our disposal. In addition, very good reproducibility is found and the probes remain functional for months. One drawback they present is a slightly reduced lifetime against crashes onto the sample surface, probably due to the lower magnetic material present at the apex. However, similar effects have been observed using super sharp commercial probes as well.

Using these deposition conditions, a 20 nm thick Co layer was sputtered onto an *AFM* chip (*Nanosensors PPP*) and the resulting topography is shown in figures 4.3.a-c. The reason for imaging the chip is to get a realistic idea of the Co growth onto the silicon tip. A resulting flat surface with a root mean square (*RMS*) roughness of (0.25 ± 0.05) nm is obtained. The grain size, extracted from the autocorrelation function along the fast scan direction, is approximately 20 nm. These values were found not to change in great measure for the typical thicknesses used to coat the magnetic sensors.

The lower row of figure 4.3 describes the magnetic properties of the cobalt thin film. The *MFM* image in figure 4.3.d shows the as grown magnetic state of the metallic layer, where a predominant in-plane magnetization with *cross-tie* [14] domain walls is observed. The hysteresis loops (fig. 4.3.e), measured at room temperature by *VSM* under maximum applied fields of 1.7 T, confirm the preference for the magnetization to orient in the sample plane. A high remanent magnetization of

[14] A. Hubert and R. Schäfer, "Magnetic Domains" (Springer, Berlin 1998)

82% the saturation value is found in figure 4.3.e when the field is applied *IP*. This, together with the shape anisotropy taking place when the Co layer is deposited onto a sensing tip, helps the magnetic moments to remain mainly oriented along the pyramid surface. However, the orientation of the spins at the end of the tip will depend on the apex shape and on the way the cobalt layer covers it up. There is substantial variability in the apex shape from tip to tip, which is intrinsic to the fabrication methods. In addition, the normal angle at which cobalt reaches the surface can cause inhomogeneities in its thickness at the very end of the tip. Thus, knowing the exact configuration seems to be a hard task.

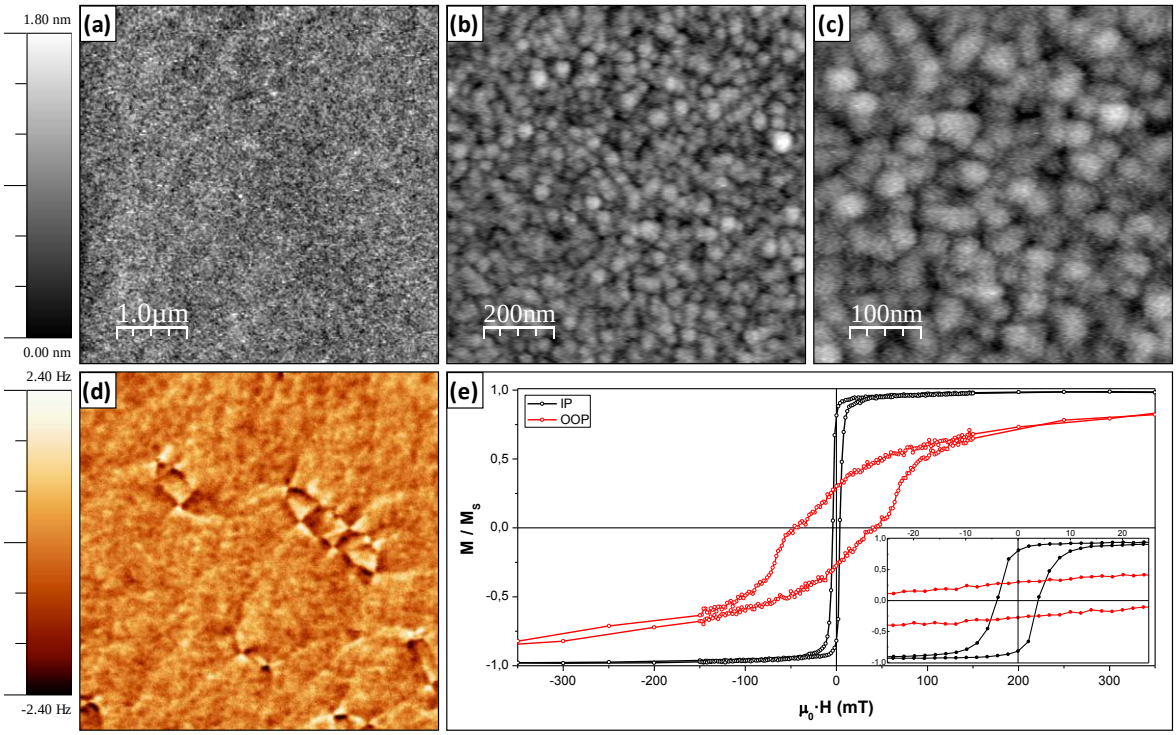

Figure 4.3: The cobalt coating. ***(a)*** *(5x5) µm², **(b)** (750x750) nm² and **(c)** (375x375) nm² topographic images of a 20 nm thick Co layer grown onto an AFM chip (Nanosensors PPP) under the conditions used for coating the tip. **(d)** (5x5) µm² MFM image of the same sample, showing a predominant IP magnetization with the presence of cross-tie domain walls. **(e)** In-plane (IP) and out-of-plane (OOP) hysteresis loops show the preference of the magnetization to remain IP.*

After deposition, the resulting home-coated *MFM* probes were characterized with a standard hard disk, using the *3D modes* explained in chapter 2.2. As sketched in figure 4.4.a, a hard disk is mapped and conventional topographic and *MFM* images are first obtained (fig. 4.4.b). Then, the slow scan direction is disabled; instead, an external *OOP* field is swept after each fast scan. The resulting $\Delta f(X,H)$ map shows a reversal in the magnetic contrast, which is attributed to a flip in the magnetization of the tip and is used to quantify its switching field (fig. 4.4.c-d). A transition regime is often observed close before the switching field, in which a poorly defined contrast can be seen. This is caused by local rotation of spins at the very end of the probe and depends on the relative

angle between the cantilever and the sample surface. Interesting effects associated to this reorientation of the magnetic moments at the apex will be studied in chapter 5.

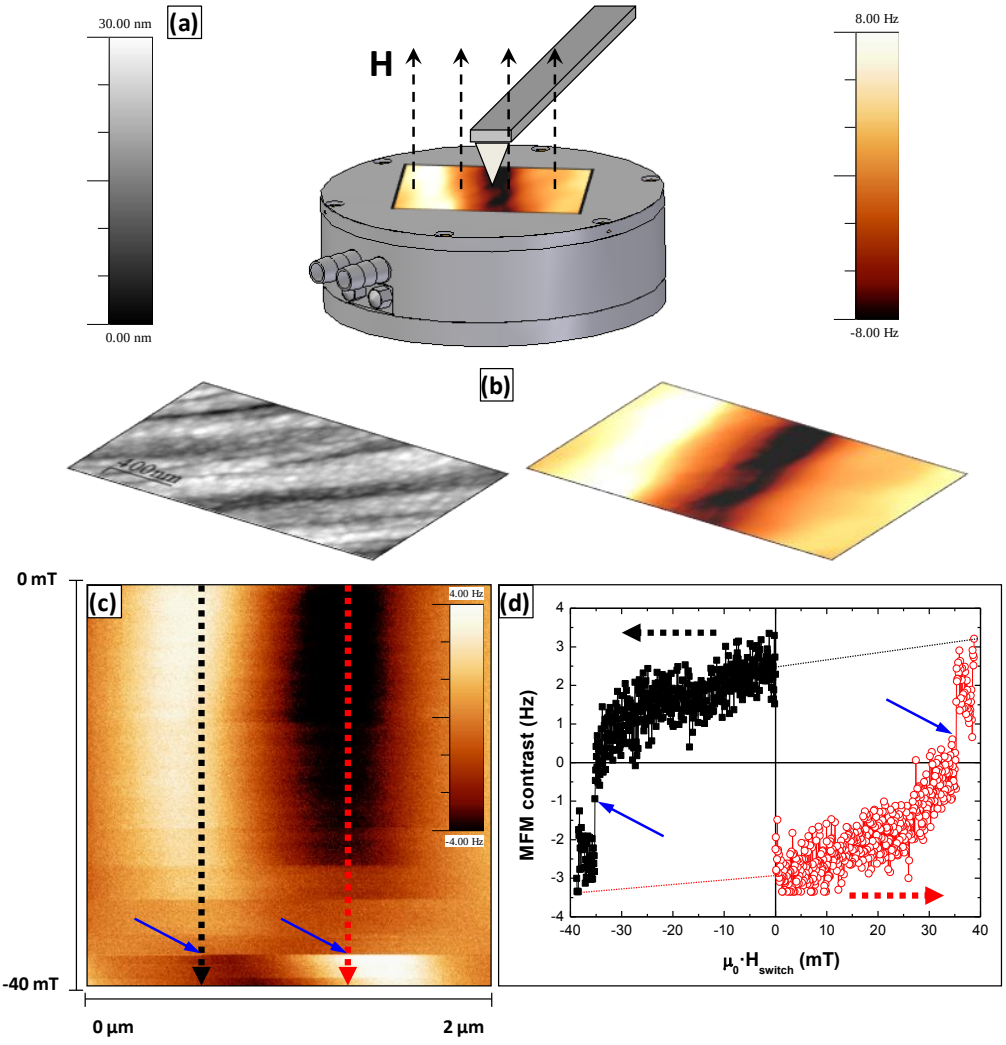

Figure 4.4: Switching field of MFM tips. ***(a)*** *Applying OOP fields with an electromagnetic,* ***(b)*** *topographic and MFM images are obtained.* ***(c)*** *Using the 3D modes, a contrast inversion reflects the switching field of the probe.* ***(d)*** *Evolution of the contrast in the 3D mode image for two regions with opposite stray field polarities.* ***Note****: the red profile in (d) has been shifted to positive fields for practical purposes. No smoothing has been applied to data.*

Using this approach, the extracted mean switching field for 20 nm thick tips (from a total of 30 measurements including three different homemade probes) yields $\mu_0 \cdot \bar{H}_{switch} = (31 \pm 4)\, mT$. This value is similar to those for commercial probes [13] and allows for reliable *MFM* measurements in a wide range of applied fields. A significant variability is observed, which can be attributed to several factors. First, the interaction with a magnetic sample is used to extract this useful parameter of the probes. Repeating the same experiment at different tip-sample distances alters the influence that the sample stray field has in the apex. In addition, even if the same parameters are used (oscillation amplitude and tip-sample separation), dissimilar regions of the sample will influence

the sensor in a different manner. As it was already mentioned, the relative tip-sample angle turns out to play its role as well. Former factors can be controlled to some extent. However, although a good reproducibility has been achieved, the resulting coating at the tip apex varies slightly from tip to tip. Nevertheless, eventual changes are expected to take place in the tip geometry and composition during the realization of the experiments the tips are intended for. Thus, we believe this reported variability in the switching field value not to be particularly relevant.

2. Lateral resolution

In this section, we present a comparison of the *MFM* lateral resolution between the homemade sensors presented above and three different sorts of commercial probes. The first one is a low cost model, *BudgetSensors Multi75M*, whose price is comparable to the estimated cost of our homemade ones. However, they lack good resolution and are then suitable for testing experiments or samples with domains hundreds of nanometers in size. The second one, *Nanosensors PPP-LM-MFMR*, has a reduced amount of magnetic coating on it and is appropriate for relatively soft samples (see fig. 4.1.b). They show an improved performance, as compared to previous tips, but their cost is significantly increased. The third option is the so-called "super sharp" *MFM* tips, *Nanosensors SSS-MFMR*, which are specific for performing high resolution magnetic force microscopy measurements. However, their price is twice as high as for the second kind of tips.

For these experiments, a very high density hard disk with perpendicular anisotropy was used, based on a CoCrPt alloy and courtesy of *Toshiba*. The domain size in it is around 25 nm. Three brand new probes of each kind were chosen and standard *MFM* images were measured with an oscillation amplitude of 14 nm at a retrace distance of 15 nm from the topographic setpoint. The best results obtained for each case are shown in figure 4.5. In the last row, data from a homemade probe with a layer thickness of 25 nm are shown. Having a look at the column on the left, where (2x2) μm^2 images are displayed, the lower resolution of both the *Multi75M* and *Nanosensors PPP-LM-MFMR* probes is readily seen. On the contrary, the super-sharp tips seem to have a similar performance. Even more evident becomes the difference with the two first kinds when the image size is decreased down to (500x500) nm^2, as seen on the right column. In the case of *Multi75M*, only large domains – composed of large series of neighboring domains with parallel magnetization – are resolved (fig. 4.5.a). Using *Nanosensors PPP-LM-MFMR* tips, quite better results are obtained (fig. 4.5.b) but the lateral resolution is far from being enough to resolve individual domains. In agreement with its label name, the super sharp tips yield the best resolved images of all commercial probes (fig. 4.5.c). Nevertheless, at least as good results are obtained with the homemade sensors, as observed in figure 4.5.d. Very good lateral resolution is achieved and domains are resolved.

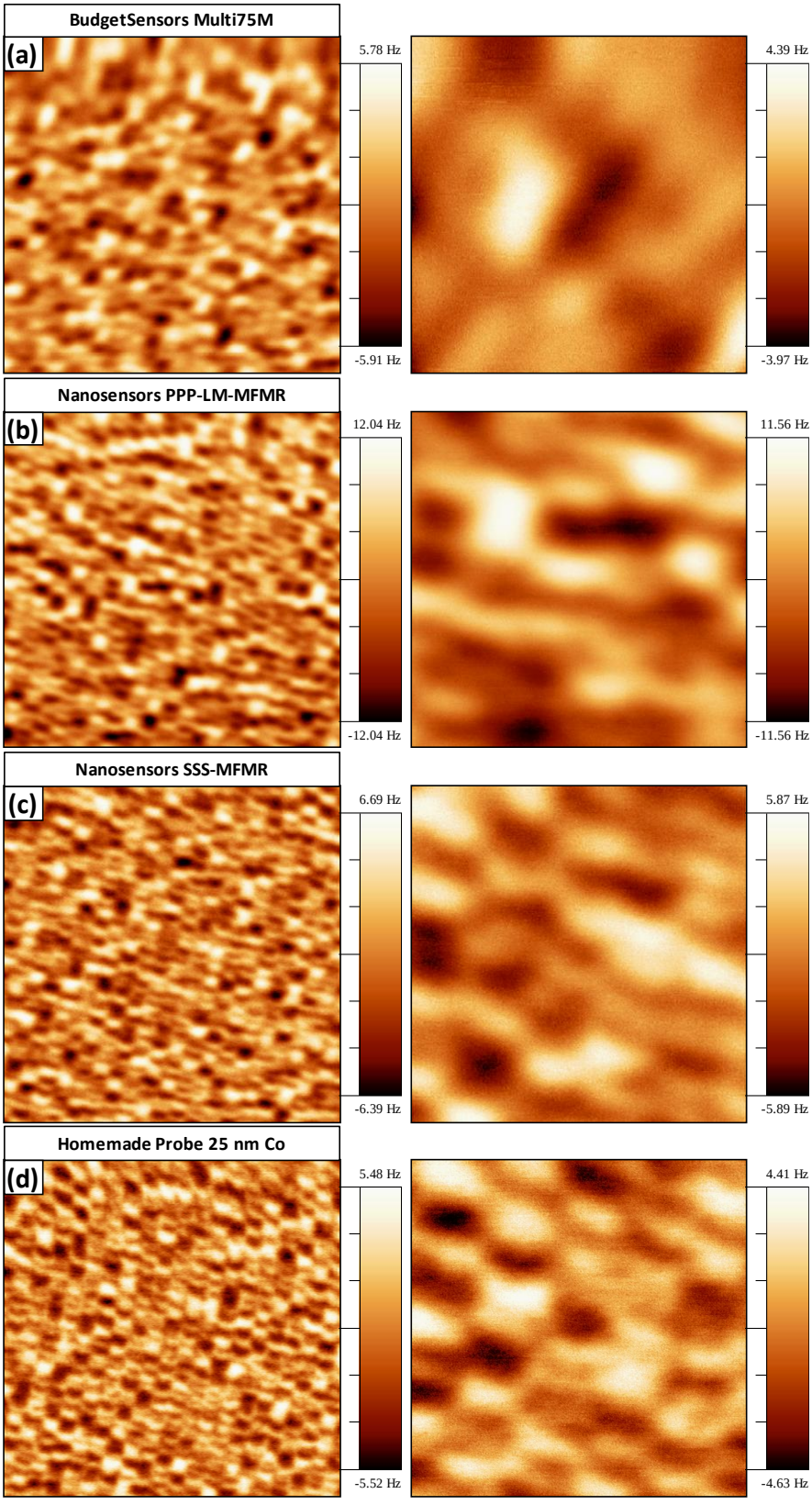

Figure 4.5: The comparison. *Lateral resolution obtained with* ***(a)*** *BudgetSensors Multi75M,* ***(b)*** *Nanosensors PPP-LM-MFMR,* ***(c)*** *Nanosensors SSS-MFMR and* ***(d)*** *homemade tips with a 25 nm thick Co coating on the front sides. Images on both columns are the same size: (2x2)* μm^2 *(left) and (0.5x0.5)* μm^2 *(right).*

Depending on the sample features, one might need to even further increase the lateral resolution. This could be achieved by reducing the cobalt thickness deposited onto the *AFM* tips, at the expense of reducing their magnetic sensitivity. Figure 4.6 displays *MFM* images of the same hard disk with a homemade tip having a 20 nm thick coating. As can be seen in figure 4.6.d, domains are perfectly resolved. It is important to note that pictures taken with different probes correspond to different regions of the same hard disk. In particular, the ones obtained with the 20 nm thick coating describe an area of the disk where domains have alternating orientations (i.e. a region where no information is recorded), whereas in the other cases groups of neighboring domains with parallel orientations are common, indicating that some information is stored there.

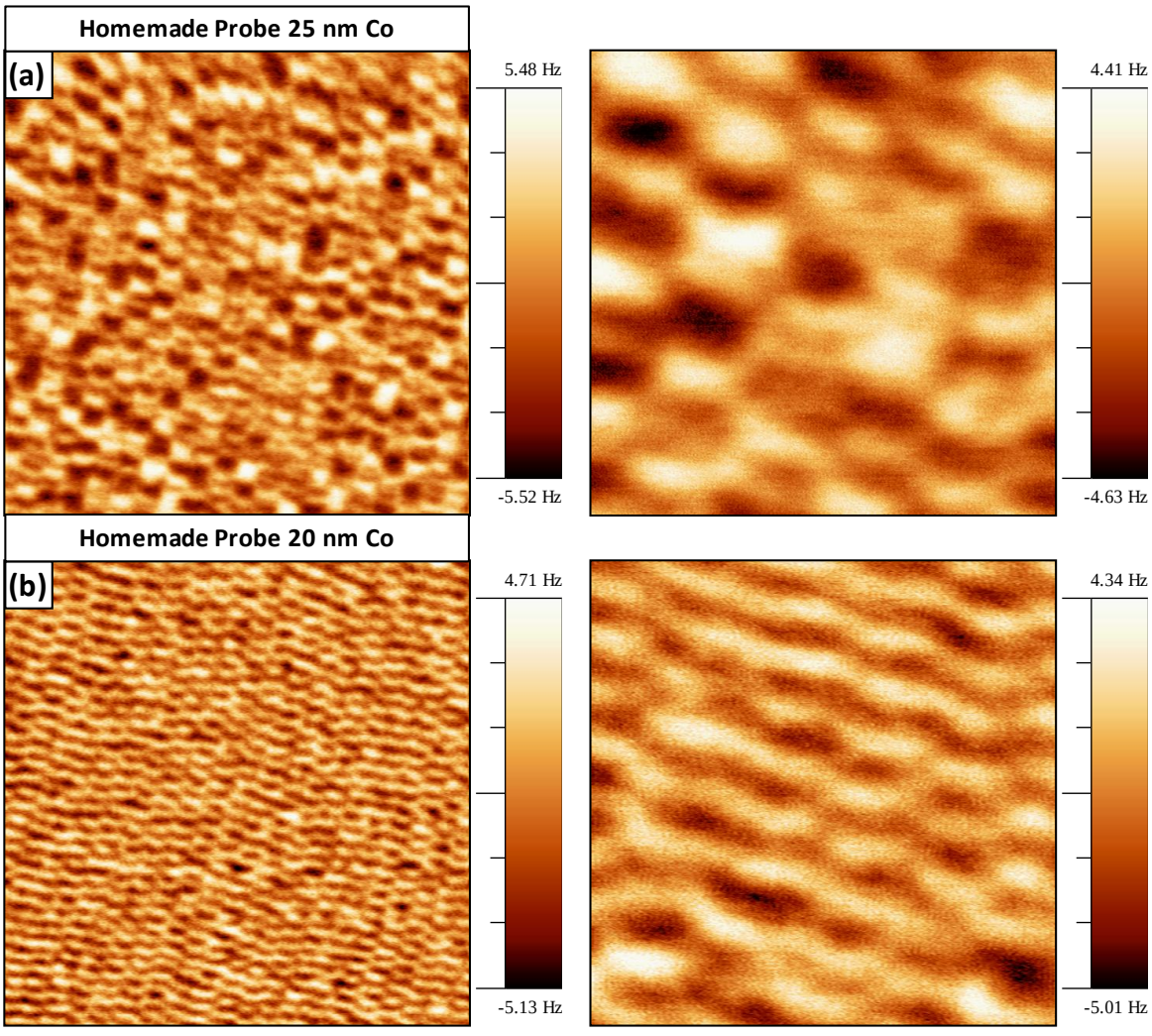

Figure 4.6: The 20 nm cobalt tip. *MFM images of the same high density HD, recorded with homemade probes with* ***(a)*** *a 25 nm thick Co coating and* ***(b)*** *a 20 nm Co coating. Images on both columns are the same size: (2x2)* μm^2 *(left) and (0.5x0.5)* μm^2 *(right).*

A latter proof of the lateral resolution of this 20 nm thick coated *MFM* tip is shown in figure 4.7. There, a high resolution topographic image of the hard disk surface displays grains in the order of 10 nm in lateral size, a remarkable resolution even for standard *AFM* probes (fig. 4.7.a). Its corresponding *MFM* image shows a series of bright and dark contrasts associated to successive magnetic domains with *OOP* magnetization (fig. 4.7.b). The frequency shift along the profile drawn in the *MFM* image is displayed in figure 4.7.c and proves the distance between domains to be around 25 nm. No smoothing has been applied to the profile data. The price one has to pay to reach such a high lateral resolution is a lower magnetic sensitivity. In the case shown in figure 4.7, the magnetostatic interaction between the tip and the hard disk is large enough to ensure *MFM* experiments of specific low moment samples are feasible with that tip. However, this is not always the case and lower sensitivities are sometimes obtained.

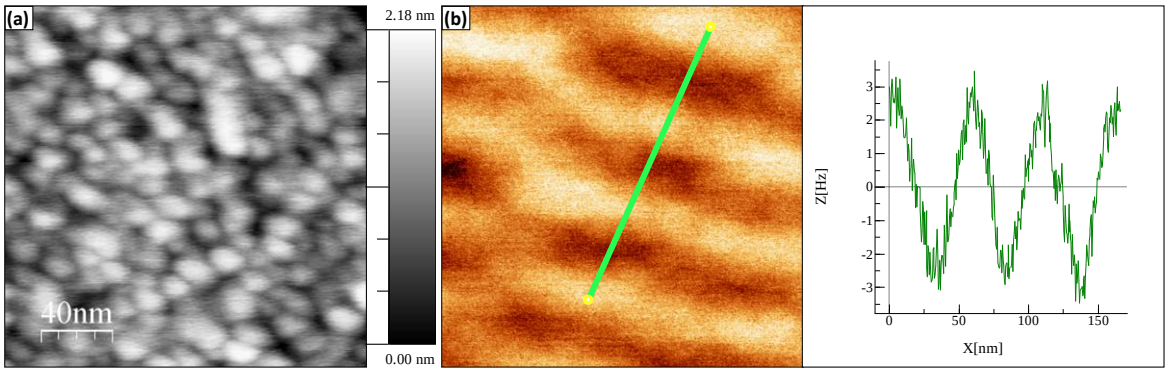

Figure 4.7: The spatial resolution. (a) *Topography of the high density HD, recorded with a 20 nm homemade tip. The lateral resolution is around 10 nm.* ***(b)*** *Corresponding MFM image showing single domains with alternating OOP orientations.* ***(c)*** *Frequency shift profile along the line shown in (b) that gives an inter-domain distance of ~ 25 nm.*

3. Experimental examples

Succesful applications of the *MFM* sensors described in this chapter have already been shown in sections 2.2, 2.4, 3.2 and 3.3, the latter two proving their capability to separate electrostatics from magnetostatics using the *MFM-KPFM* combination. In addition to them, two practical examples are given below, where both a remarkable lateral resolution and low magnetic disturbance are achieved. In the first one, more detail is given about the *DW*s present in the Co stripes described in section 2.4. In addition, images are shown that achieve chemical sensitivity with an outstanding lateral resolution of 5 nm. The second example tries to give an idea of the reduced stray field associated to these probes. A metastable state is studied in polycrystalline cobalt circular dots, where two vortices mediate the magnetization reversal process. This work is part of a collaboration with Dr. *Farkhad Aliev*, from the *Universidad Autónoma de Madrid*.

Study of domain walls in Co stripes with competing anisotropies

As was mentioned in chapter 2.4, previous works found in the literature on nanostripes with perpendicular anisotropy lack good resolution and no information about the domain walls can be inferred. Being able to resolve the *DW* structure unveils the processes involved in the magnetization reversal. This has been accomplished by using a 20 nm home-coated tip.

We already reported the different domain structures present in these stripes. In addition, the magnetization reversal mechanism taking place was thoroughly described for the particular case of the 750 nm wide stripe, where single vortex *DWs* mediated the process (see figure 2.31 for more details). The good performance shown by the homemade sensors described here led us to study in more detail the structure of the domain walls. For the case of the stripe just mentioned, high resolution *MFM* images were taken and are presented in the bottom row of figure 4.8. In the remanent configuration, two single vortex *DWs* are placed very close to each other and remain quite the same for small field variations (fig. 4.8.a-b). As the field increases further, the vortex in the lowermost *DW* moves from the right side of the stripe (fig. 4.8.b) to the left one (fig. 4.8.c) and subsequent contrast inversion takes place along the wall. The observance of a contrast reversal in a *DW* is a proof of its vortex character. Interestingly, even although the other domain wall annihilated during the process and is not present anymore, the remaining one is located at the same position.

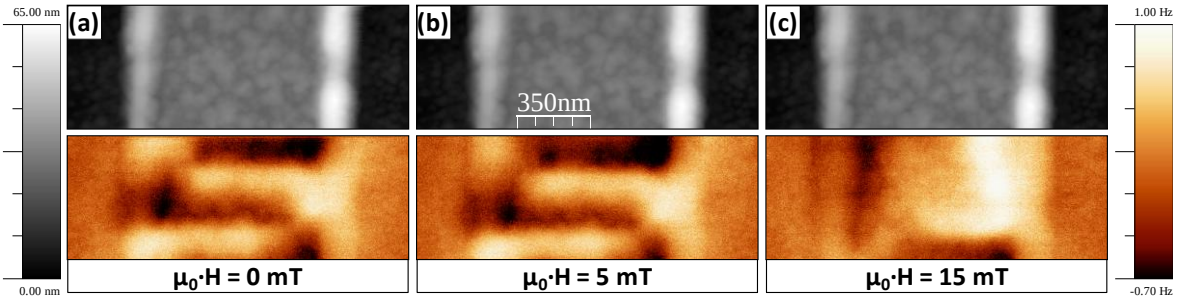

***Figure 4.8: Domain wall ripple**. **(top)** Topographic and **(bottom)** MFM images of the 750 nm wide epitaxial Co stripe. A ripple structure with a period of around 130 nm can be observed in the single vortex DWs.*

The resolution of the magnetic images is such that domain wall corrugations become even noticeable in figures 4.8.a-b. Instead of showing a straight shape, those walls describe a wavy path that is resolved in the experimental images, from which a periodicity of around 130 nm is estimated. We believe this domain wall ripple to minimize the total energy of the system and to arise from the internal structure of the cobalt layer.

In addition to this beautiful result, we studied the *DWs* present in slightly wider stripes. Figure 4.9 displays images of three different walls present in the 850 nm wide stripe in its remanent configuration, after saturation along the main axis. A more complex configuration seems to be present, as compared to the single vortex walls described so far. At first sight, these three *DWs* do not seem to be of the same kind; however, by taking a careful look it is possible to infer the same spin configuration in each one of them.

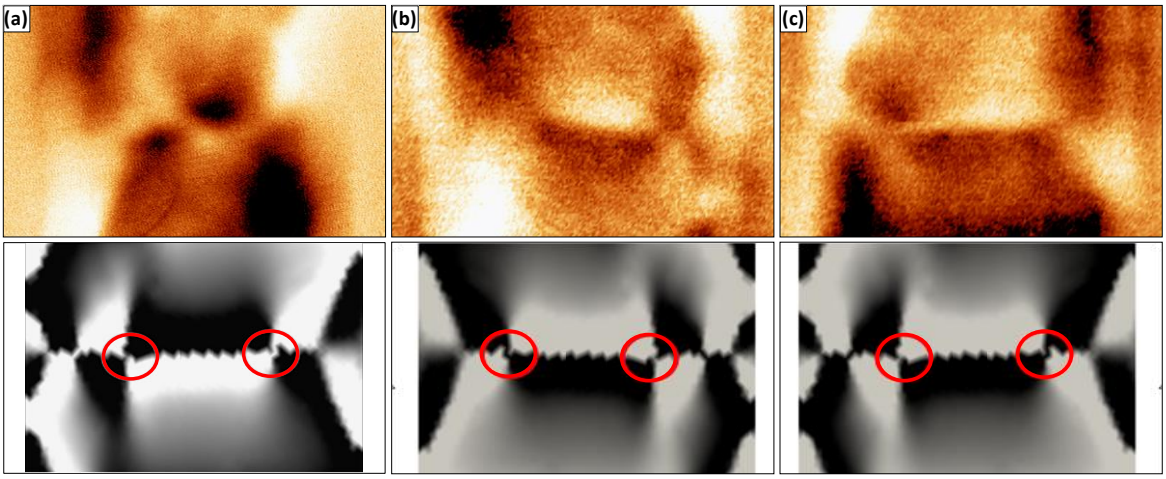

***Figure 4.9. Double vortex walls in Co stripes**. (top) High-resolution MFM images of the 850 nm wide stripe, at remanence, and (bottom) simulated images, showing DWs with two vortices at the position indicated with red circles.*

Further insight into the spin distribution within the *DWs* is provided by micromagnetic simulations. The contrast observed in the simulated images shown in figure 4.9 reproduces experimental data to a good extent. Relevant information we extract from them is the existence of two vortices within the walls, whose location is highlighted with red circles. Thus, we suggest the cross-like regions observed in the experimental images to arise from the presence of two vortices.

As is demonstrated in figure 4.10, two different kinds of *DWs* are simultaneously present in the same stripe, formed by either one or two vortices. No evident correlation seems to exist between the two kinds and both appeared repeatedly along the nanostructure. In general, for stripes of similar widths and for a large range of fields around remanence, single and double vortices *DWs* are formed. Resolving the micromagnetic structure present in these stripes opens up the possibility of using simulations to get a closer idea about the mechanisms involved. Thus, the effort made in developing sensors that allow for achieving very well defined images has translated into added information one can extract from conventional *MFM* measurements.

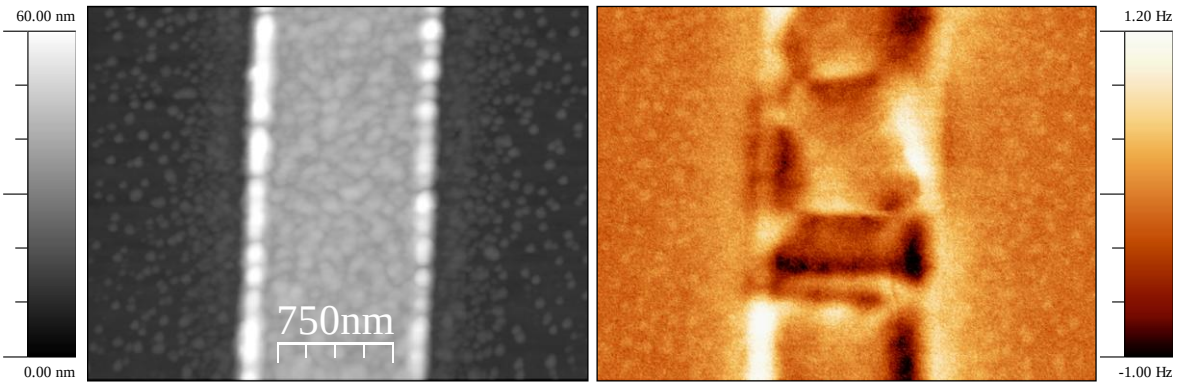

Figure 4.10: Two kinds of DWs at the same time. *In this MFM image of the 850 nm wide element, it is possible to see single and double vortex walls in the remanent state.*

Having shown the capability of these sensing tips to study the magnetic properties of samples, we will now give another brief example regarding their chemical sensitivity. During the topographic scan, strong Δf variations are often observed, a good example of which is exhibited in figure 4.11. According to the famous *Cleveland*'s formula (refer to chapter 5 for further information), if one assumes both the *PLL* and the topographic feedbacks to work ideally, figures 4.11.b and e yield a map of the energy dissipation during the experiment. In general, different materials are expected to interact and dissipate energy in different ways so these images might be interpreted as compositional maps. Different materials seem to be present: the cobalt forming the stripe, the silicon substrate and grains of an adsorbed material on top of the cobalt.

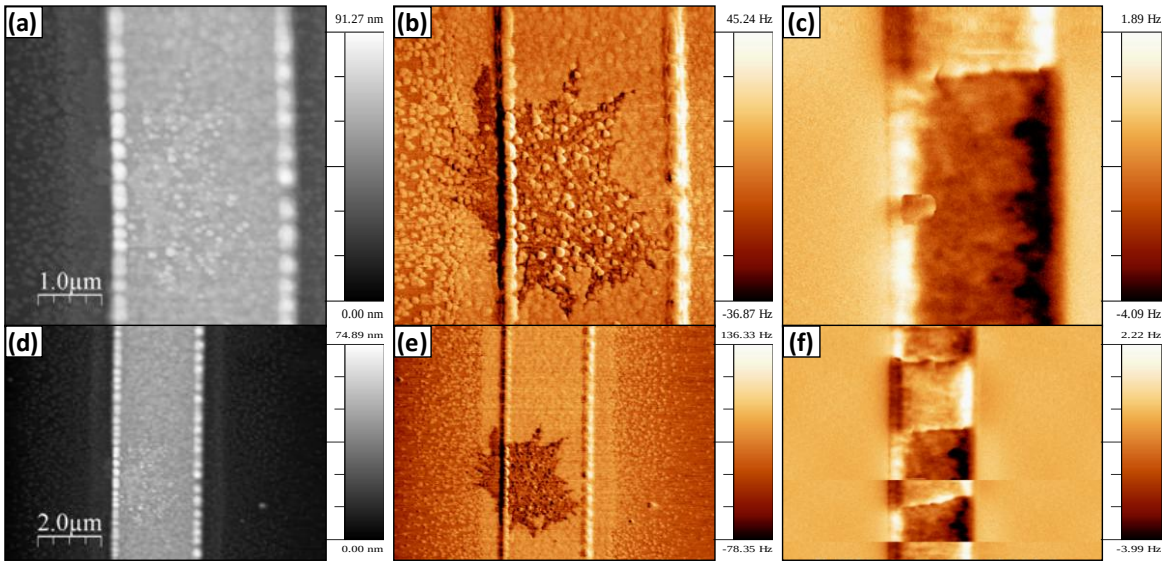

Figure 4.11: Chemical sensitivity. *Material sensitivity of the homemade tips when measuring the cobalt stripe 1.6 µm wide described in section 2.4.* ***(a) & (d)*** *Topography and the corresponding* ***(b) & (e)*** *frequency shift maps during the same scan.* ***(c) & (f)*** *MFM images of the same region.*

A well defined dark stain covering a big part of the magnetic stripe is present in figures 4.11.b and e. Its origin could be the presence of a different material adsorbed on the cobalt or even underneath; the fact that the stain does not extend over the substrate seems to indicate that the unexpected substance was adsorbed after the sample fabrication. Less repulsive force gradients originate from the tip-stain interaction, as compared to the interaction with the remaining materials present in the sample. In this sense, chemical sensitivity can be achieved with a high lateral resolution. Eventual charging and electrostatic effects are unlikely, as no relevant frequency shifts are recorded during the retrace scan (figure 4.11.c, f). Notice that, apart from a series of higher grains, no remarkable feature is observed within the stain region in the topographic images. Fortunately, this accidental adsorption does not have any influence in the magnetic behavior of the sample, as is deduced from the *MFM* images.

An additional example of the 350 nm wide stripe is provided in figure 4.12. Taking a look at the frequency shift map obtained this time during the topographic scan (fig. 4.12.b), two features stand out. The first one is the lateral resolution achieved; the second one is the sensitivity to discern between the different materials present in the sample. The outstanding detail of this image becomes even more evident when zooming in, as is shown in figure 4.12.d. There, a grain as small as 5 nm is resolved and yields a frequency variation of 190 Hz compared to the surrounding region. This requires the *PLL* to apply a voltage of 1.95 V – in order to track the resonance frequency of the cantilever – over a noise level of around 5 mV, representing a signal-to-noise ratio of around 400 for such a tiny particle.

Although remarkable as well, the corresponding magnified topography lacks such outstanding detailed information (fig. 4.12.c). Thus, higher resolution seems to be achievable through the dissipation map; this issue will be further discussed in chapter 5. It is important to note that figure 4.12.b and d show raw data without manipulation. In addition, we recall that experiments were carried out in ambient conditions.

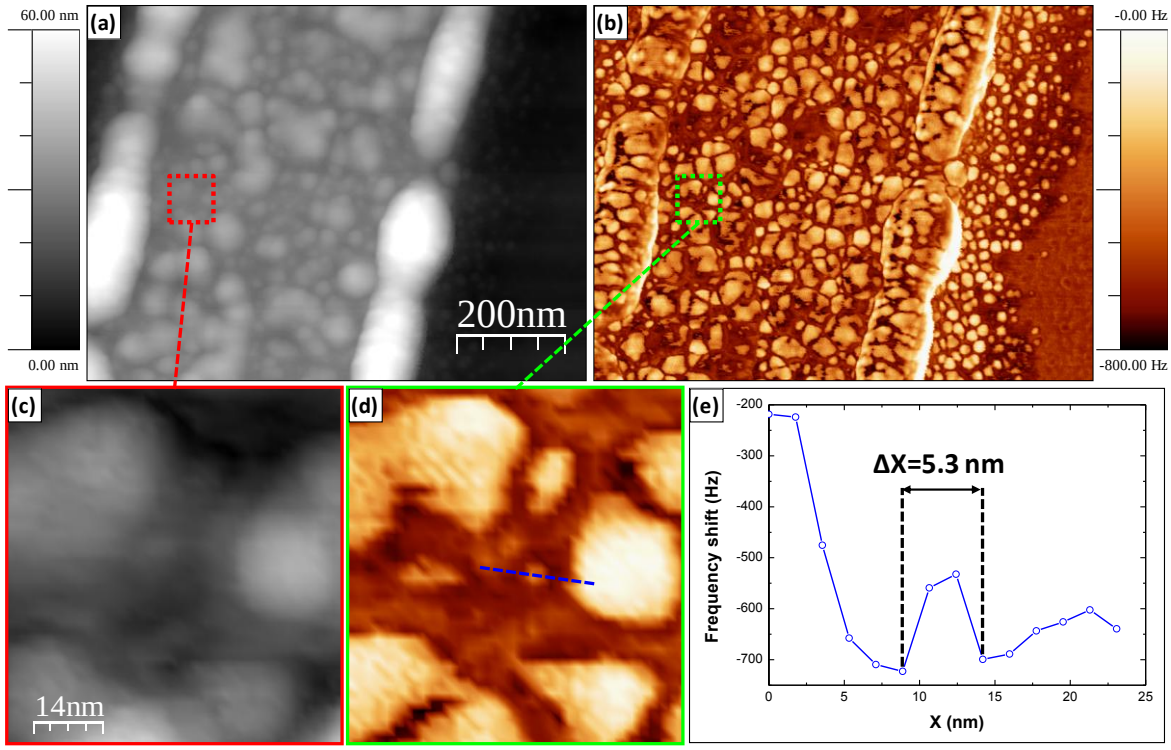

Figure 4.12: Lateral resolution in chemical sensing. (a) *Topography and* ***(b)*** *frequency shift images of the 350 nm wide stripe (see section 2.4) recorded during the topographic scan.* ***(c)*** *&* ***(d)*** *Magnified images of the framed regions in (a) & (b), respectively.* ***(e)*** *Profile drawn in (d), where a peak around 5 nm in width yields a signal-to-noise ratio of 400.*

Observation of magnetic vortices in Co circular dots

In this second brief example, we study the formation of vortices in square arrays of circular Co dots that were fabricated by electron beam lithography (*EBL*) and lift-off techniques. The polycrystalline dots are 20 nm thick and 1 μm in diameter and their separation distance is 1 μm. This collaboration gave rise to a paper published during the first year of my thesis [15] and a second one is currently in preparation [16].

Even although magnetic vortices were theoretically predicted long time ago [14,17], the vortex core was not experimentally observed until quite recent magnetic force microscopy [18] and spin polarized tunneling microscopy [19] measurements. The interest in this particular spin configuration arises from the possibility of its implementation as a key element in a new type of high density storage media [20]

[15] F. G. Aliev, D. Dieleman, A. A. Awad, A. Asenjo, **O. Iglesias-Freire**, M. García-Hernández and V. Methlushko, Proceedings – 12th International Conference on Electromagnetics in Advanced Applications (2010), 160-163
[16] **Ó. Iglesias-Freire**, A. A. Awad, V. Methlushko, F. G. Aliev and A. Asenjo (*in preparation*)
[17] C. Kittel, Review of Modern Physics 21 (1949) 541
[18] T. Shinjo, T. Okuno, R. Hassdorf, K. Shigeto and T. Ono, Science 289 (2000) 930-932
[19] A. Wachowiak, J. Wiebe, M. Bode, O. Pietzsch, M. Morgenstern and R. Wiesendanger, Science 298 (2002) 577
[20] S. Bader, Review of Modern Physics 78 (2006) 1

and the introduction of vortices in spin polarized current driven spintronic devices such as vortex based spin torque oscillators [21], as well as its possible implantation in logic operation devices [22]. Although a single vortex configuration has already been shown in the equilibrium state of figure 4.1.b, some experimental and theoretical works [23,24,25] report on the possibility of having an intermediate double vortex configuration in circular magnetic dots, for a wide range of fields between saturation and the single vortex state.

Initial attempts to measure this sample with low moment commercial probes were unsuccessful. After trying with homemade tips of different thicknesses, the best results were found for the 20 nm thick coating. In order to support the idea of having two vortices, micromagnetic simulations were used to simulate the reversal process in a cylindrical nanostructure 1035 nm in diameter and 20 nm in thickness, using a cubic cell size of (5x5x5) nm^3. On the way from saturation, they predict the formation of a double vortex structure, in which both vortices interact with each other and describe a correlated movement with both an azymuthal and radial components.

As usual when dealing with lithographed samples, the effects of the resist used during the patterning process can be observed in the topographic image shown in figure 4.13. Nevertheless, dots with well defined circular shapes are in general seen. The resulting *MFM* measurements under the influence of an *IP* magnetic field, as well as the simulated images obtained with *OOMMF*, are also presented in the same figure. The experiment shows a beautiful domain structure, in which a leaf-like contour line defines the frontiers between regions with different spin orientations (red arrows have been plotted in two of the simulated images to help with the interpretation). They can be interpreted as hybrids between Néel and vortex domain walls, in which the magnetization remains in the sample plane with the exception of the singularities at the vortex cores.

The two vortices (highlighted with red circles in the first simulated image) have opposite chiralities and evolve in a synchronous way describing trajectories that seem to be correlated to each other. In the first *MFM* image of the sequence, both vortices have recently nucleated and their cores are located at the center of the cross-like contrasts present in the top-left and bottom-right regions of the dot. As the field is swept, both cores move along the edges of the leaf-like feature to the opposite side of the dot in a symmetric way. During this reversal process, the leaf-like feature in the center gets wider and distorted, so that vortices do not annihilate at the exact opposite points

[21] V. S. Pribiag, I. N. Krivorotov, G. D. Fuchs, P. M. Branganca, O. Ozatay, J. C. Sankey, D. C. Ralph and R. A. Buhrman, Nature Physics 3 (2007) 498-503
[22] R. P. Cowburn and M. E. Welland, Science 287 (2000) 1466
[23] T. Pokhil, D. Song and J. Nowak, Journal of Applied Physics 87 (2000) 6319
[24] I. L. Prejbeanu, M. Natali, L. D. Buda, U. Ebels, A. Lebib, Y. Chen and K. Ounadjela, Journal of Applied Physics 91 (2002) 7343
[25] C. A. F. Vaz, M. Kläui, L. J. Heyderman, C. David, F. Nolting and J. A. C. Bland, Physical Review B 72 (2005) 224426

from where they nucleated. Finally, they approach the edge of the nanostructure and annihilate, leaving the main component of the *IP* magnetization along the vertical direction and reversed from the initial situation. Notice the outstanding agreement observed between the experiment and simulations. Not only the leaf-like feature is experimentally observed but also evolution of the vortices position is predicted.

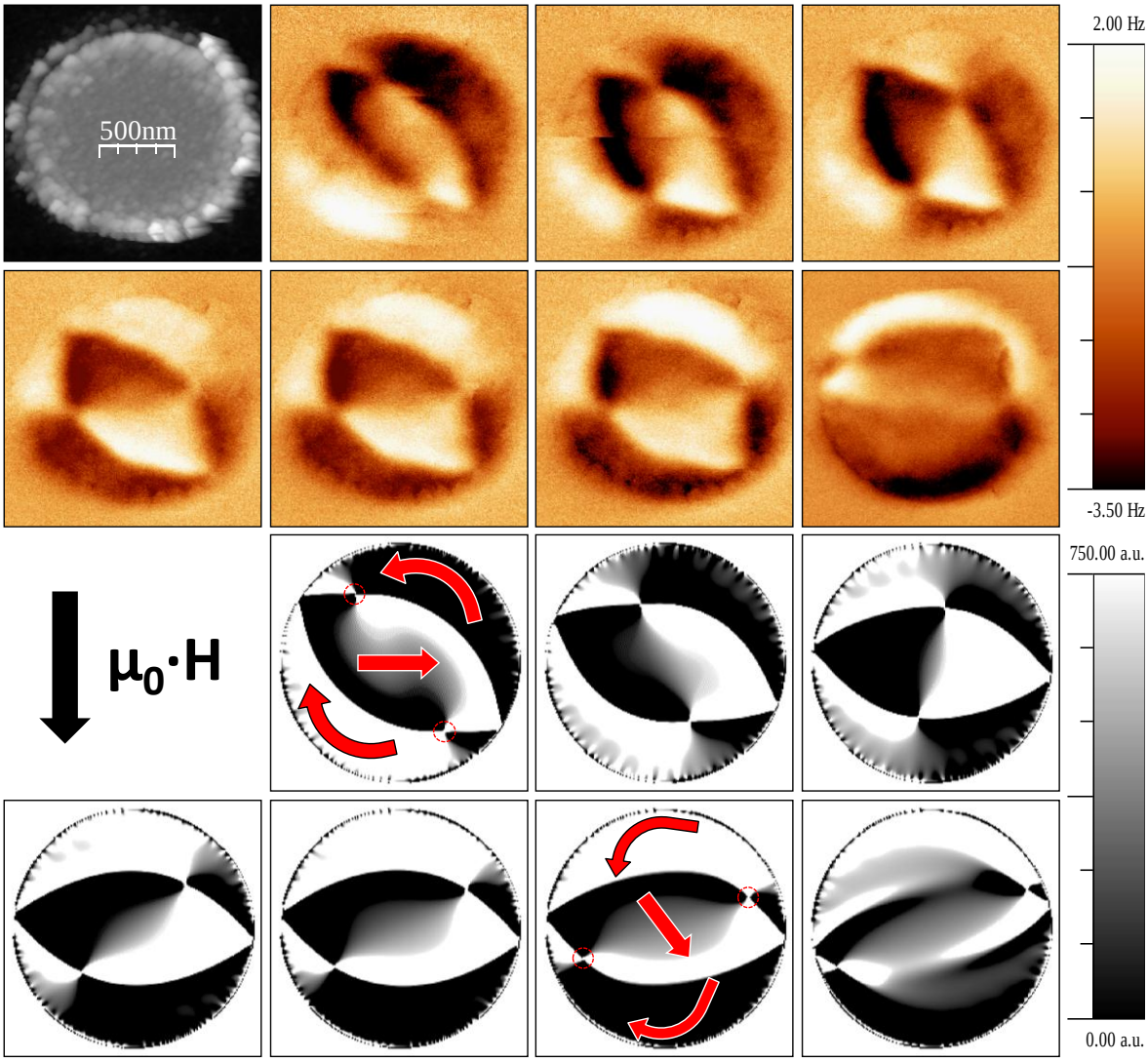

Figure 4.13: The double vortex state. *Topography, MFM images and dynamic simulated states of a cobalt dot 1 μm in diameter and 20 nm thick, taken under an IP field along the vertical direction. The field sequence in the MFM maps was: -5 mT, 0 mT, +3 mT (upper row), +5 mT, +7 mT, +10 mT and +20 mT (lower row), after negative saturation.*

Again, simulations prove to be a helpful tool for the interpretation of *MFM* images. This reversal process has already been reported [24] and the authors were able to successfully describe the mechanism involved. For doing so, experiments were done scanning the tip at height distances of 100-200 nm, resulting in low resolution images that are presented highly equalized to sharpen the domain boundaries. In another report [23], authors claims to have recorded the reversal process of

single and double vortex states by means of *MFM* in $Ni_{80}Fe_{20}$ circular dots of variable thicknesses; however, none of them is actually achieved since the stray field of the tip in their experiments is too strong and induces rotation of spins in the soft sample. A study on tip-induced *MFM* artifacts will be described later in section 5.3.

In our case, it was possible to obtain simultaneously topographic and magnetic maps of this metastable state with a remarkable detail, even when the vortices were located close to the morphological edges. The reduced influence of our sensing tips allowed tracking the topographic profile and obtaining *MFM* images at a lift height of 30 nm over the tip-sample distance used during the topographic scan, resulting in a considerable enhanced definition in the magnetic images reported in figure 4.13. Thus, a combination of reduced influence and high resolution has been achieved while studying a sample that is very sensitive to external perturbations.

4. Micromagnetic simulations

With the idea of getting a general overview of the sensors described in this chapter, *3D* simulations were carried out to estimate their stray field and are briefly discussed here. The ferromagnetic coating in most commercial *MFM* probes is usually deposited onto the whole tip, whereas only one side is mainly covered in our case. Therefore, two different geometries were designed for the simulations: the first one consists of a hollow cone with a 16 nm thin wall and a semi-angle of 10 º (fig. 4.14.a), whereas the second one corresponds to a half of the former region (fig. 4.14.b).

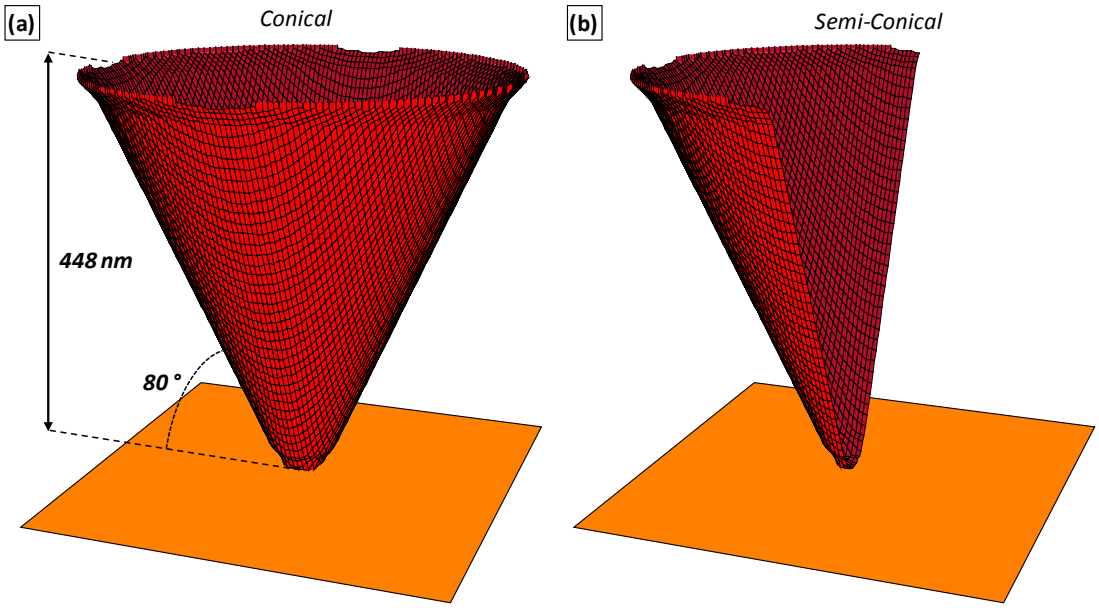

Figure 4.14: The simulated tips. *View of the simulated* ***(a)*** *conical and a* ***(b)*** *semi-conical tips.*

A spherical apex with a 16 nm radius was defined at the end of the nanostructures and made to join the conical region in a continuous way. This radius is a bit larger than the nominal value (≈ 10 nm) given by the manufacturer of the *AFM* probes, onto which the magnetic coating is deposited. The final thickness is 16 nm in both cases and the standard parameters for polycrystalline cobalt were used (M_S=1.4·10^6 A/m, k_1=0 and A=3·10^{-13} J/m). Due to computing restrictions, only the last 448 nm of the sensing tip were simulated, with a cell size of (2 x 2 x 4) nm^3, and an additional empty volume 60 nm in height was included below the apex. In order to account for the influence of the remaining part of the tip that is not considered here, a boundary condition was introduced that defines a magnetic field B_z=1 T applied to those cells in the uppermost layer of figure 4.14, in which magnetic material is present. This bounding value does not affect other regions of space, apart from those spins at the border of the tips.

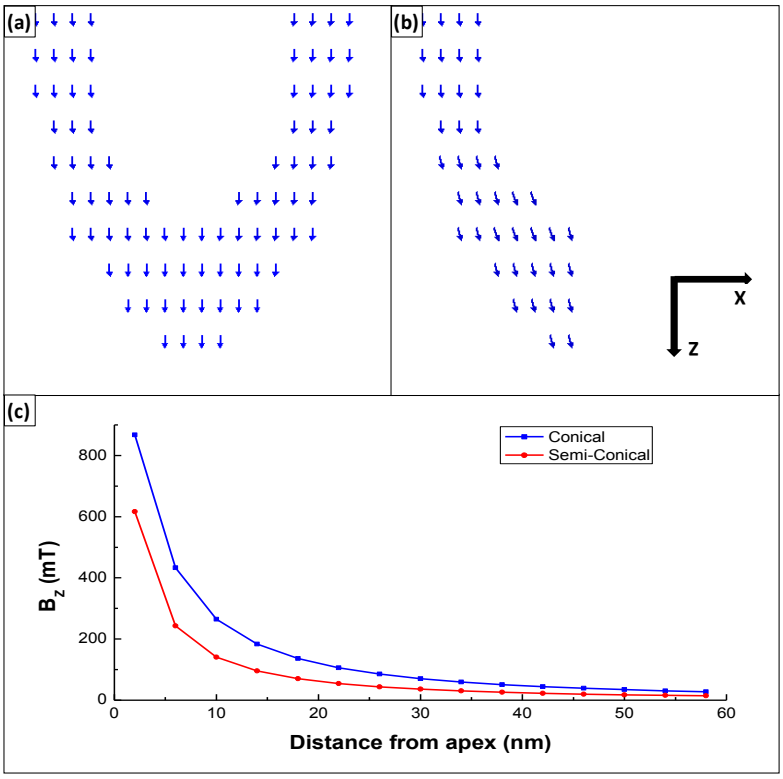

***Figure 4.15: The remanent state**. Orientation of spins in the remanent state at the apex of **(a)** the conical and **(b)** the semi-conical tips. **(c)** Simulated decay of the axial component of the stray field for both tips, as a function of distance.*

After saturating the tips along the axial direction, the field was switched off and the most stable distribution of the magnetization was obtained. Then, the remanent stray fields emerging from both tips were calculated in the empty volume up to distances of 60 nm from the apex. In both cases, the magnetic moments at the apex have a predominant *OOP* component, as can be seen in figures 4.15.a and b. The *OOP* component of the field is often considered crucial as it can irreversibly modify the magnetic state of the measured sample. Figure 2.15.c shows the decay with distance of

the *OOP* stray fields of both probes. A significantly stronger axial field is generated by the conical probe, which can be attributed to the larger amount of magnetic materials present in the tip.

The *IP* component can also be relevant depending on the domain structure, a good example of which is the vortex configuration – much more sensitive to *IP* fields. A comparison between the spatial distributions of B_X is shown in figure 4.16, corresponding to a separation distance of 20 nm from the apex. The tip apex is located at the center of the *XY* plane and the same color bar has been used for both cases, making it easier to compare them. Again, lower field values are attributed to the semi-conical probe.

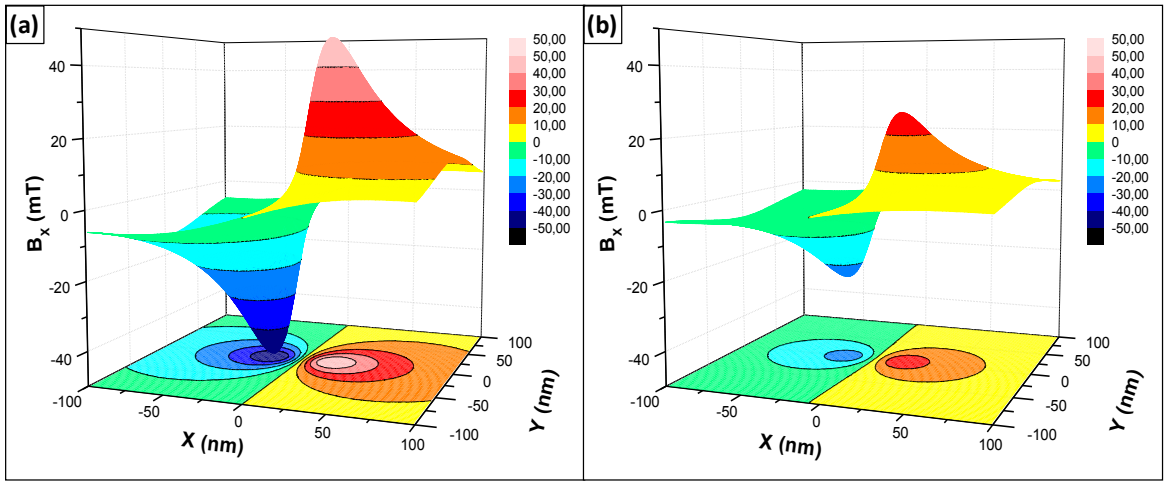

Figure 4.16: The X component. *Isometric view of B_X at a separation distance of 20 nm from the tip apex, for* ***(a)*** *the conical and* ***(b)*** *the semi-conical probes. The apex is placed in the origin of the XY plane.*

Nevertheless, in order to account for the total *IP* component of the field, the modulus $B_{IP}=(B_X^2+B_Y^2)^{1/2}$ must be considered. This is shown in figure 4.17 in separate columns for each geometry, again at a separation distance of 20 nm. The maximum *IP* fields are reached at points not right below the tip apex but displaced laterally around 20 nm from the tip position. A radial symmetry is observed for the conical shape, which in turn suggests that the use of cubic cells does not introduce relevant errors in the results (fig. 4.17.a).

On the contrary, an asymmetric field originates from the semi-conical sensor, with the highest values reached at the opposite side of the magnetic coating (fig. 4.17.b). Note that, as sketched in figure 4.15.b, the magnetic material is present in the region of space where $X<0$. As can be observed by zooming-in on the central region of the map (fig. 4.17.d), the points of lowest *IP* field are not located right below the apex position; instead, they are displaced by a few nanometers to the side where the magnetic coating covers the *AFM* probe.

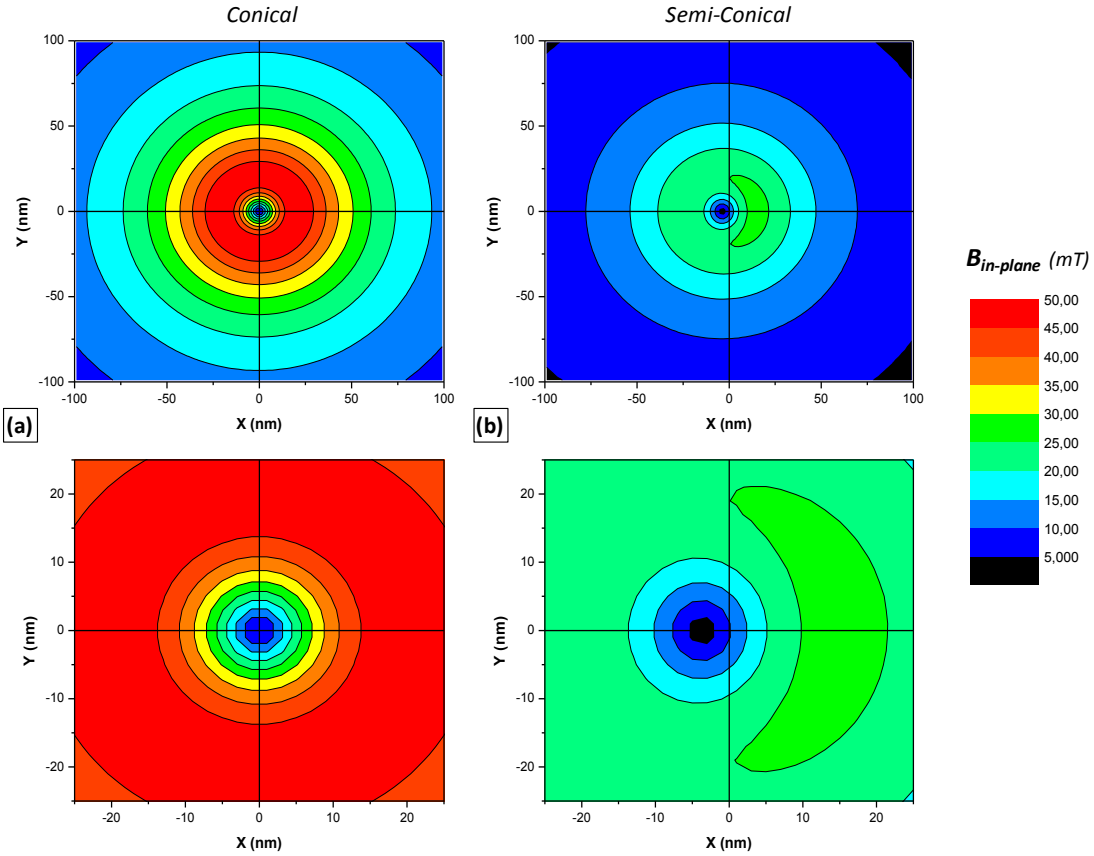

Figure 4.17: The IP component. *Color map of the IP component of the stray field coming out from the* ***(a)*** *conical and* ***(b)*** *semi-conical, at a distance of 20 nm.*

Thus, with these brief calculations we showed that, given a fixed deposition of ferromagnetic material, semi-conical geometries interact in a reduced way with the sample. In addition, spins at the apex of this semi-conical like *MFM* probes are predicted (and indeed observed) to be more sensitive to external perturbations, making them good candidates for the study of magnetic dissipation, as will be discussed next in the following chapter. The asymmetry found with this half coated probes is not considered to be relevant, since spins at the apex have a predominant *OOP* component. Thus, *MFM* measurements reflect mainly the *Z* component of the magnetization.

As conclusions, in this chapter we described the fabrication and characterization of homemade *MFM* sensors, using a fast and low cost method that allows us tuning the probe to the sample characteristics. A remarkable lateral resolution, both topographic and magnetic, is achieved. In addition, a reduced stray field was demonstrated by measuring the evolution of a double-vortex state in Co dots, while tracking the topography during the measurement. Enhanced chemical sensitivity is also shown for the case of Co stripes, in which a resolution of 5 nm is reached with a signal-to-noise ration of 400. Last, micromagnetic simulations suggest half coated probes to generate a reduced stray field, as compared to fully coated tips of the same thickness.

Chapter 5: Extracting useful information from magnetic dissipation

Measuring dissipation in scanning force microscopy relies on extracting physical information from either tip or sample by recording variations in the cantilever oscillation. In general, non-conservative interactions give rise to a decrease in the oscillation amplitude of the lever, as some energy is transferred in every oscillation cycle into dissipative processes. The first demonstration of dissipation experiments was reported by *Denk* and *Pohl* [1], who analyzed the resonance of an oscillating cantilever with a metallic tip in electrostatic interaction with a heterostructured semiconducting sample. In that experiment, the cantilever oscillation was damped by *Joule* dissipation of charge carriers, which were moved by the oscillating electric field produced by the tip vibration, an effect that was already commented in chapter 3. The authors pointed out that the damping deduced from the resonance analysis could also be obtained from the excitation amplitude needed to maintain a constant oscillation amplitude.

In general terms, there can be multiple causes for this dissipation of energy such as electron tunnelling [2,3,4], non-contact friction [5] or atom rearrangements induced by short range interactions between tip and sample [6,7,8]. Atomic resolution has also been obtained in dissipation experiments with non-contact dynamic force microscopy, the first report of them studying the Si(111) 7x7 surface [9]. Quantitative dissipation measurements generally show a large variation, in some cases not even agreeing on the relative magnitude [10,11]. The accuracy and reliability of these results is controversial, as extensive studies have shown that spurious instrumental artifacts might be present during the experiment performance [12,13].

[1] W. Denk and D. W. Pohl, Applied Physics Letters 59 (1991) 2171
[2] L. Cockins, Y. Miyahara, S. D. Bennett, A. A. Clerk, S. Studenikin, P. Poole, A. Sachrajda and P. Grütter, Proceedings of the National Academy of Science 107 (2010) 9496-9501
[3] S. D. Bennett, L. Cockins, Y. Miyahara, P. Grütter and A. A. Clerk, Physical Review Letters 104 (2010) 017203
[4] L. Cockins, Y. Miyahara, S. D. Bennett, A. A. Clerk and P. Grütter, Nano Letters (2012) 709-713
[5] M. Kisiel, E. Gnecco, U. Gysin, L. Marot, S. Rast and E. Meyer, Nature Materials 10 (2011) 119-122
[6] N. Oyabu, P. Pou, Y. Sugimoto, P. Jelinek, M. Abe, S. Morita, R. Pérez and Ó. Custance, Physical Review Letters 96 (2006) 106101
[7] H. J. Hug and A. Baratoff, Noncontact Atomic Force Microscopy, edited by S. Morita, R. Wiesendanger and E. Meyer (Springer-Verlag, Berlin, 2002), p. 395
[8] S. Alireza Ghasemi, S. Goedecker, A. Baratoff. T. Lenosky, E. Meyer and H. J. Hug, Physical Review Letters 100 (2008) 236106
[9] R. Lüthi, E. Meyer, M. Bammerlin, A. Baratoff, L. Howald, C. Gerber and H-J. Güntherodt, Surface Review Letters 4 (1997) 1025
[10] L. Nony, A. Baratoff, D. Schär, O. Pfeiffer, A. Wetzel and E. Meyer, Physical Review B 74 (2006) 235439
[11] G. Langewisch, H. Fuchs and A. Schirmeisen, Nanotechnology 21 (2010) 345703
[12] A. Labuda, K. Kobayashi, D. Kiracofe, K. Suzuki, P. H. Grütter and H. Yamada, AIP Advances 1 (2011) 022136
[13] A. Labuda, Y. Miyahara, L. Cockins and P. H. Grütter, Physical Review B 84 (2011) 125433

In particular, dissipation in magnetic force microscopy has been studied by few groups in the world, mainly by the end of last century. It has been reported to arise from tip-induced magnetization changes in magnetic samples and this effect is commonly undesired when carrying out *MFM* experiments. If one assumes that the magnetic structure of the tip remains constant, then the localized dissipation signal can be attributed to magnetoelastic interactions, eddy currents or variations in pinning potentials. Remarkably, damping images usually show more details and seem to have a higher resolution than the force gradient images yielded by *MFM*.

In this chapter, we describe our ongoing work on this field and present some results already obtained studying magnetic dissipation with *MFM*; this corresponds to the last and most innovative part of this thesis. On the one hand, we have observed that different phenomena can be responsible for this dissipation of energy and that a counterintuitive decrease of dissipation can take place in some specific cases by going closer to the sample. On the other hand, we demonstrate that care should be taken when interpreting *MFM* results, since dissipative processes can introduce features in the images that should not be considered as part of the sample's domain structure. Remarkably, a method is shown to obtain *3D* maps of the magnetic field emerging from the studied sample, with very high spatial resolution.

1. Fundamentals beneath dissipation in AFM

A very simple formula deduced by *Cleveland* and co-workers [14] is commonly used to calculate the energy dissipated in scanning probe force experiments. It relies on the fact that, in equilibrium, the average rate at which energy is fed into the cantilever must equal the average rate at which energy is dissipated by the cantilever and the interacting tip:

$$P_{input} = P_{cantilever} + P_{tip} \qquad \textbf{(5.1)}$$

where we can express the instantaneous power as:

$$P = \frac{dW}{dt} = \frac{\vec{F} \cdot d\vec{l}}{dt} = \frac{F_z \cdot dz}{dt} = F_z \cdot \dot{z}(t)$$

$z(t) = A \cdot \sin(\omega t + \phi)$ describing the deflection from equilibrium of the end of the cantilever. The first term on the right side of equation **5.1** is attributed to energy dissipated by the body of the

[14] J. P. Cleveland, B. Anczykowski, A. E. Schmid and V. B. Elings, Applied Physics Letters 72 (1998) 2613

cantilever moving in a viscous environment and is well modelled, to a first approximation, by a viscous damping of the form:

$$F_{damping} = \mu \cdot \dot{z}(t) \tag{5.2}$$

Integrating over a complete cycle, the average dissipated power yields:

$$\langle P_{cantilever} \rangle = \frac{1}{T} \cdot \int_0^T \mu \cdot \dot{z}(t)^2 \cdot dt = \frac{\mu \cdot \omega^3 \cdot A^2}{2\pi} \cdot \int_0^{\frac{2\pi}{\omega}} \cos^2(\omega t + \phi) \cdot dt = \frac{\mu \cdot \omega^2 \cdot A^2}{2}$$

Notice that the viscous damping coefficient μ was implicitly considered to remain unchanged over time, i.e. over distance, so that it could be taken out of the integral. Experimentally, it is easier to calculate μ by measuring the cantilever spring constant k, the resonance frequency ω_0 and the quality factor Q:

$$\mu = \frac{k}{\omega_0 \cdot Q}$$

so:

$$\langle P_{cantilever} \rangle = \frac{k \cdot \omega^2 \cdot A^2}{2 \cdot \omega_0 \cdot Q} \tag{5.3}$$

On the other hand, the term on the left side of equation **5.1** describes the power delivered to the tip by the driver, which results in an elastic force such that:

$$F_{excitation} = k \cdot [z(t) - z_{driver}(t)]$$

where the sinusoidal displacement of the exciting piezoelectric is $z_{driver}(t) = A_{driver} \cdot \sin(\omega t)$. A similar analysis for the average input power of the system yields [15]:

$$\langle P_{input} \rangle = \frac{1}{T} \cdot \int_0^T k \cdot [z(t) - z_{driver}(t)] \cdot \dot{z}(t) \cdot dt =$$

$$= \frac{\omega^2 \cdot k \cdot A}{2\pi} \cdot \int_0^{\frac{2\pi}{\omega}} [A \cdot \sin(\omega t + \phi) - A_{driver} \cdot \sin(\omega t)] \cdot \cos(\omega t + \phi) =$$

[15] The same result is obtained integrating: $\langle P_{input} \rangle = \frac{1}{T} \cdot \int_0^T k \cdot [z(t) - z_{driver}(t)] \cdot \dot{z}_{driver}(t) \cdot dt$, since all the power input by the driving piezo is supposed to be transmitted to the oscillating lever.

$$= \frac{\omega^2 \cdot k \cdot A}{2\pi} \cdot \left[\left(\frac{A}{2 \cdot \omega} \right) \cdot \sin^2(\omega t + \phi) \Big|_0^{\frac{2\pi}{\omega}} - \left(\frac{A_{driver} \cdot \cos(\phi)}{2 \cdot \omega} \right) \cdot \sin^2(\omega t) \Big|_0^{\frac{2\pi}{\omega}} + A_{driver} \cdot \sin(\phi) \cdot \int_0^{\frac{2\pi}{\omega}} \sin^2(\omega t) \cdot dt \right] \Rightarrow$$

$$\langle P_{input} \rangle = \frac{\omega \cdot k \cdot A \cdot A_{driver}}{2} \cdot \sin(\phi) \qquad \textbf{(5.4)}$$

As a result, combining equations **5.1**, **5.3** and **5.4** we obtain *Cleveland*'s formula for the experimental dissipation of energy associated to tip-sample interactions:

$$\boxed{\langle P_{tip} \rangle = \frac{1}{2} \cdot \frac{k \cdot A^2 \cdot \omega}{Q} \cdot \left[Q \cdot \frac{A_{driver}}{\mathrm{A}} \cdot \sin(\phi) - \frac{\omega}{\omega_0} \right]} \qquad \textbf{(5.5)}$$

Note that the reason that Q and ω_0 appear in equation **5.5** is to express the viscous damping coefficient μ in terms of experimentally accessible quantities. It does not imply that the resonant frequency nor the quality factor of the interacting cantilever remain the same, it only assumes that the viscous damping coefficient describing the damping of the body of the lever remains unchanged.

Further simplifications depend on the operating mode used in the experiment. We distinguish between four different cases:

- **Amplitude modulation AFM (*AM-AFM*)**. In particular, if no phase locked loop (*PLL*) is used, the drive frequency is typically chosen to be ω_0 and the free amplitude of the cantilever turns out to be $A_0 = Q \cdot A_{drive}$. With this:

$$\langle P_{tip} \rangle = \frac{1}{2} \cdot \frac{k \cdot A^2 \cdot \omega_0}{Q} \cdot \left[\frac{A_0}{\mathrm{A}} \cdot \sin(\phi) - 1 \right]$$

  An important consequence of former equation is that, if the tip loses no energy, then the amplitude and the phase are not independent and $\phi = \arcsin\left(\frac{A}{A_0}\right)$. In *AFM* experiments, phase imaging is performed with the amplitude held constant by the feedback loop used to map the topography, so it is only when the tip-sample interaction losses vary that phase contrast will be observed. However, this might not be the case during the retrace scan in *MFM* measurements as different interactions are present compared to the first scan. There,

since no feedback maintains the amplitude constant, conservative interactions such as magnetism also cause phase shifts that subsequently modify the oscillation amplitude *A*. In this situation, no separation between conservative and dissipative interactions can be made.

- **Amplitude modulation *AFM* with a *PLL***. If a *PLL* is implemented, another feedback loop tracks the resonance peak by setting $\phi = {}^{\pi}/_{2}$, so that:

$$\langle P_{tip} \rangle = \frac{1}{2} \cdot \frac{k \cdot A^2 \cdot \omega}{Q} \cdot \left[\frac{A_0}{\mathrm{A}} - \frac{\omega}{\omega_0} \right] \qquad \textbf{(5.6)}$$

In this case, non-dissipative interactions connect changes in the resonance frequency to variations in the oscillation amplitude in the form $\omega = \omega_0 \cdot \frac{A_0}{A}$. In other words, conservative interactions modify the elastic constant $k_{effective} = k_0 - \frac{\partial F_z}{\partial z}$ in such a way that attractive forces "soften" the cantilever and give rise to larger amplitudes and vizeversa, for constant excitation signals as is usually the case in *AM-AFM*. Hence, during the topographic scan – and disregarding eventual errors in the main feedback – one can associate variations in the oscillation frequency to dissipative processes. Again, in *MFM* measurements one would expect changes in the oscillation amplitude due to non-dissipative magnetostatic interactions that shift the resonance frequency. However, such variations are predicted to be very small and strong frequency shifts are necessary to register this effect. For instance, for a cantilever with a free resonance frequency ω_0=70 kHz and a free oscillation amplitude A_0=10 nm, frequency shifts of 100 Hz result in an amplitude change of 15 pm, below the thermal noise level at room temperature.

- **Frequency modulation *AFM* (*FM-AFM*)**. In this operating mode, the one most commonly used when measuring in vacuum environments, a third feedback loop is used to keep the oscillation amplitude constant. For doing so, a variable *P-I* gain multiplies the excitation signal in a controlled way:

$$V_{exc} = R(t) \cdot A_{drive} \cdot \sin(\omega t)$$

This variable gain *R(t)* accounts for eventual deviations of the amplitude from a chosen setpoint value:

$$R(t) = P \cdot \left[A(t) - A^{setpoint} \right] + I \cdot \int_0^t \left[A(t') - A^{setpoint} \right] \cdot dt'$$

It thus carries the information about energy losses of the lever. As a result, the mean dissipated power must be expressed as a function of this driving signal [16]:

$$\langle P_{tip} \rangle = \frac{1}{2} \cdot \frac{k \cdot A^2 \cdot \omega_0}{Q} \cdot \left[\frac{V_{exc}}{\mathrm{V_{exc,0}}} - \frac{\omega}{\omega_0} \right] \qquad \textbf{(5.7)}$$

where $V_{exc,0}$ is the voltage needed to maintain the oscillation amplitude far from the surface. Frequency shifts caused by pure conservative interactions provoke variations in the oscillation amplitude that are counterbalanced by tuning the voltage driving the piezoactuator. Topographic maps in *FM-AFM* correspond to surfaces of constant ω, so any feature observed in the V_{exc} is related to dissipative processes taking place during the topographic scan.

- **Drive-amplitude modulation *AFM* (*DAM-AFM*)**. This operating mode [17] is essentially equivalent to *FM-AFM* with the particularity that the topographic feedback does not keep the oscillation frequency constant but the excitation voltage instead. Thus, dissipative interactions during the topographic scan will now be recorded in the frequency shift channel. On the contrary, power losses will give rise to contrast in the driving voltage map during the *MFM* acquisition of data.

Energy dissipation in magnetic materials

The study of energy dissipation by means of magnetic force microscopy has been reported by few groups. It is based on the analysis of the oscillation damping to quantify the energy transferred from the tip to the magnetic sample and correlate it with some physical property. The first report was published by Grütter and co-workers [18], where they state that generation of phonons in the sample is an inevitable consequence, as the *AC* component of the stray field emerging from the tip leads to oscillations of the magnetic moments that create strain due to magnetoelastic coupling. In their model [18,19], dissipated energy in the order of tenths of fW is predicted, in agreement with their experimental results. As a proof of the usefulness of this magnetic dissipation imaging, the authors were able to distinguish between Bloch and Neél domain walls [18,20] by deducing the *DW* response

[16] C. Loppacher, R. Bennewitz, O. Pfeiffer, M. Guggisberg, M. Bammerlin, S. Schär, V. Barwich, A. Baratoff and E. Meyer, Physical Review B 62 (2000) 13674-13679
[17] M. Jaafar, D. Martínez-Martín, M. Cuenca, J. Melcher, A. Raman and J. Gómez-Herrero, Beilstein Journal of Nanotechnology 3 (2012) 336-344
[18] P. Grütter, Y. Liu, P. LeBlanc and U. Dürig, Applied Physics Letters 71 (1997) 279-281
[19] Y. Liu, B. Ellman and P. Grütter, Applied Physics Letters 71 (1997) 1418-1420
[20] Y. Liu and P. Grütter, Journal of Applied Physics 83 (1998) 7333-7338

to in-plane and out-of-plane components of the tip stray field; additionally, they state to have detected magnetic structures in antiferromagnetically coupled multilayers not observable by standard magnetic force microscopy [20].

There are other possible dissipative mechanisms besides magnetoelastic distortions of the crystalline lattice. Eddy currents originated in both tip and sample by the magnetic flux variation as the probes oscillates were estimated by Liu and co-workers [19] to dissipate 7 orders of magnitude less energy than magnetostrictive processes do, thus being out of the detection limit. However, eddy current damping is pointed out to be the major contribution to the dissipation observed over superconducting regions in Nb films [21]. Proksch and co-workers [22] measured peak dissipation features of 300 fW at the domain wall positions; however, they interpret them as begin associated with irreversible domain wall motion induced by the oscillating tip in a repetitive way, seeming to reflect micromagnetic defects that act as pinning sites. The domains also showed significant dissipation in their experiment that was attributed to modulated rotation in the magnetization caused by the tip field. According to their estimations, even if the stray field of the *MFM* probe is larger than the bulk coercive field of a sample, local modifications to the domain structure may be reversible in the sense that the global demagnetizing forces from the unperturbed portions of the sample can be sufficient to correct for the localized influence of the tip once it has moved on to another area. Although not directly measuring energy dissipation, different groups [23,24] have been able to measure this tip-induced reorientation of spins in the sample by intentionally enhancing the tip-sample mutual influence. The local susceptibility was estimated by adding the contrasts of two *MFM* images obtained with reversed magnetization orientations.

It is worth noting that the dissipation measured by *MFM* does not represent the entire magnetic power being dissipated by the probe. Because the cantilever is constrained to move vertically, lateral forces do not produce dissipation measurable via the amplitude drop. The energy dissipated in such processes is provided by the sample scanner instead and not by the piezoelectric driving the cantilever. It is also important to note that the cantilever provides a time averaged picture of the dissipated power and the measurable dissipation originates in processes being cycled repeatedly at the cantilever resonant frequency. Since the cantilever needs roughly Q oscillations to equilibrate, the response of the cantilever to a single, non-repeating event will be averaged over Q oscillations, causing it to appear Q times smaller than the same event happening repeatedly. In fact, a dissipation feature in an image might be a combination of repeated and single events.

[21] M. Roseman and P. Grütter, Applied Surface Science 188 (2002) 416-420
[22] R. Proskch, K. Babcock and J. Cleveland, Applied Physics Letters 74 (1999) 419-421
[23] S. Foss, R. Proksch, E. D. Dahlberg, B. Moskowitz and B. Walsh, Applied Physics Letters 69 (1996) 3426-3428
[24] E. Zueco, W. Rave, R. Schäfer, A. Hubert and L. Schultz, Journal of Magnetism and Magnetic Materials 190 (1998) 42-47

2. Negative dissipation gradients in magnetic force microscopy

Here, we describe a study of the dependence of magnetic dissipation as a function of distance by means of *MFM*, an ongoing work in collaboration with Prof. *Juan José Sáenz* from the *Universidad Autónoma de Madrid*. Experimental evidence is presented for a **counterintuitive monotonous reduction of the dissipation** as the distance between tip and surface decreases, so that increasing the tip-sample magnetic interaction can result in a reduction of magnetic losses. This behavior, which takes place when spins in the tip point parallel to those in the sample, can be understood in terms of hysteresis phenomena involved in the reorientation of the magnetic moments located at the tip apex. The magnetic response under an oscillating field is found to be strongly dependent on the polarity of the static stray field of the sample. Measured magnetic losses of few fW are in agreement with the quasi-static micromagnetic simulations performed by the collaborating group. This work is still open and will be submitted for peer reviewed publication in the next months.

We set ourselves the goal to measure magnetic losses arising from a strongly coupled system comprised of a CoNi multilayer film and a commercial *Nanosensors PPP-MFMRK* probe, as sketched in figure 5.1. The tip coercivity was previously measured to be about 35 mT by using the *MFM* based technique described in chapter 4. In order to reduce the capillarity effect between the tip and the sample surface, experiments were performed in low humidity conditions (below 5%). Hysteresis loops of the CoNi film reveal the existence of high perpendicular anisotropy with a coercive field of 165 mT and a remanent magnetization of 87 % the saturation value. The average domain size measured by *MFM* is around 140 nm for the demagnetized state.

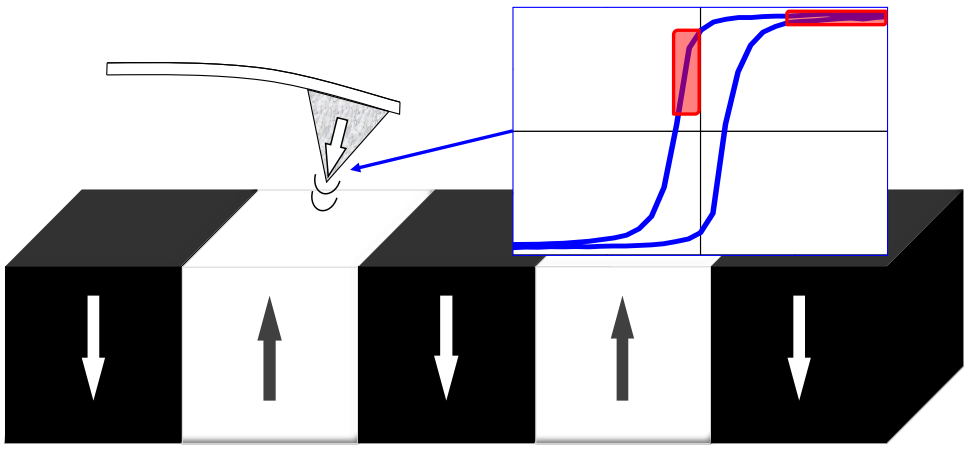

Figure 5.1: Description of the experiment. *A sample with a strong OOP magnetization and average domain size of 140 nm has been studied. During the oscillation, the tip is subject to AC magnetic fields, as depicted in the hysteresis loop.*

Topographic, oscillation amplitude and frequency shift images were recorded simultaneously with the tip scanning over the surface, as shown in figure 5.2, in ambient conditions. The amplitude modulation mode was used with a *PLL* enabled that tracks the resonance frequency, so that topography corresponds to constant oscillation amplitude images. Thus, contrast observed in the amplitude images taken during the topographic scan indicates deviations from the setpoint value and represents the main feedback error signal. As usual, a second scan is then performed retracing the topographic profile at a lift height of 30 nm, where the amplitude and frequency shifts can be obtained at a constant tip-sample distance with the main feedback disabled.

The average power dissipated by tip-sample interactions can be obtained from data in figure 5.2, using equation **(5.6)**. The spring constant was estimated to be $k \approx 1.6$ N/m, the quality factor $Q \approx 150$, the natural resonance frequency $f_0 = 70220$ Hz with a free oscillation amplitude $A_0 \approx 16$ nm. The resulting dissipation maps are displayed in figures 5.2.d and .h. Dissipative processes occurring at **low distances** seem to be dominated by ***van der Waals*** interactions, as a strong correlation is observed between the dissipation map in figure 5.2.d and the main feedback error (fig. 5.2.b). As it can be readily seen, the topographic feedback was not optimized and such deviations from a constant tip-sample distance cause higher topographic features to dissipate larger power. By having a look at figure 5.2.c, one can observe the magnetic domains mixed up with the topographic pattern in the frequency shift image taken at low distance. This interaction cross-talk could be partially due to the relatively large oscillation amplitudes used in the experiments (a setpoint value of 11 nm was used here) causing the tip to describe a trajectory along regions where different interactions are predominant. In any case, this confirms the strong magnetostatic coupling between tip and sample.

On the contrary, during the 30 nm lifted scan the dissipation map (fig. 5.2.h) reproduces the *MFM* contrast (fig. 5.2.g) to a very good extent. In fact, as it is customary, a higher lateral resolution is achieved in the dissipation image [18,22], being able to resolve features **below 10 nm** in size (see the peak in fig. 5.2.e). Thus, energy dissipation at such separation distances is mainly caused by the mutual stray field influence in both the tip and the CoNi multilayer. Interestingly, an experienced *MFM* user quickly identifies some **fancy stains** in figure 5.2.g, also observed in figure 5.2.f. They have the same shape as the attractive domains but are a bit shifted from their positions to the bottom-right direction. Strikingly, the dissipation map reveals them to be the **less dissipative areas** of the image, whereas the **highest power loss rates** are found in their **contour lines** (fig. 5.2.h).

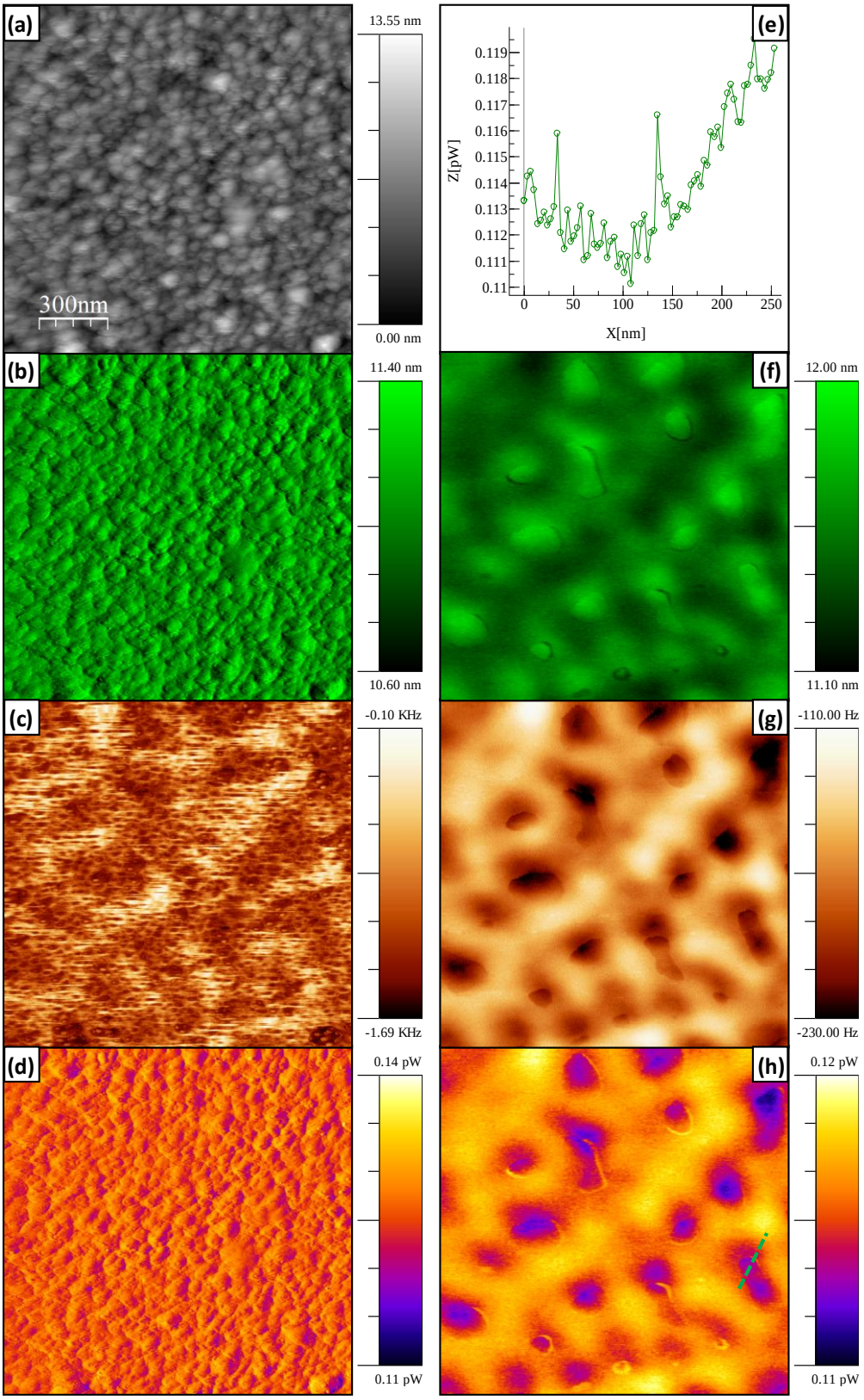

Figure 5.2: The sample (a) *Topography and corresponding* ***(b)*** *&* ***(f)*** *oscillation amplitude,* ***(c)*** *&* ***(g)*** *frequency shift and* ***(d)*** *&* ***(h)*** *dissipation images of the CoNi multilayer film. (a)-(d) were measured while tracking the topography and (f)-(h) correspond to the 30 nm lifted scan.* ***(e)*** *Profile in the retrace dissipation image (h), showing a 5 fW peak with a lateral resolution below 10 nm.*

These unusual features might be caused by **sudden rotation of spins** in the tip, once a sufficiently strong *Z* component of the sample stray field is reached. The shape anisotropy of an *MFM* probe forces its spins to point along a specific direction, usually considered to be perpendicular to the sample surface (*Z* axis). If the probe scans the surface at a non-perpendicular angle, a misalignment occurs between the stray field and the tip's magnetization, so that for strong enough torques the magnetization should be able to rotate away from its shape induced position. This might happen close to the central areas of the attractive domains (see the strength of the magnetostatic coupling in the scale bar of figure 5.2.g), giving rise to an enhanced *MFM* contrast and a lower dissipation once the magnetic moments point parallel to the field. The highly dissipative contour lines indicate the transition regions where the magnetic torque reaches the critical value, in such a way that the magnetization flips from the two stable positions during one oscillation cycle in a reversible – though hysteretic – way. As will be described in more detail in section 5.3, care must be taken if one wants to extract conclusions from these *MFM* images as the fancy stains originate from processes taking place in the sensing probe and not in the sample.

It was just mentioned that more attractive magnetostatic interactions yield less dissipative contrast. This makes sense thinking in terms of the system trying to reach a minimal *Zeeman* energy. Applying small *AC* fields to a sample close to its saturation state is not expected to cause much power loss, since the small susceptibility give rise to minor loops that barely show hysteretic behavior (see sketch in figure 5.1). On the contrary, larger susceptibilities occur on the repulsive side of a hysteresis loop, i.e. when the tip scans over a repulsive domain. Thus, *AC* fields should provoke a stronger damping in the cantilever oscillation in this case. *Grütter* and co-workers [18] already realized the importance of the magnetization polarity with respect to the stray field direction to explain dissipation maxima and minima in their results.

Keeping in mind this idea that the closer to saturation a sample is the less dissipation one expects, an accurate evaluation of the **dependence of energy losses on distance** was carried out using a variation of the *3D modes* explained in chapter 2.2. In this case, the *MFM* probe was scanned along a specific direction parallel to the sample surface (*X* in figure 5.3.a) while the separation distance *z* was gradually decreased down to contact. Properly selecting the scan direction allows for visualizing the interaction with magnetic domains of alternating polarities as a function of distance. Oscillation amplitude and frequency shift data were recorded simultaneously and are shown in the left column of figure 5.3, together with the calculated dissipated power. On the right, profiles corresponding to their respective evolutions with distance are plotted for two cases: over an attractive and over a repulsive domain. Note that no topographic feedback was enabled during the realization of this experiment so the tip starts tapping the surface for different *z* values depending on the local roughness. In order to simplify the interpretation of *MFM* images, the horizontal axis

on the profiles shown was renormalized so that zeros correspond to the distance at which the topography was recorded in figure 5.2, i.e. $A_{OSC}\,(z_{piezo}=0)$ = 11 nm. Black contrast in figure 5.3.b (notice the scale bar) stands for amplitudes below this setpoint value, thus reflecting the topographic roughness of the surface. At such distances, the influence of magnetostatics is masked by *van der Waals* interactions and the amplitude is not sensitive to the domain polarity.

The resonance frequency of the oscillating cantilever (fig. 5.3.a) reflects the long range character of the magnetostatic interaction with the CoNi sample, detectable at distances up to tens of nanometers far away from the surface. The domain polarity is also reflected in the amplitude image for a wide range of separation values (fig. 5.3.b). In addition, a significant difference in power loss is observed scanning over parallel and antiparallel domains; however, both curves in figure 5.3.c converge to the same value for distances around 75 nm. This means that, within the experimental noise, no domain sensitivity is present in the damping over such value, whereas the conservative interaction is still distinguishable in the frequency shift up to around 100 nm from the sample. Since noise is averaged and filtered out by statistics, a difference between domains is indeed observed in the experimental images for distances close to 150 nm.

The dissipation profile for repulsive interactions shows a slight **increase of 1-2 fW** as the tip approaches the surface (black profile in the inset of figure 5.3.c). The same happens to the oscillation amplitude, which decreases by around 1 angstrom in the last 70 nm range displayed in the inset of figure 5.3.b before the probe starts tapping on the surface. On the contrary, a surprising **negative dissipation gradient** is clearly seen if an attractive interaction is present (red profile in figure 5.3.c). This means that, for a relatively large range of distances, the closer you get the less energy you need to make the tip oscillate.

It may sound counterintuitive but if magnetic losses are dominant, that is something one could expect from the argument sketched before. Due to the oscillatory movement, the end of the tip is subject to minor cycles with their corresponding energy loss, superimposed on a *DC* bias field. Going towards the surface results in a fast raise of the stray field, which can be interpreted as an enhanced biasing towards the saturation region of the hysteresis loop. Under such circumstances, the area enclosed by the minor loop during one oscillation cycle decreases for lower gaps (see fig. 5.1). However, a subtle consideration must be taken into account: even if the amplitude remained constant while approaching the surface, the field range that the probe is subject to would not. The field gradient is not homogeneous but increases rapidly for low distances. The same oscillation amplitude thus becomes equivalent to a much larger field range. For the limit of very small oscillations and a dipolar sample, the field range applied during the minor hysteresis loop increases so as to z^{-4}.

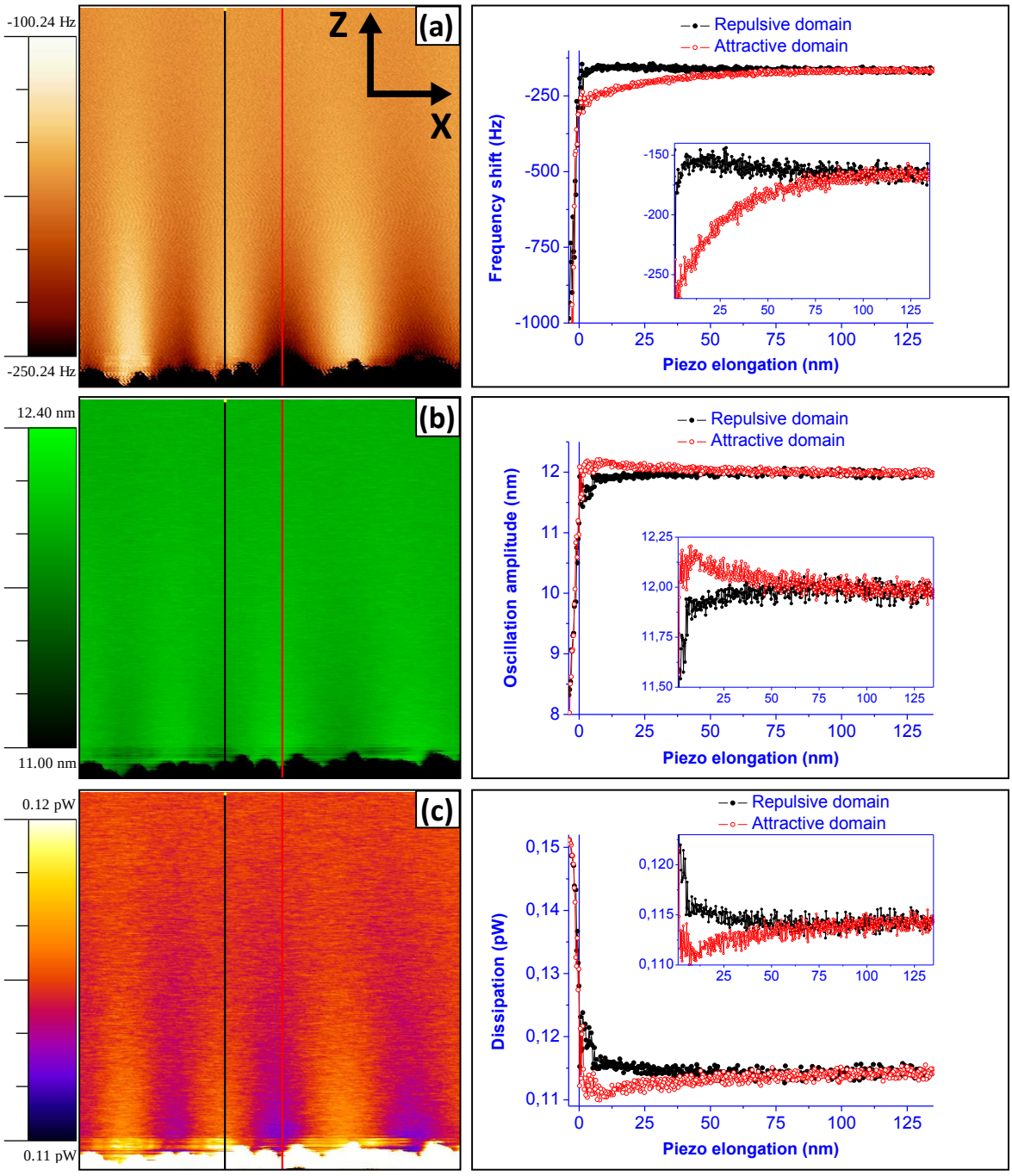

Figure 5.3: 3D modes (I). *The tip was scanned along a 1.5 μm distance parallel to the sample surface (horizontal axis) while varying the tip-sample separation by 150 nm (vertical axis). Left column:* ***(a)*** *Frequency shift,* ***(b)*** *oscillation amplitude and* ***(c)*** *dissipated power images. Right column: Profiles corresponding to the colored lines seen in the images on the left. Red/black profiles give information about the dependence on distance over an attractive/repulsive domain. The horizontal axis on the profiles was renormalized so that zero corresponds to the distance of the topography feedback.*

Although this argument provides a simple qualitative explanation for our experimental findings, the actual losses (i.e. the area enclosed within a minor hysteresis loop) must be estimated from a

microscopic model. The microscopic mechanisms behind the energy loss in minor hysteresis loops have been largely discussed in the literature [25] but are still far from being fully understood [26]. In order to obtain some quantitative data, ***3D* micromagnetic calculations** were performed using the *OOMMF* code. The tip was modeled as a square based pyramid (see fig. 5.4.a) coated with a 51 nm thick cobalt layer, with a saturation magnetization M_S=1.4·10^6 A/m, a magnetocrystalline anisotropy constant K_1=5.3·10^5 J/m^3 and a exchange stiffness A=3.0·10^{-11} J/m. The numerical calculations were performed using 3 nm side cubic cells. The sample was simulated as a 36 nm thick film and its magnetization was kept fixed during the simulation (M_S^{sample}=3.3·10^5 A/m), either parallel or antiparallel to the tip magnetization.

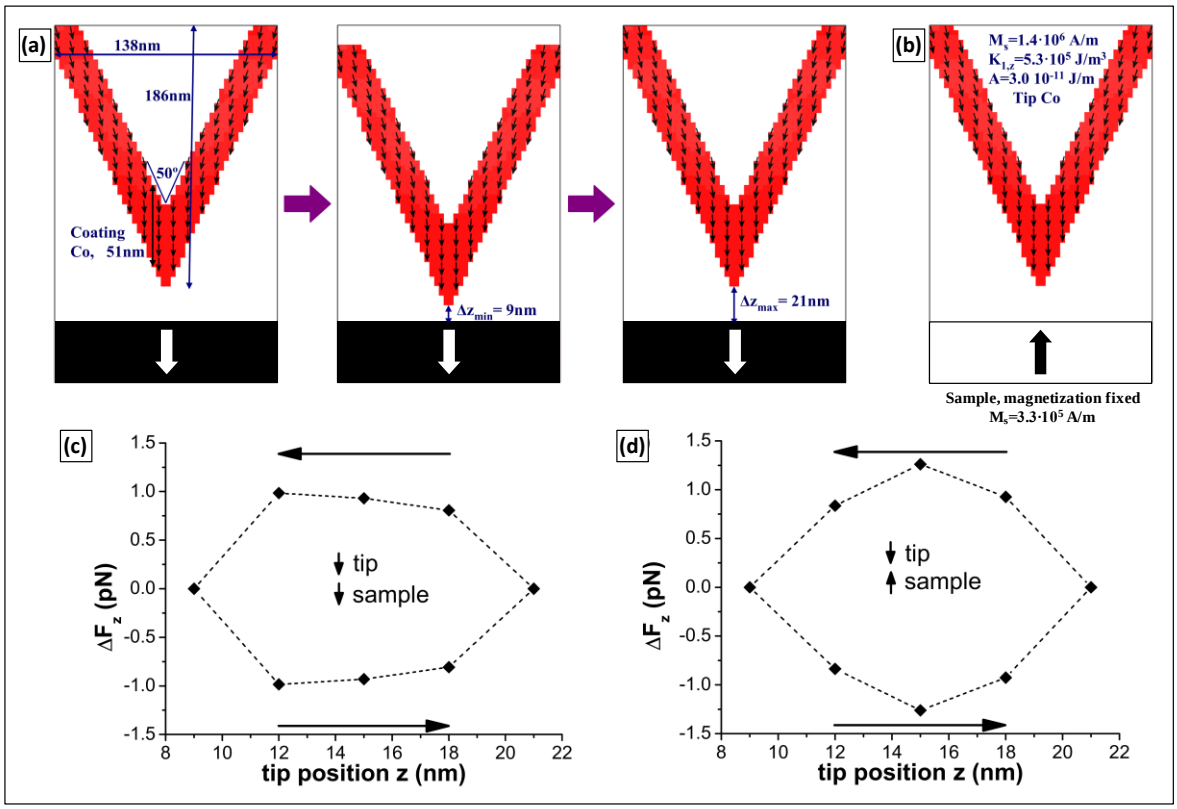

Figure 5.4: Micromagnetic simulations. (a)-(b) *Sketch of the tip-sample configuration used in the calculations for (a) attractive and (b) repulsive interactions.* ***(c)-(d)*** *Hysteresis loops in the tip-sample force as function of the separation distance during one oscillation cycle, obtained for the (c) parallel and (d) antiparallel configurations.*

To simulate the tip oscillation, the tip apex is initially located in the centre of the domain (of width 138 nm) and 21 nm above the sample surface, moved down to a tip-sample separation of 9 nm using 3 nm steps and, then, it is retracted back to the initial position. In the initial magnetic

[25] D. C. Jiles and Y. Melikhov, "Modeling of nonlinear behavior and hysteresis in magnetic materials", Handbook of magnetism and advanced magnetic materials (Wiley Online Library, 2007)
[26] A. Berger, S. Mangin, J. McCord, O. Hellwig and E. E. Fullerton, Physical Review B 82 (2010) 104423

configuration of the tip, all spins are pointing downwards and in every step the magnetization is fully relaxed before moving the tip; this final magnetization being the starting configuration for the next step. We repeat the approach and retract cycle twice, but only use the second one in order to avoid 'memory' effects of the initial magnetic configuration. The tip magnetization presents a hysteretic behavior and so does the magnetic force between the two objects. Let us label the *z* component of the magnetic force during the approach and retract curves, at a given separation distance, as $F_{z,\downarrow}$ and $F_{z,\uparrow}$, respectively. Deviations of the force from the average value during the second cycle ($\Delta F_{z,\downarrow}=F_{z,\downarrow}-\langle F_z\rangle$ and $\Delta F_{z,\uparrow}=F_{z,\uparrow}-\langle F_z\rangle$) are depicted in figures 5.4.c-d for both cases, where the average force is $\langle F_z\rangle=(F_{z,\downarrow}+F_{z,\uparrow})/2$.

In order to quantify the dissipated power, an oscillation frequency similar to the experimental case was chosen, namely f=75 kHz. The resulting values are $P_{\downarrow\downarrow}$=1,2 fW for parallel and $P_{\downarrow\uparrow}$= 1,4 fW for antiparallel domains, respectively. As in the experimental case, larger power losses take place when the sample domains point antiparallel to the magnetization in the tip. However, these values differ by two orders of magnitude from the measured dissipations presented above. Reasons for theses larger values might be the mutual influence and subsequent losses also taking place in the sample, larger field gradients and larger amounts of interacting spins being present in the real case. An additional source of damping could be caused by a raise of the viscous damping coefficient with decreasing distance, which was implicitly assumed to remain constant in equation **5.2**. This increase can be explained in terms of the enhanced friction of the air layers as the gap between tip and sample diminishes, especially at very low separations.

As both sorts of damping are expected to change gradually with distance, it thus becomes difficult to potentially separate their contributions. If, eventually, a considerable amount of spins suddenly flips as a consequence of the field emerging from the sample, a correlation to purely magnetic dissipation could be obtained. Such sudden jumps were indeed observed as **dissipative contour rings** in figure 5.2.h and magnetic energy losses in the order of a few fW are in good agreement with the experimental peak measured in figure 5.2.e. Thus, this simple model successfully explains energy dissipated by relatively small regions of the interacting tip.

Useful information may also be extracted by studying the **dependence on distance of such unusual dissipative rings**. This is shown in figure 5.5, where a lower oscillation amplitude of 9 nm was used. The three-dimensional regions subtended by these rings can be clearly distinguished in the three images shown, having parabolic cross sections. It was already mentioned that a stronger attraction takes place at points within this parabolic volume, which becomes evident if one compares the values of the red profiles in figures 5.5.a and 5.3.a (see insets). In addition, the

amplitude grows by over 1 nm and power losses drop pronouncedly, after the probe has entered this region.

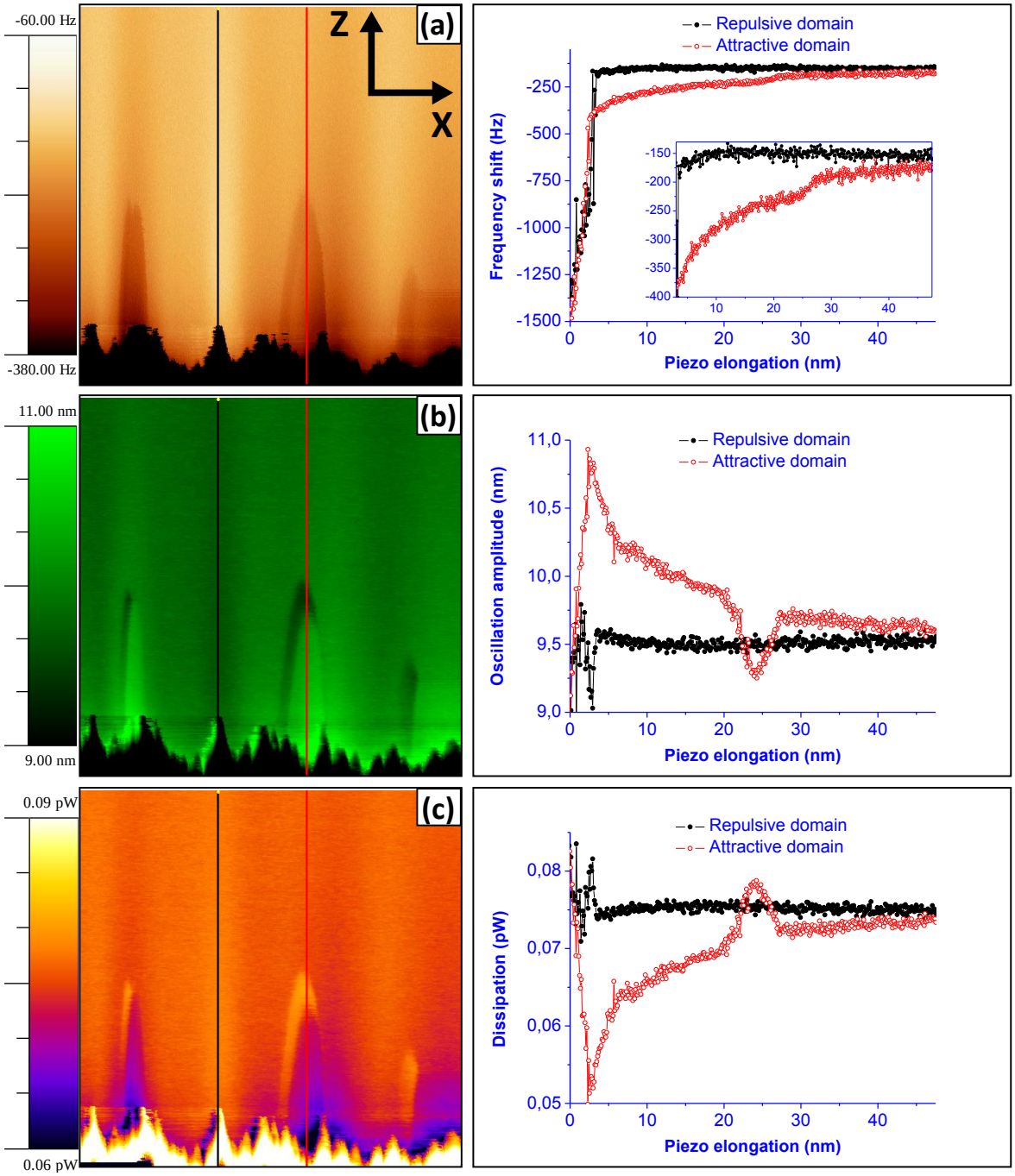

Figure 5.5: 3D modes (II). *The tip was again scanned horizontally along 1.5 µm while sweeping the tip-sample distance by 60 nm, with an oscillation amplitude of 9 nm. A bump and subsequent changes in the* ***(a)*** *frequency shift,* ***(b)*** *amplitude and* ***(c)*** *dissipation images (left column) and profiles in them (right column) are clearly visible.*

Interestingly, the contour lines observed in figure 5.2.h appear as a bump in the profiles plotted on the right column of figure 5.5. These humps reveal more attractive interactions with enhanced dissipation, which can be attributed to rotation of spins during the oscillation cycle. The height of the peak on the red dissipation profile shown in figure 5.5.c reveals a dissipated power of **7 fW**, the same order of magnitude as the numerical prediction given above. Leaving behind the transition and going well into the parabolic region gives rise to a considerably larger dissipation drop, as compared to the former situation described in figure 5.5. This reflects a gradual reorientation of magnetic moments towards the sample stray field, instead of being sudden rotations.

It is important to note that the same tip was used in all experiments shown throughout this work. Structural, geometric and even compositional changes at the tip apex are expected since a considerable number of force-versus-distance curves where performed going down to contact. Such changes caused variability in the observation of the rings; nevertheless, they were usually observed at some area of the sample. The reason why they were not present in figure 5.3 is that a particular scan direction was chosen.

It is particularly interesting to study the shape of the parabolic cross sections described above and a practical application can be reached. In fact, physical information can be extracted from them. This will be commented on the very next section and micromagnetic simulations will be used to support our statements.

In conclusion, we have measured the energy loss associated to hysteretic processes going on under the mutual influence of an *MFM* probe and a highly coupled magnetic sample with perpendicular anisotropy. Both are subject to minor hysteresis loops during each oscillation cycle, biased by the *DC* field at the mean tip-sample distance. The tiny amount of energy dissipated in this process can be measured during the *MFM* data acquisition and its evolution with varying distance may be studied. As a main consequence, a counterintuitive behavior of the dissipation versus the tip-sample distance was found for the case of domains parallel to the magnetization in the probe. Micromagnetic calculations yield a dissipation value in the order of few fW, which is in agreement with power losses caused by relatively small amounts of spins flipping their magnetization. Large mutual influence reflects in much higher dissipations of the order of hundreds of fW. A similar drop of energy loss by decreasing distance is predicted for the case of ferroelectric materials with domains of opposite polarities, when using biased metallic probes, as long as the electrostatic mutual influence approaches the saturation regime of the hysteresis loops.

3. Tip-induced artifacts in MFM images

This section concentrates on a specific application of the study of magnetic dissipation. It was developed during one of my stays in the group of Prof. *P. H. Grütter* at the *McGill University of Montreal* and resulted in one article published in the beginning of 2013 [27]. In it, we encourage *MFM* users to be careful when measuring under certain circumstances in order to avoid misinterpreting the contrast observed in magnetic force microscopy images by tip related artifacts.

For this study, an array of permalloy dots, 20 nm thick and 1 μm in diameter, was electron beam evaporated through a SiN stencil (*Protochips DTM-25232*) on to a SiN membrane (*Norcada NT025C*). Images were obtained under an in-plane magnetic field and high vacuum conditions, using a home built magnetic force microscope in the host group operating in frequency modulation mode with a phase locked loop (*NanoSurf, easyPLL*). The *MFM* cantilever was oscillated in self-oscillation mode with a phase shifter and a proportional-integral controller to maintain a constant oscillation amplitude. All measurements presented here were carried out using the same tip (*Smart Tip SC-35-M*, with spring constant k=2.8 N/m, resonance frequency f=67.5 kHz and quality factor 10^4), with a 35 nm thick CoNi coating deposited onto one of its sides. Unless otherwise specified, the oscillation amplitude was 10 nm.

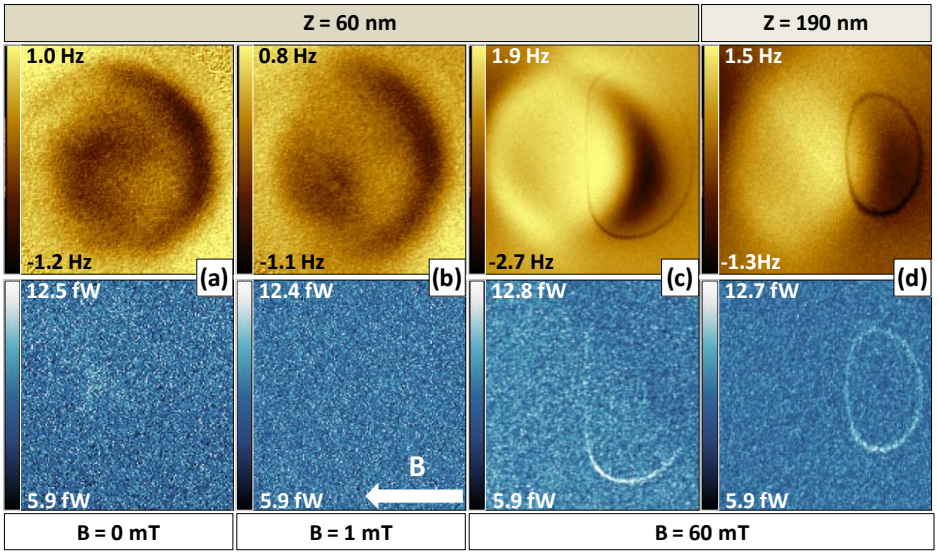

Figure 5.6: The sample. *Frequency shift (upper row) and dissipation (lower row) images of a permalloy dot acquired under different magnetic fields using the same MFM probe at a scanning height of* ***(a)****–****(c)*** *60 nm and* ***(d)*** *190 nm. Size of the images: (1.2x1.2) μm^2. Frequency shift values have been zeroed in the substrate. Dissipation maps were calculated using equation* ***(5.7)****, since experiments were carried in high vacuum conditions (10^{-6} mbar) with an additional feedback that keeps the oscillation amplitude constant.*

[27] **Ó. Iglesias-Freire**, J. R. Bates, Y. Miyahara, A. Asenjo and P. H. Grütter, Applied Physics Letters 102 (2013) 022417

As it was studied in chapter 2, the ground state configuration of circular magnetic dots of such dimensions in relatively low applied fields (few mT) is the single vortex state. As seen in figure 5.6.b, applying an in-plane magnetic field (insufficient to expel the vortex) results in the vortex being slightly displaced from the center. Notice that the corresponding dissipation images do not present any particular feature, apart from a faint contrast due to a slight tip-induced movement of the vortex (fig. 5.6.a-b).

However, when performing constant-height *MFM* imaging with the same tip under higher *IP* magnetic fields, an unusual feature appears both in the oscillation frequency and dissipation channels (fig. 5.6.c-d). *MFM* images do not display the usual contrast observed for single domains nanostructure, were regions with concentration of magnetic poles yield only white-black areas at the ends of the magnetic element. There, this typical imaging contrast is superimposed on a relatively bright, homogeneous background observed only over the magnetic dot. This is due to a partial canting of the tip magnetization away from the vertical direction due to the external field and the subsequent sensitivity to both in and out of plane components of the stray field emerging from the sample, i.e., $\Delta\omega=\Delta\omega(\partial^2 B_x/\partial z^2,\ \partial^2 B_z/\partial z^2)$ (notation in figure 5.7). In addition, a ring appears at the right side of the dot, surrounding the area of attractive magnetic poles.

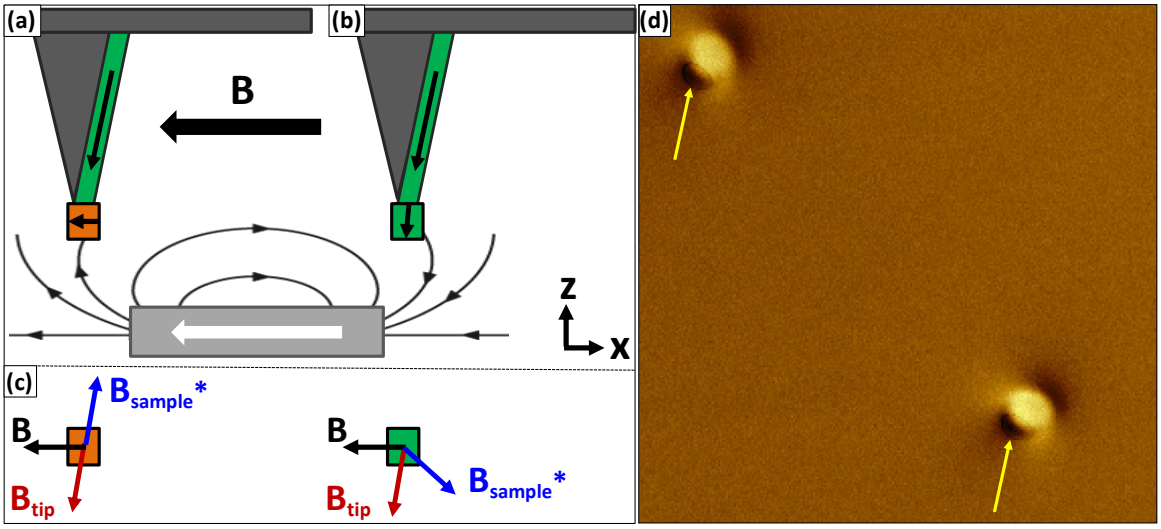

Figure 5.7: The suggested explanation. *Sketch of the proposed behavior of the MFM tip under an IP field (black arrow).* ***(a)*** *The softer domain at the apex is mainly oriented parallel to the external field direction.* ***(b)*** *In certain regions, the influence of the sample stray field can switch its magnetization.* ***(c)*** *Local direction of the external magnetic field (B), stray field from the sample ($B_{sample*}$) and effective field due to the magnetic coating on the tip side (B_{tip}), in those situations presented in (a) and (b).* ***(d)*** *MFM image showing two rings highlighted by yellow arrows, in two different nanostructures.*

As shown in figures 5.6.c-d, although there is a change in both the shape and size of the ring with varying tip-sample distance, the feature remains present. It is important to note that this behavior was reproducible for all the dots explored. A proof of that is presented in figure 5.7.d, where two rings of the same size are simultaneously present in two different nanostructures. Unfortunately, the (10 x 10) μm^2 image was recorded with a pixel area of (40 x 40) nm^2 and a lousy resolution was obtained. It indirectly gives an idea of the reduced lateral size of the ring walls, which is well below the specified pixel size. Furthermore, a remarkably low power loss is associated to them, in the order of tenths of fW and comparable to the experimental noise. Such high sensitivity was possible since experiments were carried out in vacuum conditions, where the enhanced quality factor of the oscillating cantilever (close to 70 times larger than in the experiments shown in previous section) allows for detecting much smaller changes.

The unexpected lines in the magnetic images remind of the dissipative contour lines observed and described in previous section. This gives us a hint to explain this phenomenon, thus attributing them to the influence the sample has in the sensing probe that causes some spins to orientate along the local field once a critical value is reached. In the following, we will assume that the *MFM* tip has **two different magnetic regions**, as described in figure 5.7: the thin film deposited on one of the side walls of the pyramid and a magnetically **softer region at the tip apex**. The region at the apex may switch its magnetization due to the influence of the local magnetic field. This magnetization switching in the tip gives rise to a sudden variation of the magnetostatic interaction between tip and sample, causing changes in the cantilever dissipation as well as in the frequency shift, which is determined by the force gradient ($\Delta\omega \approx - \omega_0/2k \cdot \partial F/\partial z$). In this simple description, three different components contribute to the field at the tip apex: the external field (created by an external magnet and labeled as B in fig. 5.7), the effective field (accounting for exchange and magnetostatic couplings) created by the thin film deposited on the side wall (B_{tip} in fig. 5.7), and the field emerging from the magnetic sample ($B_{sample*}$). Note that only the last contribution depends on the relative tip-sample position.

Based on this simple tip model, we now present the results obtained from micromagnetic simulations using *OOMMF*, which were carried out for a permalloy dot with the same dimensions as in the experiment. The stray field emerging from the resulting spin distribution was calculated in an empty volume above it. Standard permalloy parameters (saturation magnetization M_S=860 kA/m, exchange stiffness A=13·10^{-12} J/m, magnetocrystalline anisotropy K_1=0 J/m^3) and a cubic cell of side 5 nm were used. Figure 5.8.a shows the simulated equilibrium magnetization under an external field of B=60 mT applied along the horizontal direction, analogously to the experimental case. The magnetic field created by the sample under these conditions is evaluated and constant B_z^* surfaces (or iso-surfaces) are analyzed. These iso-surfaces display all points in space where the Z

component of the sample stray field reaches a specific value. Different values of B_z^* show qualitatively similar behavior, an example of which is presented in figure 5.8.b. This corresponds to all points in the region above the sample in which the *Z* component of the stray field emerging from the *Py* dot is B_z^* = -14.0 mT. A certain field range of ± 0.3 mT around the central value is considered, which accounts for statistical deviations from the critical value.

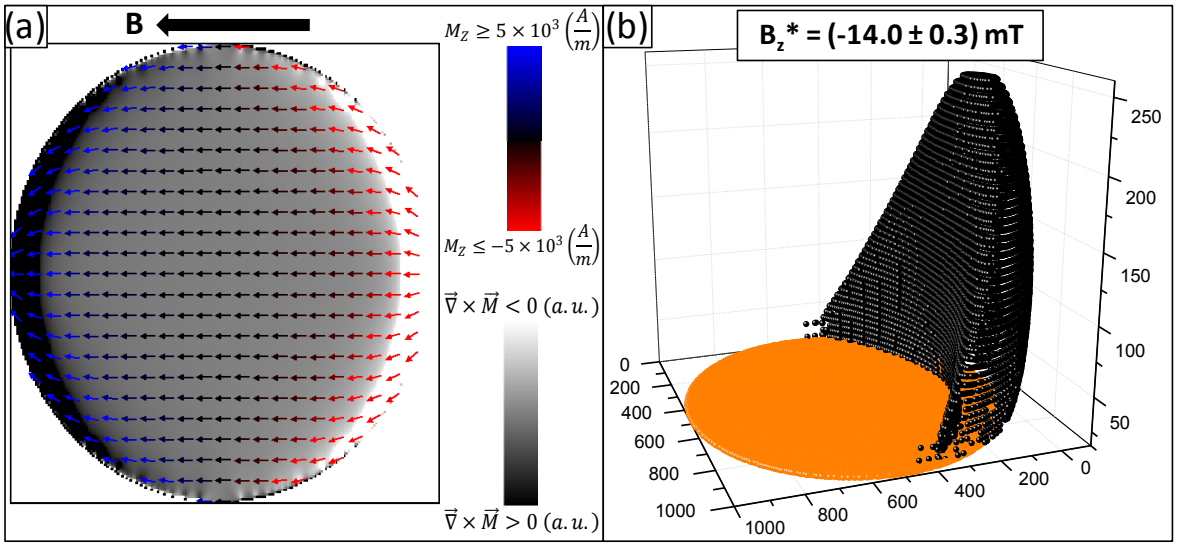

Figure 5.8: Simulations. (a) *Simulated magnetization distribution of a Py dot under an external field of 60 mT applied along the horizontal direction.* ***(b)*** *Magnetic field emerging from the magnetization distribution shown in (a). In black, the points in which B_{z^*}=(-14.0 ± 0.3) mT. The orange region represents the Py dot.*

The predicted magnetic state of the Py dot is a quasi-saturated single domain state. The calculated iso-surface displays a parabolic shape that resembles the features observed in former section (see figure 5.5). The maximum lies above the region of the sample with a highest density of negative magnetic poles (since a negative value of B_z^* was chosen). This simulation strongly supports the assumptions made in previous section, where the magnetic field coming out of the sample was considered to be responsible for changes in the tip configuration. Let us now look for a deeper understanding of current results. Our *MFM* images were taken at constant height from the sample surface. Therefore, by taking slices of the calculated *3D* paraboloid at different heights, we can compare their shape to the rings observed in the experimental images, as is done in figure 5.9. Both experimental data and simulations show that the ring shape becomes rounder and it gets smaller, as the separation distance increases. Furthermore, in both cases the ring wall widens as the probe withdraws and comes closer to the ceiling of the paraboloid, corresponding to a tip sample separation of around 250 nm. Note that no data treatment was performed trying to reproduce the experimental results. The bounding value used in this example, B_z^* = (-14.0 ± 0.3) mT, was chosen trying to get the best fit to the experimental data.

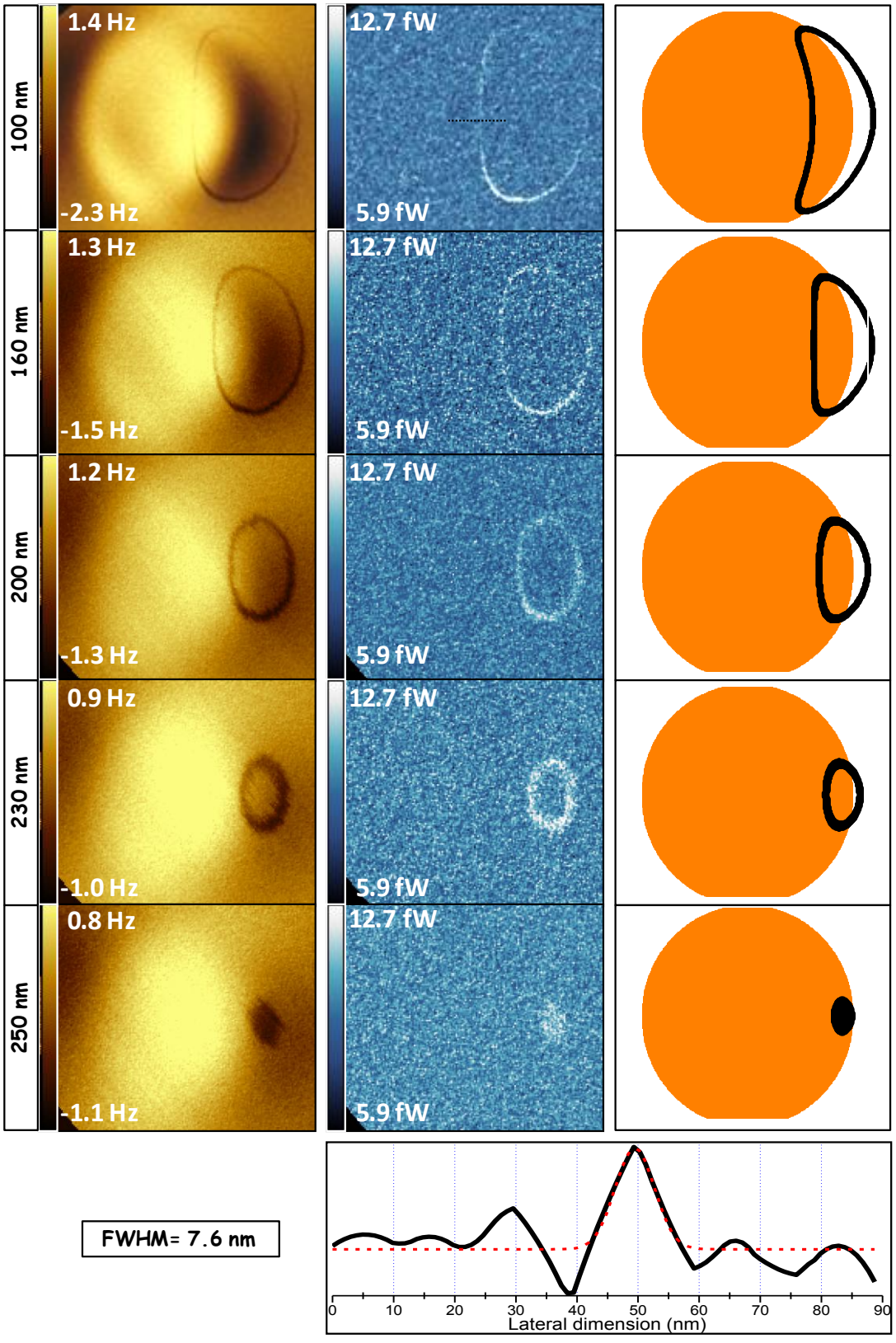

Figure 5.9: Experiment vs Theory. (left column) *Frequency shift and* ***(central column)*** *dissipation data, compared to* ***(right column)*** *the simulations (XY-cross sections in figure 5.8.b), at increasing tip-sample distance.* ***(Bottom)*** *Profile along the black dashed line in the dissipation image at 100 nm yields a FWHM of 7.6 nm. Size of the experimental images: (1.5x1.2)* μm^2.

This outstanding agreement supports the proposed model. When the tip is far from the sample, spins in the softer region at the apex orient themselves along the direction of a strong external field (figure 5.7.a). Whenever a critical value of B_z^* (the *Z* component of the stray field emerging from the sample) is reached as the tip approaches the concentration of magnetic poles, a switching of the magnetization in the softer domain takes place (fig. 5.7.b). This switching causes the ring feature to appear both in the frequency shift and dissipation images and it thus should not be interpreted as part of the sample domain structure. In fact, the ring corresponds to a contour line of the critical field B_z^*, suggesting that the observed phenomenon can be used to obtain *3D* maps of the sample stray field. As observed in the profile plotted in figure 5.9, the spatial resolution reached for these features is **below 8 nm** at a lift height of 100 nm. This resolution was actually limited by the pixel size (7.8 nm). Notice that neither the *MFM* nor the power loss images show a significant change in the regions inside the rings in figure 5.9. There, magnetostatic interactions look similar and no significant dissipation is detected over the experimental noise, as compared to figures 5.2 and 5.5. This suggests that only a considerably small portion of the tip is flipping the spin orientation; as a consequence, the averaged magnetic interaction remains quite the same. In fact, the dissipation peaks measured in this work are around 20 times smaller than the ones presented in previous section.

Further support for this tip-induced dissipation model comes from the fact that these rings appear solely on one side of the dot, i.e., the magnetization switching in the tip is dependent on the **direction of the stray field** from the sample. The tip magnetization is mainly oriented along the side wall of the pyramidal tip, indicated as the green region in figure 5.7.a. The magnetization at the apex switches only when both the *Z* components of B_{tip} (effective field due to the tip side coating) and B_{sample}^* (sample stray field) are parallel and add to each other (fig. 5.7.b). On the other side of the sample, these two components point to opposite directions and the resulting field is thus insufficient to induce the switching. In the case when small fields are applied (fig. 5.6.a-b), the shape anisotropy of the tip suffices to keep the magnetization at the apex along the out of plane direction at every point. As a consequence, no ring is present in the images.

The proposed model predicts another measurable effect: the width of the observed rings should depend on the oscillation amplitude. As sketched on the left column in figure 5.10, larger oscillation amplitudes should allow the tip to pass through the critical paraboloid for a wider range of pixels (effectively thickening the imaging "plane" in the *Z* direction) to produce wider rings. Successive measurements were performed at a mean scanning lift height of 230 nm for three different amplitudes. As expected, larger oscillation amplitudes reveal thicker rings (right column in figure 5.10). At large enough amplitudes, the tip crosses the critical iso-surface at every single point within the limits of the ring, yielding a disk instead (fig. 5.10.c and f).

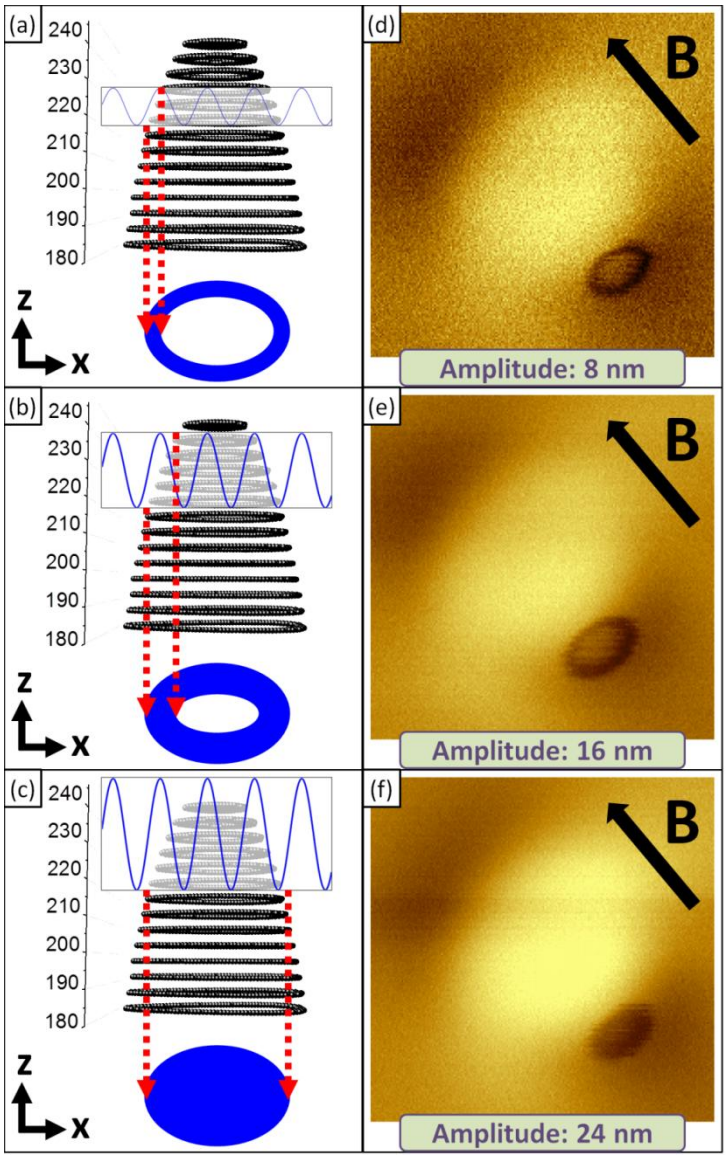

Figure 5.10: Dependence of the ring on the oscillation amplitude. ***(a)–(c)*** *X-Z cross sections from figure 5.8.b (z>180nm is shown).* ***(d)–(f)*** *MFM images showing this effect, at a mean separation of 230 nm.*

In summary, we showed that *MFM* tips can be a source of artifacts that may lead to misinterpretation of domain configurations in magnetic samples. Our simple proposed model assumes an *MFM* tip structure with two distinct domain regions: a hard single domain covering most of the tip side wall and a small, softer domain at the tip apex whose magnetization can switch by the influence of the sample. The model can describe the rings observed in experimental *MFM* and dissipation data. We performed micromagnetic simulations to validate the proposed model, which yielded excellent agreement with the experimental observation. We also suggest that this kind of tip can measure three dimensional maps of the *Z* component of the magnetic field emerging from the sample. Remarkably, a very high spatial resolution below 8 nm at tip-sample distances over 100 nm was achieved and limited, in the case shown, by the pixel size.

Conclusions

i - Magnetization reversal processes have been studied by **Variable Field Magnetic Force Microscopy (VF-MFM)** in different samples. First, the magnetostatic coupling between neighboring permalloy nanostripes separated 500 nm from each other is observed experimentally to not be significant. Micromagnetic simulation predict different couplings for stripes with small longitudinal or transversal separations, with a reversal that starts at the border of the simulated area and propagates in a chain reaction to the closest stripe. As a result, following article has been published:

***[1] Ó. Iglesias-Freire**, M. Jaafar, L. Pérez, O. de Abril, M. Vázquez and A. Asenjo, Journal of Magnetism and Magnetic Materials 355 (2014) 152-157*

Second, a useful MFM-based operating mode has been introduced, in which the tip is scanning along one profile while the external field is changed. This allows for quantification of critical fields in individual nanomagnets and examples in single domain nanostripes have been presented. As a result, following paper has been published:

***[2]** M. Jaafar, L. Serrano-Ramón, **O. Iglesias-Freire**, A. Fernández-Pacheco, M. R. Ibarra, J. M. de Teresa and A. Asenjo, Nanoscale Research Letters 6 (2011) 407*

Cylindrical $Fe_{68}Co_{27}Cu_5$ nanowires with a modulated diameter have carefully been studied with VF-MFM. The resulting complex contrast has been interpreted as having two origins: the modulated shape -that causes the locally strong divergence of the magnetization- and morphological roughness arising from the growth of the grains -that yields weaker divergence. Simulations are used to help discern the single domain states from states with pinned domain walls. A paper reporting on these results will be submitted shortly.

Epitaxial cobalt stripes grown onto vicinal Si substrate are shown to have a magneto-crystalline easy axis along the short side of the nanostructures. The evolution of the domain structure against the stripe width is studied and the reversal processes carefully detailed. In addition, a remarkable resolution is obtained that allows for identifying the walls as single or double-vortex *DWs*. This work has been published in the following article:

***[3]** Yu. P. Ivanov, **Ó. Iglesias-Freire**, E. V. Pustovalov, O. Chubykalo-Fesenko y A. Asenjo, Physical Review B 87 (2013) 184410*

Last, the domain structure of *LSMO* nanoislands is studied by *MFM* and compared to simulations. Depending on the dimensions, different structures are observed. The crystalline anisotropy is believed to play a role in the orientation of the single-domain smallest islands. This is described in:

[4] *J. Zabaleta, M. Jaafar, P. Abellán, C. Montón,* ***O. Iglesias-Freire****, F. Sandiumenge, C. A. Ramos, R. D. Zysler, T. Puig, A. Asenjo, N. Mestres y X. Obradors, Journal of Applied Physics 111 (2012) 024307*

ii - Successful separation of **electrostatic and magnetostatic signals** has been demonstrated by introducing a *Kelvin Probe Force Microscopy* (*KPFM*) feedback during the *MFM* experiments. It has been used to extract the real domain configuration in cobalt stripes with strong electrostatic effects, a work that was published in 2011:

[5] *M. Jaafar,* ***O. Iglesias-Freire****, L. Serrano-Ramón, M. R. Ibarra, J. M. de Teresa y A. Asenjo, Beilstein Journal of Nanotechnology 2 (2011) 552-560*

In addition, this *KPFM-MFM* combination has allowed the characterization of magnetic stray field gradients emerging from *MFM* tips with graphene based *Hall* sensors, by getting rid of the spurious Coulomb deflections of electrons in the graphene layer. Two articles have resulted from this collaboration:

[6] *V. Panchal,* ***Ó. Iglesias-Freire****, A. Lartsev, R. Yakimova, A. Asenjo and O. Kazakova, IEEE Transactions on Magnetics 49 (2013) 3520-3523*
[7] *R. K. Rajkumar, A. Asenjo, V. Panchal, A. Manzin,* ***Ó. Iglesias-Freire*** *and O. Kazakova, Journal of Applied Physics 115 (2014) 172606*

iii - A low time consuming and low cost method of **customizing *MFM* probes** has been presented. These homemade sensors show high performance, in terms of spatial resolution (having demonstrated magnetic lateral resolution below 25 nm), reduced stray field (by mapping a double-vortex state in circular Co dots while tracking the topography) and chemical sensitivity (where a resolution of 5 nm with a signal-to-noise ratio of 400 was shown). Regarding the study of magnetic vortices in circular nanostructures, I co-authored the following article:

[8] *F. G. Aliev, D. Dieleman, A. A. Awad, A. Asenjo,* ***O. Iglesias-Freire****, M. García-Hernández y V. Metlushko, Electromagnetics in Advanced Applications (ICEAA), 2010 International Conference on, (2010) 160-163*

iv - Last, by studying the **magnetic energy losses** caused by the oscillating tip-sample separation, we showed that *MFM* tips can be a source of artifacts that may lead to misinterpretation of domain configurations in magnetic samples. This work has been published in the following article:

***[9] Ó. Iglesias-Freire**, J. R. Bates, Y. Miyahara, A. Asenjo and P. H. Grütter, Applied Physics Letters 102 (2013) 022417*

v - Finally, I have published two articles that illustrate the **multidisciplinary** character of this thesis and have not been mentioned before. The first one came out from a parallel work I carried out during one of my research stays at the *McGill University*. It deals with charge accumulation in *FIB* patterned SiN stencils, arising from implanted Ga^+ ions, which strongly influenced the growth and magnetic properties of $Ni_{97}Fe_3$ nanostructures. The reference can be found in:

***[10]** J. R. Bates, Y. Miyahara, J. A. J. Burgess, **Ó. Iglesias-Freire** and P. H. Grütter, Nanotechnology 24 (2013) 115301*

Last, I performed conductivity measurements in multiferroic nanocomposites using *C-AFM*, in the framework of a collaboration involving several research groups at the *Material Science Institute of Madrid*. It has recently been published in:

***[11]** M. Algueró, J. Ricote, M. Torres, H. Amorín, A. Alberca, **O. Iglesias-Freire**, N. Nemes, S. Holgado, M. Cervera, J. Piqueras, A. Asenjo y M. García-Hernández, ACS Applied Materials & Interfaces 6 (2014) 1909*

Conclusiones

i – Se han estudiado procesos de inversión de la imanación en diferentes muestras, por medio de microscopía de fuerza magnética de campo variable. En primer lugar, se ha observado que el acoplamiento magnetostático entre nanohilos vecinos no es significativo para separaciones de 500 nm. Simulaciones micromagnéticas predicen acomplamientos diferentes para elementos con pequeñas separaciones longitudinales o transversales, con una inversión que comienza en los extremos del área simulada y se propaga en una reacción en cadena al hilo más cercano. Como resultado, se ha publicado el siguiente artículo:

***[1] Ó. Iglesias-Freire**, M. Jaafar, L. Pérez, O. de Abril, M. Vázquez and A. Asenjo, Journal of Magnetism and Magnetic Materials 355 (2014) 152-157*

En segundo lugar, se ha introducido un modo de medida basado en *MFM* en el cual la punta escanea continuamente un perfil topográfico determinado, mientras se varía gradualmente el campo externo. Ello permite la cuantificación de campos críticos en nanoestructuras individuales y se presentan ejemplos para el caso de nanohilos planos de cobalto. El siguiente artículo ha resultado de esta investigación:

***[2]** M. Jaafar, L. Serrano-Ramón, **O. Iglesias-Freire**, A. Fernández-Pacheco, M. R. Ibarra, J. M. de Teresa and A. Asenjo, Nanoscale Research Letters 6 (2011) 407*

Además, se han estudiado nanohilos cilíndricos de $Fe_{68}Co_{27}Cu_5$ con un diámetro modulado. El complejo contraste resultante ha sido atribuido a dos causas: la geometría modulada (que provoca una fuerte divergencia local de la imanación) y una rugosidad morfológica que surge del crecimiento de los granos cristalinos (y que provoca una divergencia más atenuada). Se han usado simulaciones para ayudar a distinguir los estados monodominio de estados con paredes de dominio ancladas. Planeamos enviar un artículo con estos resultados para su evaluación en una revista de prestigio en las próximas semanas.

Por otro lado, se ha mostrado que nanohilos planos de cobalto epitaxial, crecidos sobre un sustrato de silicio vicinal, poseen un eje fácil magneto-cristalino a lo largo del eje corto de las nanoestructuras. Se ha detallado cuidadosamente la evolución de la estructura de dominios, en función de la anchura del nanohilo. Asimismo, se ha obtenido una resolución espacial destacable que permite indentificar las paredes de dominio como de tipo un vórtice o de doble vórtice. Este trabajo ha sido publicado en el siguiente artículo:

[3] *Yu. P. Ivanov,* ***Ó. Iglesias-Freire****, E. V. Pustovalov, O. Chubykalo-Fesenko y A. Asenjo, Physical Review B 87 (2013) 184410*

Por último, se ha estudiado la estructura de dominios de nanoislas de *LSMO* mediante *MFM* y se ha comparado con simulaciones. Dependiendo de las dimensiones, se observan diferentes estructuras. Creemos que la anisotropía cristalina desempeña un papel en la orientación de las partículas más pequeñas, en estado monodominio. Esto se encuentra detallado en:

[4] *J. Zabaleta, M. Jaafar, P. Abellán, C. Montón,* ***O. Iglesias-Freire****, F. Sandiumenge, C. A. Ramos, R. D. Zysler, T. Puig, A. Asenjo, N. Mestres y X. Obradors, Journal of Applied Physics 111 (2012) 024307*

ii – Se ha demostrado la separación exitosa de señales electrostática y magnetostática, mediante la introducción de un feedback *Kelvin Probe Force Microscopy* (*KPFM*) durante el experimento de *MFM*. Esta implementación se ha usado para extraer la configuración de dominios real en nanohilos planos de cobalto con fuertes efectos electrostáticos, un trabajo que fue publicado en 2011:

[5] *M. Jaafar,* ***O. Iglesias-Freire****, L. Serrano-Ramón, M. R. Ibarra, J. M. de Teresa y A. Asenjo, Beilstein Journal of Nanotechnology 2 (2011) 552-560*

Además de ello, esta combinación de *MFM-KPFM* ha permitido caracterizar gradientes de campo magnético emanando de puntas de *MFM* mediante dispositivos *Hall* de grafeno, al deshacerse de las deflexiones coulombianas de electrones en la capa de grafeno. Dos artículos han resultado de esta colaboración:

[6] *V. Panchal,* ***Ó. Iglesias-Freire****, A. Lartsev, R. Yakimova, A. Asenjo and O. Kazakova, IEEE Transactions on Magnetics 49 (2013) 3520-3523*
[7] *R. K. Rajkumar, A. Asenjo, V. Panchal, A. Manzin,* ***Ó. Iglesias-Freire*** *and O. Kazakova, Journal of Applied Physics 115 (2014) 172606*

iii – Se ha presentado un método rápido, simple y económico de personalizar puntas de *MFM*. Estas puntas caseras muestran un gran comportamiento en términos de resolución espacial (habiendo demostrado una resolución lateral magnética por debajo de 25 nm), reducido campo emergente (mediante el mapeado de un estado de doble vórtice en estructuras circulares de cobalto) y sensibilidad química (donde se ha mostrado una resolución de 5 nm con una relación señal/ruido

de 400). Con respecto al estudio de vórtices magnéticos en nanoestructuras circulares, soy coautor del siguiente trabajo:

[8] *F. G. Aliev, D. Dieleman, A. A. Awad, A. Asenjo,* ***O. Iglesias-Freire****, M. García-Hernández y V. Metlushko, Electromagnetics in Advanced Applications (ICEAA), 2010 International Conference on, (2010) 160-163*

iv – Además, mediante el estudio de pérdidas de energía magnética, hemos mostrado que las puntas de *MFM* pueden ser una fuente de artefactos que lleven a una interpretación errónea de las configuraciones de dominios en muestras magnéticas. Este trabajo ha sido publicado en el siguiente artículo:

[9] Ó. Iglesias-Freire*, J. R. Bates, Y. Miyahara, A. Asenjo and P. H. Grütter, Applied Physics Letters 102 (2013) 022417*

v – Finalmente, he publicado dos artículos que ilustran el carácter multidisciplinar de esta tesis y que no han sido mencionados anteriormente. El primero de ellos resultó de un trabajo paralelo desarrollado durante una de mis estancias de investigación en la *McGill University*. Trata sobre la acumulación de carga en máscaras de nitruro de silicio con un patrón fabricado por *FIB*, como consecuencia de los iones de Ga^{+} implantados, que influyen fuertemente en el crecimiento y propiedades magnéticas de nanoestructuras de $Ni_{81}Fe_{19}$. La referencia a este trabajo puede encontrarse en:

[10] *J. R. Bates, Y. Miyahara, J. A. J. Burgess,* ***Ó. Iglesias-Freire*** *and P. H. Grütter, Nanotechnology 24 (2013) 115301*

Por último, realicé medidas de conductividad en nanocompuestos multiferroicos, usando *C-AFM*, en el marco de una colaboración que involucra a varios grupos de investigación del *Instituto de Ciencia de Materiales de Madrid*. Ha sido recientemente publicado en:

[11] *M. Algueró, J. Ricote, M. Torres, H. Amorín, A. Alberca,* ***O. Iglesias-Freire****, N. Nemes, S. Holgado, M. Cervera, J. Piqueras, A. Asenjo y M. García-Hernández, ACS Applied Materials & Interfaces 6 (2014) 1909*